NATIONAL & INTERNATIONAL SCIENTIFIC EVENTS

39th IAHR World Congress

Venue: Palacio de Congresos de Granada
Location: Granada, Spain

Begins: July 4, 2021
Ends: July 9, 2021

50th International Congress and Exposition on Noise Control Engineering

Venue: Marriott Wardman Park
Location: Washington, USA

Begins: August 1, 2021
Ends: August 4, 2021

25th International Congress of Theoretical and Applied Mechanics

Venue: MiCo Congress Centre
Location: Milano, Italy

Begins: August 22, 2021
Ends: August 27, 2021

20th International Conference on Soil Mechanics and Geotechnical Engineering 2021

Venue: International Convention Centre
Location: Sydney, Australia

Begins: September 12, 2021
Ends: September 17, 2021

18th International Conference on Microwave and High Frequency Applications (AMPERE 2021)

Venue: Chalmers University of Technology
Location: Gothenburg, Sweden

Begins: September 13, 2021
Ends: September 16, 2021

14th Mediterranean Congress of Chemical Engineering

Venue: Gran Via Venue, Pavillion 3
Location: Barcelona, Spain

Begins: September 14, 2021
Ends: September 17, 2021

17th International Symposium on Biopolymers (ISBP 2021)

Venue: Congress Center Le Regent
Location: Crans-Montana, Switzerland

Begins: September 14, 2021
Ends: September 17, 2021

2021 International Conference on Smart Transportation and Future Mobility (CSTFM 2021)

Venue: Virtual Environment
Location: Frankfurt, Germany

Begins: September 17, 2021
Ends: September 19, 2021

8th World Congress on Engineering and Technology (CET 2021)

Venue: The Grand Dynasty Culture Hotel
Location: Xi'an, China

Begins: October 22, 2021
Ends: October 24, 2021

42nd Ibero-Latin-American Congress on Computational Methods in Engineering (XLII CILAMCE)

Venue: Virtual Environment
Location: Rio de Janeiro, Brazil

Begins: November 09, 2021
Ends: November 12, 2021

IEEE 40th International Conference on Consumer Electronics

Venue: Tuscany Suites and Casino
Location: Las Vegas, USA

Begins: January 07, 2022
Ends: January 09, 2022

The 35th International Conference on Micro Electro Mechanical Systems

Venue: Tokyo International Forum
Location: Tokyo, Japan

Begins: January 09, 2022
Ends: January 13, 2022

Abstracted & Indexed in:

TR Dizin Mühendislik ve Temel Bilimler Veri Tabanı |
CrossRef | Google Scholar | MIP Database | StuartxChange | ResearchBib | Scientific Indexing Services (SIS)

HITTITE

HJSE Official Journal of Hitit University Volume 8, Issue 2, 2021 dergipark.org.tr/en/pub/hjse

ISSN 2148-4171

HİTİT UNIVERSITY

JOURNAL OF SCIENCE & ENGINEERING

HITTITE

HJSE Official Journal of Hitit University Volume 8, Issue 2, 2021 dergipark.org.tr/en/pub/hjse

Volume 8, Issue 2, 2021

dergipark.org.tr/en/pub/hjse

JOURNAL OF SCIENCE & ENGINEERING
HITTITE

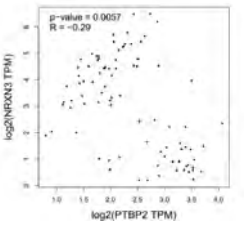

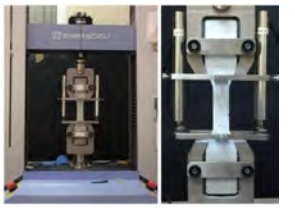

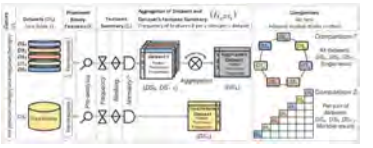

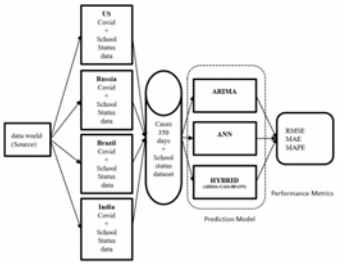

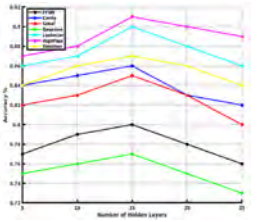

JOURNAL OF SCIENCE & ENGINEERING
HITTITE

CONTENT

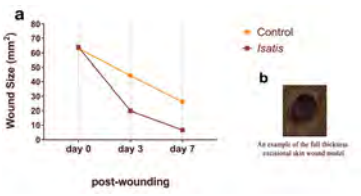

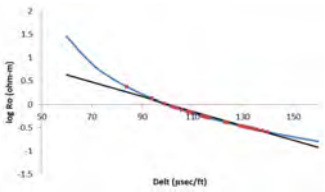

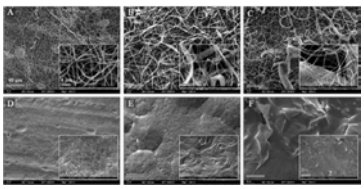

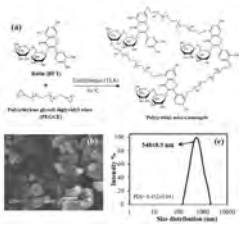

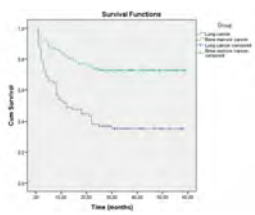

Owner
Prof. Dr. Ali Osman ÖZTÜRK on behalf of Hitit University

Editor-in-chief
Prof. Dr. Ali KILIÇARSLAN

Associate Editors
Prof. Dr. D. Ali KÖSE
Assoc. Prof. Dr. Öncü AKYILDIZ

Production
Assoc. Prof. Dr. Kazım KÖSE
Res. Asst. Dr. Erhan ÇETİN
Res. Asst. Mustafa Reşit HABOĞLU
Res. Asst. Harun Emre KIRAN
Res. Asst. Ömer Faruk TOZLU
Lect. Tugrul YILDIRIM

Editor's Office
Tel: +90 364 227 45 33 / 12 36
Fax: +90 364 227 45 35
Email: alikilicarslan@hitit.edu.tr

Subscription Service:
Tel: +90 364 227 45 33 / 12 82
Fax: +90 364 227 45 35
Email: hjse@hitit.edu.tr

EDITORIAL BOARD

Journal Name	: HITTITE JOURNAL OF SCIENCE AND ENGINEERING
Year	: 2021
Managing Editor	: Prof. Dr. Ali KILIÇARSLAN
Managing Office	: Hitit University Faculty of Engineering
Managing Office Tel	: +90 364 227 45 33 / 12 36
Publication Language	: English
Publication Type	: Peer Reviewed, Open Access, International Journal
Delivery Format	: 4 times a year (quarterly)
Print ISSN	: 2149-2123
Online ISSN	: 2148-4171
Publisher Address	: Hitit Üniversitesi Kuzey Kampüsü Çevre Yolu Bulvarı 19030 Çorum / TÜRKİYE
Publisher Tel	: +90 364 227 45 33/1236

This new issue of Hittite Journal of Science and Engineering contains twelve manuscripts from the disciplines of chemistry, molecular biology and genetics, bioengineering, petrolium engineering, civil engineering, computer science and engineering. These manuscripts was first screened by Section Editors using plagiarism prevention software and then reviewed and corrected according to the reviewer's comments. I would like to express my gratitude to all our authors and contributing reviewers of this issue.

I would like to thank to the new President of Hitit University, Prof. Dr. Ali Osman Öztürk, for his support and interest in HJSE and also to the Section Editors of HJSE, namely Prof. Dr. Dursun Ali Kose and Assoc. Prof. Dr. Oncu Akyildiz, as well as our Production Editors Assoc. Prof. Dr. Kazim Kose, Mustafa Reşit Haboğlu, Dr. Erhan Çetin, Tugrul Yildirim, Harun Emre Kıran and Ömer Faruk Tozlu for their invaluable efforts in making of the journal.

It's my pleasure to invite the researchers and scientists from all branches of science and engineering to join us by sending their best papers for publication in Hittite Journal of Science and Engineering.

Prof. Dr. Ali Kilicarslan

Editor-in-Chief

Hittite Journal of Science and Engineering, 2021, 8 (2) 85
ISSN NUMBER: 2148-4171
DOI: 10.17350/HJSE19030000218

Erratum to: Analysis of miRNA-Mediated ceRNAs In The Pathogenesis of Renal Cell Carcinoma: An In Silico Approach

Orcun AVSAR
Hitit University, Department of Molecular Biology and Genetics, Corum, Turkey

Article History:

Online: 2021/06/30

***Correspondence to**: Orcun Avsar, Hitit University, Molecular Biology and Genetics, 19030, Corum, Turkey*
E-Mail: orcunavsar.gen@gmail.com
Phone: +90 (364) 227 1658

CAUSE OF ERRATUM

The author recognized that some references are excluded and positioned in incorrect places due to the reference manager software after the manuscript [E1] is published. Immediately, the author requested from the journal for the corrections of the errors as follows.

INTRODUCTION

..... diseases such as cancer [9, 10, E2].

.....pathogenesis of diverse cancers [11, 12, E2, E3].

MATERIAL AND METHODS

..... 'Verified Target Module' [E3, 13].

..... ceRNA activity of the defined miRNAs [E3, 14].

..... (in the exonic region) and downstream [E3, 15].

..... used for the analysis of gene expression [E2, E3, 16].

References

E1 Avsar O. Analysis of miRNA-Mediated ceRNAs in the pathogenesis of renal cell carcinoma: an in silico approach. Hittite Journal of Science and Engineering 7 (2020) 223-238.

E2 Altay DU, Ergun S. In silico analysis of biomarker potentials of miRNA-mediated ceRNAs in gastric neoplasms. Middle Black Sea Journal of Health Science 5 (2019) 106-119.

E3 Ergun S. In silico analysis of biomarker potentials of miRNA-mediated ceRNAs in prostate cancer. Dicle Medical Journal 45 (2018) 415-429.

Appendix

Table A.2. The list of genes including T-UCR in their exonic regions according to the study [15].

Hittite Journal of Science and Engineering, 2021, 8 (2) 87–96
ISSN NUMBER: 2148–4171
DOI: 10.17350/HJSE19030000219

Realization of Gesture Control Application on Openmv Board Using Optical Flow in Real-Time Video Images

Bulent Turan
Tokat Gaziosmanpasa University, Department of Computer Engineering, Tokat, Turkey

ABSTRACT

OpenMV Board is designed for purpose of non-complex image processing applications. It is an image processing sensor that has been a MicroPython embedded operating-system(OS).

In the study, it is aimed to develop gesture control applications for electrical household appliances and small budget devices. Therefore, the hardware to be used should be cheap and the algorithm should be simple. Thus three gesture control applications have been developed by using OpenMv board for use in different electrical appliances. These are 1-level control, 2-multi-component simple system control and 3-page flip. The algorithms used in the study are independent of the user because they are optical flow-based. Thus, the use of low-cost simple gesture control applications for industrial purposes (electrical appliances) can be realized.

Algorithms developed for applications were written on the OpenMV IDE. These application results were monitored in real-time through the IDE. In addition, the algorithm developed for level control has been embedded and tested on an SD card on OpenMv independent of OpenMV IDE. During the test, output information was generated using OpenMV pins and the level indicator created using yellow, green and red LEDs connected to the pins was checked real-time. Thus, the algorithm was tested on a computer-independent embedded system.

Article History:
Received: 2020/12/01
Accepted: 2021/03/29
Online: 2021/06/30

***Correspondence to**: Bülent Turan,*
E-mail: bulent.turan@gop.edu.tr;
Phone: +90 505 737 6766.

Keywords: Gesture control, Low-cost control with image processing, Simple gesture control applications, Image processing sensors, Open source SmartCam

INTRODUCTION

Today, developments in the field of human-computer interaction (HCI) exponentially grows. HCI is most fundamentally carried out with keyboard and mouse. Humanity has been making efforts to develop the channel of interaction in this field. Today touch screens (especially indispensable on mobile devices), wearable devices, etc. are actively used in HCI. The technologies developed in this area and the studies that are still in progress can vary widely according to the purpose and place of use. For example, using webcam images to control of the cursor on the computer screen with the eye movements [1]. Control of smart TV, etc. systems [2, 3], control of humanoid robots [4], control with palm movement of the in-car multimedia device [5] can be realized by detecting and tracking of body movements with Kinect camera images.

Studies in the field of HCI began in the 1980s [6]. Especially in the 2000s, studies have intensified. Due to the fact that gesture control concerns all parts of the body, special sensors can be used in the region where the studies are focused and the data obtained can be processed with different methods. For example, only data received with an accelerometer are processed using statistical analysis methods [7, 8], while images captured with cameras are processed using image processing methods [9, 10, 11, 12, 13, 14, 15, 16, 17, 18, 19]. Also, both data received using the PIR sensor and accelerometer were used together with image processing methods and statistical analyzes [20, 21]. Even, studies were to determine the gestures to be accepted by the users and have been conducted out to determine which gesture will be used for what purpose [7, 22]. In addition, there are studies to compare the studies in the literature. These studies also determine the advantages and secrets of the techniques used under different conditions [23, 24].

Study;

• Within probability of use in small/daily household appliances,

• Low cost,

• It consists of gestures that each user can simply perform

They were designed to develop gesture control algorithms.

To this end, the gestures were first identified to enable the user requests to be digitized. In determining the gestures, similar studies [7,20] have been examined. It has been tried to choose the gestures that will be catchy and unforgettable for users. Determined gestures should be able to digitize user requests such as level control, multi-component system control, page flip application. It must also consist of hand movements that can be easily repeated by each user.

In order to lower the application cost, the source code (without licensing and programming problems) and circuit diagrams must be accessible by the public, capable of cost-effective image processing (only determination of the direction of movement is sufficient), and supported by the embedded OS. The preferred OpenMV Board is an image processing sensor with MicroPython embedded OS that meets all these requirements. Image processing sensors can be developed from simple to complex for very comprehensive image processing applications. This can lead to a very wide range of costs. However, the study focuses on the movement direction of the user's hand movements and the follow-up of the sequential movements. OpenMV board allows the cost of the hardware to remain at the desired levels.

A wide range of work in the field of gesture control leads to different levels of technology at the same time. On the one hand, high technology studies including machine learning, artificial intelligence, image processing techniques and 3D are continuing in the laboratory. These studies are used in developed and specific applications today. However, they are high-cost applications. On the other hand, a single image processing function for industrial purposes and software algorithms can be carried out. Especially in applications such as simple home appliances and in-car multimedia control, it is possible to achieve sufficient results with optics flow information in the moving image and optimized studies with a good software algorithm. In such studies, many gestures can be defined when a steady determination and follow-up of organs such as hands, fingers, body, and eyes can be made. Using these gestures, many control applications can be performed. Simple industrial applications can be controlled with simple image processing methods by identifying a small number of gestures. For example, if we only want to perform a control operation on a multimedia system, it is sufficient to perform a few basic checks such as switching on/off, changing channels, increasing or decreasing the volume. Or, it is sufficient to perform the controls in the form of on-off, forward-back page-turning for the reading of an electronic book.

In this study, no organs of the user were detected and followed in the images captured from the camera. The aim of the study was to determine the direction of movement in a real-time image. With the algorithm developed using motion direction data, certain movements have been determined in a stable manner. Thus, the algorithm developed can be operated quickly on a card with a camera module and used for industrial purposes.

RELATED WORK

In the literature, it has been tried to develop gesture control applications by using different equipments. Some of those;

Image Processing Based Gesture Control Studies

Lee et all. have tried to develop a smart TV system with body movements. They used a Kinect camera in their study. Program opening, channel switching (increase/decrease), web page scrolling, return to homepage and exit are all expressed by separate body movements [2]. The necessity of using a special camera for this study is a disadvantage in terms of cost. Communication with the television can only be achieved by standing up and determined body movements. The challenge of standing up and the difficulty of carrying out wide-area movements is another disadvantage of this study.

Bellmore et al. have preferred Kinect camera in their work. They used to face and gesture control in their study [3]. It has similar disadvantages with other work with Kinect cameras. The method also requires a separate calibration for each user. The calibration stage can be unsuccessful according to the user's special situation (plenty of clothes, bags etc., having children, etc.) [3]. This is a major disadvantage because it can not be used in simple applications. Yavşan used a Kinect camera in his study, detected human upper body movements in real-time, and transferring them to a humanoid robot, simulating the human being by the robot [4]. A similar study was performed without using Kinect

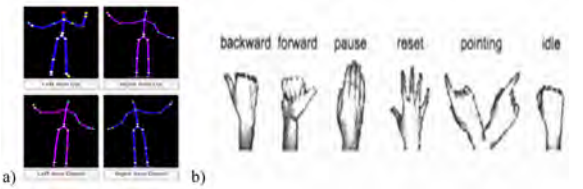

Figure 1. a) Kinect based 3D human gestures [5] b) Akyol et al. gestures and functions they use in their study [10]

camera by Kaura [15]. He captures images of the palm of the user at close range and morphologically determined the direction of motion and guided the robot [15]. On the other hand, Raghu produced control signals by detecting and following his hand similarly. He developed the application in a Matlab environment and did not use it as embedded [16].

Rahman et al. in their work, aimed to control the in-car multimedia device with hand movements. Due to the use of simple hand movements in the narrow space [5], there are many similarities with my study. However, in this study, the use of a Kinect camera will obviously affect the cost negatively. In addition, only one application was developed in the study [5]. The developed application in the study, is similar to the proposed multi-component simple system control algorithm in my study. But the other two algorithms do not meet. The sample images they use for the detection of movements with the Kinect camera was shown in Fig 1a.

In another study, an image processing-based gesture control algorithm was recommended. In this study, both the camera used and simple gestures in the narrow space was recommended for the control process [10]. For this reason, it is advantageous for simple systems. However, in order for the study to be carried out, the hand must be recognized and followed up [10]. Recognition and tracking increase the processing load in such applications. For this reason, it can be advantageous in real-time applications by reducing the processing load and removing the recognition and follow-up operations from the algorithms. The sample images they use for the detection of movements are shown in Fig 1b.

Accelerometer Based Gesture Control

Mantyjarvi et al. planned the gesture control based on the accelerometer. In their study, they examined what different users prefer for different functions and the complexity of these movements [8]. In general, it was observed that the movements that the users prefer for different functions differ [8]. Generally;

On – off	->	push –pull
Next – previous	->	right-left
İncrease – decrease	->	up – down

They stated that hand gestures on the right can be accepted to represent functions on the left. [8]. These gestures, which are determined for accelerometer-based studies, can be used in image processing-based applications.

Also, Kela and al. were worked to identify gestures for accelerometer-based VCR control [7]. Similarly, in this study next and previous were expressed in the same way with right and left movements by users. Up and down movements are adopted for play and stop. As a result, the acceptance of the gestures may vary slightly depending on the characteristics of the device to be controlled

MATERIALS

These algorithms developed in the study will be run on the OpenMv board. OpenMV; It has a 216 MHz ARM Cortex M7 processor, 512 KB RAM, 64 KB heap space, MicroPython embedded operating system and a 0.3 MP camera which can be captured 640x480 sized grayscale image [25]. The IDE has been developed by the developer to program the OpenMv board. Applications can be developed with MicroPython embedded OS. In addition, the developer presents examples of card-specific image processing functions available to programmers.

Some examples of applications and functions offered by the developer are given below.

- Image filters
- Optical flow function
- Morphologic functions
- Edge functions
- Feature detection
- Face detection
- Eye tracking
- Color tracking
- Motor control applications
- Machine learning applications
- Barcode applications

In addition, applications and functions continue to be developed by the developer.

The study focuses on the movements in the image. Therefore, it is important to determine the optical flow as stable. The optical flow application on the OpenMV board is performed with the find_displacement function. The function is applied to two consecutive images and returns the changes in x-direction (delta_x), y-direction (delta_y), and response coefficient between the previous image and the next image. The fact that the response value is close to 1 indicates the high-reliability rate. It is accepted that there is no trouble as long as the response value is above 0.2

Table 1. Optical flow application (find_displacement) made in OpenMV compared with optical flow application (estimateFlow) made in MATLAB.

	find_displacement OpenMV	*estimateFlow MATLAB*
input	*Consecutive two images of gray level*	*Consecutive two images of gray level*
output	*Delta_x, Delta_y, Response*	*Vx, Vy, Orientation, Magnitude*

- Delta_x; Gives information about the change in x-direction within the image
- Delta_y; Gives information about the change in y-direction within the image.

• Vx ; X variable of change rate calculated separately for each pixel

• Vy ; Y variable of change rate calculated separately for each pixel

Similarly, the estimateFlow function gives information about the changes in x and y direction in the values obtained from MATLAB optical flow application. However, MATLAB's estimateFlow function gives these values based on pixels. This provides an advantage for some applications. For example, when there is more than one movement in the image, comprehensive studies can be done by determining regionally different movements. However, in studies where it is desired to determine a single movement, these values should be processed and updated to give a single output. This is an additional process load for the programmer.

• Response ; It is the coefficient of confidence for Delta_x and Delta_y

• Orientation ; Gives the phase angle of the optical flow in radians.

• Magnitude ; Express the amplitude of the optical flow

The response value calculated with the find_displacement function is produced for each image, while the orientation and magnitude values calculated with the estimateFlow function are produced separately for each pixel.

In this study, it has been performed the find_displacement function on OpenMV card is aimed to determine a single movement at the same time. Simple gesture control applications using the find_displacement function with OpenMV card can easily be performed.

"Hand movements planned to be used in order to control any simple device have been given in Fig. 2. It was foreseen that hand movements can be detected at a distance of 10-60 cm from the camera. In practice, it was not planned to develop image processing techniques to find hand or hand position within the image. Instead, the detection of the direction of movement and the determination of the directions of successive motion have been sufficient to carry out the control application. At this point, it can be assumed that movements (such as any object) will occur outside the hand

Figure 2. Respectively right-left, up-down, rotate clockwise- rotate counterclockwise and push-pull hand gestures

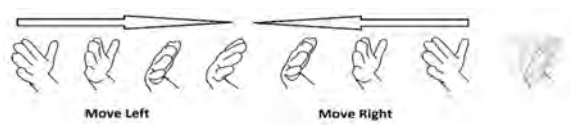

Figure 3. Page turning gesture

movement in the area of interest (ROI) of the camera and that the control operation will be unstable. In order to solve this problem in the study, it was planned to activate the control system with a combination of sequential movement. Also In addition, the control system has been deactivated when no significant movement was taken for a certain period of time.

METHOD

Three different algorithms and one application have been developed on OpenMV card. These;

- Level control algorithm,
- Multi-component Simple System Control algorithm,
- Page turning algorithm.
- Level control application

These controls can be performed using many different methods. Electronic based control systems that detect and operate the on-off switch time, systems that perceive the pressure force as an analog and adjust the level according to the magnitude of the force, level controls using a potentiometer, can be done with electromechanical, electronic or even computerized control methods.

Today, these controls can be performed using image processing methods. However, it takes time for the comprehensive control applications realized by image processing to be economically achievable. From this point of view, the applications developed out within the study aim to bring the advantages of image processing methods to the users without increasing the cost even in the simplest and cheapest electrical/electronic appliances.

In industrial R & D studies, simple, result-oriented, stable and at the same time low-cost solutions are preferred for the production stage. Thus, companies develop themselves in terms of competitiveness. High-cost solutions are therefore not preferred as much as possible. However, in case of obligation, also high-cost solutions are preferred.

Level Control Algorithm

Level control has been using often in many places in the industry and in our daily lives. For example, level control has been carried out in many applications in our daily life such as the voice of a multimedia device, opening level of the vehicle glass, light intensity level.

In the study, in order to develop an image processing based level control algorithm, it has been decided to use the circular gesture of the index finger. Movement of the index finger rotate clockwise and rotate counterclockwise was used for level control. By turning the index finger rotate clockwise, the level was increased and the level was redu-

ced by moving the index finger in the opposite direction. Although the level of the maximum level in the systems to be controlled varies, the level is expressed as a percentage in most systems. In other words, the ratio is expressed as corresponding to the %ratio. Due to the general use in this direction, the level of the study was decided to be in the range of 0-100. Therefore, the level value was limited to 0-100 in order to be compatible with many real-life applications.

Of the application developed, for realization on OpenMv Cam, the algorithm given below has been followed.

Level Control Algorithm

- Delta_x ve Delta_y is detected,
- Delta_x and Delta_y's polarization (Positive or Negative) is detected and saved,
- When the polarization of either Delta_x or Delta_y changes, the new polarization of both is determined and the last four polarizations are saved,
- Compare the last four polarizations of Delta_x and Delta_y,

CONTROL LEVEL is increased if appropriate to the combination given below		CONTROL LEVEL is reduced if appropriate to the combination given below	
Delta _ x	*Delta _ y*	*Delta _ x*	*Delta _ y*
+	−	+	+
+	+	+	−
−	+	−	−
−	−	−	+

The results obtained by moving the index finger clockwise and counter-clockwise using the software prepared in the OpenMV IDE were given in Fig. 4.

Fig 4 will be seen when examined, the clockwise movement of the index finger increases the level value. The counter-clockwise movement of the index finger decreases the level value. The level is called "CONTROL LEVEL" in the developed software and algorithm.

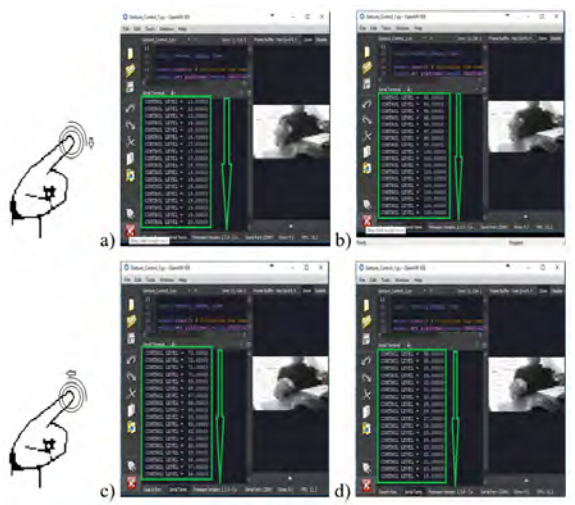

Figure 4. a-b Clockwise rotation c-d counter-clockwise rotation gesture and resulting output values

The level is set in the range 0-100 and the level resolution in this range is 1 unit, it takes some time to adjust the level values in this long-range. In addition, it is necessary to repeat the sequential rotational movements in the same direction. Although random movements in the sensor visual field may cause changes in the level value, it is not possible to have a change in the continuous same direction as a result of random movements. Also, the average change in random movements will be zero. For this reason, no key movement combination has been planned for the use phase of the developed algorithm.

Multi-Component Simple System Control Algorithm

Many products for the end-user (home appliances etc.) have more than one component to be controlled.

For example, the following devices, etc. which we use in daily life, include multi-component systems;

- Paddle box; engine level and lighting level,
- Microwave oven; program selection and duration,
- Electrical oven; program selection, heat and time,
- Multimedia systems (radio, cd player, aux); source selection channel selection and volume adjustment,

In these systems, is first determine which component to control, then we adjust the level of the component. Therefore, in this study, it is necessary to determine the gestures that produces at least two different results. For the realization of this selection was determined right-left, up-down hand movements. With up-down palm movements the desired component was selected, the level of the component was controlled with another gesture (right-left palm movements).

In the study, it was preferred to use the up-down and right-left gestures in front of the camera of the palm for multi-component system control. In multi-component system control, the level limits of the components may vary. At the same time, the number of components may vary. In the study, the algorithm was developed for two components consisting of three levels. If necessary, the number of components and the operating range of the components can be updated via an algorithm.

Negative objects and gestures incoming to ROI should not adversely affect to component selection and levels. For this, a lock of gesture combinations has been developed. Component selection and level control cannot be performed, if it does not occur the gesture combinations. However, after a certain time the control operation has been completed the lock of gesture combinations was automatically activated.

The lock combination was carried out by the user moving of the palm to form a square up-right-down-left in succession against the camera. This lock combination was controlled in the second step of the algorithm.

Of the application developed, for realization on OpenMv Cam, the algorithm given below has been followed.

Multi-Component Control Algorithm

- Delta_x ve Delta_y is detected,
- Combination of lock gesture took place -> is control active. Or no -> is control pasive
- Lock timeout is checked

$$\begin{pmatrix} \text{If } |delta\_y| > |delta\_x| \text{ and } delta\_y < 0 \Rightarrow number_1 = number_1 + 1 \\ \text{If } number_1 \geq 20 \Rightarrow \boldsymbol{control_1 = 1}, number_1 = 0 \\ \text{If } |delta\_x| > |delta\_y| \text{ and } delta\_x > 0 \text{ and } control_1 = 1 \Rightarrow number_2 = number_2 + 1 \\ \text{If } number_2 \geq 20 \Rightarrow \boldsymbol{control_2 = 1}, number_2 = 0 \\ \text{If } |delta\_y| > |delta\_x| \text{ and } delta\_y > 0 \text{ and } control_2 = 1 \Rightarrow number_3 = number_3 + 1 \\ \text{If } number_3 \geq 20 \Rightarrow \boldsymbol{control_3 = 1}, number_3 = 0 \\ \text{If } |delta\_x| > |delta\_y| \text{ and } delta\_x < 0 \text{ and } control_3 = 1 \Rightarrow number_4 = number_4 + 1 \\ \text{If } number_4 \geq 20 \Rightarrow \boldsymbol{control_4 = 1}, number_4 = 0 \end{pmatrix}$$

- If there is movement in ROI when the lock is active,

$$\begin{pmatrix} \text{If 150 cycles (approx. 5 sec) no gesture (or any motion) is detected, the lock is disabled.} \\ \text{If gesture (or any motion) is detected, the lock remains active and the number of cycles is reset.} \end{pmatrix}$$

the direction of movement is determined.

$$\begin{pmatrix} \text{If } |delta\_x| > |delta\_y| \text{ and } delta\_x > 0 \text{ and } control_4 = 1 \Rightarrow \text{direction of gesture } \boldsymbol{RIGHT} \\ \text{If } |delta\_x| > |delta\_y| \text{ and } delta\_x < 0 \text{ and } control_4 = 1 \Rightarrow \text{direction of gesture } \boldsymbol{LEFT} \\ \text{If } |delta\_x| < |delta\_y| \text{ and } delta\_y > 0 \text{ and } control_4 = 1 \Rightarrow \text{direction of gesture } \boldsymbol{DOWN} \\ \text{If } |delta\_x| < |delta\_y| \text{ and } delt\_y < 0 \text{ and } control_4 = 1 \Rightarrow \text{direction of gesture } \boldsymbol{UP} \end{pmatrix}$$

- *direction of gesture UP ⇒ CONTROL ACTIVE level is increased (0,1,2,3)*
- *direction of gesture DOWN ⇒ CONTROL ACTIVE level is reduced (3,2,1,0)*
- *direction of gesture RIGHT and CONTROL ACTIVE level 0 ⇒ no action is taken*
- *direction of gesture RIGHT and CONTROL ACTIVE level 1 ⇒ The motor level is increased (0,1,2,3)*
- *direction of gesture RIGHT and CONTROL ACTIVE level 2 ⇒ The light level is increased (0,1,2,3))*
- *direction of gesture LEFT and CONTROL ACTIVE level 0 ⇒ no action is taken*
- *direction of gesture LEFT and CONTROL ACTIVE level 1 ⇒ The motor level is reduced (3,2,1,0)*
- *direction of gesture LEFT and CONTROL ACTIVE level 2 ⇒ The light level is reduced (3,2,1,0))*

Multi-Component Control Algorithm developed by following the algorithm given below was run real-time on OpenMV IDE by connecting with OpenMV. Outputs obtained during the study are given in Fig. 5.

In practice, 2 components are controlled with CONTROL ACTIVE. When CONTROL ACTIVE is 0, no component is controlled. When the CONTROL ACTIVE is 1, the Motor Level operation is checked. The Motor Level has 4 levels of operation. If Motor Level = 0, the motor does not work, if Motor Level = 1-3, motor operation level sets.

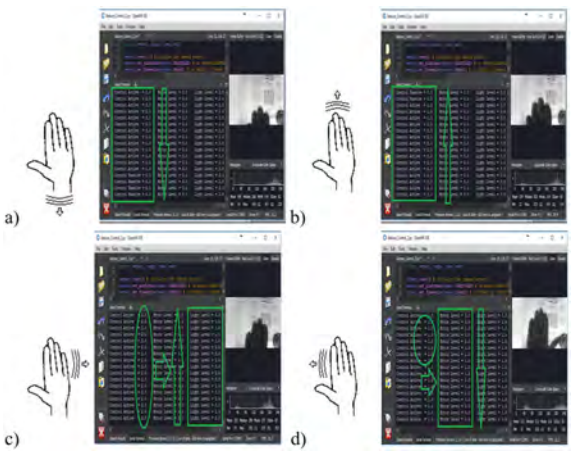

Figure 5. a-b Up and down c-d right and left movements of the palm and output values obtained

If CONTROL ACTIVE = 2, Light Level operation is checked. The Light Level has 3 levels of operation. If Light Level = 0, Light does not work, if Light Level = 1-2, Light operation level sets.

As can be seen from Fig 5, the UP-DOWN movement of the palm allows us to select the component to be controlled. (CONTROL ACTIVATE = 0-2). The RIGHT-LEFT movement of the palm allows the value of the component to be increased or decreased. (Engine Level = 0-1-2-3).

Page Turning Algorithm

In many virtual book applications such as e-books, e-catalogs, is performed page turn process using any of the physical contact methods (touch, clicks etc.). Similarly, in many digital applications, up-down, right-to-left shifts are performed using physical contact methods. Whereas these processes can also be physical contactless with OpenMv Cam. In this application, page-turning and page reversal turning was performed with image processing-based gesture control.

In fact, the page-turning process and page reversal turning differ in real-life. However, when this process is considered as the turn of the pages of a book in a digital environment with the image processing, the gesture of the hand in one direction can be regarded as turning the page in this direction, and the reverse gesture of the hand direction can be considered as the page reversal turning. In this dilemma, which is logically correct, it may be problematic if the gestures are performed consecutively. For example, the page-turning gesture must be repeated 10 times for the book to turn 10 pages. However, this gesture will be done 10 times in the forward direction and 9 times in the reverse direction, and in fact only 1 page-turning will be performed.

Elimination of this problem, which direction we want to turn the page (forward-back) depends on our ability to transfer to the smart camera. Push gesture has been used to transfer of this data to the smart camera. The direction of rotation turning of the page is determined by the pushing gesture. Also with page-turning gesture it is turning at the desired number. Each push action changes the current position (page-turning/page reversal turning). Thus, page-turning and reverse page-turning gestures are prevented from interfering with each other.

Of the application developed, for realization on OpenMv Cam, the algorithm given below has been followed.

Page Turning Algorithm

- Delta_x ve Delta_y is detected,
- Page turning direction determined,

$$\left(\begin{array}{c} reverse = 0 \Rightarrow \text{forward} \quad / \quad reverse = 1 \Rightarrow \text{backward} \\ Check\ the\ push\ gesture \\ (\text{If } delta\_x < 0 \ and \ delta\_y > 0 \Rightarrow \text{condition} = \text{condition} + 1) \\ push\ gesture\ occured \Rightarrow change\ page\ turning\ direction \\ \left(\begin{array}{l} \text{If condition} \geq 25 \ and \ reverse = 1 \Rightarrow reverse = 0, \text{condition} = 0 \\ \text{If condition} \geq 25 \ and \ reverse = 0 \Rightarrow reverse = 1, \text{condition} = 0 \end{array}\right) \end{array}\right)$$

- The page turning gesture is detected and the page is turned forward if the turn direction is forward

$$\left(\begin{array}{c} \text{If } |delta\_x| > |delta\_y| \ and \ delta\_x < 0 \ and \ reverse = 0 \Rightarrow number_1 = number_1 + 1 \\ \text{If } number_1 \geq 5 \Rightarrow forward\ page\ turning, \qquad number_1 = 0 \end{array}\right)$$

- The page turning gesture is detected and the page is turned backward if the turn direction is backward

$$\left(\begin{array}{c} \text{If } |delta\_x| > |delta\_y| \ and \ delta\_x > 0 \ and \ reverse = 1 \Rightarrow number_2 = number_2 + 1 \\ \text{If } number_2 \geq 5 \Rightarrow backward\ page\ turning, \qquad number_2 = 0 \end{array}\right)$$

No need for any lock combinations for this algorithm. Because if the user is doing right or left random movements in front of the camera, it is not already focused on the page. This is not a problem for the operation of the system. The software developed by following the given algorithm was run on OpenMV IDE by connecting with OpenMV. Outputs obtained during the real-time operation were given in Fig. 6.

When Fig. 6 are examined, it has been seen that the algorithm changes the detection direction after each push motion. For example, when a pushing gesture was performed while sensing page turn movement in the forward direction, the software stops detecting the page turn movement in the forward direction and begins to detect the page turn movement in the reverse direction.

Level Control Application

The program written with the algorithm developed for level control has been embedded in the OpenMV image sensor. Thus, the suitability to work on the embedded system has been tested. There is actually no difference between running the software on the OpenMV card and working on the OpenMV IDE. Because the OpenMV IDE was developed to match the capabilities of OpenMV Cam. Hence, the software is performing the same performance on the IDE and on the card.

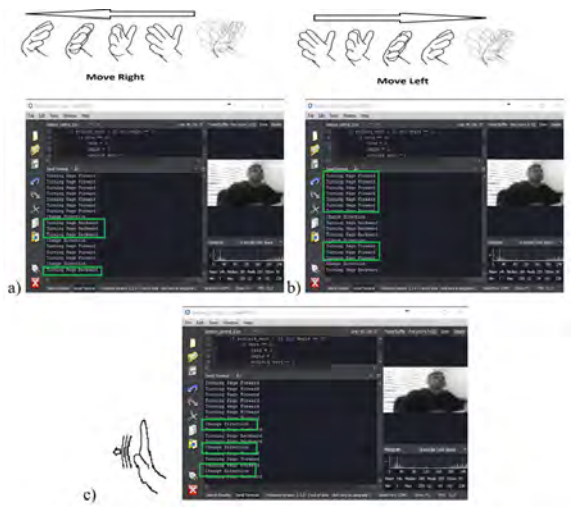

Figure 6. a) Right page b) left page-turning gesture and resulting output values c) Push gesture and output values obtained

OpenMV Cam has serial and parallel communication pins (I/O) for communication with other hardware (electronic cards, sensors, indicators, etc.). In the developed application, parallel communication was preferred due to the fact that the number of pins is sufficient and the possibility of direct supply (no additional equipment is needed). However, UART, I2C, SPI serial communication pins can also be used in studies where the number of pins is not sufficient or more comprehensive studies.

The program prepared by following the Level Control Algorithm was applied to the level indicator by using 10 steps led (4 green-3 yellow-3 red). Normally, the program outputs 0-100 level and 1 unit resolution. However, since the use of 100 indicator leds would not be very efficient during the application, the data resolution transferred to the external environment was reduced by 10 times. Only 10 different levels have been transferred to external environment using OpenMV pins. The indicator control was made using the pins on the OpenMv. In the table 2 are the OpenMv I/O and

Table 2. OpenMv I/O and control level

OpenMv I/O	*Control Level*	*Led Level*
Pin0	*0-10*	*1 Green*
Pin1	*10-20*	*2 Green*
Pin2	*20-30*	*3 Green*
Pin3	*30-40*	*4 Green*
Pin4	*40-50*	*5 Yellow*
Pin5	*50-60*	*6 Yellow*
Pin6	*60-70*	*7 Yellow*
Pin7	*70-80*	*8 Red*
Pin8	*80-90*	*9 Red*
Pin9	*90-100*	*10 Red*

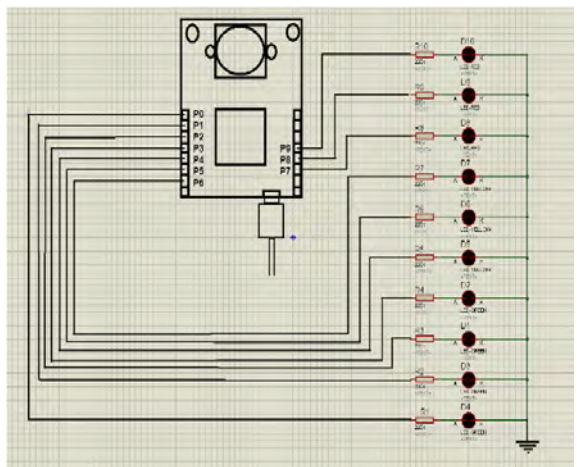

Figure 7. Level control application circuit diagram

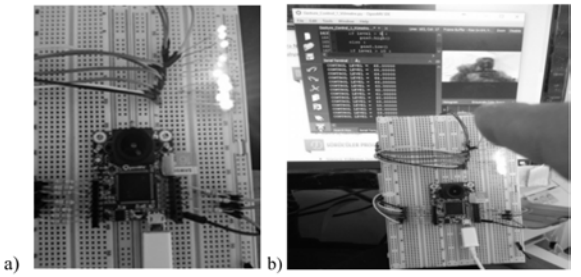

Figure 8. Level control application images

indicator levels. The circuit diagram of the developed level control application was given in Fig. 7 and output images were given in Fig. 8.

RESULTS

In this study, image processing-based gesture control algorithms has been developed to be used in low-cost embedded systems. The cost of such embedded systems affects hardware and software together. Since the scope of the software to be developed is wide or includes advanced image processing methods, it will have a negative effect on the cost as it will increase the hardware requirement. Therefore, the software to be developed should be able to run on small budget hardware. In this study OpenMV Cam was preferred as hardware. The algorithms used in the study are based on the find_displacement function that can be implemented on OpenMV Cam. Thus, gesture control applications can be realized with low-budget hardware without using advanced image processing methods.

OpenMv board was used to develop gesture control applications. Applications developed using the researcher's developed functions, on the OpenMv IDE have worked stably. The study has been used the find_displacement function based which developed by the researcher. This function provides the determination of the changes occurring between consecutive images. Thus, the researchers can develop a gesture control application by following the direction of movements in the image. Developed as a raw image sensor, OpenMv can be used as an image sensor by the users/researchers. MicroPython embedded OS based functions were available for users to develop applications on OpenMV.

The level control, multi-components simple system control and page-turning algorithms developed in the study, can be embedded on the OpenMV board and can be used to control any multimedia device or any household electrical appliance. OpenMV source code and schematic drawings are open to help reduce costs. It contributes to a positive increase in cost-performance ratio. Thus, the OpenMV image sensor can be used as hardware in low-cost industrial applications. However, the software also to be used together with the hardware should not contain high technology. Otherwise, the cost will adversely affect the performance ratio. At the same time, high-tech software on low-cost hardware cannot already be implemented. For example, operations with the Kinect camera cannot be performed on OpenMV Cam.

In this study, the software based on the developed algorithms were not developed specifically for a particular user. So it can be used by all users. In addition, they do not require calibration at every restart as in some applications. However, the system response may not be the same for every user. Because each user's preferred movement speed and styles vary. According to the way users perform gestures, the system can make more mistakes for some users. However, although the users tend to make different choices, the necessary corrections for the control will occur spontaneously after certain usage.

In the study "Optical flow-based gesture motion direction recognition method", up-down and right-left directions are determined. It has been stated that it is sufficient to detect movements in the same direction twice for these determinations. The algorithm has been developed accordingly. It is like the Multi-Component Simple System algorithm in my study. Success rates in the study are not given in numerical values. In both studies, the system is independent of the user. At the same time, the user's success in using the system is related to the usage experience. The most important difference between the two studies is the wide range of level control (Level Control Algorithm) and the page turning control (Page-Turning Algorithm). These controls are not carried out in the study [26].

Pathak and Jalal [27] determined eight different hand movement directions (right-left, up-down and intermediate directions) in their studies. With different combinations of these directions of movement, they identified the words

Table 3. Test results

	Level Control Algorithm		*Multi-Component Control Algorithm*		*Page Turning Algorithm*	
	inexperienced	*experienced*	*inexperienced*	*experienced*	*inexperienced*	*experienced*
Person1	*False*	*True*	*False*	*True*	*True*	*True*
Person2	*True*	*True*	*True*	*True*	*False*	*True*
Person3	*True*	*True*	*False*	*True*	*False*	*True*
Person4	*False*	*True*	*False*	*True*	*False*	*True*
Person5	*True*	*True*	*True*	*True*	*True*	*True*
Total	*60%*	*100%*	*40%*	*100%*	*%40*	*100%*

in the Indian sign language. With the method they developed, they first used 15% of the recorded images to create the sequential code combination and the remaining 85% for testing. As a result, they achieved 90.4% success. The focus on sign language of the study is the difference. They expressed the recurring direction determinations as residuals and filtered them. Because repeatedly repeated direction determinations cause incorrect code combinations [27]. In the method proposed in this study, repetitive direction determinations express the level change and are not filtered. The method suggested in the study is independent of the user, as it focuses on the direction of movement as in this study.

Hand movements should not be too fast or too slow in order to be detected correctly and to ensure stable operation of the algorithms. In general, it is thought that the user experience will experience the stable operation of the algorithms and calibrate the movement speed itself. At the same time, during the application phase, the movement speeds were approximately determined as follows.

• Clockwise or counter-clockwise rotation speed is 1 turn/sec for the Level Control Algorithm.

• Up-down or right-left movements speed is 0.5 level/sec for Multi-Component Control Algorithm.

• Right or left page-turning gestures speed is 1 sec for Page Turning Algorithm.

After the developed algorithms were completed, they were tested by 5 person who used the system for the first time. Test results are given below.

After the users were informed, they were enabled to use the applications. In the Table 3, the first use results and the results after experiencing the applications for a certain period of time are given. In the first use, Level control, Multi-component control and page-turning algrithms were realized with 60%, 40% and 40% success, respectively. However, after the users experienced the applications, 100% success rate was achieved for all applications.

CONCLUSION AND RECOMMENDATIONS

• Developed algorithms can be run independently from the computer when embedded on OpenMV. Therefore, it is suitable for embedded system design.

• In the development phase, algorithms were tested by different users via OpenMV IDE and no differences were determined. In fact, the study has been based only on the determination of the direction of movement. Therefore, it does not have the ability to distinguish users.

• It was anticipated that the movements will be performed with an average speed, the number of repetitions in the successive data is determined according to this prediction. For this reason, the rate of producing false results is increased in very fast and very slow-motion combinations. However, due to the fact that the machines to be controlled are machines such as small appliances etc, the erroneous results will not be a big problem and the users will adjust their movement speed according to the embedded system as in all technological devices.

The study was carried out on the OpenMV board. Special hardware can be developed for the developed algorithms. Also, applications are independent of the user but dependent on movement speed. The stable operating range can be expanded by developing filters for moving speed.

CONFLICT OF INTEREST

Authors approve that to the best of their knowledge, there is not any conflict of interest or common interest with an institution/organization or a person that may affect the review process of the paper.

References

1. Turan B, Eskikurt Hİ, Can MS. An aplication based on artificial neural network for determining viewpoint coordinates on a screen. Elektronika Ir Elektrotechnika 22 2 (2016) 86–91. DOI: http://dx.doi.org/10.5755/j01.eie.22.2.7586
2. Lee WPO, Kaoli C, Huang JY. A smart TV system with body–gesture control, tag–based rating and context–aware recommendation. Knowledge–Based Systems 56 (2014) 167–178. https://doi.org/10.1016/j.knosys.2013.11.007
3. Bellmore C, Ptucha R, Savakis A. Interactıve dısplay using depth and RGB sensors for face and gesture control. Western New York Image Processing Workshop, 2011. https://doi.org/10.1109/WNYIPW.2011.6122883.
4. Yavşan E, Uçar A. Gesture imitation and recognition using Kinect sensor and extreme learning machines. Measurement 94 (2016) 852-861.
5. Rahman ASMM, Saboune J, Saddik AE. Motion–path based in car gesture control of the multimedia devices. DIVANet '11 Proceedings of the first ACM international symposium on Design and analysis of intelligent vehicular networks and applications 69–76, 2016. https://doi.org/10.1145/2069000.2069013.
6. Bhuiyan M, Picking R. Gesture–controlled user interfaces, what have we done and what's next?. 2009. http://citeseerx.ist.psu.edu/viewdoc/download?doi=10.1.1.562.6140&rep=rep1&type=pdf. (accessed 13 11 2018).
7. Kela J, Korpipaa P, Mantyjarvi J, Kallio S, Savino G, Jozzo L, Marca S. Accelerometer–based gesture control for a desing environment. Personal and Ubiquitous Computing (2006) 285–299. https://doi.org/10.1007/s00779–005–0033–8
8. Mantyjarvi J, Kela J, Korpipaa P, Kallio S. Enabling fast and effortless customisation in accelerometer based gesture

interaction. MUM '04 Proceedings of the 3rd international conference on Mobile and ubiquitous multimedia 25–31, 2004. https://doi.org/10.1145/1052380.1052385

9. Hackenberg G, McCall R, Broll W. Lightweight Palm and Finger Tracking for Real–Time 3D Gesture Control. 2011 IEEE Virtual Reality Conference, 2011. https://doi.org/10.1109/VR.2011.5759431.
10. Akyol S, Canzler U, Bengler K, Hahn W. Gesture control for use in automobiles. IAPR Workshop on Machine Vision Applications, Nov. 28–30, 2000. The University of Tokyo, Japan. https://pdfs.semanticscholar.org/fb51/6222c7c87f42872a28ff8fc74139447b1280.pdf. (accessed 13 11 2018).
11. Bizzotto N, Costanza A, Bizzotto L, Revis D, Sandri A, Mangan B. Leap motion gesture control with osirix in the operating room to control imaging. Surgical Innovation, 2014. https://doi.org/10.1177/1553350614528384.
12. Cohen CJ, Beach G, Foulk G. A Basic Hand Gesture Control System for PC Applications. IEEE Xplore Digital Library, 2001. https://doi.org/10.1109/AIPR.2001.991206.
13. Gallo L, Placitelli AP, Ciampi M. Controller–free exploration of medical image data: Experiencing the Kinect. 2011 24th International Symposium on Computer–Based Medical Systems (CBMS), 2011. https://doi.org/10.1109/CBMS.2011.5999138.
14. Doğan RÖ, Doğan H, Köse C. Virtual Mouse Control with Hand Gesture Information Extraction and Tracking. 23nd Signal Processing and Communications Applications Conference (SIU) 2015. https://ieeexplore.ieee.org/stamp/stamp.jsp?arnumber=7130228. (accessed 10 12 2019).
15. Kaura HK, Honrao V, Patil S, Shetty P. Gesture Controlled Robot using Image Processing. (IJARAI) International Journal of Advanced Research in Artificial Intelligence, Vol. 2, No. 5, 201, 2013 https://pdfs.semanticscholar.org/ff0f/20e3dbbdf257ec3ca36be4ed251036b49e11.pdf. (accessed 13 11 2018).
16. Chowdary PRV, Babu MN, Subbareddy TV, Reddy BM, Elamaran V. Image Processing Algorithms for Gesture Recognition using MATLAB. 2014 IEEE International Conference on Advanced Communication Control and Computing Technologies (ICACCCT), 2014. https://doi.org/10.1109/ICACCCT.2014.7019356.
17. Kar S, Banerjee S, Jana A, Kundu D, Chatterjee D, Ghosh S, Mitra D, Gupta SD. Image Processing Based Customized Image Editor and Gesture Controlled Embedded Robot Coupled with Voice Control Features. (IJACSA) International Journal of Advanced Computer Science and Applications 6 (2015) 11. https://pdfs.semanticscholar.org/f000/be3e91d69dc8ce1f87ae32ae7e5395b09b86.pdf. (accessed 13 11 2018).
18. Osimani C, Piedra–Fernandez JA, Ojeda–Castelo JJ, Iribarne L. Hand Posture Recognition with Standard Webcam for Natural Interaction, WorldCIST 2017. Advances in Intelligent Systems and Computing, vol 570 (2017) Springer.
19. Hsiang–Yueh L, Hao–Yuan K, Yu–Chun H. Real–time Hand Gesture Recognition System and Application. Sensors and Materials, Vol. 30, No. 4 (2018) 869–884.
20. Schacher JC. Gesture control is sounds in 3D space. Proceedings of the 2007 Conference on New Interfaces for Musical Expression (NIME07), New York, NY, USA, 2007. http://www.nime.org/proceedings/2007/nime2007_358.pdf. (accessed 13 11 2018).
21. Erden F. Hand gesture recognition using two differential PIR sensors and a camera. 2014 22nd Signal Processing and Communications Applications Conference (SIU), 2014. https://doi.org/10.1109/SIU.2014.6830237.
22. Şahin A. Hacking the Gestures of Past for Future Interactions. M.Sc. THESIS, 2013 http://muep.mau.se/bitstream/handle/2043/15700/Atilim%20Sahin%20–%20Hacking%20the%20Gestures%20of%20Past%20for%20Future%20Interactions.pdf?sequence=2&isAllowed=y. (accessed 13 11 2018).
23. Rautaray S, Agrawal A. Vision based hand gesture recognition for human computer interaction: a survey. Artif. Intell. Rev. 43 (2015) 1–54
24. Munir O, Ali AN, Javaan C. Hand Gesture Recognition Based on Computer Vision: A Review of Techniques. Journal of Imaging 6(8) 2020 73.
25. OpenMv Cam M7 Specifications, (2017). ttps://openmv.io/products/openmv–cam–m7 . (accessed 14 11 2018).
26. Optical flow–based gesture motion direction recognition method, https://patents.google.com/patent/CN104331151A/en
27. Pathak B, Jalal AS. Motion Direction Code–A Novel Feature for Hand Gesture Recognition. Advances in Intelligent Systems and Computing, vol 798 2019. Springer

Hittite Journal of Science and Engineering, 2021, 8 (2) 97–102
ISSN NUMBER: 2148–4171
DOI: 10.17350/HJSE19030000220

Study on the Investigation of the Fatigue Behavior of Engineered Cementitious Composites with High Tenacity Polypropylene (HTPP) Fibers

Mert Tatarca[1] **Burak Felekoglu**[1] **Eren Godek**[2]
[1]Dokuz Eylul University, Department of Construction Materials, Izmir, Turkey
[2]Hitit University, Department of Construction Technology, Corum, Turkey

ABSTRACT

In this study, the fatigue behavior of Engineered Cementitious Composites incorporating high tenacity polypropylene fiber was investigated. The strain curves, cycle numbers, crack numbers and stiffness values were obtained from the experiments carried out with the load-controlled fatigue method at 80, 90 and 110% stress level (maximum stress/ultimate static strength). In conclusion, at 80% stress level, average 1127 cycles, 1.37% the unit deformation capacity and 6 cracks were achieved. At 90% stress level, 215 cycles, 1.89% the unit deformation capacity and 8 cracks were obtained. In the specimens where 110% stress level was applied, the average number of cycles was decreased to 38 cycles, the unit deformation capacity increased up to 2.60% and the average number of cracks also doubled and raised to 15 cracks. Additionally, the average stiffness values of 8.68 and 9.57 GPa were obtained in the first cycles at 80% and 90% stress levels, it was observed that the stiffness values gradually decreased with increasing cycles. Although high strain values were achieved at the 110% stress level, micro cracks were formed suddenly due to the very high applied loading and the rigidity values remained low since the first cycle due to the plastic deformation.

Keywords: HTPP fiber, ECC, Fatigue, Cyclic loading, Secant modulus

Article History:
Received: 2020/12/20
Accepted: 2021/03/31
Online: 2021/06/30

***Correspondence to**: Mert Tatarca,*
E-mail: merttatarca@windowslive.com;
Phone: +90 554 293 2411

INTRODUCTION

Fatigue is a complex thermic and mechanical incident which can result thaw, wear and decomposition occurring in the materials due to repetition of loads and unloads, periodically [1]. Especially in some structures, which exposed to loads such as traffic, thermal changing, winds, sea waves and earthquakes, the rigidity of the structures decrease and collapse [2]. Construction materials can lose their strength when loaded periodically with sufficient repetition between two specified limit values of loads even the loads below their load bearing capacity.

In general, there are two basic loading methods to investigate of fatigue behavior of materials. First method is load controlled method that based on stress level and most common method (Fig. 1a). The other method is called deformation controlled method that facilitates particular analysis of stress and strain in local areas (Fig. 1b) [3]. Additionally, fatigue loads are separated to two parts as low cyclic and high cyclic loading. Low cyclic loading is defined by loading at a high stress level and making a small number of cycles. On the other hand, high cyclic loading is characterized by loading at the low stress level and making lots of number of cycles [4].

Concrete is one of the most used construction material today. During various loading conditions, a crack is formed at the cross section of concrete which reached to load bearing capacity. This cause to lose entire load bearing capacity of concrete rapidly without using all mass of concrete. Due to this situation, it is become very common that usage of macro or micro fiber into the concrete which in order to prevent abrupt collapse failure and much more take advantage of mass of concrete [5]. Poor performance of plain concrete under cyclic loading has been reported by various researchers [6,7]. By using these kinds of fibers, it is possible to enhance mechanical performance of concrete under fatigue loading [8]. Many fiber types are adopted to cement-based composites due to the developed concrete technology.

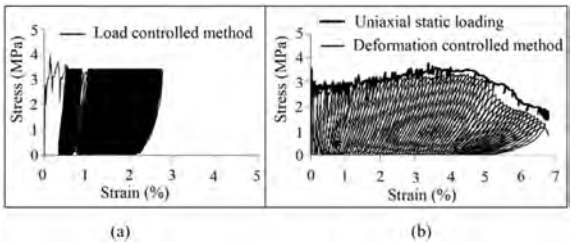

Figure 1. The typical demonstrations for a) Load controlled method; b) Deformation controlled method.

Substitution of the steel fibers into concrete, which are the first advanced fibers of modern times, increase load bearing capacity, crack growth resistance and fatigue strength [4, 9]. In recent years, cement-based composites which are produced with using fibers such as poly-vinyl alcohol (PVA), high tensile polypropylene fibers (HTPP) and polyethylene (PE), are considered that will indicate superior performance under the fatigue loading [10]. These composites which demonstrate high ductility and toughness under tensile, flexural and shear loading owing to strain-hardening behavior, are called ECC (Engineered Cementitious Composites). High toughness and ductility feature of these composites are provided by their multiple cracking behaviors. Owing to this behavior, ECC demonstrate strain-hardening unlike plain and conventional fiber reinforced composites [11]. After the first crack is occurred at the weakest section of the composites, loads mentioned upward which cause propagation of crack abruptly, are held by fibers and transmitted to the other uncracked sections of matrix. Then, additional cracks occur in the sections where the load is transferred. This repetitive event prevents sudden collapse and achieve deformation hardening behavior and energy absorption capacity of composites rises considerably when compared to plain composites [12]. There are studies showing that the performance of these polymeric fiber reinforced composites can also be increased under fatigue loads. Mechtcherine and June (2007) studied the fatigue behavior of PVA-ECC under load controlled method and deformation controlled method. Under the fatigue loading, secant modulus of composites was calculated and change of rigidity of these composites were investigated in addition to cycle and cracks numbers. When the hysteresis curves were examined, it was observed that composites had high stiffness values at low deformation values in the initial cycles. Decreases in stiffness values were also observed with expanding hysteresis curves and increasing deformation values as the number of cycles increased [13]. Another study conducted by Sui (2018), compared the fatigue performance of PVA-ECC and PE-ECC under flexural loading at the rates of 50%, 65, 80 and 90 of the flexural strength under static loading. Due to the inability of fibers to be actively used under low fatigue loading of ECC and because fatigue loads are mostly carried by the matrix at low fatigue loading, less crack numbers and deformation values were obtained. With the increase in the stress level, the fibers being more active and the ability to make multiple cracks give more favorable results in terms of fatigue life and reach high deformation capacities [14].

Nowadays, there are abundant studies conducting with PVA or PE fibers composites [15-19]. The commonly used fiber type in the literature is mostly PVA. Last decade, ECC produced with HTPP fiber (HTPP-ECC), which are considered as new generation polymeric fibers, has growing interest. HTPP-ECC differs from PVA-ECC due to fiber and fiber-matrix interaction properties. There are studies on the flexural and tensile performances of HTPP-ECC [5, 20]. However, fatigue performance of HTPP-ECC under flexural and tensile stress has been investigated, rarely. Jin and Li (2019) has investigated fatigue performance of HTPP-ECC which used on wind turbine tower under 4-point flexural loading at 70, 80 and 90% of their static strength and it was reported that fatigue life of HTPP-ECC was 50 times longer compared to plain concrete [21].

Apart from the study which mentioned upward, it is seen that there is not enough research on the fatigue behavior of HTPP-ECC. In order to fill this gap and to contribute to the literature, fatigue performance of HTPP-ECC under different stress levels has been investigated within the scope of the study. For this purpose, dog-bone shaped tensile specimens were produced and they were subjected to tensile fatigue loading at 80, 90 and 110% of tensile strength. Thus, it was planned to better understand the low cycle dynamic effects at the high stress value as earthquake loads and examine the correlation between deformation ability and cycle capacity of ECCs at the different stress levels. In addition to this, it was aimed to contribute to literature by examining fatigue life and stiffness changes of composites.

MATERIAL AND METHODS

Within the scope of the experimental program, previously designed matrix adopted from the study that it is compatible with HTPP fiber [20]. The water/cement ratio of the mixture was 1.10 and powder material/cement ratio was 2.5. The composites were labelled as HCF and mixture ratios were presented in Table 1. CEM I 42.5 R type cement and Granulated Blast Furnace Slag (GBFS) were used. Chemical, physical and mechanical properties of the cement is shown at Table 2.

Chemical and physical properties of GBFS is shown in Table 3. HTPP fibers were used in fiber phase of the mixture. Physical and mechanical properties of HTPP fibers are shown at Table 4.

The volume of the mixture was determined as 4 dm^3 for pouring process. In mixing process laboratory type Ho-

bart mixer was used. Cement and GBFS were mixed for 3 minutes, then water was added and mixed for another 3 minutes. After that, HTPP fibers by 2% of total mixture volume was added to the mixture and superplasticizer additive was added in order to distribute the fibers homogeneously to the whole matrix and the mixing process was continued for 3 more minutes. 12 samples were taken into dog-bone shaped steel molds. The dimensions of molds were shown in Fig. 2, which were manufactured in accordance with the recommendation of the Society of Japanese Civil Engineers [22]. After the specimens stayed for two days in molds, they removed and stayed for 28 days in lime-saturated curing pool at 20±2°C.

Shimadzu branded tensile tester was used for measurement of fatigue performance of the specimens under tensile fatigue tests. The device has 50 kN load capacity and capable of repeated loading at 0.05 Hz with three cycles per minute,

Table 1. Mixture ratio of HCF.

Ingredients	Cement	Granulated Blast Furnace Slag	Water	Super-plasticizer	HTPP fiber
kg/m³	424	1059	466	8	18

Table 2. Chemical, physical and mechanical properties of the CEM I 42.5 R cement.

Chemical Analysis (%)								
SiO_2	Al_2O_3	Fe_2O_3	CaO	MgO	Na_2O	K_2O	SO_3	Cl-
18.57	4.95	3.11	63.94	0.98	0.37	0.75	3.07	0.006

Mechanical and Physical Properties							
Compressive Strength (MPa)			Specific gravity (g/cm³)	Specific surface (cm²/g)	Residue on 0.090 mm sieve (%)	Residue on 0.045 mm sieve (%)	Soundness (mm)
2 days	7 days	28 days					
27.2	39.9	49.3	3.09	3370	0.7	19.3	0.5

Table 3. Chemical and physical properties of Granulated Blast Furnace Slag.

Chemical Analysis (%)						
SiO_2	Al_2O_3	Fe_2O_3	CaO	MgO	SO_3	Cl-
39.98	11.06	0.77	32.95	10.26	0.34	0.0075

Physical Properties				
Ignition loss (%)	Specific gravity (g/cm³)	Specific surface (cm²/g)	Residue on 0.090 mm sieve (%)	Residue on 0.045 mm sieve (%)
2.34	2.87	5500	0	0.40

Table 4. Physical and mechanical properties of HTPP fibers.

Specific gravity (g/cm³)	Diameter (μm)	Length (mm)	Fiber aspect ratio	Tensile strength (MPa)	Modulus of elasticity (GPa)	Elongation at failure (%)
0.91	12	10	833	850	6	21

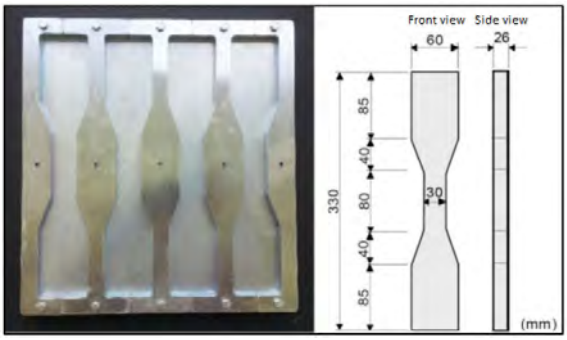

Figure 2. Dog-bone shaped steel molds [22].

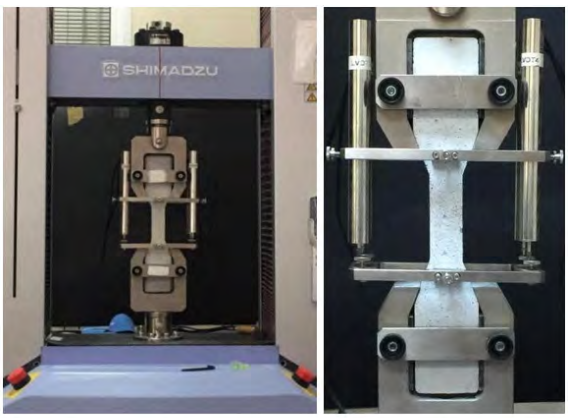

Figure 3. a) Laboratory countertop type tensile test machine, b) tensile test setup.

load measurement accuracy ± 1% between 1/1 and 1/1000 of the load cell capacity, vertical test area 1250 mm, horizontal test area (between columns space) is 500 mm countertop type (Fig. 3a). The bottom of the tensile mechanism has embedded, the upper side has jointed pin configure and it is allowed to apply of uniaxial tensile load to specimens. In order to measure displacement of the specimens during the test, four extensometers were used (Fig. 3b).

3 specimens from the prepared twelve specimens, exposed to static tensile test for the determination of tensile strength and unit deformation. The uniaxial tensile test carried out with speed of 0.5 mm/min. Tensile strengths were calculated by dividing the maximum stress to cross-sectional area of the composite and corresponding strain value to the maximum stress was determined as unit deformation. Remaining nine specimens exposed to load controlled fatigue test at the stress levels of 80%, 90 and 110 of the tensile strength. During the test, frequency was set up constantly 0.05 Hz so as to each last take 20 seconds. After the fatigue failure tests were ended, the stress-strain curves of the specimens were drawn and the number of cycles were determined. The secant modulus values at 1., 10., 100., 1000. and the last cycle were computed as shown at Fig. 4 and the change of secant modulus values were investigated. In the equation, E_{sec}: Secant modulus, σ_{max}: Maximum applied

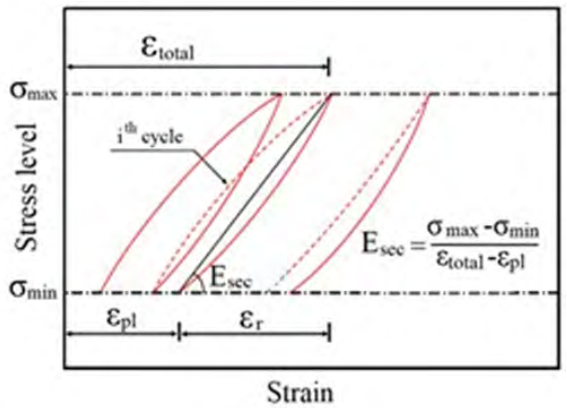

Figure 4. Computing method of change of the secant modulus [23].

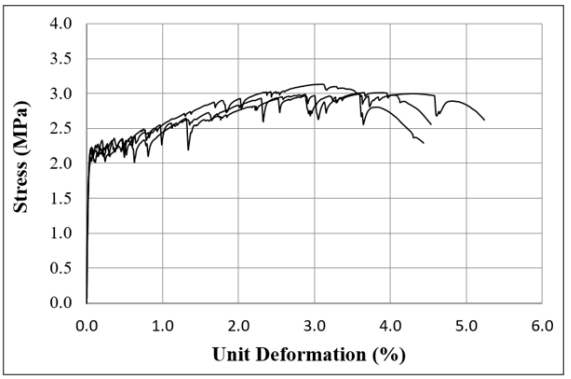

Figure 5. The stress-strain curve of uniaxial static tensile tests.

stress, σ_{min}: Minimum applied stress, ε_{total}: Total strain, ε_{pl}: Sum of plastic strain, ε_r: Recoverable strain. Finally, fatigue life graphs were drawn by the data obtained from stress-strain curves.

RESULTS AND DISCUSSION

Uniaxial Static Tensile Test Results

Uniaxial static tensile tests were executed on 3 specimens, in order to determine the tensile strength of composites. The stress-strain curves were shown in Fig. 5, maximum stress and corresponding unit deformation values that obtained from these curves, are given Table 5. The average tensile strength and the average unit deformation values of 3 specimens were determined as 3.05±0.06 MPa and 3.84±0.54 %, respectively.

Table 5. The results of the uniaxial static tensile tests.

Specimen	*Ultimate tensile static strength (MPa)*	*Tensile static strain (%)*
HCF-1	*2.99*	*4.45*
HCF-2	*3.13*	*3.12*
HCF-3	*3.02*	*3.96*
Average	*3.05 ± 0.06*	*3.84 ± 0.54*

Fatigue Test Results

The stress-strain curves of cyclic loadings were given in Fig. 6. The applied stress, the unit deformation values, the number of cycles and cracks were calculated by using the curves and given in Table 6. On the graphs, 1., 10., 100., 1000. and the last cycles of specimens are demonstrated different colors and at this cycles, rigidity changes (E_{sec} values) of the specimens have been calculated which is goingto to be discussed in the next section (Fig.7).

When the graph at 80% stress level was examined (Fig. 6a), it was observed that the specimens exhibited average 1127 cycles, 1.27% unit deformation value and 6 cracks before the collapse failure (Table 6). When fatigue loading was increased to 90% stress level, the average number of cycles decreased to 215 and the unit deformation value increased to 1.89% (Fig. 6b; Table 6). There was no significant change in the average number of cracks, the average number of cracks was determined to be 8. In the series where the highest stress level was applied (110%), the specimens exhibited an average of 38 cycles despite being exposed to dynamic loading at a level above the static strength, and the average

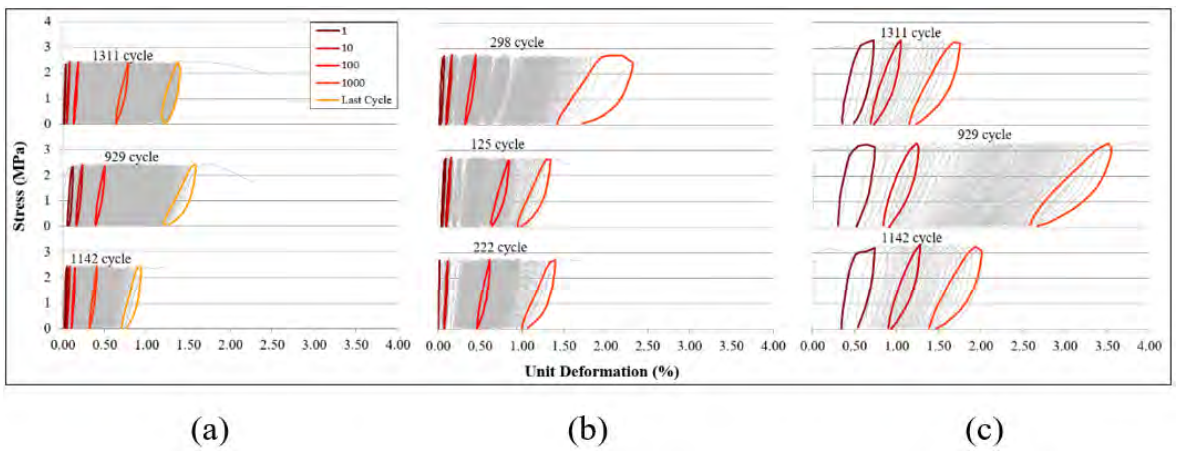

Figure 6. Fatigue tests graphs applied at the different stress levels a) 80%, b)90%, c) 110%.

Table 6. Fatigue test results obtained at 80, 90 and 110% stress levels.

Specimen	Applied stress (MPa)	Unit deformation (%)	Cycle (N)	Crack number (n)
HCF80-1		1.01	1142	5
HCF80-2	2.435	1.72	929	5
HCF80-3		1.40	1311	7
Average		1.37 ± 0.29	1127 ± 156	6
HCF90-1		1.71	222	9
HCF90-2	2.740	2.07	125	7
HCF90-3		2.53	298	9
Average		1.89 ± 0.46	215 ± 71	8
HCF110-1		1.92	19	13
HCF110-2	3.350	2.07	27	18
HCF110-3		3.83	67	15
Average		2.60 ± 0.86	38 ± 21	15

number of cracks doubled and reached to 15 (Fig. 6c; Table 6). Compared to other series, the significant increase in multiple cracking behavior increased the unit deformation value of the samples to an average of 2.60%.

Secant Modulus Results

Within the scope of the study, the changes of secant modulus (E_{sec}) were calculated and given in Fig. 7. At the 80% and 90% stress levels, the change of E_{sec} values were found to be similar to each other's. At the beginning, both series exhibited high E_{sec} values however these values decreased by increased number of cycles. It was determined that average number of cycle was 1127 at the 80% stress level and 215 at the 90% stress level. Although high unit deformation values were achieved in the samples exposed to 110% stress level, the E_{sec} values were calculated remarkably low when compared to 80 and 90%. The reason for this is thought to be the early micro cracking as a result of the relatively high dynamic loading. With the triggering of multiple crack mechanism, the rapid increase in the number of micro cracks in a short time caused high plastic deformation in the samples (Fig.7). This situation caused the E_{sec} values to remain at lower values compared to the other series since the first cycle.

The stress-cycles to failure graph (S-N) is presented in Fig. 8. As expected, the number of cycles to failure gradually increased with decreased stress level. Also, there was a strong correlation with a correlation coefficient of R = 0.99.

CONCLUSION

In this study, the fatigue performance of HTPP-ECC has been investigated at 80, 90 and 110% stress levels by load controlled method. The results are given below:

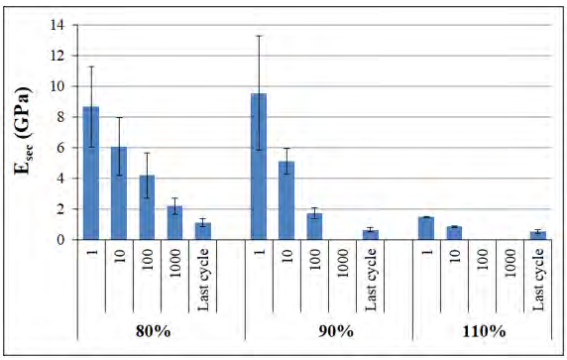

Figure 7. The graph of secant modulus changes of HTPP-ECCs at the different stress level.

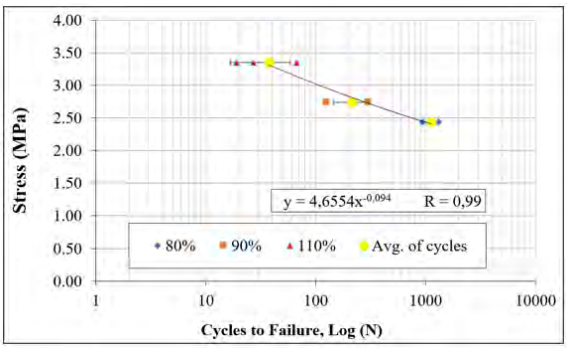

Figure 8. The stress-cycles to failure graphs (S-N) obtained from at 80, 90 and 110% stress level values.

• As a result of the static tensile test, the composites exhibited an average tensile strength of 3.05 ± 0.06 MPa and an average unit deformation of 3.84 ± 0.54 %. By using HTPP fibers in the production of ECC has increased both the tensile strength and unit deformation when compared to conventional cement-based composites.

• When the number of cycles performed at three stress levels are examined, it is seen that high cycle numbers are reached at low stress level. With the increase in the stress level, decrease in the number of cycles were observed due to the higher tensile stress value the material is exposed to.

• The most valuable part of this study as a contribution to the literature is that HTPP-ECC have reached an average of 38 cycles, although it is loaded with a stress much higher than its tensile strength (110% stress level). It is thought that the reason for this is that the fatigue loading speed is faster than the static tensile loading speed, so the HTPP fibers in the composite take a much more active role and can withstand considerable cycles at these levels with the feature of more active multiple crack behavior.

• The secant modulus (E_{sec}) of the samples loaded at 80% and 90% stress levels were obtained higher, initially. However, these values gradually decreased as the number of cycles increased. Although high strain values were reached

in the samples exposed to a fast loading above the capacity with 110% stress level, the secant modulus values remained lower when compared to 80 and 90% stress level. This phenomenon can be explained by the fact that the relatively high dynamic loading triggers the multiple crack mechanism early and the rapid increase in the number of micro cracks in a short time causes high plastic deformation in the samples.

CONFLICT OF INTEREST

Authors approve that to the best of their knowledge, there is not any conflict of interest or common interest with an institution/organization or a person that may affect the review process of the paper.

AUTHOR CONTRIBUTION

Mert Tatarca designed and carried out the experiments. Mert Tatarca and Eren Gödek researched literature, analyzed the data and wrote the manuscript. Burak Felekoğlu supervised the study and helped with the review process of the final manuscript.

References

1. Baradan B. Material Information for Civil Engineers, Dokuz Eylul University Faculty of Engineering Press, Izmir, Turkey, 2011 (in Turkish)
2. Müller S, Mechtcherine V. Fatigue behaviour of strain–hardening cement–based composites (SHCC). Cement and Concrete Research 92 (2017) 75–83.
3. Alam BA. Fatigue performance of engineered cementitious composites. Doctoral Dissertation, Middle East Technical University, Ankara, Turkey, 2016.
4. Paranjape AS. The flexural fatigue performance of high volume synthetic fiber reinforced concrete. Master of Applied Science, Dalhouse University, Nova Scotia, Canada, 2007.
5. Gödek E. Development of practical polymeric fiber reinforced cementitious composites. Master's Thesis, Dokuz Eylül University Institute of Science in Civil Engineering, Izmir, Turkey, 2016 (in Turkish)
6. Forgeron, DP. The combined effects of flexural fatigue cycles and freezing and thawing cycles on the flexural properties of plain and fiber reinforced concrete. Doctoral Dissertation, Nova Scotia, Canada, 2005.
7. Mailhot T, Bissonnette B, Saucier F, Pigeon M. Flexural Fatigue Behavior of Steel Fiber Reinforced Concrete Before and After Cracking. Materials and Structures 34 (2001) 351–359.
8. Qiu J, Yang EH. Micromechanics–based investigation of fatigue deterioration of engineered cementitious composite (ECC). Cement and Concrete Research 95 (2017) 65–74.
9. Lee MK., Barr BIG. An overview of the fatigue behaviour of plain and fibre reinforced concrete. Cement and Concrete Composites 26(4) (2004) 299–305.
10. Suthiwarapirak P, Matsumoto T, Kanda T. Multiple cracking and fiber bridging characteristics of engineered cementitious composites under fatigue flexure. Journal of materials in civil engineering 16(5) (2004) 433–443.
11. Sherir MA, Hossain K. Lachemi M. Structural performance of polymer fiber reinforced Engineered Cementitious Composites subjected to static and fatigue flexural loading. Polymers 7(7) (2015) 1299–1330.
12. Li VC, Wu C, Wang S, Ogawa A, Saito T. Interface Tailoring for Strain–hardening PVA–ECC. ACI Materials Journal 99(5) (2002) 463–472.
13. Mechtcherine V, Jun P. Stress–strain behaviour of strain–hardening cement–based composites (SHCC) under repeated tensile loading. Fracture mechanics of concrete structures (2007) 1441–1448.
14. Sui L, Zhong Q, Yu K, Xing F, Li P, Zhou Y. Flexural fatigue properties of ultra–high performance engineered cementitious composites (UHP–ECC) reinforced by polymer fibers. Polymers 10(8) (2018) 892.
15. Matsumoto, T., Wangsiripaisal, K., Hayashikawa, T., & He, X. Uniaxial tension–compression fatigue behavior and fiber bridging degradation of strain hardening fiber reinforced cementitious composites. International Journal of Fatigue 32(11) (2010) 1812–1822.
16. Müller, S., & Mechtcherine, V. Fatigue behaviour of strain–hardening cement–based composites (SHCC). Cement and Concrete Research 92 (2017) 75–83.
17. Yu, K., Li, L., Yu, J., Wang, Y., Ye, J., & Xu, Q. Direct tensile properties of engineered cementitious composites: A review. Construction and Building Materials 165 (2018) 346–362.
18. Suthiwarapirak, P., Matsumoto, T., & Kanda, T. Multiple cracking and fiber bridging characteristics of engineered cementitious composites under fatigue flexure. Journal of Materials in Civil Engineering 16(5) (2004) 433–443.
19. Alam, B. A. Fatigue performance of engineered cementitious composites, Doctoral dissertation, Middle East Technical University, 2016.
20. Yildirim, T., Keskinates, M., Godek, E., Tosun Felekoglu, K., Felekoglu, B., & Onal, O. Strain Analysis of Multiple Cracking Fiber Reinforced Composites by Digital Image Correlation: Evaluation of Parameter Effects. Technical Journal 31(1) (2020) 9711–9731.
21. Jin Q, Li VC. Development of Lightweight Engineered Cementitious Composite for durability enhancement of tall concrete wind towers. Cement and Concrete Composites 96 (2019) 87–94.
22. Japan Society of Civil Engineers. Recommendations for Design and Construction of High Performance Fiber Reinforced Cement Composites with Multiple Fine Cracks (HPFRCC), Japan, 1–88, 2008.
23. Malek A, Scott A, Pampanin S, MacRae G, Marx S. Residual Capacity and Permeability–Based Damage Assessment of Concrete under Low–Cycle Fatigue. Journal of Materials in Civil Engineering 30(6) (2018) 04018081.

Hittite Journal of Science and Engineering, 2021, 8 (2) 103–121
ISSN NUMBER: 2148–4171
DOI: 10.17350/HJSE19030000221

Gaining New Insight into Machine-Learning Datasets via Multiple Binary-Feature Frequency Ranks with a Mobile Benign/Malware Apps Example

Gurol Canbek
ASELSAN, Ankara, Turkey

Article History:
Received: 2021/01/08
Accepted: 2021/03/08
Online: 2021/06/30

***Correspondence to**: Gurol Canbek, ASELSAN, 06200, Ankara, TURKEY*
E-Mail: gurol@canbek.com, gcanbek@aselsan.com.tr

ABSTRACT

Researchers compare their Machine Learning (ML) classification performances with other studies without examining and comparing the datasets they used in training, validating, and testing. One of the reasons is that there are not many convenient methods to give initial insights about datasets besides the descriptive statistics applied to individual continuous or quantitative features. After demonstrating initial manual analysis techniques, this study proposes a novel adaptation of the Kruskal-Wallis statistical test to compare a group of datasets over multiple prominent binary features that are very common in today's datasets. As an illustrative example, the new method was tested on six benign/malign mobile application datasets over the frequencies of prominent binary features to explore the dissimilarity of the datasets per class. The feature vector consists of over a hundred "application permission requests" that are binary flags for Android platforms' primary access control to provide privacy and secure data/information in mobile devices. Permissions are also the first leading transparent features for ML-based malware classification. The proposed data analytical methodology can be applied in any domain through their prominent features of interest. The results, which are also visualized in three new ways, have shown that the proposed method gives the dissimilarity degree among the datasets. Specifically, the conducted test shows that the frequencies in the aggregated dataset and some of the datasets are not substantially different from each other even they are in close agreement in positive-class datasets. It is expected that the proposed domain-independent method brings useful initial insight to researchers on comparing different datasets.

Keywords:
Machine learning; Binary classification; Dataset comparison; Malware analysis; Feature engineering; Quantitative analysis.

INTRODUCTION

The success and performance of Machine Learning (ML) algorithms closely depend on the datasets used, their sample and feature spaces, and sampling quality. Researchers who build a classifier that is trained and tested on a dataset publish their classification performances in terms of standard metrics such as accuracy, true positive rate, or F1 [1]. The classifiers are compared with other classifiers that are trained and tested on different datasets via the same performance metrics. The datasets are usually not compared or analyzed. On the other hand, researchers who wish to enrich their datasets usually merge new datasets they acquired from other sources without analyzing them. They could not be sure how these datasets are different from the existing ones.

Indeed, some statistical methods could be used to describe datasets. However, those statistical approaches summarize a dataset based on a single feature that is usually continuous. A box plot, for example, visualizes and compares the descriptive statistics such as mean, median, range, and outliers [2]. Likewise, the statistics related to the shape of the feature distribution, such as skewness, kurtosis, and the number of peaks, can be analyzed [3]. Dataset profiling based on other statistical properties such as timeliness (freshness of the samples), sample duplication, and feature density gives extra insight among the compared datasets [4]. Nevertheless, interpreting and comparing statistical figures alone are not convenient; besides, they are usually not suitable for discrete or qualitative features. To avoid such problems,

new methods should be developed to give insights about one or comparatively more than one dataset. Better, the methods should be enhanced by visualization.

This study has proposed a method to compare datasets by adapting the Kruskal-Wallis test with a novel approach to compare the medians of a prominent feature's frequencies to determine if the samples come from the same population or equivalently having the same distribution. This study aims to provide a new method for the researchers to compare more than one dataset over the common binary features. The study also adopts three visualization techniques to assess the comparisons based on the proposed method's outputs. A developed API described in Appendix A to calculate and visualize the method is provided to conduct such comparisons conveniently.

The method was tested and evaluated on Android mobile benign applications and malware datasets in the literature. The mobile malware classification problem was chosen because it is a critical emerging cyber security field where ML-based classification approaches are highly studied and practiced in the literature and the industry to enhance the capacities related to the human factor [5]. The results of the proposed comparison method summarized in Section 6 are encouraging, and shed light on using datasets on malware classification. Note that the proposed method is not specific to malware analysis, and it is expected that it could be used in any other area for comparing datasets in binary and even multi-class classification problems.

The rest of the paper is organized as follows. Section 2 introduces the classification problem domain. Section 3 describes and demonstrates techniques for an initial manual analysis of the reviewed datasets, namely basic quantitative comparison of sample/feature spaces and binary-feature space graphical analysis. It summarizes the negative and positive-class datasets to be compared in this study. Two suggested graphics, one of which is provided online as an interactive chart, to support such analysis are also demonstrated. Section 4 presents the followed methodology and the activities for comparing the datasets from different perspectives, including how to aggregate datasets. Section 5 explains the proposed comparison method based on a novel adaptation of the Kruskal-Wallis test. Section 6 provides the dataset comparison results enhanced with the suggested visualization techniques. The last two sections present the discussion and summarize the advantages of the proposed comparison methods and outline this study's contributions. Appendix A lists online supplementary materials (open-source API, interactive chart, and datasets). Appendix B surveys the related chosen pieces of work about Android application permissions and highlights the Android permission mechanism's significant aspects related to static malware analysis.

THE CASE STUDY CLASSIFICATION PROBLEM DOMAIN

The following subheadings introduce the case study problem domain, the binary features to be used in comparisons, and dataset usage in the related literature.

Android Mobile-Malware Classification Problem

Android is a mobile platform that provides a large number and a wide range of mobile applications. Android applications are developed by anyone and released on third-party application markets besides the official market named Google Play. Despite this diversity, the platform could be the target of malicious people who develop or make injections into existing applications that exposes some risks against end-users. Malware authors develop and use different techniques in those applications appearing as legitimate to overcome the platform's security or exploit human factors. Therefore, mobile malware detection, which labeling a given application as 'benign' ('negative') or 'malign' ('positive', also known as 'malware'), is one of the urging areas to be studied by the security sector and academia. Experts examine the applications manually with the help of specialized tools (e.g., reverse engineering software) and decide whether they are benign or malign. This human-involved process is called malware analysis [6]. In addition to dynamic malware analysis that concentrates on applications' behaviors observed at run-time, static malware analysis examines binaries, files, and codes to classify Android malware from benign applications [7].

Mobile Application Permission Requests as Features

Manual analysis is impossible to conduct, considering the excessive number of applications. Solely in Google Play Store, on average, 3,700 new mobile applications are released every day [8]. To some degree, machine learning comes as a promising solution to classify malware among many mobile applications based on various features [9]. Android's permission mechanism limits the specific operations performed by applications or provides ad hoc access to particular data at the end-users discretion [10]. If an application is required to initiate a phone call without going through the standard dialer user interface for the user to confirm the call, for example, it must manifest or request CALL_PHONE permissions. Please, refer to Android API (Application Programming Interface) documentation for the list of the permissions and their descriptions [11]. For static analysis, application permissions requested are the first natural and noticeable (i.e., prominent) feature category to be examined among the wide

range of possibilities. The dynamic analysis could also take application permissions into account [12]. Requested permissions could not provide conclusive evidence that an application conducts malicious activity. However, not requested permissions could generally absolve applications from possible abuses, and some of the requested permissions are notable in most malign applications. Android application permissions have been used as a prominent feature in many ML studies on static malware analysis, some of which are reviewed in Appendix B.

Some might argue that the change in Android 6.0 (API level 23) deferring permission check from install time to run time should affect the permission feature and related studies. This ostensible change will not affect the underlying mechanism shortly. Only the permission ranks will be reordered, but the features are still discriminative from an inter-class perspective. For further information, see the Appendix reviewing Android mobile malware detection literature, explicitly focusing on application permission request features.

Mobile Application Datasets

It is observed that the related literature compares classification performances with others via performance metrics, and the researchers do not consider the similarities or dissimilarities among the datasets they used. Moreover, the literature has not explicitly compared the datasets used in those studies. Whereas the performance of supervised machine learning algorithms closely depends on the datasets used, their sample sizes, sampling quality, and class ratios. Android mobile application datasets can hold many features that can be used for comparing different datasets such as the range or distribution of the application's creation date that maybe not definite or other metadata, even the exact hash of the application samples. Nevertheless, these features could be arbitrary or manipulative, comparing permission features that are still at the core of the Android security mechanism. Hence, application permissions were chosen as a prominent feature category to compare the datasets.

AN INITIAL MANUAL ANALYSIS OF THE DATASETS

Before describing the proposed method and providing the results obtained from the case study domain, namely Android mobile malware detection, a manual analysis and comparison approach is described. Such an approach is also valuable to show the difference between the manual and the proposed method. The proposed method is then verified by a demonstration that examines and compares negative (benign) datasets and positive (malign) used in various binary classification (malware classification) studies based on binary features (application permission requests) as summarized in Table 1.

The initial manual analysis conducted in this study comprises the following two techniques:

Table 1. The aspects of demonstrating dataset comparison for the case study classification domain.

Binary Classification	*Demonstration*
Classification problem (domain)	*Android mobile malware classification*
Examples (samples)	*Android mobile applications*
Negative class label	*"Benign" application*
Positive class label	*"Malign" application or "Malware"*
Prominent binary features	*Android application permission requests (shortly 'application permissions' or 'permissions')*
Example binary feature	*CALL_PHONE: It allows an application to initiate a phone call without going through the Dialer user interface for the user to confirm the call.*
Binary feature values	*0: No permission is given for the application (not allowed, default)* *1: The permission is given (allowed)*
Missing values	*Datasets might have a missing value (i.e. they do not have at least one sample (application) with the specific binary feature).* *Such features are taken as default 0 (not allowed) in dataset comparisons.*
Number of features	*Minimum: 69 and maximum: 118*
Compared datasets	*Five pairs (negative/positive class) of datasets (DS_1, DS_2, DS_3, DS_4, and DS_5) and one positive-only dataset (DS_6). An aggregated dataset (DS_A) per class is also generated, as described in Section 4. The details are provided in Table 2.*

Table 2. Summary of sample and feature spaces of the benign (negative) and malign (positive) dataset.

Dataset	Name	Authors and reference	m_N	PREV	m_P	n_N	n_P
			Sample space			Feature space	
DS_0	Touchstone Dataset[1]	Lindorfer et al., [13]	264,303	60%	399,353	84	90
DS_1	Contagio	Aswini and Vinod, [14]	254	52%	280	94	81
DS_2		Wang et al.[15][2]	310,926	2%	4,868	83	69
DS_3		Yerima et al., [16][2]	1,000	50%	1,000	99	75
DS_4	Android Malware Genome Project	Jiang and Zhou [17]		100%	1,260		83
DS_5		Peng et al., [18]	207,865	0.2%	378	118	73
DS_A	Aggregated Dataset	$DS_1 - DS_5$	520,045	1%	7,786	59	47
$-DS_6$		Hoffmann et al., [19]	136,603		6,187		
$-DS_7$	Contagio	Sarma et al., [20]	158,062		121		
$-DS_8$		Canfora et al., [21]			400		
$-DS_9$		Peiravian and Zhu, [22][2]	1,250		1,260		
$-DS_{10}$		Felt et al., [23]	900				

1. Original dataset name: ANDRUBIS
2. The positive-class datasets contain AMGP samples.

Basic Quantitative Comparison of Sample/Feature Spaces: The negative and positive class datasets are described based on sample space and feature space sizes. The distribution of positive/negative class ratios is another critical attribute for quantitative dataset comparisons.

Binary-Feature Space Graphical Analysis: The binary-feature space per dataset is analyzed and compared via the following attributes:

- The frequency distribution of the features that are common in all the datasets (a dataset might have a missing value, i.e. binary-feature)

- The change in top-ranked features (a bump-chart is recommended; an interactive version is also provided online).

After elaborating the manual analysis, the next sections describe the possible approaches to compare datasets (i.e. the types of the comparison activities), provides the definition and description of the proposed comparison method, and finally demonstrates the results when the method is applied to the reviewed datasets.

The Datasets

This study reviewed six academic studies providing Android mobile benign and malign datasets. These datasets are used to demonstrate some initial manual analysis techniques and the proposed comparison method. The following subsections describe each technique and present the results for the reviewed datasets.

Basic Quantitative Comparison of Sample/ Feature Spaces

Table 2 lists the basic quantitative information for the datasets and introduces the related studies that are also reviewed in Appendix A. The two dimensions, namely sample-space size (m) and feature-space size (n), are valid for any datasets, whereas prevalence (*PREV*; The proportion of total positive samples (m_p), e.g., having a malign characteristic, in total sample size [$m_p + m_N$]) is determined by comparing sample-space sizes of the positive and negative class datasets. In the related literature, it is observed that authors compare their malware classification performance with others, most of which are based on different benign and malign datasets. The method proposed in this study can help to compare those datasets. Highlighting once again, there has been no large-scale comparative study on comparing datasets used for mobile malware classification encountered in the literature. However, it was not possible to see to what extent the proposed aggregation and comparison methods can be valid. A more recent independent study is used for assessing validity. Lindorfer et al. [13] presented their findings based on a dataset collection called "ANDRUBIS" from a wide range of sources.

The DS_0 dataset listed in the first row in Table 2 has not only a higher number of samples but also the highest number of malware (positive-class examples) compared with ot-

her datasets. Thus, it was selected as a kind of correctness measure that is called 'touchstone' in this study, to support verifying the comparisons. In this study, the permission frequencies in DS_1 to DS_5 datasets per class were also aggregated into single combined values. The aggregated dataset, named DS_A is used to search for their consistencies among the datasets and to provide a baseline for further research. The aggregated frequencies are calculated by the weighted arithmetic mean of frequencies in individual datasets according to dataset sample sizes per class, as explained in Section 4 in detail. This is a natural calculation approach considering combining all the datasets into one dataset named DS_A (ignoring the duplicate samples due to the same samples existing in one or more datasets). Note that the aggregated dataset (DS_A) and the touchstone dataset (DS_0) are entirely different and independent.

Note that two published datasets were combined, one from 2011 and one from 2012 in [18] into one dataset (DS_5). The six datasets (DS_6 – DS_{11}) encountered in the literature were excluded from this study due to the following reasons. The DS_9 dataset [22] is the same as the original DS_4 dataset [17]. The datasets DS_8 [21], DS_{10} [23] have missed one class. Only the top ten permissions were published for DS_6 [19], and only the top 20 permissions were published for DS_7 [20], but the whole feature space could not be obtained for this study.

Binary-Feature Space Graphical Analysis

As seen in Table 2, dataset sample sizes, prevalence, and feature space sizes of the datasets are dispersed. Sample sizes and equal class sample sizes (i.e. near 50% prevalence) are critical for generalization and unbiased classification. The low number of samples and low prevalence rates also cause limited credibility in the literature. The feature-space sizes and elements (permissions existing in each dataset) are also different in Table 2. Moreover, frequencies and ranks of permission requests vary from dataset to dataset.

Binary-feature frequency distribution

Fig. 1 shows the frequency distribution of the prominent binary features in negative and positive-class datasets together in one graphic, including only the common features (i.e. the permissions existing in all the datasets per class). The lower left part shows the distribution for the positive-class, while the upper right part is for the negative-class in reverse order of binary-feature frequency. The permissions within five datasets (from DS_1 to DS_5) and aggregated dataset (DS_A) are sorted according to the touchstone dataset's (DS_0) permissions with descending frequency order of corresponding class. Fig. 1 also exhibits a discrepancy between the datasets per class when the permissions are ordered according to DS_0. The proposed method helps to assess the discrepancy, as explained in the next sections.

Nevertheless, interpreting Fig. 1, the following findings were deduced:

- Negative-class datasets, except for dataset DS_1 having very few samples, are more similar to the touchstone dataset than positive-class ones.

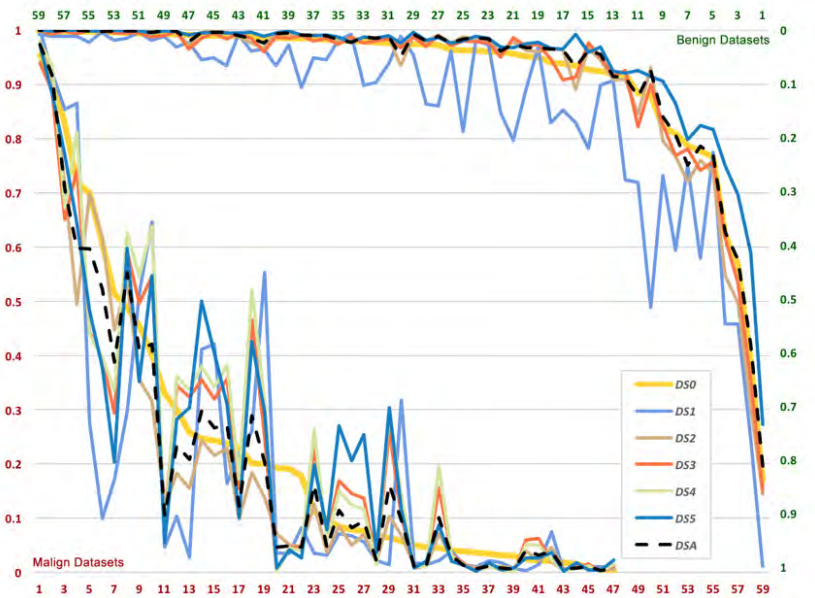

Figure 1. Binary-feature frequency distribution: Lower-Left Group: Frequency distribution of 47 common permissions in positive-class datasets and Upper-Right Group: Frequency distribution of 59 common permissions in negative-class datasets. Common permissions are the intersection of all datasets per class and sorted according to the corresponding touchstone dataset (DS_0, with thicker gold colored lines).

- The distribution of aggregated datasets (DS_A) seems closer to the touchstone dataset (DS_0) than individual datasets.

The first finding suggests that positive classes (generally abnormal entities like malware in provided applications or illness for a medical classification or diagnosis test) possess high variability (or entropy). The second one implies that the aggregation of different datasets reduces noise and enhances sampling. Concerning the first finding, this is especially valid for the example domain where malware propagating by repackaging benign applications are the most common ones that request one or more extra permission from benign ones [24]. For the second finding, as seen in the dataset DS_1 example, the low number of samples does not provide sufficient generalization; therefore, they should be used with caution in machine learning applications.

The top binary feature ranks

Fig.s 2 and 3 show the changes in the ranks of permissions between DS_0, DS_1, …, DS_5 for positive and negative-class datasets, respectively, for the top 15 permissions only (for the sake of simplicity). The readership is encouraged to visit http://tabsoft.co/32CQGIP for interacting with the online chart prepared for this study in full-intersected permission space coverage.

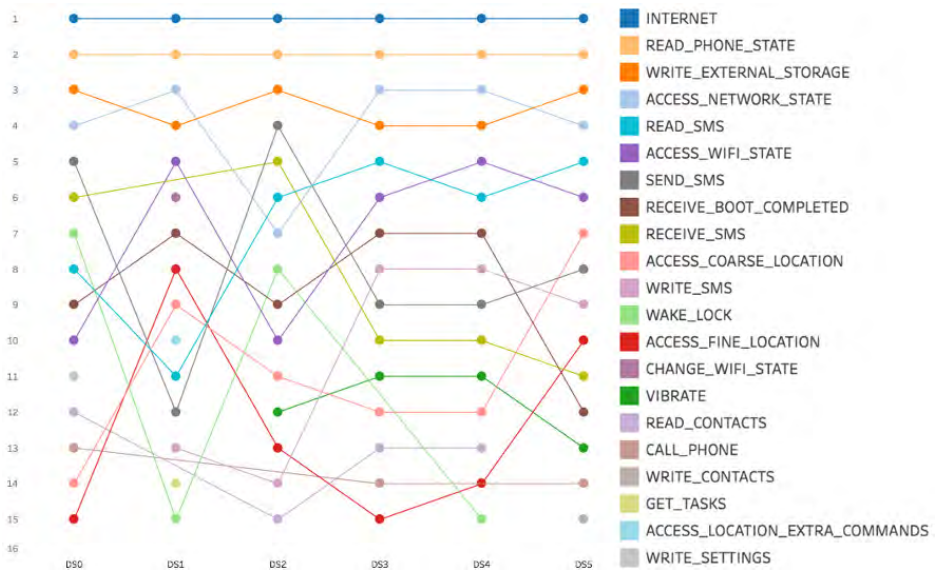

Figure 2. Ranked top 15 permissions for positive-class (malign) datasets (from DS_0 to DS_5). Visit http://tabsoft.co/32CQGIP for full data and an interactive chart.

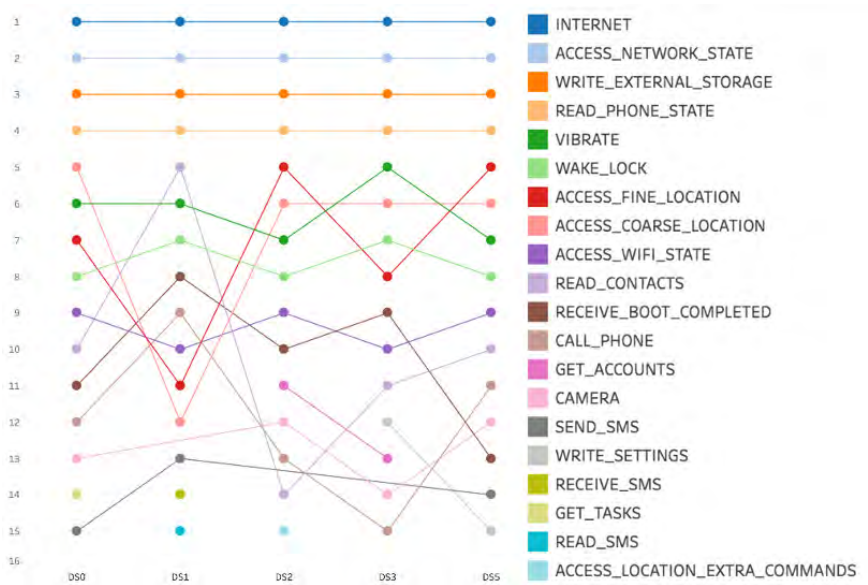

Figure 3. Ranked top 15 permissions for benign datasets (from DS_0 to DS_5)

Please, refer to Android API documentation for descriptions of the permissions (at developer.android.com). Considering the top 15 permissions in positive-class datasets, Fig. 2 shows DS_3 with DS_4, and DS_4 with DS_5 are relatively similar rankings for corresponding features (permissions). Using an interactive chart hovering on permissions (circles) in the DS_0 dataset's column, you can see that DS_0 with DS_5 are also similar rankings (although they are not adjacent).

Concerning negative-class datasets, Fig. 3 shows DS_2 with DS_5 and DS_0 with DS_5 are relatively similar rankings considering the top 15 permissions. If positive-class (Fig. 2) and benign-class (Fig. 3) feature ranks are compared, the top two permissions are the same in all the malign datasets while the top four ones in benign datasets. This supports the interpretation of high variability in malign datasets in Fig. 1 above. These two types of graphs help to analyze and compare datasets, but it is manual and may be subjective. Therefore, it is necessary to measure similarities that provide more accurate results.

METHODS

Fig. 4 describes the general methodology followed in this study. The permissions were collected directly from different negative and positive-class datasets of the related six studies. Some of the authors were contacted to receive their datasets covering all the permission requests (i.e. full feature space for a dataset). After pre-analyzing the permission request features, their frequencies (i.e. ratio of the number of samples requesting permission to total sample size) were calculated for each class, and binary features were ranked according to these frequencies per each dataset from the most frequent to the least frequent.

For a dataset with c binary class (positive (P) or negative (N)), the existing n_c binary features $\{x_1, x_2, ..., x_{n_c}\}$ are presented as X vector. $f_{X_c DS_i}$ denotes binary-feature frequencies vector for i. dataset. $F_{X_c DS_i}$ denotes ranked feature-frequencies vector and holds ranks within the same datasets instead of frequencies. The ranked feature-frequencies vector for the aggregated dataset (DS_A) per each class was calculated by applying a weighted average of feature frequencies in each dataset (from DS_1 to DS_5) and ranked from top to bottom as shown in Eq. (1) where m_{P_i} and m_{N_i} denote the total sample size of i. dataset per c class, and S_c is the number of datasets compared.

$$F_{X_{c=P,N} DS_A} = \text{rank}\left(\frac{\sum_{i=1}^{S_c} f_{X_c DS_i} \cdot m_{c_i}}{\sum_{i=1}^{S_c} m_{c_i}} \right) \quad (1)$$

The ranked binary-feature frequencies per negative and positive classes are compared between:

- (Comparison-1) all the dataset including the touchstone dataset (DS_0) and the aggregated dataset (DS_A)
- (Comparison-2) pair of all the datasets (e.g., between DS_1 and DS_A or DS_1 and DS_0)

The results of the two comparisons on the reviewed datasets are given in Section 6.

NEW METHOD: COMPARISON VIA ADAPTED KRUSKAL-WALLIS TEST

The Kruskal-Wallis test is a nonparametric test to calculate the null hypothesis assuming that independent samples are from the same population. The test, which was developed by and named after Kruskal and Wallis [25], is an extension of the Wilcoxon Rank Sum Test on two groups. As a nonparametric test, the Kruskal-Wallis test does not assume that populations have normal distributions. The test is applicable for measurement variables as well as nominal variables classifying observation values into discrete categories (like binary features) among at least three or more samples.

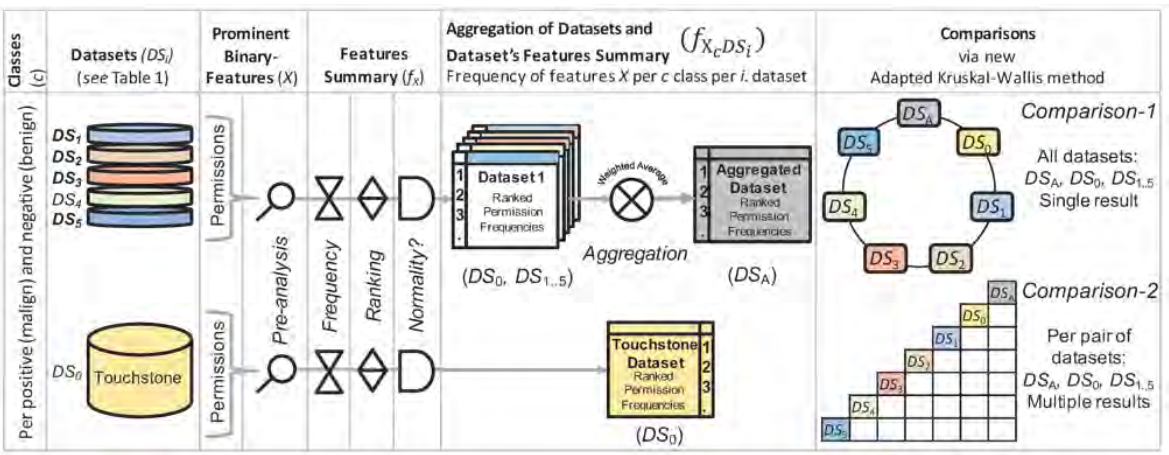

Figure 4. Activity flows for comparing datasets via feature frequency ranks.

This test is based on ranks instead of the original observation values (i.e. frequencies). This makes the test much insensitive to outliers that make it more suitable for this experimental study on the negative (benign) and positive (malign) mobile applications like other practical research studies such as clinical ones [26]. The ranks are calculated across all the samples by ordering the observation values from smallest (a rank of 1) to largest and could be fractional. The sum of the ranks per sample is also calculated.

Typical usage of the Kruskal-Wallis test in machine-learning is using as a filtering method for feature selection in high-dimensional datasets [27,28]. It is appropriate for not only binary classification but also multi-class classification problems [29]. The literature has successfully used the test on analyzing and comparing data with different characteristics, for example, censored data [30] and microarray gene expression data [31], but also addressed the limitations when applied in high dimensional low sample size data (shallow datasets) [32]. Another usage of the Kruskal-Wallis test, along with the one-way analysis of variance test, Friedman's test, in ML is in testing the statistical significance between the different individual classifiers (i.e. whether a classifier is significantly different from the others) [33]. The significance in algorithm factors or parameters such as the data-size effect or fitness values is also tested with the Kruskal-Wallis test [34,35]. From an information security perspective, the test was used for evaluating different alternatives, such as measuring differences in password behaviors and attitudes between research participants [36] or selecting more discriminative features in the forensic analysis [37]. It was encountered that only one study uses the Kruskal-Wallis test in malware analysis in the literature. Asmitha and Vinod [38] employ the test for selecting prominent features from benign and malign applications on the Linux desktop platform. According to their classification experiment, the Kruskal-Wallis test achieves slightly better than the other feature selection methods. The review reveals that the literature uses the test in comparing the dataset's features and classifier's performances. However, it is not used to compare datasets. This study explores and proposes such usage demonstrated in real-world datasets in a specific domain.

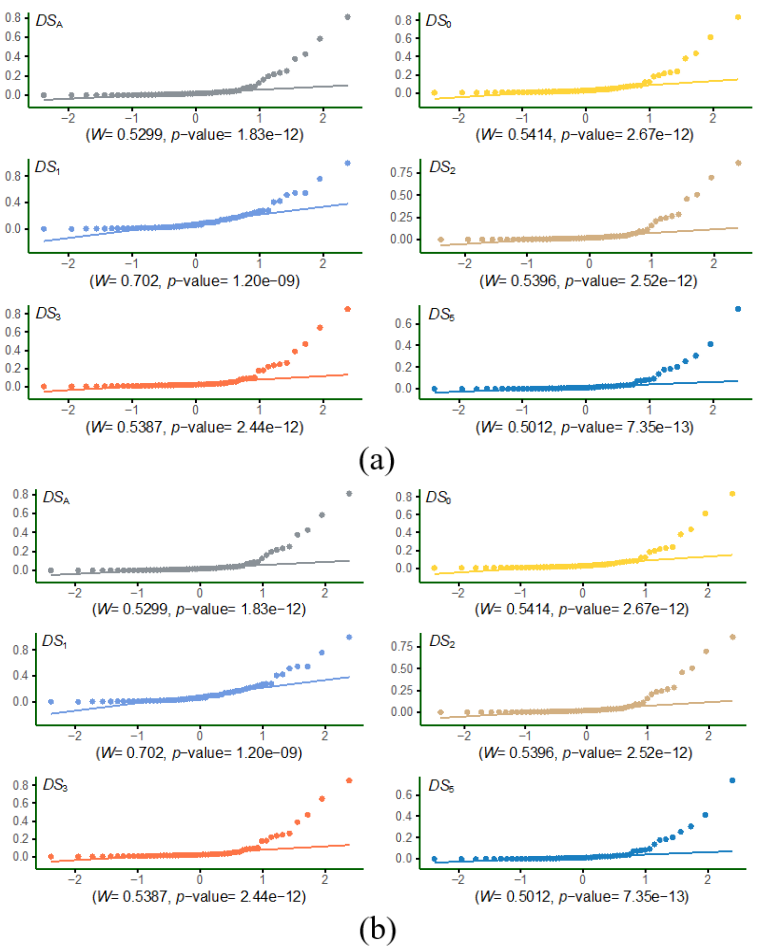

Figure 5. Normality check by Quantile-Quantile chart with Shapiro-Wilk test values and p-values. y-axis shows binary-feature frequencies for (a) positive-class datasets (b) negative-class datasets. Note that some of the frequency values (points) are outside the corresponding normal distribution indicated by a shaded area.

Normality Check

Before applying the proposed adapted Kruskal-Wallis test, we must ensure that the frequencies do not present a normal distribution [39]. If a normal distribution exists, the distribution can be entirely defined by using merely two parameters: mean and standard deviation, which may be used for dataset comparison statistically instead of this method.

Two supportive approaches are employed for checking normality:

- A formal method by using the Shapiro-Wilk Test
- A manual method by drawing Quantile-Quantile charts

Eq. (2) is the Shapiro-Wilk test explicitly written for binary-classification datasets where a_j normalized standard normal-order statistics and $\overline{f_{X_c DS_i}}$ is the mean value for an *i.* dataset:

$$W_{DS_i} = \frac{(\sum_{j=1}^{n_{cmn}} aj \cdot f_{x_c\, DS_{ij}})^2}{\sum_{j=1}^{n_{cmn}} (f_{X_c DS_{ij}} - \overline{f_{X_c DS_i}})^2} \quad (2)$$

W is between 0 and 1, and lower *W* values against the corresponding test table value indicate the rejection of the normality null hypothesis. Fig. 5 shows not only the quantile-quantile chart but also the Shapiro-Wilk test values with *P* probability values (*p*-values) for each dataset in x-axes.

Lower *W* values, or better specifically, lower corresponding *p*-values (less than 0.05 for 95% significance level), reject the normal distribution. Here we have *p*-values that are even very close to zero (more than 99% significance level). Note that the original Shapiro-Wilk test is suitable for less than 50 observations. In this study, Royston's [40] extension is used here to avoid such a limit. Benign and malign datasets have 59 and 47 common (intersected) feature-space sizes (n_{cmn}). Ensuring non-normality, the test can be employed as described in the following subsection.

Adapted Kruskal-Wallis Test

In the standard notation, given *C* samples with *N* number of total observations in all samples combined, with n_i observations yielding the sum of the ranks as R_i in the *i.* sample, the Kruskal-Wallis Test value (*H*) is calculated by the following equation:

$$H = \frac{12}{N(N+1)} \sum_{i=1}^{C} \frac{R_i^2}{n_i} - 3(N+1) \quad (3)$$

Eq. (4) has specifically annotated for the reviewed dataset comparisons where S_c is the total number of datasets in this study (seven for positive, six for negative, including aggregated dataset DS_A). *N* in Eq. (3) corresponds to the total of samples' common (intersected) feature-space size (n_{cmn}) (7x59 for negative-class, 6x47 for positive-class). R_i corresponds to $\text{rank}(f_{x_c D_i})$, the sum of binary-feature frequencies ranks in the *i.* dataset. Rank orders are determined within all the datasets as if there is one dataset where the lowest value corresponds to the lowest rank. Fractional ordering is used for ties by averaging orders.

$$H = \frac{12}{S_c \cdot n_{cmn} \cdot (S_c \cdot n_{cmn} + 1)} \sum_{i=1}^{S_C} \frac{\text{rank}(f_{p_C DS_i})^2}{n_{cmn}} - 3(S_C \cdot n_{cmn} + 1) \quad (4)$$

Low *H* values or low *p*-value as an approximate chi-square statistic (with $S_c - 1$ the number of degrees of freedom, DoF) in the range [0, 1] rejects the null hypothesis that independent samples are from the same population.

RESULTS

The following subsections provide comparison results for all the datasets together (Comparison-1) and per pair of all the datasets (Comparison-2).

Comparison-1 (All)

The proposed adapted Kruskal-Wallis test was conducted for all the permission frequencies in negative and positive-class datasets (touchstone, aggregated, and four negative-class or five positive-class datasets, respectively) listed in Table 2. The conducted test produced two different results per class. Table 3 displays the summary of the test. The *p*-values less than the significance level ($\alpha = 0.05$) reject the null hypothesis that the samples in negative-class datasets are from the same population concerning ranks of the frequencies of the same permission features or "negative-class datasets are different from

Table 3. Dataset comparison summary based on adapted Kruskal-Wallis method.

Class (c)	n_{cmn}	S_c *(DoF)*	*H*	*p-value*	*Test Result**
Positive (Malign)	*47*	*Seven datasets (6)*	*2.45*	*0.8735*	*Failed to reject the null hypothesis*
Negative (Benign)	*59*	*Six datasets (5)*	*27.84*	*3.92e-05*	*Rejected*

* Significance level, $\alpha = 0.05$

each other". In comparison, we could not conclude if the positive-class datasets are different, although the *p*-value is close to 1. The alternative hypothesis indicating "dissimilarity" assumes that at least one dataset comes from a different population than the others.

The *H* value obtained by Eq. (4) is merely for stating whether the group of datasets together differs in some way. This is important because one could not express this evidently by analyzing and comparing the samples as tried in Section 3.3 via different graphs. However, the dissimilarity of individual datasets should also be interpreted separately afterward.

Comparison-2 (Pairs) with Suggested Visualization Techniques

Comparison-2 shows the similarity test per pairs of the dataset. Instead of giving the results in a cross-tabular fashion, three visualization techniques are recommended:

1) Multiple comparisons of mean ranks

2) All-in-one binary-feature frequency descriptive statistics

3) Complete clustered pairwise comparison of *p*-values.

The suggested visualization techniques demonstrated in Fig.s 6 and 7 are straightforward, informative, and easy to interpret.

Visualization-1 (Multiple comparisons of mean ranks)

The first visualization technique depicts the pairwise comparison of the datasets based on rank means calculated by the Kruskal-Wallis test. The graph is developed by using MATLAB's multi compare functionality [41]. The interactive version of the graph shows the mean rank difference between a selected dataset and the others. The findings of the multiple comparisons of mean ranks to be highlighted are

- "No positive-class datasets have mean ranks significantly different from the aggregated positive-class dataset (DS_A)," as shown in Fig. 6 (b) (Kruskal-Wallis test can reject the null hypothesis even the means or medians are the same. Therefore, p-values are valid.).
- The same findings are not valid for negative-class datasets. However, four datasets, including the aggregated dataset (DS_A), have mean ranks significantly different from the benign (DS_1) dataset, as shown in Fig. 7 (b).
- Interestingly, mean ranks are not significantly different for DS_1 and the touchstone dataset DS_0.

Visualization-2 (All-in-one binary-feature frequency descriptive statistics)

Violin with a box-plot comparison diagram in Fig.s 6 and 7 (b) show the following binary-feature frequency descriptive statistics for negative and positive-class datasets:

- ranges (min/max values shown in vertical line ends),
- quartiles (lower and upper shown in the bottom and top edges of boxes),
- medians (horizontal line in box),
- means (black dot),
- outliers (pink dot), and
- probability densities (violin shape).

The significant difference of negative-class DS_1 and no-significance difference among positive-class datasets can be observed in Visualization-2 graphs (see the shapes of the violins). Note that DS_1 has the smallest samples for both classes.

Visualization-3 (Complete clustered pairwise comparison of p-values)

The third visualization technique that is originally designed as an API in R by the author. The API displays the *p*-values for all the pairs of datasets. Pairwise dataset comparisons with heatmap diagrams in Fig.s 6 and 7 (c) present a complete set of comparison information. It shows colored *p*-values for the null hypothesis indicating similarity between the paired datasets. Datasets are also hierarchically clustered by Euclidean distances of *p*-values (i.e. their similarities). In other words, the datasets in row/columns are reordered according to row or column means and then hierarchically clustered using Euclidean distance. A similar group of datasets is shown as horizontal and vertical dendrograms.

The findings complying with the Comparison-1 shown in Table 3 are

- We could not reject the null hypothesis that each pair of the positive-class datasets are from the same population with ultimately high p-values. DS_0 and DS_1 have 0.7989 *p*-values at a minimum.

- The following dataset pairs are significantly different from each other: DS_A vs. DS_1 (with p-value: 8e-04), DS_A vs. DS_5 (with p-value: 0.00001), DS_1 vs. DS_2 (with p-value: 0.0021), and DS_1 vs. DS_3 (with p-value: 0.0361). For others, we could not reject the null hypothesis.

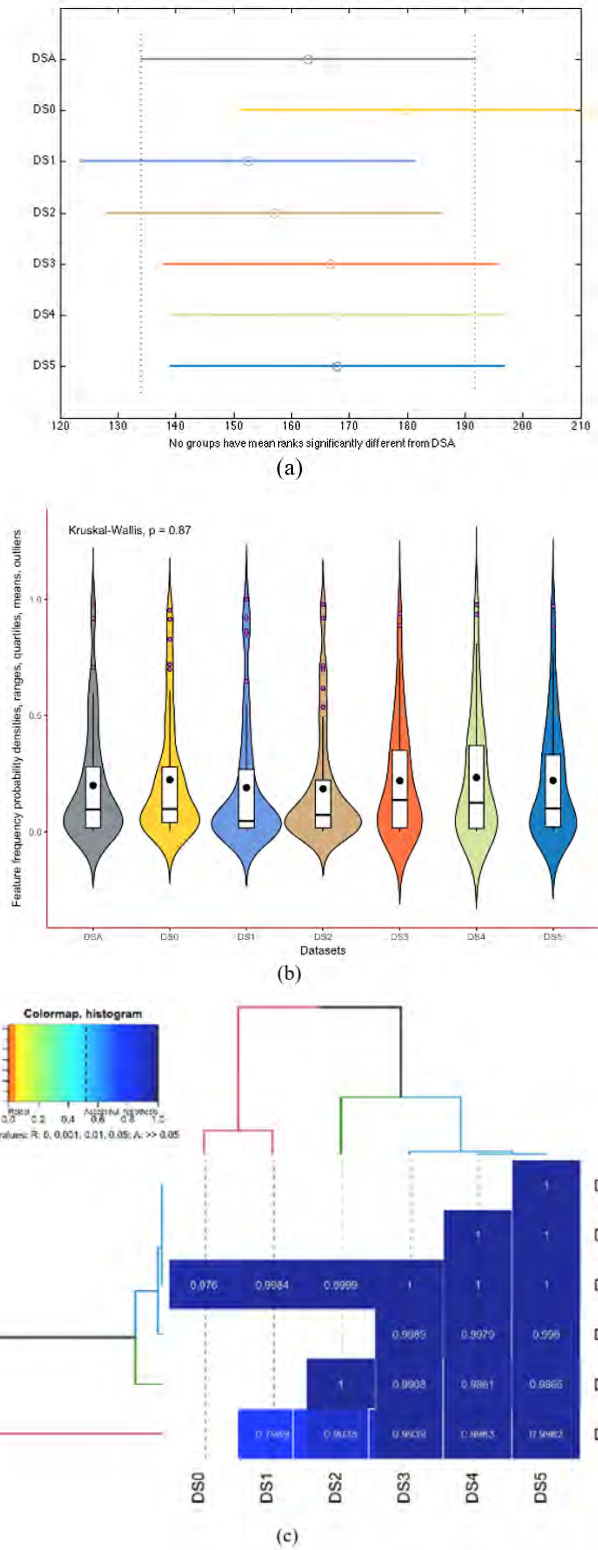

Figure 6. Comparison graphs for malign datasets: (a) multiple comparisons of mean ranks (graph shows DS_A comparison) (b) violin with a box-plot comparison diagram (c) Pairwise dataset comparisons with heatmap diagram

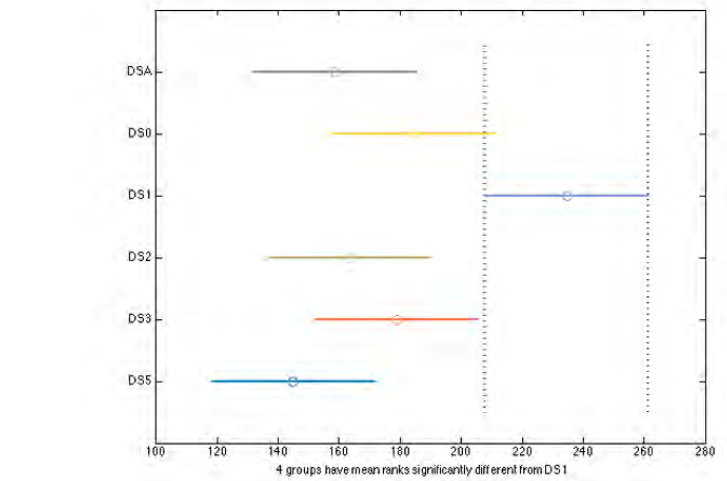

(a)

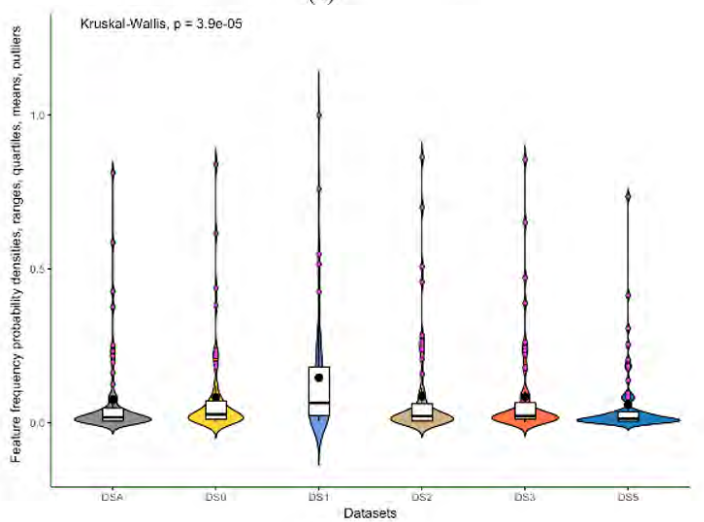

(b)

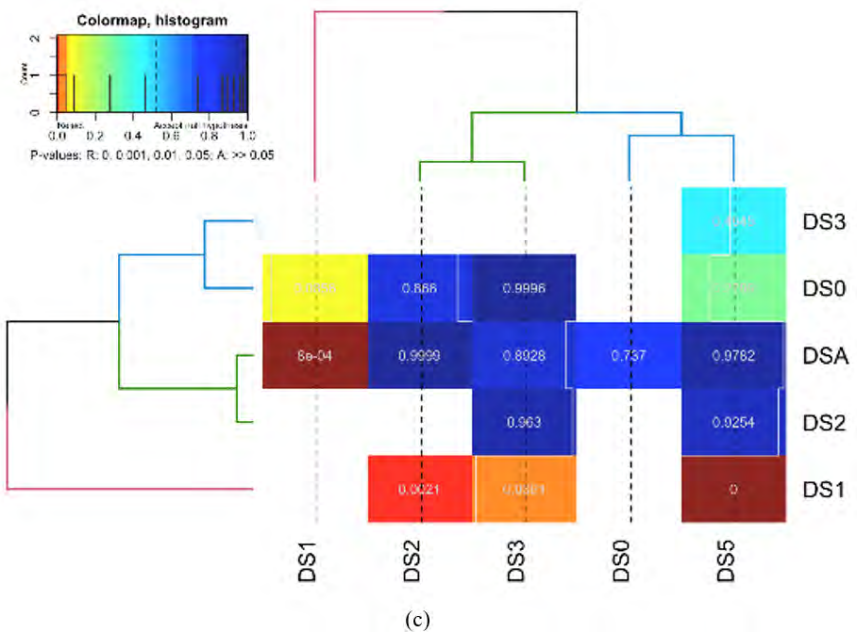

(c)

Figure 7. Comparison graphs for benign datasets: (a) multiple comparisons of mean ranks (graph shows DS_1 comparison) (b) violin with a box-plot comparison diagram (c) Pairwise dataset comparisons with heatmap diagram

Touchstone vs. Aggregated Datasets Comparison

Overall assessment of the test results suggest the following two highlighted findings of touchstone and aggregated datasets:

- For the comparison of the touchstone and aggregated datasets: There is no significant difference between the datasets DS_0 and DS_A. Rank means the difference between these datasets is 17.2 (162.9 and 180.1) for positive-class and 26.1 (158.6 and 184.7) for negative-class, as shown in Fig.s 6 and 7 (b).

- For the comparison between each dataset and the aggregated dataset (DS_A): Fig.s 6 and 7 (b) show that the malign datasets are more similar to the aggregated dataset than the touchstone dataset. Considering the touchstone dataset (DS_0), the DS_4, DS_5, and DS_3 malign datasets and DS_3 and DS_2 are the most similar datasets to the touchstone dataset so that their sampling approaches are quite successful.

DISCUSSION

Two aspects addressed in this study are discussed in this section: first the issues and findings specific to the case study domain and the prominent feature category, second, the issues related to the proposed comparison method.

Firstly, permission requests are leading clues to anticipate the purpose of Android applications not only for regular users but also for malware analysts who use them as a prominent feature category to classify malware. A fundamental problem with much of the literature on mobile malware classification on the Android platform is that they use different datasets and focus on the results of their classification. However, the comparison of the datasets has not been dealt with in-depth.

Comparison of performances of malware classification attempts with various ML algorithms cannot be consistent without knowing the difference of the used datasets. To study this gap, this study has compared the permissions ranked by request frequencies of different datasets of the seven reviewed academic works. The ANDRUBIS dataset, as it is called the "touchstone" dataset in this study, was used as a verification dataset for comparing the similarity of binary-feature (permissions) frequencies of individual datasets.

This study has conducted a focused review of the literature and highlighted the different issues around permissions to classify Android mobile malware. In summary, it is concluded that;

- The Android permissions and frequency of permission requests do continue to hold its invaluable contribution to statically classify Android applications as long as they are selected comparatively and continuously updated;

- Satisfactory results were obtained showing that frequently requested permissions extracted benign/malign applications, as well as the permissions dominantly requested by malign applications, should be the first statistical features to examine for static malware analysis and dynamic analysis further;

- Comparing the performance of malware classification, the published research should consider the comparison of their datasets and others;

- Authors could use the proposed dataset comparison method and initial manual analysis approaches to compare their datasets with others easily. The permission-requests feature distribution could also be used as an indicator to examine datasets;

- Reducing the number of top permissions that are considered may provide more accurate comparison statistics; and

- The characteristics of the feature used for comparison, especially the factors affecting its frequency, should be scrutinized (as discussed in Appendix A). Eliminating this kind of external effect makes comparisons more accurate.

The followings are the summary of the overall findings in the conducted test on the case study domain:

- Further evidence has been provided on the effect of good sampling of negative-class (benign applications) and positive-class (malign or malware) datasets in static malware analysis research in the literature, which pointed towards the idea that even a small number of well-selected datasets could present a sufficient level of representation comparing the touchstone dataset.

- There is still a need for continuously updating samples to adapt to the existing trends in benign and malign applications.

Secondly, concerning the proposed comparison method, the Kruskal-Wallis test was conducted with a completely different approach. The test is typically applied through a single ordinal variable (apart from categorical or interval variables), for example, "levels of blood cholesterol" with different observations in more than two samples. For the

proposed approach, the frequencies of the specific number of the same binary features, namely Android mobile application permission requests, are used as the observations in each dataset. In this manner, it is possible to create a kind of 'imitated' ordinal variable per dataset that could be expressed as 'the frequency of any binary feature of a specific number of requested permissions in the compared dataset.' The datasets were compared by using this variable. The comparison via binary-feature frequencies by this method has the following advantages:

- It provides a single metric (a test value (H) with easy to interpret p-value indicator) for similarity among datasets.

- This test also shows the similarity positions for all datasets without pairwise comparisons, which could be time-consuming and hard to analyze.

The method does not require any preference for the choice of parameter settings (except default significance level); therefore, it can be used as-is. The comparison does not need the feature-space details of all the samples in the dataset; the frequencies of the prominent binary features are sufficient. This is practical considering the difficulties or obstacles in sharing the datasets. The provided API facilitates the comparison process providing results and generating graphs for the recommended visualization techniques. The results that were reported from the complete perspective in this study are promising. The subject matter experts can find the methodology convenient and insightful. At least, the method addresses the dissimilarity among the datasets allowing the researchers and experts to focus. Nevertheless, theoretical validation cannot be found; therefore, more simulations should be conducted. The future work will be validating the method in synthetic datasets.

This study also includes comparing the individual datasets with the aggregation of the datasets. Aggregating compared datasets spots the missing frequent and rare patterns in samples. Thus, adding different samples having those missing patterns could improve the overall sampling quality of a dataset in hand.

Regarding the novel adaptation of the Kruskal-Wallis test, there could be some controversy surrounding the imitation of the ordinal variable. Instead of using values of a single variable from different observations for each sample (e.g., INTERNET permission request frequencies observed per dataset), using the values of a group of variables from different observations may seem unconventional. However, it becomes more understandable and valid for the test when the variable is stated as "the binary-feature frequency values of a specific group of observations". Upon suggesting this approach, other studies in different domains could try the usability of the methods.

Limitations comparison of the datasets over common features seems to discard the real differences among datasets. In this case, the missing values (i.e. nonexistent features) should also be reported in the comparisons. Nevertheless, as the datasets become large, having at least one sample per feature, the comparison over common features becomes more representative.

The comparison approaches and the proposed method has been demonstrated in real-world datasets. The manual analysis generally supports the results. Furthermore, the fact that the malign DS_2 and DS_3 datasets have the same samples as the malign DS_4 (Android Malware Genome Project) dataset is also validated via the clustered complete pairwise comparison of p-values in Comparison-2 (DS_3 and DS_4 in one dendrogram, which is then in the upper dendrogram with DS_2, as shown in vertical dendrograms in Fig. 6).

CONCLUSION

The researchers mostly focus on selecting and optimizing ML classification algorithms and improving the achieved performance expressed in terms of conventional performance metrics such as accuracy and F1. Selecting and maintaining a dataset is a secondary concern for not only classification problems but also clustering problems. Both in practice and the literature, performance metrics are the only criteria to claim success or improvement in a specific classification problem domain whereas the datasets are not taken into account in comparison of different studies.

The initial manual analysis of datasets demonstrated in Section 3 provides little insight and requires efforts for preparing summary data and related graphics. Basic quantitative comparison of sample and feature spaces presents the preliminary perspective in compared datasets whereas binary-feature space graphical analysis provides more detail. Especially, feature ranks are more understandable to readers; however, the approximation used on calculating the ranks according to the frequencies decreases. The precision, related calculations, and analyses are simplified.

To help to avoid such inefficiencies in the manual analysis of datasets, this study proposed a novel adaptation of the Kruskal-Wallis test. In the proposed method, instead of providing a single ordinal variable, a kind of variable was created, indicating the frequencies of the binary features. The features are selected from the intersection of existing features in all of the compared datasets. Each of those frequencies is provided as if they are the observations per da-

taset. Then the tests are conducted based on these variables in the case study domain. It is observed that the results of manual analysis for the case study domain and the proposed method are coherent. Although the method and approaches provided in this study were applied to the mobile malware domain, they could be used in other domains having a binary-feature space vector.

The demonstration in the case study domain has shown that the method gives clear and measurable initial insights to see the differences among available datasets. The researchers can publish the dataset comparison test results among their dataset and the other datasets along with the classification performance metrics. The method can also be particularly useful for the practitioners and researchers to compare different open ML datasets provided in different platforms such as Kaggle. It can be used in data mining, data quality, and data profiling activities. The provided API given in Appendix A supports the possible future uses of the method. Finally, it is expected that the proposed comparison method and findings potentially lead to practical improvements in dataset collection, sampling, profiling, and mobile malware analysis and provide a measurable indicator for comparing the used and related datasets.

CONFLICT OF INTEREST

Author approve that to the best of their knowledge, there is not any conflict of interest or common interest with an institution/organization or a person that may affect the review process of the paper.

References

1. Canbek G, Sagiroglu S, Taskaya Temizel T, Baykal N., Binary classification performance measures/metrics: A comprehensive visualized roadmap to gain new insights, in: 2017 International Conference on Computer Science and Engineering (UBMK), IEEE, Antalya, Turkey, 2017: pp. 821–826. doi:10.1109/UBMK.2017.8093539.
2. Ostertagová E, Ostertag O, Kováč J., Methodology and Application of the Kruskal-Wallis Test, Applied Mechanics and Materials. 611 (2014) 115–120. doi:10.4028/www.scientific.net/AMM.611.115.
3. Piringer H, Berger W, Hauser H., Quantifying and comparing features in high-dimensional datasets, in: Proceedings of the International Conference on Information Visualisation, IEEE, London, 2008: pp. 240–245. doi:10.1109/IV.2008.17.
4. Canbek G, Sagiroglu S, Taskaya Temizel T., New techniques in profiling big datasets for machine learning with a concise review of Android mobile malware datasets, 2018 International Congress on Big Data, Deep Learning and Fighting Cyber Terrorism (IBIGDELFT). (2018) 117–121. doi:10.1109/ibigdelft.2018.8625275.
5. Andrade RO, Yoo SG., Cognitive security: A comprehensive study of cognitive science in cybersecurity, Journal of Information Security and Applications. 48 (2019) 1–13. doi:10.1016/j.jisa.2019.06.008.
6. Canbek G, Sagiroglu S, Baykal N., New comprehensive taxonomies on mobile security and malware analysis, International Journal of Information Security Science (IJISS). 5 (2016) 106–138. http://www.ijiss.org/ijiss/index.php/ijiss/article/view/227.
7. Surendran R, Thomas T, Emmanuel S., A TAN based hybrid model for android malware detection, Journal of Information Security and Applications. 54 (2020) 1–11. doi:10.1016/j.jisa.2020.102483.
8. Clement J., Average number of new Android app releases via Google Play per month as of May 2020, New York, 2020. https://www.statista.com/statistics/276703/android-app-releases-worldwide.
9. Suarez-Tangil G, Tapiador JE, Peris-Lopez P, Ribagorda A., Evolution, detection and analysis of malware for smart devices, IEEE Communications Surveys & Tutorials. 16 (2014) 961–987. doi:10.1109/SURV.2013.101613.00077.
10. Deypir M, Horri A., Instance based security risk value estimation for Android applications, Journal of Information Security and Applications. 40 (2018) 20–30. doi:10.1016/j.jisa.2018.02.002.
11. Android, Manifest.permission, Android Developers. (2020). https://developer.android.com/reference/android/Manifest.permission.html (accessed September 2, 2020).
12. Cen L, Gates C, Si L, Li N., A probabilistic discriminative model for Android malware detection with decompiled source code, IEEE Transactions on Dependable and Secure Computing. 12 (2015) 400–412. doi:10.1109/TDSC.2014.2355839.
13. Lindorfer M, Neugschwandtner M, Weichselbaum L, Fratantonio Y, Van Der Veen V, Platzer C., ANDRUBIS - 1,000,000 apps later: a view on current Android malware behaviors, in: 3rd International Workshop on Building Analysis Datasets and Gathering Experience Returns for Security (BADGERS), Wroclaw, Poland, 2014: pp. 3–17.
14. Aswini AM, Vinod P., Droid permission miner: Mining prominent permissions for Android malware analysis, in: The 5th International Conference on the Applications of Digital Information and Web Technologies (ICADIWT), IEEE, Bangalore, India, 2014: pp. 81–86. doi:10.1109/ICADIWT.2014.6814679.
15. Wang W, Wang X, Feng D, Liu J, Han Z, Zhang X., Exploring permission-induced risk in Android applications for malicious application detection, IEEE Transactions on Information Forensics and Security. 9 (2014) 1828–1842. doi:10.1109/TIFS.2014.2353996.
16. Yerima SY, Sezer S, McWilliams G., Analysis of Bayesian classification-based approaches for Android malware detection, IET Information Security. 8 (2014) 25–36. doi:10.1049/iet-ifs.2013.0095.
17. Jiang X, Zhou Y., Android Malware, Springer, Raleigh, NC, USA, 2013.
18. Peng H, Gates C, Sarma B, Li N, Qi Y, Potharaju R, Nita- Rotaru C, Molloy I., Using probabilistic generative models for ranking risks of Android apps, in: 19th Conference on Computer and Communications Security (CCS), ACM, New York, New York, USA, 2012: pp. 241–252. doi:10.1145/2382196.2382224.
19. Hoffmann J, Ussath M, Holz T, Spreitzenbarth M., Slicing droids: Program slicing for smali code, in: SAC '13 Proceedings of the 28th Annual ACM Symposium on Applied Computing, Coimbra, Portugal, 2013: pp. 1844–1851. http://dl.acm.org/citation.cfm?id=2480706 (accessed October 22, 2013).
20. Sarma B, Li N, Gates C, Potharaju R, Nita-Rotaru C, Molloy I., Android permissions: A perspective combining risks and benefits, in: 17th Symposium on Access Control Models and Technologies (SACMAT), ACM, New York, New York, USA, 2012: pp. 13–22. doi:10.1145/2295136.2295141.
21. Canfora G, Mercaldo F, Visaggio CA., A classifier of malicious Android applications, in: The 8th International Conference on Availability, Reliability and Security (ARES), IEEE, Regensburg, 2013: pp. 607–614. doi:10.1109/ARES.2013.80.
22. Peiravian N, Zhu X., Machine learning for Android malware detection using permission and API calls, in: IEEE 25th International Conference on Tools with Artificial Intelligence

(ICTAI), IEEE, Herndon, VA, 2013: pp. 300–305. doi:10.1109/ICTAI.2013.53.
23. Felt AP, Chin E, Hanna S, Song D, Wagner D., Android permissions demystified, in: Proceedings of the 18th ACM Conference on Computer and Communications Security (CCS), ACM Press, New York, New York, USA, 2011: p. 627. doi:10.1145/2046707.2046779.
24. Canbek G, Baykal N, Sagiroglu S., Clustering and visualization of mobile application permissions for end users and malware analysts, in: The 5th International Symposium on Digital Forensic and Security (ISDFS), IEEE, Tirgu Mures, 2017: pp. 1–10. doi:10.1109/ISDFS.2017.7916512.
25. Kruskal WH, Wallis WA., Use of Ranks in One-Criterion Variance Analysis, Journal of the American Statistical Association. 47 (1952) 583–621. http://www.jstor.org/stable/pdf/2280779.pdf?_=1463988119080.
26. Theodorsson-Norheim E., Kruskal-Wallis test: BASIC computer program to perform nonparametric one-way analysis of variance and multiple comparisons on ranks of several independent samples, Computer Methods and Programs in Biomedicine. 23 (1986) 57–62. doi:10.1016/0169-2607(86)90081-7.
27. Bommert A, Sun X, Bischl B, Rahnenführer J, Lang M., Benchmark for filter methods for feature selection in high-dimensional classification data, Computational Statistics and Data Analysis. 143 (2020) 1–19. doi:10.1016/j.csda.2019.106839.
28. Vora S, Yang H., A Comprehensive Study of Eleven Feature Selection Algorithms and their Impact on Text Classification, in: Computing Conference, London, United Kingdom, 2017: pp. 440–449. doi:10.1109/SAI.2017.8252136.
29. Boulesteix AL, Tutz G., Identification of interaction patterns and classification with applications to microarray data, Computational Statistics and Data Analysis. 50 (2006) 783–802. doi:10.1016/j.csda.2004.10.004.
30. Chen Y, Datta S., Adjustments of multi-sample U-statistics to right censored data and confounding covariates, Computational Statistics and Data Analysis. 135 (2019) 1–14. doi:10.1016/j.csda.2019.01.012.
31. Yu C, Zelterman D., A parametric model to estimate the proportion from true null using a distribution for p-values, Computational Statistics and Data Analysis. 114 (2017) 105–118. doi:10.1016/j.csda.2017.04.008.
32. Von Borries G, Wang H., Partition clustering of high dimensional low sample size data based on p-values, Computational Statistics and Data Analysis. 53 (2009) 3987–3998. doi:10.1016/j.csda.2009.06.012.
33. Semwal VB, Singha J, Sharma PK, Chauhan A, Behera B., An optimized feature selection technique based on incremental feature analysis for bio-metric gait data classification, Multimedia Tools and Applications. 76 (2017) 24457–24475. doi:10.1007/s11042-016-4110-y.
34. Yang C, Ji J, Liu J, Liu J, Yin B., Structural learning of Bayesian networks by bacterial foraging optimization, International Journal of Approximate Reasoning. 69 (2016) 147–167. doi:10.1016/j.ijar.2015.11.003.
35. Rueda R, Ruiz LGB, Cuéllar MP, Pegalajar MC., An Ant Colony Optimization approach for symbolic regression using Straight Line Programs . Application to energy consumption modelling, International Journal of Approximate Reasoning. 121 (2020) 23–38. doi:10.1016/j.ijar.2020.03.005.
36. Alomari R, Thorpe J., On password behaviours and attitudes in different populations, Journal of Information Security and Applications. 45 (2019) 79–89. doi:10.1016/j.jisa.2018.12.008.
37. Zhang D, Li Q, Yang G, Li L, Sun X., Detection of image seam carving by using weber local descriptor and local binary patterns, Journal of Information Security and Applications. 36 (2017) 135–144. doi:10.1016/j.jisa.2017.09.003.
38. Asmitha KA, Vinod P., Linux Malware Detection using non-Parametric Statistical methods, in: 2014 International Conference on Advances in Computing, Communications and Informatics (ICACCI), IEEE, New Delhi, 2014: pp. 319–332.
39. Zorn C., Shapiro-Wilk Test, Encyclopedia of Social Science Research Methods. (2004) 1305.
40. Royston JP., Algorithm AS 181: The W Test for Normality, Applied Statistics. 31 (1982) 176–180.
41. MathWorks, Multiple Comparison Test - MATLAB multcompare, (2020). http://www.mathworks.com/access/helpdesk/help/toolbox/stats/multcompare.html (accessed September 2, 2020).
42. Enck W, Ongtang M, McDaniel P., On lightweight mobile phone application certification, in: 16th Conference on Computer and Communications Security (CCS), ACM, New York, New York, USA, 2009: pp. 235–245. http://www.patrickmcdaniel.org/pubs/ccs09a.pdf.
43. Pearce P, Felt AP, Nunez G, Wagner D., AdDroid: Privilege Separation for Applications and Advertisers in Android, in: Proceedings of the 7th ACM Symposium on Information, Computer and Communications Security - ASIACCS '12, ACM Press, Seoul, Korea, 2012: p. 71. doi:10.1145/2414456.2414498.
44. Sanz B, Santos I, Laorden C, Ugarte-Pedrero X, Bringas PG, Alvarez G., PUMA: Permission usage to detect malware in Android, in: International Joint Conference CISIS-ICEUTE-SOCO Special Sessions, Springer Berlin Heidelberg, Ostrava, Czech Republic, 2013: pp. 289–298.
45. Canbek G., "Prominent Binary-Feature (Permissions) Frequencies for Android Mobile Benign Apps and Malware Datasets", Mendeley Data, V1, https://doi.org/10.17632/ptd9fnsrtr.1

APPENDIX A. SUPPLEMENTARY MATERIAL

A.1. DsFeatFreqComp – Dataset Feature-Frequency Comparison R Package

The developed open-source API provides two categories of important functionality for dataset manipulation and visualization conducted and recommended in this study.

Address: https://github.com/gurol/dsfeatfreqcomp

Visualization functions (as appeared in Fig.s 5 – 7):

- plotDsFreqDistributionViolin
- plotQQ
- plotPairwiseDsPValuesHeatMap

Dataset manipulation functions:

- loadDsFeatFreqsFromCsv2
- meltDataFrame

- loadPairwiseDsComparisonOfMeanRanks
- getPairwiseDsPValueMatrix

More information is provided in the developed package. The installation is also described in the GitHub address above.

A.2. Online Interactive Bump Chart for Permission Ranks for Intersection of Malign/ Benign Datasets

The online interactive dataset comparison chart appeared in Fig.s 2 and 3. The number of top binary features can be changed per class. Tooltips provide extra information.

Address: https://tabsoft.co/32CQGIP

A.3. Prominent Binary-Feature (Permissions) Frequencies for Android Mobile Benign Apps and Malware Datasets

The datasets compared in this study are provided online at Mendeley Data.

Address: http://dx.doi.org/10.17632/ptd9fnsrtr.1

APPENDIX B. RELATED EXAMPLE-DOMAIN WORKS

Since 2009 starting from the first version of Android, some studies have published frequent permission requests on benign/malign samples as a part of their static malware analysis. The following paragraphs outline the studies' review by only examining some of their highlights on permissions to explain the different aspects of permissions. As one of the earlier studies, Enck et al. [42] examined permission requests of 311 malicious applications and heuristically defined eight combinations of 13 permissions as the rules to signal malware. Table B.1 shows the rules decomposed in this study. Expressing their research solely based on a narrow set of permission combinations as a "certification" or "risk mitigation" process may cause misunderstanding. It is suggested that naming such an approach as 'suspiciousness indicator' for binary decisions or 'suspiciousness score' for rating the decision.

A composed rule is stated as "an application must not receive phone state, record audio, and access the Internet." In contrast, the actual threat is not requesting the permissions but allowing an application to record audio upon getting phone state (upon incoming or outgoing call), which is possible only by examining the code or catching the behavior

Table B.1. Decomposition of Rule-Based Classification in [42].

		RULES (Combination of permissions)							
PERMISSIONS	*Number of rules*	*R1*	*R6*	*R7*	*R8*	*R2*	*R3*	*R4*	*R5*
SEND_SMS	1			X					
RECEIVE_SMS	1		X						
READ_PHONE_STATE	1					X			
INSTALL_SHORTCUT	1				X				
UNINSTALL_SHORTCUT	1				X				
PROCESS_OUTGOING_CALLS	1						X		
ACCESS_FINE_LOCATION	1							X	
ACCESS_COARSE_LOCATION	1								X
SET_DEBUG_APP	1	X							
RECEIVE_BOOT_COMPLETED	2							X	X
WRITE_SMS	2		X	X					
RECORD_AUDIO	2					X	X		
INTERNET	4					X	X	X	X
Number of permissions involved in the combination		1	2	2	2	3	3	3	3

at run-time on dynamic analysis. One question that needs to be asked is how the permissions chosen in the rules are sufficient to indicate the suspiciousness, which is not elaborated in [42].

One of Android's permission mechanism's nontrivial aspects is the distinction between the request and the actual use of permissions. Android application developers can declare a permission request, but there is no related action in the existing code that needs the existence of that permission granted. In a related study, Felt et al. [23] examined Android applications' permission requests. They evaluated whether the applications need the requested permissions based on their generated API (Application Programming Interface) permission map. They implemented a tool to scan the API calls to determine the required permissions and compare them with those requested. The generated result shows that about one-third of the examined 940 sample applications are over-privileged, violating the least privilege principle in information security. The study is based on API-level 8 (2010) with 85% coverage and 134 permissions and finds that 6.5% of all API calls depend on permission checks. The authors address the following reasons for developers to request unnecessary permissions:

- Being misled by permission names (e.g., MOUNT_UNMOUNT_FILESYSTEMS, ACCESS_NETWORK_STATE, and ACCESS_WIFI_STATE)

- Making unnecessary permission requests for the intents of deputy applications even though the deputy application already requested them (e.g., asking INSTALL_PACKAGES for Google Play deputy application, CAMERA for default camera, INTERNET for opening a URL (Uniform Resource Locator) in a browser, and CALL_PHONE for default Phone Dialer)

- Requesting permissions for unprotected methods such as 'getters' (e.g., no need to ask WRITE_SETTINGS for only calling getters [not setters] for Settings Content Provider)

- Pasting code snippets found on the Internet having inaccurate permission requests

- Requesting deprecated permissions (e.g., ACCESS_GPS or ACCESS_LOCATION has been deprecated since 2008)

- Forgetting the permission requested for tests (e.g., ACCESS_MOCK_LOCATION) and trials

- Requesting invalid 'Signature' or 'SignatureOrSystem' permissions that are silently refused since they are valid for the applications signed by the device manufacturers

- Requesting permissions intentionally in advance for future versions.

These reasons do certainly cause discrepancies in permission request frequencies, which should be considered as a significant noise in mostly benign datasets. However, it could be hypothesized that malware authors tend to develop malware requesting the minimal set of necessary permissions to avoid falling under suspicion.

Another attribute is advertisement libraries that are immensely used in Android applications. However, they cause over privilege in applications and consecutively mislead the analysis of permission requests for malware classification. Pearce et al. [43] examined 964 sample applications and found that some of the permissions requested by applications do not need for their functionalities but requested on behalf of advertisement libraries. Fig. B.1 shows the prepared depiction of the top permissions causing 'over privilege by advertisement' as they called it. The application category is another attribute that characterizes the permission requirements of applications. For instance, an application in the 'Games' category tends to request certain permissions than those in other categories such as the 'Shopping' category. Sarma et al. [20] present an approach that evaluates an application's permissions with those requested from other applications in the same category. They proposed a warning mechanism as 'the first line of defense' to inform the given application's permissions frequency compared with its category's permissions frequencies. Permissions rarely used by the category trigger a warning. Peng et al. [18] suggested using probabilistic generative models instead of frequency analysis to formulate a suspiciousness score for applications. The preferred scoring approach is based on the application's permission requests besides its category.

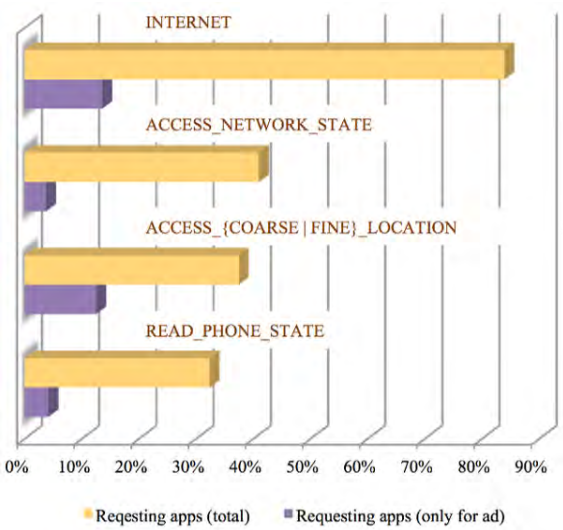

Figure B.1. The top permission requests cause over privilege due to the advertisement libraries, derived from [43].

Permissions in Android have other related attributes such as API-level, at which the permission is introduced, permission types (i.e. standard or custom), protection level, permission group, and used hardware or software features. The number of studies examining these additional attributes is very few. Sanz et al. [44] add informational used features as declared by 'uses-permissions' tags in an Android manifest file beside the permission requests. These features could be used for clustering permissions.

Besides the declarative static features extracted from an Android manifest file and Google Play data, as seen in the studies summarized above, some studies combine permissions with actual code structures, especially with Android API calls. Peiravian and Zhu [22] focus on the combination of permissions and API calls on potentially benign/malicious application classifications. Another observable attribute about permissions is comparing the number of requested permissions between benign and malicious applications. The executors of the "Android Malware Genome Project" Jiang and Zhou [17] conducted a very comprehensive analysis of Android malware, malware families' characteristics, propagation methods, triggering conditions, and payloads and permission usage. Analyzing 1,260 malware and 1,260 benign applications, they found that the malware usually requested more permissions than the benign applications, which are consistent with the other observations in the literature [13,15,18,19,22,44].

The study by Hoffman et al. [19] is noteworthy for expressing the possibility of data leakage threat by the existence of a specific pair of permissions. One permission is for accessing the critical or sensitive data (e.g., device information, contacts, location), and the other is for delivering them to the attacker (INTERNET permission with the overwhelming majority). Searching for critical permission combinations is not limited to permission pairs as in the indication of data leakage; more than two prerequisite permissions could also foresee other threats or abuse of privileges. Going beyond [21,42], Hoffman et al. [19] suggested, without giving sufficient explanation, a small number of suspicious permission patterns that are heuristically combined by logical connectives comprising not only ANDs but also ORs.

Yerima et al. [16] looked for the answers to 'which cardinality of the feature sets does yield a better result?' and 'which type or types of feature category generates more accurate classification result?' Comparing the top 30 permissions ranked by mutual information (MI), they concluded that a small number of features are sufficient, namely application permission requests and code attributes such as command calls, intent filters, embedded binaries, and API calls. The features could be used for statically classifying benign and malign applications at an underestimated performance. Wang et al. [15] examined the Android permission mechanism from different aspects and pointed to a different discriminative pattern in permission requests. Instead of reviewing a single or combination of a few permissions, the distribution of all permissions requested by applications could be used to classify applications as malign or benign. Aswini and Vinod [14] categorized the permissions according to their occurrence in two classes and assessed their contribution to classification. The common permissions occur at the intersection of two classes. Common and discriminant permissions are applied in different machine learning algorithms. They suggested that the common permissions have more influence on accurate classification. The ones having high inter-class variance are categorized as common prominent features. Another finding of the study in feature selection, contrary to assumptions, was the bottom BNS (Bi-Normal Separation) permissions exhibit better accuracy than the top BNS permissions because the distribution of top ones was nearly the same for both classes.

In summary, the review of related works highlights that several issues are related to permissions and the usage of permissions as a prominent feature for classifying malware such as

- effect of the combination of individual permissions, application category, and advertisement libraries,
- noise in permission request frequencies caused by over-privileged applications, and
- selection of the prominent permissions for achieving more successful classification.

However, as described in the examples of 'over privilege by advertisement' [43] and 'rule-based classification' [42] above, discriminative malign permissions' frequencies still provide a valuable indicator for practical malware classification.

Hittite Journal of Science and Engineering, 2021, 8 (2) 123–131
ISSN NUMBER: 2148–4171
DOI: 10.17350/HJSE19030000222

Hybrid Machine Learning Model Coupled with School Closure For Forecasting COVID-19 Cases in the Most Affected Countries

Yildiran Yilmaz[1] **Selim Buyrukoglu**[2]
[1]Recep Tayyip Erdogan University, Department of Computer Engineering, Rize, Turkey
[2]Cankiri Karatekin University, Department of Computer Engineering, Cankiri, Turkey

ABSTRACT

Coronavirus disease (Covid-19) caused millions of confirmed cases and deaths worldwide since first appeared in China. Forecasting methods are essential to take precautions early and control the spread of this rapidly expanding pandemic. Therefore, in this research, a new customized hybrid model consisting of Back Propagation-Based Artificial Neural Network (BP-ANN), Correlated Additive Model (CAM) and Auto-Regressive Integrated Moving Average (ARIMA) models were developed for the purpose of forecast Covid-19 prevalence in Brazil, US, Russia and India. The Covid-19 dataset is obtained from the World Health Organization website from 22 January, 2020 to 6 January, 2021. Various parameters were tested to select the best ARIMA models for these countries based on the lowest MAPE values (5.21, 11.42, 1.45, 2.72) for Brazil, the US, Russia and India, respectively. On the other hand, the proposed BP-ANN model itself provided less satisfactory MAPE values. Finally, the developed new customized hybrid model was achieved to obtain the best MAPE results (4.69, 6.4, 0.63, 2.25) for forecasting Covid-19 prevalence in Brazil, the US, Russia and India, respectively. Those results emphasize the validity of our hybrid model. Besides, the proposed prediction models can assist countries in terms of taking important precautions to control the spread of Covid-19 in the world.

Keywords: Covid-19, Neural network, ARIMA, Time series, Correlated additive model

Article History:
Received: 2021/01/15
Accepted: 2021/05/18
Online: 2021/06/30

Correspondence to: *Yıldıran Yılmaz,*
Recep Tayyip Erdogan University,
Department of Computer Engineering
E-mail: yildiran.yilmaz@erdogan.edu.tr

INTRODUCTION

Humanity has faced an outbreak (Covid-19) first time after the second world war. The origin of Covid-19 is Wuhan, China and it was announced initially in December 2019 [1]. By 6 January 2021, the spreading of this outbreak is quite fast around the world, and more than 87.2 million people have infected over 192 countries [2]. Besides, 1.88 million people have died due to Covid-19. To date, various time-series forecasting models have played an important role in the maintenance of health public systems. Additionally, governments obtain information about the spread and consequences of infectious diseases through these models. In this sense, governments have taken some precautions to reduce the spreading speed of Covid-19 based on the results of these models, such as declare a curfew at regular intervals, quarantines etc. [3]. In the field of case forecasting, various studies have been proposed to predict Covid-19 cases. More detailed information about the proposed studies are available in the literature (Literature Review Section.).

In literature, even if the proposed studies have provided promising results, to the best of our knowledge, no work has focused on a hybrid model for predicting Covid-19 cases by exploiting the impacts of school closure and interruption of face to face education in countries with the highest number of Covid-19 cases. Thus, we proposed a new hybrid model combining the ARIMA model, CAM(Correlated Additive Model) and Back-Propagation Artificial Neural Network algorithm (BP-ANN) which is one of the contributions of this study. It proposes a novel correlated additive model (CAM) in contrasts to the traditional hybrid models. In our study, correlation is calculated between the number of the actual case and school closure situation in the US, Brazil, Russia and India. Then, a correlation rate (CoR) is obtained for each country. Finally, CoR is multiplied by the additive model to create CAM. A case study was carried out before we formed the final version of the CAM. In this case, the additive model was divided and multiplied by CoR, respectively. At the end, we decided

to use CAM based on the case study in the way that the additive model is multiplied by CoR. Thus, the purpose of this paper is to build a new hybrid model based on the ARIMA model, CAM and BP-ANN to forecast Covid-19 cases in the US, Brazil, Russia and India. Moreover, no work has focused on the performance comparison of the popular machine learning algorithm, statistical model and hybrid model for prediction of the Covid-19 cases in the US, Brazil, Russia and India.

The aforementioned countries were selected since they are the most affected countries in the world by Covid-19 on 6 January 2021. More detailed information on the dataset is available in Dataset Description Section. We believe that our study helps governments and health organisations in terms of reducing the spreading speed of Covid-19. Performance metrics of these models are compared in terms of Root Mean Squared Error (RMSE), Mean Absolute Error (MAE) and Mean Absolute Percentage Error (MAPE). The contributions are listed below based on the aim of this study.

- In the initial contribution, we proposed a new BP-ANN forecast algorithm for confirmed cases of Covid-19 in the US, Brazil, Russia and India.
- The second contribution lies in developing a hybrid model for predicting covid19 cases by exploiting the impacts of school closure and interruption of face to face education in countries with the highest number of COVID cases.
- The final contribution to this study compares the most popular machine learning algorithm, statistical model and hybrid model, and then evaluates the models forecasting in multi-day ahead in the interval of one, five and ten ahead. Thus, this range of the forecasting time allows us to verify the effectiveness of the proposed forecasting models in different scenarios which helps governments and health societies in terms of reducing the spreading speed of Covid-19.

The structure of the paper is as follows: Literature Review Section provides information about the literature review. The next section introduces materials and methods which can be listed under three headings: dataset description, the theoretical background of models and the evaluation criteria of models. Results Section presents results and then the next section presents the discussion part of this study. Conclusions are drawn in the last section.

LITERATURE REVIEW

Artificial Intelligence (AI) models have been widely used both for time series and machine learning forecasting [4], [5]. A review paper (in the context of AI) is presented in [6] on the basis of Covid-19 analysis. The key aspect of AI in Covid-19 pandemic can be listed as follows: "early detection and diagnosis of the infection", "monitoring the treatment", "contact tracing of the individuals", "projection of cases and mortality", "development of drugs and vaccines", and also, "reducing the workload of healthcare workers" [7]. Covid-19's data structure is a kind of non-linear data, and its management and analysis can quickly be performed using AI. We believed that AI can be used simply to assist governments in terms of the projection of upcoming cases. In this sense, forecasting can be made with the available data on confirmed cases from governments' official website or social media etc. The forecasting would help governments about the spread and risk of the virus.

In the field of case forecasting, various studies have been presented on a daily basis. In a study, Moran's correlation algorithm has been used to analyze the spread of the Covid-19 pandemic [8]. In another study [9], a new forecasting model is presented in order to forecast the number of positive cases in China in the upcoming ten days. Adaptive neural fuzzy inference system is combined with salp swarm and enhanced flower pollination algorithms. In a different study [10], a mathematical model was developed in terms of the short time estimation of the Covid-19 outbreak's peak time and final size. It has been proposed to evaluate the human to human transmission outside of Wuhan, China. AI and statistical-based methods have been presented in the literature on time series problems. For instance, Artificial Neural Network (ANN) is used to forecast powder dispersion in a complex environment [11]. Moreover, a study has already been developed using an artificial neural network in order to diagnose Covid-19 using medical images [12]. Non-linear data mostly has been used to forecast weather condition, powder dispersion, bacteria population forecast and virus infection in different areas. In this sense, ARIMA is mostly used as a statistical-based method and then its performance is mostly compared to AI methods such as ANN models, neuro-fuzzy inferred systems, hybrid random vector functional link and henry gas solubility optimization [13]–[16]. Many researchers have stated that hybrid models mostly provides better performance compared to single based prediction systems [17]–[22].

In literature, various hybrid models have been proposed to predict Covid-19 cases. Ensemble empirical mode decomposition (EEMD) and artificial neural network (ANN) have been combined to forecast the upcoming Covid-19 cases in a study, [17]. In a different study, autoregressive integrated moving average (ARIMA) and wavelet forecasting models have been incorporated for short-term prediction for Covid-19 cases [18]. Moreover, the number of confirmed case and mortality rate has been predicted based on a hybrid model applying both adaptive network-based fuzzy inference system (ANFIS) and multi-layered perceptron

imperialist competitive algorithm (MLP-ICA) [19]. Discrete wavelet decomposition and ARIMA models have been applied in a hybrid model to forecast the casualties cases of Covid-19 [20]. Also, a new hybrid artificial intelligence (AI) model has been proposed applying the natural language processing (NLP) module and the long short-term memory (LSTM) network in order to predict the Covid-19 pandemic in China [22]. In a study, X-Ray images have been used for the recognition of Covid-19 disease based on a hybrid model including 2D curvelet transform, chaotic salp swarm algorithm and deep learning technique [21].

As highlighted in the Introduction Section, to the best of our knowledge, no work has focused on a hybrid model for predicting Covid-19 cases by exploiting the impacts of school closure and interruption of face to face education in countries with the highest number of Covid-19 cases. Thus, the initial aim of this paper is to build a new hybrid model. The next section presents the background of the proposed new hybrid model.

METHODOLOGY

This section firstly describes the Covid-19 dataset employed in this paper. Subsequently, the theoretical background of data mining models are introduced and the proposed hybrid correlated additive model (CAM) is described. Then, performance metrics such as Root Mean Squared Error, Mean Absolute Error and Mean Absolute Percentage Error for the evaluation of the data mining models are described in this section.

Dataset Description

The Covid-19 prediction model flow chart in this paper is illustrated in Fig. 1. Our work based on time series was carried out to predict the COVID-19 cases in countries with the highest number of cases by January 6, 2021, namely the US, Brazil, Russia and India. From January 22, 2020 to January 6, 2021, Covid-19 cases, which are confirmed daily in the mentioned countries, have been derived from the open datasets provided from the daily reports of the World Health Organization (WHO). The dataset was collected from https://data.world/ datasets/covid-19. The dataset of 350-day cases in the before-mentioned countries was used for experiments. Also, previous studies have shown that if time series modelling is used for prediction, the infection disease case forecasting may be more effective [23]. Therefore, time series forecasting was used in our methods as the Covid-19 cases prediction problem involve a time component. As mentioned in Introduction Section, the correlation rate is calculated based on the covid data and school status data. School status data represents whether schools are fully open, closed or partially open in the aforementioned countries as illustrated in Fig. 2.

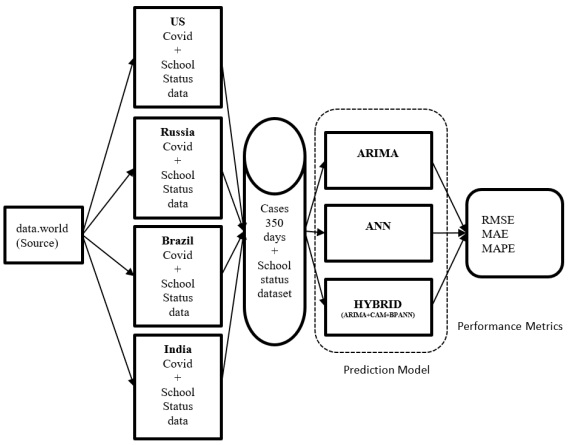

Figure 1. Infectious disease Covid-19 prediction model.

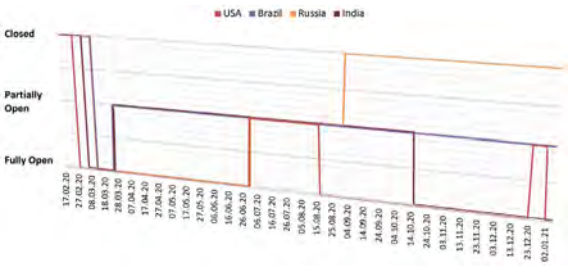

Figure 2. School status of the most affected countries during Covid19 pandemic

The Theoretical Background of Models

The data mining models implemented in this work and the proposed hybrid correlated additive model (CAM) are described in this section.

The Autoregressive Integrated Moving Average (ARIMA)

ARIMA model was firstly presented by Box and Jenkins towards the end of the 1900s [24]. In time series analysis, the aim is to reveal predictable and significant data to forecast upcoming values of the series [25], [26]. ARIMA is one of the most widely used time series models, and also, random distributions and regular changes are taken into account in the time series. ARIMA is calculated based on three parameters: ARIMA (p,d,q), where p donates the auto-regression order, d is the differencing degree, and q represents the moving average order [27]. In the process of model identification and parameter estimation, MSE rate was taken into account to select the top three ARIMA models. Then, the best model was selected using performance metrics (RMSE, MAE, MAPE). The best models for each country are highlighted with bold font in Table 1. Note that the Orange DB platform has been used to forecast the number of upcoming cases in the US, Brazil, Russia and India. Detailed information on the performance metrics is available in the the Evaluation Metrics of Models Section.

Back Propagation-Based Artificial Neural Network (BP-ANN)

An artificial neural network (ANN), which is especially capable of solving nonlinear problems, is a mathematical model designed to solve complex problems especially nonlinear problems [11]. In this regard, BP based neural networks (BP-ANN) are one of the most broadly employed neural network types, as they improve the accuracy of predictions [28]. Backpropagation (BP) networks use the method of returning the error amount in a feedforward network to the neurons in the hidden layer, thereby increase the success of its training. Fig. 3 shows backpropagation between neurons in a hidden layer. However, there is no backpropagation in the input and output layers in BP-ANN.

The learning rule of BP-ANN is based on continuously adjusting weights with the steepest descent method [19]. BP-ANN working principles can be described precisely as follows. Firstly, inputs (I) enter into the preconnected path. Then the input is modelled using randomly selected weights (W). Afterwards, the output for each neuron in the input, hidden and output layers are calculated. Subsequently, the network estimates the error (E) in the outputs by subtracting the obtained output (O) from the actual output (A). Finally, the network moves backwards to the hidden layer and modifies the weights in order to decrease the error (E). This process repeats itself until the E is reduced to the below threshold error value. The model with the ultimate optimal weights is created when the sum of the square error of the network reaches the specified minimum threshold.

In this study, a BP-ANN with a single hidden layer is used to forecast the number of Covid-19 cases as it is one of the best training algorithm improving prediction accuracy, consistent with the expression elsewhere [28]. Forecasting is performed with the BP-ANN algorithm developed in C sharp visual studio environment.

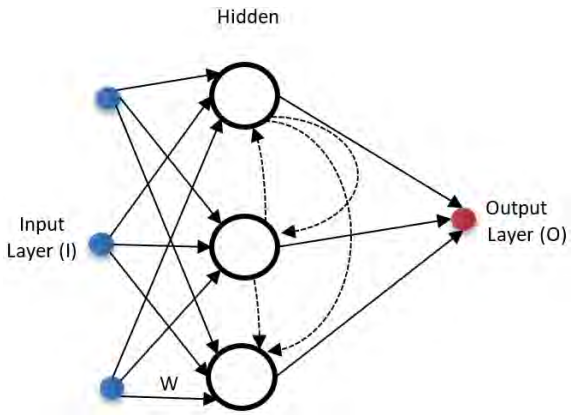

Figure 3. Backpropagation in a hidden layer

Time Series Model

The time series can be defined as a set containing the variable of observation values put in time order. This variable takes different values depending on various reasons over time [29]. Therefore, time series can be expressed as a variable value set in time order. In other words, the series obtained by performing observations at equal intervals for a certain period such as days, weeks, months, and years are called time series. For example, when the observed time series is symbolised by Y_t where t=1,2,..T, then the observations can be interpreted as Y_1,Y_2..Y_t [29].

In time series analysis, forecasting is based on analysing past data and using it to make predictions. Consequently the relationship between output (Y_t) and inputs (Y_{t-1}); Y_{t-2}; ..; Y_{t-p}) is as follows.

$$Y_t = a_0 + \sum_{j=1}^{q} a_j g\left(\beta_{0j} + \sum_{i=1}^{p} \beta_{ij} Y_{t-i}\right) + \varepsilon_t \quad (1)$$

This formula has the following variables: α_j where (j = 0,1,...,q) and β_{ij} stand for the network connection weights; p for the number of input neurons; q for the number of hidden neurons. As the single hidden layer backpropagation network is a commonly employed network model in forecasting applications [28], our network contains a single hidden layer along with input and output layers, connected by links as shown in Fig. 4.

There are 4 input, 12 hidden and 1 output neurons connected together in the introduced Back Propagation-Neural Network architecture (BP-ANN) as depicted in Fig. 4. BP-ANN uses the sigmoid activation function in neurons. The dataset for BP-ANN has created with Covid- 19 cases as inputs (or features) and forecasted value as the output. BP-ANN gives the mean squared error (MSE), root mean squared error (RMSE) and mean absolute error (MAE) values as the evaluation metrics. BP-ANN uses backpropagation to calculate weights in order to train the introduced neural network.

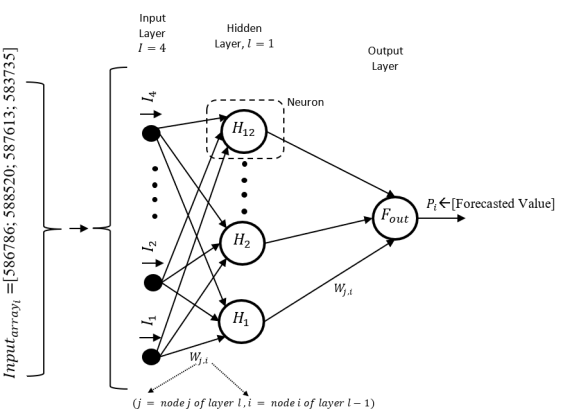

Figure 4. The architecture of the developed ANN

Proposed Hybrid Correlated Additive Model (CAM)

The proposed hybrid model is consisting of two steps. The first step analyses the linear part of the time series with the ARIMA model because ARIMA is capable of modelling the linear components in a time series. Then nonlinear time series are obtained by using ARIMA forecasted values. Once the nonlinear time series is captured, then ANN models the nonlinear components of the specified time series. In other words, the second step models the residuals from the ARIMA by employing ANN, because ANN is better at modelling the nonlinear components in a time series [11]. In order to analyse the time series, two models can be considered such as additive and multiplicative models [23]. Both models can be expressed as follows.

- Additive Model: $a_t = x_t + y_t$
- Multiplicative Model: $a_t = x_t * y_t$

In both formula, a_t stands for the actual value, x_t for linear component and y_t for the nonlinear component.

In the first step, the linear components in the time series i.e. $\{a_t, t=1,2,\ldots\}$ are issued to the ARIMA to generate the predicted forecast value i.e. $\tilde{x_t}$. Afterwards, to obtain nonlinear components termed as N_t, actual value a_t is compared with the forecasted value of the linear component $\tilde{x_t}$. The comparison is carried out as follows according to the additive model and multiplicative model.

- In the Additive Model: $N_t = a_t - \tilde{x_t}$
- In the Multiplicative Model: $N_t = a_t / \tilde{x_t}$

Consequently, a nonlinear time series termed as N_t can be generated based on the above formulas. It was decided that the best method for this investigation was to use the additive model along with the proposed method which multiplies correlation rate value and nonlinear components as described in Formula 2. Through the use of the proposed model, we were able to obtain nonlinear components and at the end, better-predicted forecast values. In our hybrid correlated additive model termed as CAM, we used the additive method then multiplied the results with the correlation rate as follows.

$$N_t = \left(a_t - \tilde{x_t}\right) * CoR \tag{2}$$

where the correlation rate (*CoR*) is the value that correlates Covid cases in four countries(US, Russia, Brazil and India) to whether schools are fully open, closed or partially open.

In the second step, nonlinear components i.e. $\{N_t, t=1,2,\ldots\}$ are given to the ANN as inputs to generate the predicted forecast value of nonlinear components i.e. $\tilde{y_t}$. The combined forecasted value can be generated as follows based on the additive and multiplicative model.

- Additive Model: $a_t = \tilde{x_t} + \tilde{y_t}$
- Multiplicative Model: $a_t = \tilde{x_t} * \tilde{y_t}$

Based on the trial and error method, we used the additive model in this experiment as it gives the best results for the Covid19 dataset.

Evaluation Metrics of Models

RMSE, MAE and MAPE can be considered as model evaluation criteria in terms of accuracy [30]. The average magnitude of the error is measured by MAE, and accuracy is measured for continuous variables. On the other hand, RMSE measures the average magnitude of the error and it is considered as the most useful error metric when huge errors are undesirable (Çinaroğlu, 2017). The value of RMSE is always bigger or equals to MAE [30]. MAPE measures the average of the absolute percentage error [32]. Note that models are considered a better fit of the data when RMSE, MAE and MAPE values are low. RMSE, MAE and MAPE are calculated by the following formulas.

$$RMSE = \sqrt{\frac{1}{N}\sum_{i=1}^{N}\left(P_i - A_i\right)^2} \tag{3}$$

$$MAE = \frac{\sum_{i=1}^{N}\left|P_i - A_i\right|}{N} \tag{4}$$

$$MAPE = \frac{1}{N}\sum_{i=1}^{N}\left|\frac{P_i - A_i}{A_i}\right| \times 100 \tag{5}$$

Three formulas have the following variables: N stands for the number of training data; A_i for the actual value; P_i for the predicted value.

RESULTS

In this section, the performance results obtained from data mining models are illustrated with figures and tables. Different ARIMA models were created using different parameters for each country as highlighted in ARIMA Section. Then the best models were selected based on MAPE rates. The selected best ARIMA models are the ARIMA (0,2,1), ARIMA (2,2,1), ARIMA (0,1,2) and ARIMA (0,2,3) for Brazil, US, Russia and India, respectively. The models were fitted to Covid-19 data well with the smallest $MAPE_{Brazil}$ = 5.21, $MAPE_{US}$ = 11.42, $MAPE_{Russia}$ = 1.45, and $MAPE_{India}$ = 2.72 rates (see Table 1).

On the other hand, the proposed new BP-ANN algorithm also provided sophisticated MAPE rates. The rates are as follows: $MAPE_{Brazil}$ = 8.27, $MAPE_{US}$ = 7.45, $MAPE_{Russia}$ = 1.7, and $MAPE_{India}$ =4.75. As seen in Table 1, ARIMA model performances are slightly better than the proposed

Table 1. Comparison of tested models with the proposed hybrid model

Country	Model	RMSE	MAE	MAPE
Brazil	ARIMA (0,2,1)	239299	171873	5.21
	ARIMA (3,1,2)	307737	263087	7.6
	ARIMA (2,1,0)	1526802	1312023	37.94
	ANN	511597	410623	8.27
	Hybrid (ARIMA+CAM+ANN)	215369	154686	4.69
US	ARIMA (1,2,1)	698729	630971	12.27
	ARIMA (3,1,1)	1532416	1326203	23.89
	ARIMA (2,2,1)	649569	583112	11.42
	ANN	410666	114362	7.45
	Hybrid (ARIMA+CAM+ANN)	357542	329522	6.4
Russia	ARIMA (0,1,2)	14244	12011	1.45
	ARIMA (0,2,1)	272771	210771	21.09
	ARIMA (2,1,1)	61897	51191	5.24
	ANN	52817	43065	1.7
	Hybrid (ARIMA+CAM+ANN)	6267	5284	0.63
India	ARIMA (3,2,1)	71582	49265	4.85
	ARIMA (0,2,3)	69635	47327	2.72
	ARIMA (1,2,2)	738307	360436	12.77
	ANN	47667	38182	4.75
	Hybrid (ARIMA+CAM+ANN)	58298	41564	2.25

new BP-ANN algorithm. One possible implication of this is that the MAPE rates between the ARIMA models and BP-ANN is few. Moreover, the proposed new customised hybrid model provided promising results among the ARIMA and BP-ANN about MAPE rates. They are $MAPE_{Brazil}$ = 4.69, $MAPE_{US}$ = 6.4, $MAPE_{Russia}$ = 0.63, and $MAPE_{India}$ = 2.25 as seen from Table 1. Fig. 5 evaluates the three models forecasting in multi-day ahead in the interval of one, five and ten forward. These models give satisfactory prediction results. In addition, it is noted that the proposed new hybrid model can be effectively used for forecasting as a better alternative to the ARIMA and BP-ANN models.

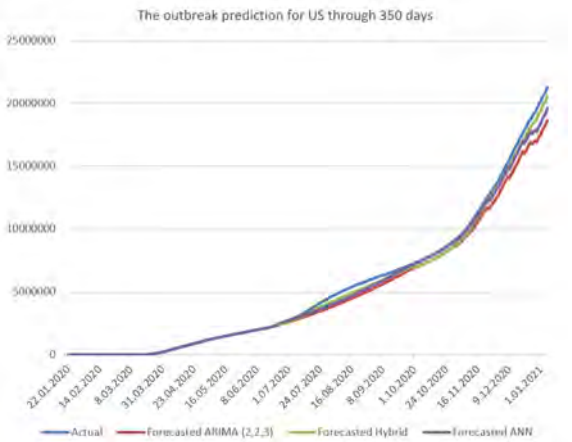

Figure 6. The Covid-19 case prediction for the US

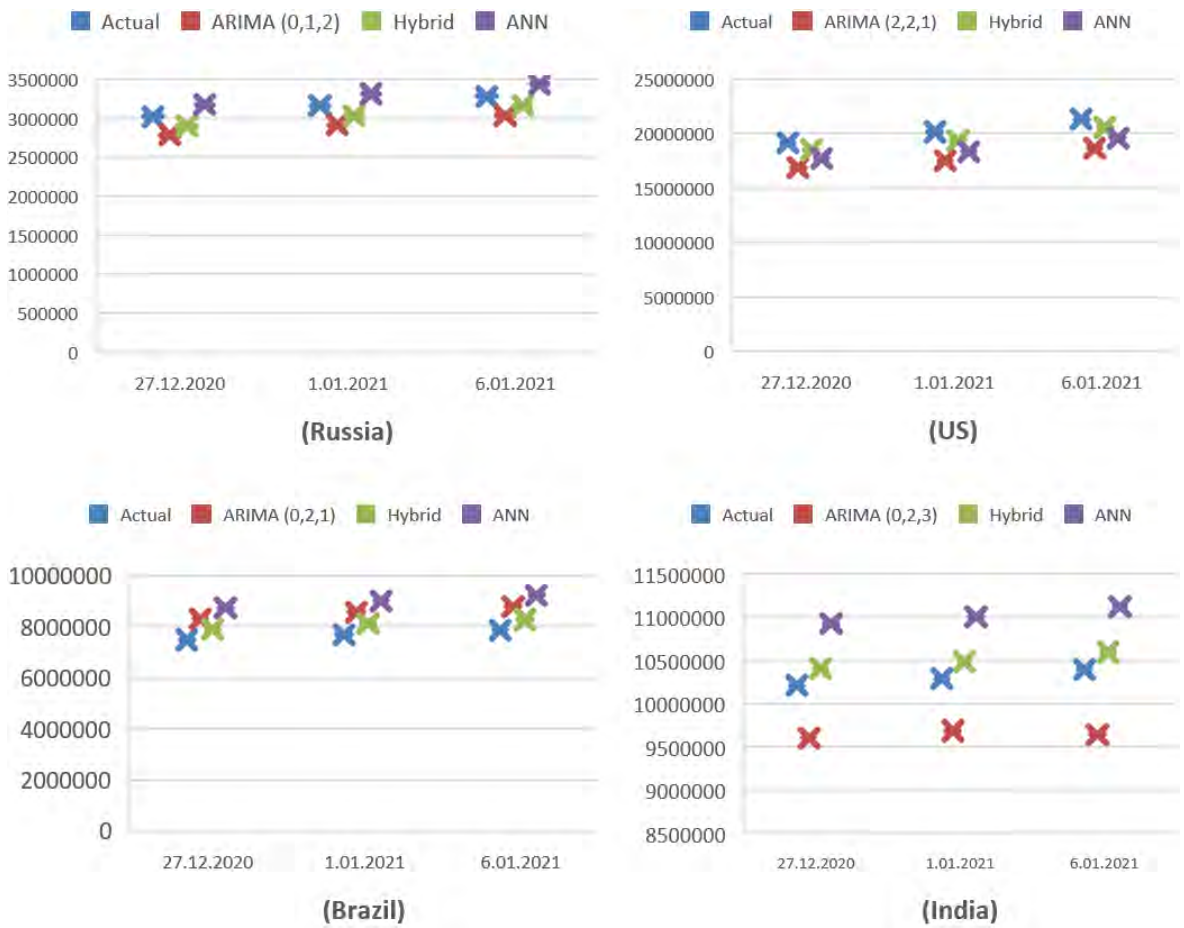

Figure 5. Multi-day ahead predictions of models at one, five and ten forward intervals for four countries.

It is apparent from Fig. 6, 7, 8, 9, that the spread of Covid-19 slightly increases for Brazil, the US, Russia and India. In the same vein, the forecast value is also slightly increasing for both ARIMA, BP-ANN and hybrid models. While the ARIMA model forecasted a closer value to the confirmed case value for Brazil, India and Russia than the proposed BP-ANN model, the BP-ANN model forecasted a closer value to the confirmed case value for the US. Among the aforementioned machine learning models, the proposed new hybrid model forecasted the best values for these countries and gave the least error rates in terms of the evaluation metrics such as RMSE, MAE and MAPE as compared in Table 1.

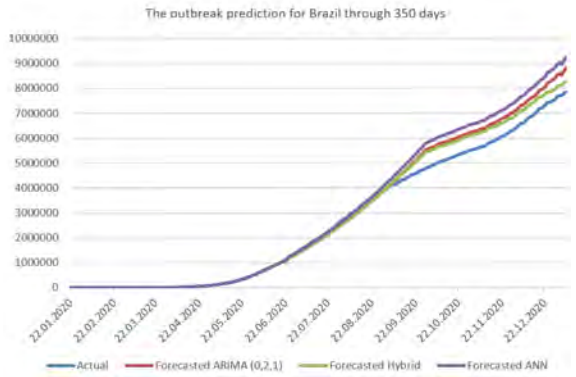

Figure 7. The Covid-19 case prediction for the Brazil

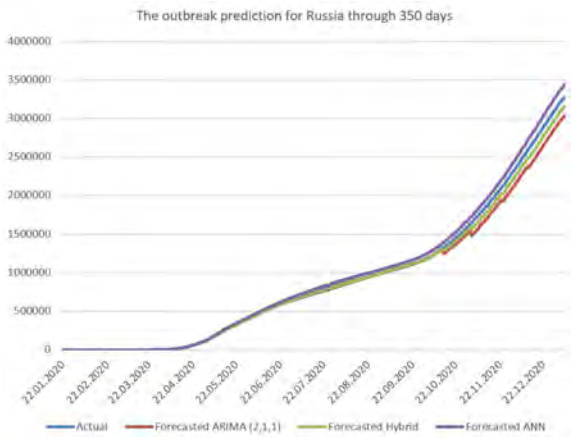

Figure 8. The Covid-19 case prediction for the Russia

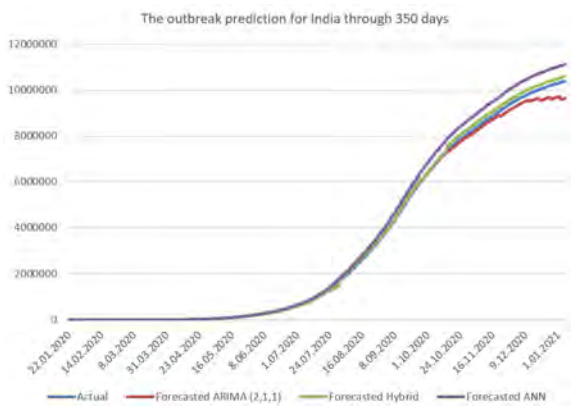

Figure 9. The Covid-19 case prediction for the India

DISCUSSION

ARIMA and BP-ANN models' well-organised construct and satisfactory forecasting performance made them popular time-series forecasting methods [33]. In this research, the current situation of the most affected four countries (Brazil, US, Russia and India) in the world by Covid-19 was highlighted, and then the number of confirmed cases in these countries were predicted with machine learning models for comparison. To the best of our knowledge, this research is the first to combine ARIMA, CAM (Correlated Additive Model), and BP-ANN models to forecast the prevalence of Covid-19 in the US, Brazil, Russia and India.

A great concern of Covid-19 is that medical treatments cannot be sufficient to treat infected patients, even if the US and Russia are the developed and rich countries. Unfortunately, the total of Covid-19 deaths in these four countries has increased dramatically during the Pandemic period. By 6 January 2021, additionally, the US, Brazil, Russia and India four worst-hit countries with 364963, 201242, 59568 and 150222 deaths, respectively. To conclude, life might return to normal as Covid-19 vaccine usage becomes widespread during this outbreak [7]. Otherwise, people may meet a great disaster because of the Covid-19 pandemic.

CONCLUSION

The following conclusions can be drawn from the present study that Covid-19 is a global and pandemic disease that can be spread rapidly; therefore, it threatens all humanity. In this regard, it is vital to predict the number of cases of this disease and to take the relevant measures immediately in countries with a high incidence. For this reason, this work was carried out to lessen the government health burden by forecasting the number of cases in countries with the highest Covid-19 outbreaks. In addition, the aim of this study was to create a more accurate prediction model than conventional models. The proposed hybrid method is an architecture that combines ARIMA, CAM (Correlated Additive Model) and the deep learning Backpropagation algorithm. In this study, two of the most commonly used time series forecasting models, ARIMA and ANN, was also used, and then they were compared with the hybrid model in terms of error rates. The forecasting performance seen in this work reveals that the Hybrid model provides the best results and secondly ARIMA gives slightly better results than the proposed BP-ANN model. We believe that the proposed hybrid model may provide more convincing results than the similar studies presented in Literature Review Section. The reason behind this is that our study proposes a novel correlated additive model (CAM) in contrasts to

the traditional hybrid models presented in Literature Review Section. Consequently, the proposed hybrid model can be used as a Covid-19 prediction application to obtain better forecasting values and take immediate measures.

CONFLICT OF INTEREST

Authors approve that to the best of their knowledge, there is not any conflict of interest or common interest with an institution/organization or a person that may affect the review process of the paper.

AUTHOR CONTRIBUTION

Public data were used in this study. The rest of all sections including conceptualisation, methodology, software, analysis, writing, review and editing were equally organised and performed by Yıldıran Yılmaz and Selim Buyrukoğlu.

References

1. Lu H, Stratton CW, Tang YW. Outbreak of pneumonia of unknown etiology in Wuhan, China: The mystery and the miracle. J Med Virol. 2020;92(4):401–402. doi:10.1002/jmv.25678
2. Worldometers.info. COVID–19 CORONAVIRUS PANDEMIC. https://www.worldometers.info/coronavirus/?utm_campaign=CSauthorbio? Published 2020. Accessed August 10, 2020.
3. Rypdal M, Sugihara G. Inter–outbreak stability reflects the size of the susceptible pool and forecasts magnitudes of seasonal epidemics. Nat Commun. 2019;10(1). doi:10.1038/s41467–019–10099–y
4. Davis JK, Gebrehiwot T, Worku M, et al. A genetic algorithm for identifying spatially–varying environmental drivers in a malaria time series model. Environ Model Softw. 2019;119(February):275–284. doi:10.1016/j.envsoft.2019.06.010
5. Scavuzzo JM, Trucco F, Espinosa M, et al. Modeling Dengue vector population using remotely sensed data and machine learning. Acta Trop. 2018;185(October 2017):167–175. doi:10.1016/j.actatropica.2018.05.003
6. Vaishya R, Javaid M, Khan IH, Haleem A. Artificial Intelligence (AI) applications for COVID–19 pandemic. Diabetes Metab Syndr Clin Res Rev. 2020;14(4):337–339. doi:10.1016/j.dsx.2020.04.012
7. Kaur SP, Gupta V. COVID–19 Vaccine: A comprehensive status report. Virus Res. 2020;288(August):198114. doi:10.1016/j.virusres.2020.198114
8. Kang D, Choi H, Kim JH, Choi J. Spatial epidemic dynamics of the COVID–19 outbreak in China. Int J Infect Dis. 2020;94(January):96–102. doi:10.1016/j.ijid.2020.03.076
9. Al–Qaness MAA, Ewees AA, Fan H, Aziz MA El. Optimization method for forecasting confirmed cases of COVID–19 in China. Appl Sci. 2020;9(3). doi:10.3390/JCM9030674
10. Kucharski AJ, Russell TW, Diamond C, et al. Early dynamics of transmission and control of COVID–19: a mathematical modelling study. Lancet Infect Dis. 2020;20(5):553–558. doi:10.1016/S1473–3099(20)30144–4
11. Lauret P, Heymes F, Forestier S, Aprin L, Pey A, Perrin M. Forecasting powder dispersion in a complex environment using Artificial Neural Networks. Process Saf Environ Prot. 2017;110:71–76. doi:10.1016/j.psep.2017.02.003
12. Narin A, Kaya C, Pamuk Z. Department of Biomedical Engineering, Zonguldak Bulent Ecevit University, 67100, Zonguldak, Turkey. arXiv Prepr arXiv200310849. 2020.
13. Babikir HA, Elaziz MA, Elsheikh AH, et al. Noise prediction of axial piston pump based on different valve materials using a modified artificial neural network model. Alexandria Eng J. 2019;58(3):1077–1087. doi:10.1016/j.aej.2019.09.010
14. Elaziz MA, Elsheikh AH, Sharshir SW. Improved prediction of oscillatory heat transfer coefficient for a thermoacoustic heat exchanger using modified adaptive neuro–fuzzy inference system. Int J Refrig. 2019;102:47–54. doi:10.1016/j.ijrefrig.2019.03.009
15. Elsheikh AH, Sharshir SW, Abd Elaziz M, Kabeel AE, Guilan W, Haiou Z. Modeling of solar energy systems using artificial neural network: A comprehensive review. Sol Energy. 2019;180(January):622–639. doi:10.1016/j.solener.2019.01.037
16. Shehabeldeen TA, Elaziz MA, Elsheikh AH, et al. A Novel Method for Predicting Tensile Strength of Friction Stir Welded AA6061 Aluminium Alloy Joints Based on Hybrid Random Vector Functional Link and Henry Gas Solubility Optimization. IEEE Access. 2020;8:79896–79907. doi:10.1109/ACCESS.2020.2990137
17. Hasan N. A Methodological Approach for Predicting COVID–19 Epidemic Using EEMD–ANN Hybrid Model. Internet of Things. 2020;11:100228. doi:10.1016/j.iot.2020.100228
18. Chakraborty T, Ghosh I. Real–time forecasts and risk assessment of novel coronavirus (COVID–19) cases: A data–driven analysis. Chaos, Solitons and Fractals. 2020;135. doi:10.1016/j.chaos.2020.109850
19. Pinter G, Felde I, Mosavi A, Ghamisi P, Gloaguen R. COVID–19 Pandemic Prediction for Hungary ; a Hybrid Machine Learning Approach. 2020.
20. Singh S, Parmar KS, Kumar J, Makkhan SJS. Development of new hybrid model of discrete wavelet decomposition and autoregressive integrated moving average (ARIMA) models in application to one month forecast the casualties cases of COVID–19. Chaos, Solitons and Fractals. 2020;135:1–8. doi:10.1016/j.chaos.2020.109866
21. Altan A, Karasu S. Recognition of COVID–19 disease from X–ray images by hybrid model consisting of 2D curvelet transform, chaotic salp swarm algorithm and deep learning technique. Chaos, Solitons and Fractals. 2020;140. doi:10.1016/j.chaos.2020.110071
22. Zheng N, Du S, Wang J, et al. Predicting COVID–19 in China Using Hybrid AI Model. IEEE Trans Cybern. 2020;50(7):2891–2904. doi:10.1109/TCYB.2020.2990162
23. Chae S, Kwon S, Lee D. Predicting infectious disease using deep learning and big data. Int J Environ Res Public Health. 2018;15(8). doi:10.3390/ijerph15081596
24. Sato RC esa. Disease management with ARIMA model in time series. Einstein (Sao Paulo). 2013;11(1):128–131.

doi:10.1590/S1679-45082013000100024
25. He Z, Tao H. Epidemiology and ARIMA model of positive-rate of influenza viruses among children in Wuhan, China: A nine-year retrospective study. Int J Infect Dis. 2018;74:61-70. doi:10.1016/j.ijid.2018.07.003
26. Benvenuto D, Giovanetti M, Vassallo L, Angeletti S, Ciccozzi M. Application of the ARIMA model on the COVID-2019 epidemic dataset. Data Br. 2020;29:105340. doi:10.1016/j.dib.2020.105340
27. Li X, Zhang C, Zhang B, Liu K. A comparative time series analysis and modeling of aerosols in the contiguous United States and China. Sci Total Environ. 2019;690:799-811. doi:10.1016/j.scitotenv.2019.07.072
28. Wang M, Wang H, Wang J, et al. A novel model for malaria prediction based on ensemble algorithms. PLoS One. 2019;14(12):1-15. doi:10.1371/journal.pone.0226910
29. Gamboa JCB. Deep Learning for Time-Series Analysis. 2017. http://arxiv.org/abs/1701.01887.
30. Karasu S, Altan A, Sarac Z, Hacioglu R. Prediction of Bitcoin prices with machine learning methods using time series data | Zaman serisi verilerini kullanarak makine öğrenmesi yöntemleri ile bitcoin fiyat tahmini. 26th IEEE Signal Process Commun Appl Conf SIU 2018. 2018:1-4. doi:10.1109/SIU.2018.8404760
31. ÇINAROĞLU S. Sağlik Harcamasini Tahmininde Makine Öğrenmesi Regresyo Yöntemlerinin Karşilaştirilmasi. Uludağ Univ J Fac Eng. 2017;22(2):179-200. doi:10.17482/uumfd.338805
32. Swamidass PM. Encyclopedia of Production and Manufacturing Management.; 2000. doi:10.1007/1-4020-0612-8
33. Wang Y, Xu C, Wang Z, Zhang S, Zhu Y, Yuan J. Time series modeling of pertussis incidence in China from 2004 to 2018 with a novel wavelet based SARIMA-NAR hybrid model. PLoS One. 2018;13(12):1-23. doi:10.1371/journal.pone.0208404

Hittite Journal of Science and Engineering, 2021, 8 (2) 133–140
ISSN NUMBER: 2148–4171
DOI: 10.17350/HJSE19030000223

A Comparative Study of Handwritten Character Recognition by using Image Processing and Neural Network Techniques

Hakan Koyuncu
Altinbas University, Department of Computer Engineering, Istanbul, Turkey

ABSTRACT

This study aims to analyze the effects of noise, image filtering, and edge detection techniques in the preprocessing phase of character recognition by using a large set of character images exported from the MNIST database trained with various sizes of neural networks. Canny and Sobel algorithms are deployed to detect the edges of the images. The Canny algorithm can produce smoother and thinner continuous edges compare to the Sobel algorithm. The structural forms were reshaped using the Skeletonization algorithm. The Laplacian filter was used to increase the sharpness of the images and High pass filtering was used to highlight the fine details in blurred images in the form of image filtering. Gaussian noise or image noise with Gaussian intensity was used in Matlab on MNIST character images with the probability density function P. The effects of noise on character images are displayed during character recognition related to Neural network properties. Neural networks are commonly used to recognize patterns among optical characters. Feedforward neural networks are deployed in this study. A comprehensive analysis of the image processing algorithms is included during character recognition. Improved accuracy is observed with character recognition during the prediction phase of the neural networks. A sample of unknown numeric characters is tested with the application of High pass filtering plus feedforward neural network and 89% average output prediction accuracy was obtained against the average number of hidden layers in the neural network. Other prediction accuracies were also tabulated for the reader's attention.

Article History:
Received: 2021/02/08
Accepted: 2021/05/23
Online: 2021/06/30

***Correspondence to**: Hakan Koyuncu, Altinbas University, Computer Engineering, 34217, Istanbul, TURKEY*
E-Mail: hakan.koyuncu@altinbas.edu.tr

Keywords:
Artificial intelligence (AI); Edge detection; Feature extraction, Gradient; Hidden layer; Image correlation; Image filtering; Noise; Optical character recognition (OCR); Pattern recognition.

INTRODUCTION

Optical character recognition, (OCR), in the field of research where images of typed, handwritten, or printed text get converted into machine-encoded text [1,3]. Optical character data can be obtained from a photo of a document, from a scanned document, or directly from a photograph [4]. The recognition technology is extensively used for data entry such as recording of passport data, invoices, receipts, or any appropriate documentation [5]. Storing printed texts in digital format requires documents to be searched, displayed, edited, processed, and stored in various ways [6]. This may be achieved by using machine processing such as translation, semantic computing, text to speech conversion, and text mining. OCR is an area or research field, [7,8], which focuses on artificial intelligence, (AI), computer vision, and pattern recognition.

Initial versions of OCR required a preparation phase where character images are deployed for training to deal with individual fonts,[9]. A high level of identification accuracy is possible with most fonts due to the new capabilities of advanced systems,[10]. Some systems can produce an approximate format of the original document at the output, [11].

Matrix matching technique compares an image with a stored symbol image on a pixel-by-pixel basis, [12]. This is also identified as "pattern matching", "pattern recognition", or "image correlation". In this case, the input symbol is correctly isolated from the rest of the image and is in a similar font with the symbol stored on the same scale. This method fits well for the typewritten text and struggles as new fonts are introduced. This is the technique, which was implemented directly, [13], with the early photocell-based OCR equipment.

There are two types of OCR algorithm which can produce a list of possible characters. Matrix matching is associated with the comparison of a character picture to a stored character on a pixel-by-pixel basis. This technique depends on the fact that the input character needs to be accurately confined from the rest of the picture.

The technique of extraction of features breaks down symbols into "features" such as lines, closed loops, the direction of the line, and intersections of line,[14]. The extraction features lower the representation dimensionality and render the method of recognition computationally effective. These characteristics are compared to an abstract vector-like representation of a character, which could be reduced to one or more prototypes. Generic feature identification techniques applied to this form of OCR in computer vision are widely used in "intelligent" handwriting recognition, and in most modern OCR applications, [15]. Closest neighborhood classifiers like the k-nearest neighborhood (k-NN) algorithm are used to equate image features with stored character features and pick the closest fit,[16].

METHODOLOGY

Neural Networks

Artificial Neural Networks are inspired by how biological neurons process data. Neural Networks have caused a great amount of enthusiasm in the field of machine learning. It has caused a great amount of success, in areas such as image processing, autonomous driving, speech recognition, and character recognition. In this study, we try to understand the effects of how noise, image filters, and edge detection affect neural networks in the preprocessing phase.

The simplest computing element in a neural network is the neuron that often can be called a unit or node. This node takes information from a particular neuron or external source and determines an output. Every input has a corresponding weight (*w*) associated with it, which is appointed according to its relative influence on other inputs. The node as defined in Fig. 1 has a function, f, for the total weighted inputs.

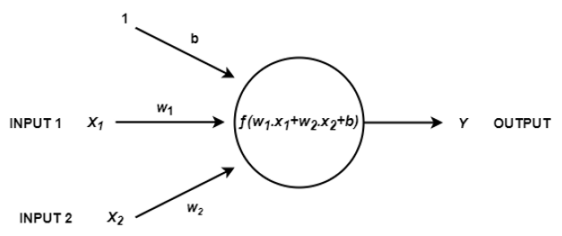

Figure 1. A single neuron.

The single neuron, shown above, receives numerical inputs X_1 and X_2. W_1 and W_2 weights correlate to inputs X_1 and X_2. An additional input 1 is also included with a bias weight b in the network. The primary task of bias, b, is to provide every neuron with a constant value in addition to the normal inputs, [17]. The Neuron output Y is determined as shown in Fig. 1. f is a non-linear function, named the Activation Function. The activation function aims at suggesting non-linearity to the neuron output. It is crucial, as real-world data is non-linear, and learning these non-linear representations would be desirable for the neurons. Each activation function takes an individual numeric value and executes a specific fixed numerical operation on it. There are a few activation functions in the literature. Fig. 2 below displays each of these activation functions:

Sigmoid

This function takes an input value and compresses it in a range of 0 and 1.

$$\sigma(x) = \frac{1}{1+e^{-x}} \tag{1}$$

Tanh

This function takes an input value and compresses it to the range between -1 and 1.

$$tanh(x) = 2\sigma(2x) - 1 \tag{2}$$

ReLU

This function is called Rectified Linear Unit, ReLU. To replace negative values with zero, it takes an input value and thresholds it.

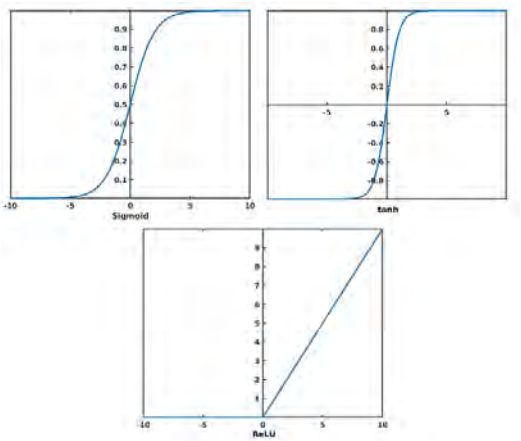

Figure 2. Different activation functions.

Feedforward Neural Network

The term Feedforward is used because the information travels forward in the network. Initially through the input nodes, followed by the hidden nodes, and finally ending at the output nodes. Feedforward networks are generally used for supervised learning where the data being trained is neither sequential nor dependent on time.

A single-layer neural network can be seen in Fig. 3 with S neurons and R number of inputs. Each of the R numbers of inputs is connected to each of the S number of neurons with a weight matrix of S rows. Inputs are $p=p_1, p_2, p_3,\ldots,p_R$ and each enters the network through weight matrix, $W=(w_{i,j})$. With b=(bi) being the bias and the output can be written as $a = f(W_p+b)$.

A neural network can have multiple layers. Each layer having its unique weight matrix W, network input vector n, bias vector b, and output vector a. The leftmost layer is called the input layer with the far right being the output layer. The layers that are in between are known as hidden layers. Depending on the task, multilayer networks can perform better compared to single-layered networks. For example, multilayer networks can be used to solve difficult complex problems such as object identification in an image. A single-layered network is only able to learn linearly separable patterns.

Fig. 4 shows a neural network with 2 hidden layers L_2 and L_3, with an output layer L_4 consisting of 2 outputs. For

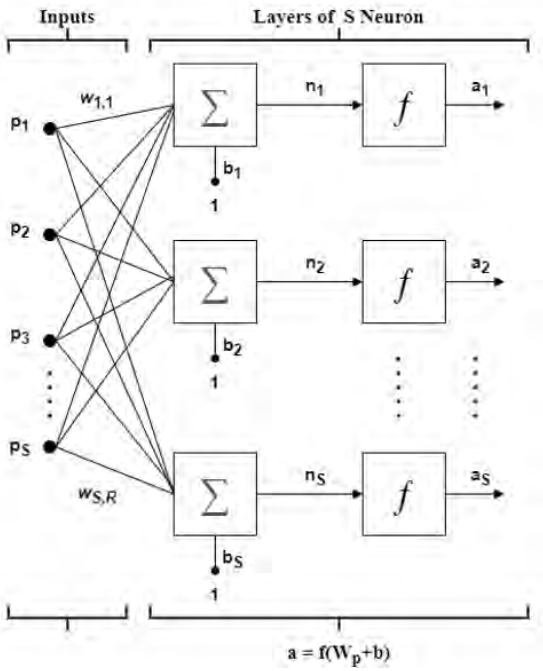

Figure 3. A single layer neural network.

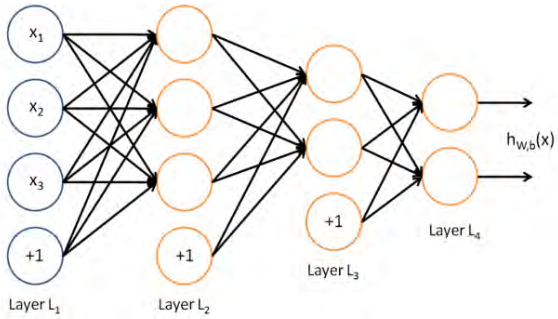

Figure 4. Multi-layer neural networks.

this network to be trained, it needs training samples (x_i, y_i) where $y_i \in R^2 \cdot R^n$ represents the n-dimensional Euclidean input space. This type of network is advantageous in cases where there is more than one output to be predicted. For example, a diagnosis application can use this network setup where vector x contains the patient to input information and output y can show the existence or absence of disease.

Canny Edge Detection Algorithm

Operator Canny is operating in a multi-stage process. Firstly, the Gaussian convolution smoothes the signal. A basic 2-D first derivative operator (like the Roberts Cross operator) is then added to the smooth image to illuminate image regions with the first strong spatial derivatives. In the gradient magnitude image, the edges give rise to ridges. Then the algorithm monitors around the top of these ridges and sets to zero all pixels that are not currently on the top of the ridge to make the output of a thin line, a method known as non-maximal suppression. There is hysteresis controlled by two thresholds in the tracking process: T_1 and T_2, with $T_1 > T_2$. Tracking can start only at a point higher than T_1 on a ridge. Tracking continues from that point in both directions until the ridge's height falls below T_2. Such hysteresis helps insure that rough surfaces do not break into several parts of the edge.

Sobel Edge Detection Algorithm

In image processing techniques Sobel operator is generally used in edge detection. The Sobel operator is convolving the image with a small, integer-valued filter which is applied vertically and horizontally. It is comparatively cost-effective in terms of computation-wise. In computation-wise Sobel operator is relatively cost-effective. Mathematically, the operator uses two 3x3 kernels convolved to the original picture to measure derivative approximations for vertical and horizontal shifts as seen in Fig. 5.

The center pixel of the masks is used for calculating the differences. The 3x3 convolution masks smoothen the image by some amount, hence it is less affected by noise. But it produces thicker edges.

-1	-2	-1
0	0	0
1	2	1

-1	0	1
-2	0	2
-1	0	1

Figure 5. Sobel horizontal and vertical kernels.

Gaussian Noise

Gaussian noise is a statistical noise that is considered to have a probability density function similar to that of the standard distribution, commonly known as Gaussian. In other terms, Gaussian-distributed values are the values the noise will take on. A Gaussian random variable z has the probability density function **P** given by:

$$P_G(z) = \frac{1}{\sigma\sqrt{2\pi}} e^{-\frac{(z-\mu)^2}{2\sigma^2}} \quad (3)$$

where z represents the grey level, μ the mean value, and σ the standard deviation. The main source of Gaussian noise in digital images appears during image acquisition. For example, sensor noise caused by poor illumination, high temperature, transmission, and electronic circuit noise. Gaussian noise can be reduced in image processing by using spatial filters to smooth out the image. An undesirable outcome of this smoothing operation may be the blurring of finer details, which correspond to the blocking of high frequencies.

Laplacian Filter

Discrete Laplace operator is often used in image processing for image enhancement purposes. The Laplacian filter highlights the areas of rapid intensity change in grayscale and hence it is used for edge detection. Derivative filters are sensitive to noise, and images are generally smoothed before applying the Laplacian filter. The Laplacian of an image, L (x, y), with I (x, y) pixel intensity values are given as:

$$L(x,y) = \frac{\partial^2 I}{\partial x^2} + \frac{\partial^2 I}{\partial y^2} \quad (4)$$

0	-1	0
-1	4	-1
0	-1	0

-1	-1	-1
-1	8	-1
-1	-1	-1

Figure 6. Examples of Laplacian kernels (center with 4 is used in this study).

For two-dimensional signals, the discrete Laplacian approximations to the Laplacian filter can be given as convolution with the following kernels in Fig. 6.

High Pass Sharpening Filter

A high pass filter is used for highlighting fine details or enhancing the details that are blurred inside an image. A high-pass filter does the opposite of a low pass filter. As low-pass filtering smooths out noise, high-pass filtering amplifies the noise to bring out the details. If the original image is not too noisy applying a high pass filter shouldn't be a problem. For example, the Kernel in Fig. 7 shows minus signs for adjacent pixels. Meaning if there is no change in pixel intensity nothing takes place however if one pixel is brighter than its immediate neighbor, it gets boosted.

0	-1/4	0
-1/4	+2	-1/4
0	-1/4	0

Figure 7. High-pass filter kernel.

Skeletonization Algorithm

Representing the structural shape of a 2D region is to reduce it to a graph. This can be obtained by the skeletonization of a region via a thinning algorithm. Thinning algorithms can be used in various fields such as inspection of circuit boards, optical character recognition, etc. It is commonly used to trim the output of the edge detection by reducing all lines to a thickness of a few pixels. The Behavior of the thinning method is obtained through structuring elements as shown in Fig. 8. It makes a total of 8 structuring elements by 90° rotations (4×2).

Consider all pixels on the boundaries of foreground regions (i.e. foreground points that have at least one back-

0	0	0
	1	
1	1	1

	0	0
1	1	0
	1	

Figure 8. Skeletonization kernels.

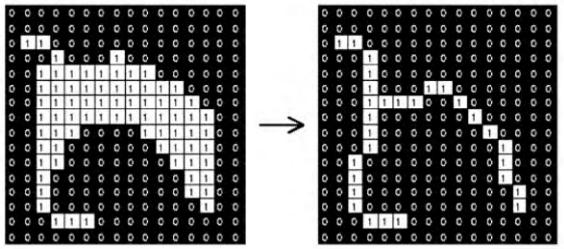

Figure 9. Thinning operation applied.

ground neighbor) in an image. Delete any such point that has more than one foreground neighbor, if doing so does not locally disconnect (i.e. split into two) the region containing that pixel. Iterate until convergence. Fig. 9 shows the result of this thinning operation on a simple binary image.

IMPLEMENTATIONS

Introduction to Neural Network

In this study, various preprocessing techniques have been applied to the MNIST dataset. The aim of applying these techniques is to observe the enhancements and accuracy in character identification. Adding information to the existing original image theoretically should improve the prediction of the neural network. Various methods were applied such as Laplacian transform for sharpening the images, Gaussian noise to observe effects of noise, and edge detection for re-representation of a character. The architectural representation of the neural network is presented in Fig. 10.

Edge Detection (Canny & Sobel) Application

Edge detection is a process used to detect and locate spatial discontinuities within the image. An Edge is identified as the finite area where the image contrast or intensity is largely changed. Edge Detection locates finite areas where there are high contrasts in intensity. Edge detection helps to collect details in an image, such as the shape, position, scale, detail sharpening, and enhancement of artifacts present in the image. Two of the most common

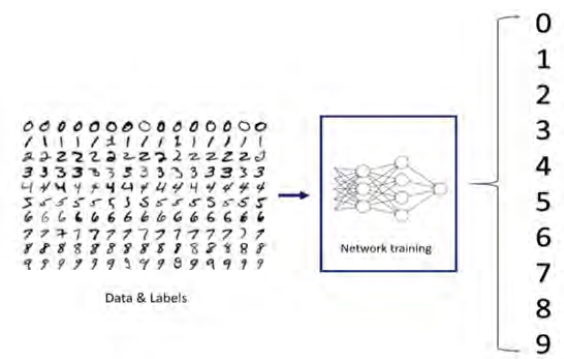

Figure 10. Neural network architecture.

Figure 11. From left a) The original image, b) Sobel edge detection, c) Canny edge detection.

algorithms for edge detection are implemented as shown in Fig. 11.

Sobel and Canny edge detection algorithms are applied to the original 28x28 pixel-sized MNIST images. Since it surrounds the entire character while performing edge detection and Sobel edge detection does not; Canny edge detection is considered for further calculations.

Canny was applied for the entire training MNIST dataset of 5000 number characters images with each has a size of 28x28 pixels. These images were used to train with their corresponding 10-bit labels. It was observed in Fig. 16 that the accuracy of an applied algorithm is measured as the percentage of true prediction with respect to total prediction. Canny edge detection produced an average of 84% accuracy while the Sobel algorithm has produced an 82.6% accuracy in character prediction. as seen in Fig.16 (blue and red color). Hence it was concluded that Canny was better than Sobel in terms of numeric character prediction.

Gaussian Noise Application

Gaussian noise, imnoise (image, 'gaussian', intensity) function in Matlab, with the probability density function P is applied on 5000 number character images of MNIST. During the implementation of Gaussian noise on images; Intensity values of 0.01, 0.1, 0.2, 0.3, 0.4 and 0.5 are deployed. Gaussian noise intensities create sets of varying noise intensity images. Each set of 5000 images were used for training purposes with their corresponding labels. The effects of additional noise in the predictions of feedforward neural networks are recorded. Various levels of Gaussian noise intensities are deployed for the training and prediction of the neural network.

The introduction of noise in character images was employed to show that the noise was an important factor. It degraded the images during testing and reduced the percentage accuracy. This can be predicted without repeating the test furthermore. It can be concluded that the addition of the noise to images would show a deterioration in all the applications. It was observed that as the amount of noise increases in character images, the accuracy of the neural network proportionally decreases. Examples of various Gaussian noise intensity levels can be seen in Fig. 12.

Figure 12. (a) Original İmage (b) Gaussian Noise 0.01 (c) Gaussian Noise 0.1.

The noisy image dataset is used to train the neural network and the resultant percentage accuracy level obtained was an average value of 75.2% as seen in Fig.16 (green color).

Laplacian Filter Application

Laplacian filter is a derivative operator. It emphasizes gray level disjunctions in an image and minimizes areas of slowly varying gray levels. By applying the Laplacian filter, images tend to obtain with grayish edge lines and other discontinuities that are all overlapped on a dark featureless background. Background details can be recovered while keeping the sharpening effect of the Laplacian operation by adding or subtracting the original and Laplacian images depending on the center coefficient. By applying the Laplacian image kernel with center value 4 in Fig. 6 on 5000 number character images of MNIST datasets, the Laplacian of these images is generated.

This can be identified as the enhancement of images. Fig. 13 shows the original image, Laplacian filtered image, and the combined image of an MNIST number character.

The combined image consists of the addition of original and Laplacian filtered images. This combined enhanced image dataset is used to train the neural network which results in average prediction accuracy of 87.4% in Fig. 16 (cyan color).

High Pass Filter Application

A high pass filtering technique is applied to see the sharpening effects on the image. Applying this filter amplifies the noise and brings the image details forward. A high pass filter kernel in Fig. 7 is applied to the character image and these images are convoluted with the kernel to generate a sharper image. 5000 images of number characters from the MNIST image database are high pass filtered. These high pass filtered images are later added

Figure 13. a) Original image, b) Laplacian filtered image, c) Laplacian filter + original image combined.

Figure 14. a) Original image (left), b) original image + High pass filtered image.

to the original image to increase the sharpening effect. These two combined images are fed into the feed-forward neural network for training purposes. A combined image of the high pass filtered image + original image is presented in Fig. 14.

At the end of the training stage, the unknown combined images of characters are tested with a feedforward neural network, and 89% average output prediction accuracy is obtained in Fig.16 (purple color).

Skeletonization Application

Skeletonization algorithm is applied to obtain the reshaping of structural shapes. The implementation of the Skeletonization algorithm yields a skeleton image. An original numeric character image is converted to a skeleton image as shown in Fig. 15. 5000 images of numeric characters are deployed from the MNIST database for skeletonization. The skeleton images of all the 5000-character images are obtained and they are inputted to the neural network for training. Once the training process is completed, at the end of the test stage for unknown characters, the prediction output accuracy is measured as 85.4% in Fig.16 (yellow color).

RESULTS AND DISCUSSIONS

Each application is carried out on 5000 MNIST images. These raw images are converted to resultant images by using different applications such as High Pass Filter, Gaussian Noise, Laplacian Filter, Canny, Sobel, Skeletonization algorithms. These resultant images are deployed to train a feedforward neural network with a different number of hidden layers for pattern recognition purposes in this study. The training of the network for each image type is the first step towards the quantization of prediction accuracy of unknown numerical characters. The number of hidden layers in a feedforward network

Figure 15. a) Original image, b) skeleton image.

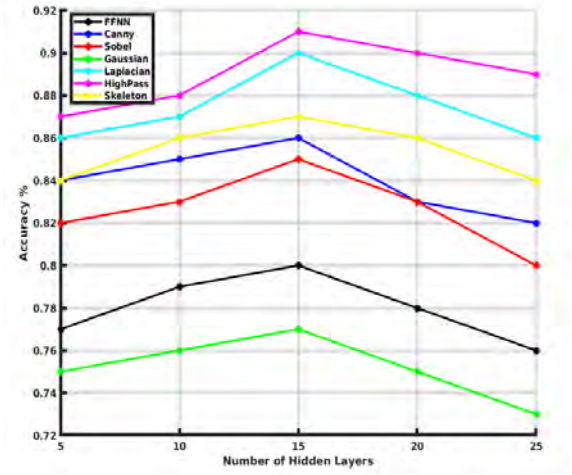

Figure 14. Output prediction accuracy of processed images for different applications versus the number of hidden layers.

where the input image data goes through is an important indicator for the output prediction accuracy of the neural network.

As the number of hidden layers changes, the image data which is going through the network also changes. Each of the affects the output prediction accuracy differently. In this study, 5 to 25 numbers of hidden layers are deployed. Optimum number of hidden layers was found to be 15 to obtain best prediction accuracies. Processed input image data are applied through these hidden layers. Hence, the prediction accuracies of different processed images through hidden layers are obtained by testing the neural network. Prediction accuracies versus the number of hidden layers are presented in Fig. 16.

It can be seen in Fig. 16 that high-pass filtering combined with the original image to increase the sharpening effect performs the highest output prediction accuracy of the neural network. The second-highest output prediction accuracy is obtained with the Laplacian filtering combined with the original image. Both application methods yield better results than the rest of the applications with the feedforward neural network. This is due to the extra enhancement, introduced with High pass and Laplacian filtering by combining the filtered image with the original image.

Edge detection algorithms, Canny and Sobel, both underperform compared to Laplacian and High pass sharpening filters. It is because edge detection algorithms only draw an outer contour of the character images. This causes a vast amount of information loss from the original data.

Canny seems to perform slightly better because of the contour drawing around the entire number character. Sobel, on the other hand, draws the contours with gaps. This small difference in edge detection techniques leads to a slight difference in the accurate prediction of the neural network trained with the Canny algorithm.

The skeletonization algorithm performs better than the edge detection algorithms. This can be possible due to the skeletonization algorithm consists of more pixel information compared to edge detection algorithms. Additionally, white pixels contribute to the learning process of the neural network. Having void regions with no information in images with applied edge detection does not contribute to the training process of the neural network. Hence accuracy prediction decreases.

Lastly, the neural network trained with added Gaussian noise to the character images performs the worst among the other application techniques. Training the neural network with noisy images leads to a worse performance compared to other applications which were predicted from the start. Hence, the prediction output accuracy is the lowest among the other applications.

CONCLUSION

It could be seen in this study that sharpening filters such as high pass and laplacian filters generated image enhancements of their original images before applied to the neural network. These enhanced images were later used to train the neural networks and give high prediction accuracy. In Literature, no study has been conducted on the comparison of different image processing techniques affecting output prediction accuracy of neural networks for character recognition.

A comparative study was proposed to transform the original MNIST images into resultant filtered images at the end of the filtering processes and use these images to train the neural network. The prediction accuracies for these image processing techniques on the character images are also investigated with respect to the number of hidden layers of the neural network.

The novelty lies in identifying the best pre-processing methods for input images to enhance them and in determining the optimum number of hidden layers in the Neural network.

The prediction accuracies are compared with respect to the number of hidden layers of the neural network. The prediction accuracy increases with sharpening filter effects and decreases with the inclusion of the noise. Unknown character images could also be exposed to similar High pass and Laplacian filtering and then applied as test inputs to the neural network to get the best prediction accuracies.

CONFLICT OF INTEREST

Author approve that to the best of their knowledge, there is not any conflict of interest or common interest with an institution/organization or a person that may affect the review process of the paper.

References

1. Yin Y, Zhang W, Hong S, Yang J, Xiong J, Gui, G. Deep learning-aided ocr techniques for chinese uppercase characters in the application of internet of things. IEEE Access 7 (2019) 47043-47049.
2. Yalniz IZ, Manmatha, R. Dependence models for searching text in document images. IEEE Transactions on Pattern Analysis and Machine Intelligence 41 (2009) 49-63.
3. Porat S, Carmeli B, Domany T, Drory T, Geva A, Tarem, A. Dynamic masking of application displays using OCR technologies. IBM Journal of Research and Development 53 (2009) 10:1-10:14.
4. Xu Y, Nagy, G. Prototype extraction and adaptive OCR. IEEE Transactions on Pattern Analysis and Machine Intelligence 21 (1999) 1280-1296.
5. Vamvakas G, Gatos B, Stamatopoulos N, Perantonis, SJ. A complete optical character recognition methodology for historical document, in: The 8th IAPR International Workshop on Document Analysis Systems, Nara, pp. 525-532, 2008 .
6. Nikola G, Dragan M, Dejan, G. System For Digital Processing, Storage and internet Publishing of Printed Textual Documents, in: Fifth National Conference With International Participation ETAI'2000, pp. 21-23, 2000.
7. Kim MD, Ueda, J. Dynamics-based motion deblurring improves the performance of optical character recognition during fast scanning of a robotic eye. IEEE/ASME Transactions on Mechatronics. 23 (2018) 491-495.
8. Morns IP, Dlay, SS. Analog design of a new neural network for optical character recognition. IEEE Transactions on Neural Networks 10 (1999) 951-953.
9. Hamad KA, Kaya, M. A detailed analysis of optical character recognition technology. International Journal of Applied Mathematics, Electronics and Computers 4 (2016) 244-249.
10. Garris MD, Dimmick, DL. Form design for high accuracy optical character recognition. IEEE Transactions on Pattern Analysis and Machine Intelligence 18 (199) 653-656.
11. Singh H, Sachan, A. A proposed approach for character recognition using document analysis with OCR, in: Second International Conference on Intelligent Computing and Control Systems (ICICCS), Madurai, India, pp. 190-195, 2018.
12. Kumar, PSJ. Adapted optimal neural network based classifier using optical character recognition engine for Tamil language. International Journal of Foundations of Computer Science 5 (2015) 30-37.
13. Budiwati SD, Haryatno J, Dharma, EM. Japanese character (Kana) pattern recognition application using neural network, in: Proceedings of the 2011 International Conference on Electrical Engineering and Informatics, Bandung, pp. 1-6, 2011.
14. Pasha S, Padma, MC. Recognition of handwritten Kannada characters using hybrid features, in: Fifth International Conference on Advances in Recent Technologies in Communication and Computing (ARTCom 2013), Bangalore, pp. 59-65, 2013.
15. Kishna NPT, Francis, S. Intelligent tool for Malayalam cursive handwritten character recognition using artificial neural network and Hidden Markov Model, in: International Conference on Inventive Computing and Informatics (ICICI), Coimbatore, pp. 595-598, 2017.
16. Chaudhari SA, Gulati, RM. An OCR for separation and identification of mixed English — Gujarati digits using kNN classifier, in: International Conference on Intelligent Systems and Signal Processing (ISSP), Gujarat, pp. 190-193, 2013.
17. Ghosn J, Bengio, Y. Bias learning, knowledge sharing. IEEE Transactions on Neural Networks 14 (2003) 748-765.

Hittite Journal of Science and Engineering, 2021, 8 (2) 141–147
ISSN NUMBER: 2148–4171
DOI: 10.17350/HJSE19030000224

Isatis Glauca Subsp. Sivasica Extract Contributes To The Diabetic Wound Healing Process By Increasing The Collagen And Nitric Oxide Content

Kaan Kaltalioglu[1] **Sule Coskun Cevher**[2]
[1]Giresun University, Espiye Vocational School, Giresun, Turkey
[2]Gazi University, Department of Biology, Ankara, Turkey

ABSTRACT

Isatis L. genus is highly endemic in Turkey and it is traditionally suggested for the wound management. In this study, we have reported the effect of the I. glauca subsp. sivasica extract on the diabetic wound healing process. A diabetic model was generated in Wistar rats using streptozotocin injection. The rats were divided into two main groups: the control group and the Isatis group. Full thickness excisional skin wounds were created by using a biopsy punch. The Isatis group was treated with single daily dose I. glauca subsp. sivasica extract (50 mg/kg). The rats were sacrificed on day 3 or day 7 after wounding. The dominant phenolic compounds identified with RP-HPLC-DAD from the Isatis extract were the benzoic acid and the vanillic acid. The *Isatis* extract significantly accelerated the wound healing process considering the wound closure rates (WCR). Moreover, the levels of collagen and nitric oxide were elevated on day 3 and day 7 by Isatis administration in the diabetic wound tissue. This data suggests that, for the first time, I. glauca subsp. sivasica extract may have the potential to promote the impaired wound healing in patients with diabetes.

Keywords:
Collagen; Diabetes mellitus; *Isatis glauca subsp. sivasica*; Nitric oxide; Wound healing.

Article History:
Received: 2021/02/25
Accepted: 2021/05/23
Online: 2021/06/30

***Correspondence to**: Kaan Kaltalioglu, Giresun University, Espiye Vocational School, 28600, Giresun, Turkey*
E-Mail: kaan.kaltalioglu@gmail.com
Phone: +90 (454) 310 14 30
Fax:+90 (454) 310 14 31

INTRODUCTION

Plants are traditionally used for medicinal purposes in the treatment of many diseases. *Isatis L.* genus (Brassicaceae), locally known as çivitotu in Turkey, has about 31 species and 15 subspecies in Turkey [1]. *Isatis L.* members are folkloric plants and are used both as an indigo plant and as a medicinal plant [2].

The members of this genus contain secondary metabolites like isatin, indicant, indirubin, tryptanthrin, p-coumaric acid, quercetin, chlorogenic acid, p-OH benzoic acid, caffeic acid [2,3] and have antioxidant, antimicrobial, anti-inflammatory and antinociceptive properties [3,4]. These plants are used for rheumatism, asthma, ulcer, constipation, fever, tumor, eczema, bite and hemorrhoid [5-7]. In addition, it has been reported that I. glauca subsp. glauca, I. glauca subsp. iconia and I. tinctoria are traditionally used for the wound healing in Turkey [8,9].

Wounding is one of the oldest and basic health problems in human history. Since the human body heals wounds by itself as an innate ability, wound healing may be overlooked. However, it is a highly complex and sensitive physiological process consisting of intertwined stages (inflammation, proliferation, remodeling) [10]. Many factors can disrupt this process and decrease the quality of life by delaying or preventing healing. Diabetes mellitus is one of these factors and is a systemic disease characterized by hyperglycemia [11]. In diabetic patients, almost all stages of the wound healing process are damaged. The diabetic wound healing process is disrupted due to the complications such as reduced collagen and growth factors production, infection, changing cellular activities, oxidative stress, vascular diseases and neuropathy [11,12].

The collagen is the dominant protein of the extracellular matrix (ECM) in the dermal layer of the skin, and is a vital element of the wound healing process [13]. Additionally, nitric oxide (NO) is a significant message molecule synthesized by various cell types in the skin during the healing process [14]. It has been reported that collagen and nitric oxide levels decrease in diabetic wounds [15,16].

Alternative treatment methods have been investigated in order to promote and accelerate diabetic wound healing process. This study was carried out to evaluate

the phenolic compounds of I. glauca subsp. sivasica (locally known as Sivas çiviti) extract and examine the effects of the extract on collagen and nitric oxide levels and wound closure rates throughout diabetic healing process on day 3 and 7.

MATERIAL AND METHODS

Plant Materials

I. glauca subsp. sivasica (Davis) Yıldırımlı samples were collected from Kemah/Erzincan province (between Kemah-Erzincan roadside, 1300-1400 m) in Turkey and were identified by Dr. Mustafa Karaköse. The voucher specimens have been deposited at the Espiye Vocational School Herbarium, Giresun University (Voucher number: ESPH 20)

Preparation of the *Isatis* Extract

The collected and identified plant samples (aerial parts) were dried under shade. Powdered samples (5 g) were extracted with methanol (100 mL) using Soxhlet apparatus. After the filtration with Whatman Millipore filter paper, methanol was evaporated by using a rotary evaporator (The yields of the extract: 15.69% w/w from dried starting material).

Reverse phase-high performance liquid chromatography method with diode array detector (RP-HPLC-DAD) analysis

The analysis was obtained according to a previously described method [17]. The gradient program was set by using the binary solvent system (A: distilled water with 2% acetic acid, B: distilled water with 70% acetonitrile, initial condition 5% B, final condition 60% B, run time 26 min). The column was operated at temperature of 30 °C. The flow of mobile phase and injection volume were adjusted as 1.2 mL/min and 10 µL, respectively. The eluted 10 phenolic acid standards and 2 flavonoids were analyzed at 280 nm by using a reversed phase column (Table 1). The validation parameters such as limits of detection (LOD) and limits of quantification (LOQ) were calculated to present much more reliably quantified results about analyses. Briefly, the phenolic compounds of the *Isatis* extract were evaluated by RP-HPLC-DAD using the calibration and validation values of the studied standard phenolic compounds (Table 1).

Induction of the Diabetes Model

This study was conducted with the approval from Gazi University Local Ethics Committee for Animal Experiments (G.Ü.ET-15.052). 24 Wistar rats were accommodated in standard cages with rat food and water (at room temperature, normal light-dark cycle). The diabetes model was induced in all rats via single dose intraperitoneal freshly prepared streptozotocin (STZ) (Sigma, USA) solution injection (60 mg/kg in sodium citrate buffer, pH 4.5). Three days after STZ injection, glucose levels were determined by a commercial glucometer, and those with above 250 mg/dL were considered as diabetic.

Induction of Wound Model

The animals were anesthetized with IM ketamine and xylazine. The dorsum of the rat was shaved and cleansed. Full thickness excisional skin wounds (six per animal) were created by using a biopsy punch (8-mm, Acu-Punch, Acuderm, USA) in all rats. The animals were randomly divided into four groups under two main groups (control and *Isatis*).

1. Control day 3: Wounded, no treatment was applied, sacrificed at post wounding day 3 (n=6)

2. Control day 7: Wounded, no treatment was applied, sacrificed at post wounding day 7 (n=6)

3. *Isatis* day 3: Wounded, the *Isatis* extract was applied, sacrificed at post wounding day 3 (n=6)

4. *Isatis* day 7: Wounded, the *Isatis* extract was applied, sacrificed at post wounding day 7 (n=6)

The *Isatis* extract was dissolved in 500 mL of physiological saline and the dose was adjusted such that 50 mg/kg of plant extract was applied to each wound (approx. 1 mL solution) based on the weight of the rats. In the treatment groups, the *Isatis* extract was applied topically to wounds via a sterile pipette as a single daily dose until sacrifice. The animals were sacrificed under anesthesia at post wounding day 3 or day 7, and wound tissue samples were collected. The collected samples were stored at – 80 °C. Simultaneously, the punch samples representing day 0 were also collected from the animals of the same groups.

Measurement of Collagen Levels

The collagen assay kit (Biocolor, UK) was used to measurement of the total collagen amount (type I-V) in the wound tissues. Collagen levels were determined according to the manufacturer's protocol and Tsuda et al. [18]. Briefly, the collected samples were homogenized in pepsin-acetic acid solution overnight, and mixed with Sircol dye reagent. Finally, the absorbances were recorded spectrophotometrically at 540 nm.

Table 1. The calibration and validation values of the studied standard phenolic compounds

No	RT	Standarts	R^2	RSD%(RT)	RSD%(Area)	LOD (mgL^{-1})	LOQ(mgL^{-1})
1	3.72±0.006	Gallic acid	0.999	0.168	4.315	0.070	0.213
2	6.74±0.019	Protocatechuic acid	0.998	0.291	5.973	0.495	1.499
3	10.13±0.029	p-OH Benzoic acid	0.999	0.290	4.817	0.224	0.680
4	11.46±0.027	Chlorogenic acid	0.997	0.239	6.177	0.512	1.550
5	13.49±0.023	Vanillic acid	0.994	0.168	6.794	0.171	0.518
6	13.84±0.032	Caffeic acid	0.999	0.235	6.861	0.058	0.175
7	14.79±0.012	Syringic acid	0.999	0.082	5.116	0.096	0.290
8	16.41±0.010	p-Coumaric acid	0.999	0.061	2.935	0.005	0.014
9	16.63±0.012	Rutin	0.999	0.075	2.855	0.311	0.942
10	18.41±0.013	Rosmarinic acid	0.999	0.069	3.388	0.162	0.492
11	18.84±0.014	Benzoic acid	0.999	0.076	2.721	0.550	1.665
12	21.71±0.019	Quercetin	0.999	0.087	2.268	0.335	1.014

Determination of NO_x Levels

The levels of NO_x in the wound tissue were evaluated according to a previously described method [19]. NO_x levels were calculated by Griess reagent assay. Briefly, the collected samples were homogenized in phosphate buffer (pH 7), and mixed with Griess reagents (N-1-naphthylethylenediamine dihydrochloride and sulphanilamide). After, the absorbances were recorded spectrophotometrically at 540 nm. Sodium nitrite and sodium nitrate solutions were used as standards.

Determination of Wound Size and Wound Closure Rate (WCR)

The wounds were photographed during the healing process. The wound sizes and the wound closure rates are assessed and measured using the ImageJ software (NIH, USA). The WCR was calculated as follows:

WCR (%) = [(wound size day 0–wound size on day 3 or 7)/wound size day 0] × 100.

Statistical Analysis

The obtained results were presented as the mean ± standard deviation (SD), and were compared using one-way ANOVA post-hoc Tukey test. Results with P<0.001 were interpreted as statistically significant (SPSS version 16, IBM, USA).

RESULTS

Phenolic Compounds

The RP-HPLC-DAD analysis revealed that *Isatis* extract contained protocatechuic acid, rutin, vanillic acid, p-hydroxybenzoic acid, rosmarinic acid, p-coumaric acid, caffeic acid, and benzoic acid (Fig. 1). Benzoic acid (6.95 mg phenolic/g extract) and vanillic acid (2.88 mg phenolic/g extract) were major phenolics in *Isatis* extract (Table 2). Gallic acid, chlorogenic acid, syringic acid and quercetin were not detected (Table 2).

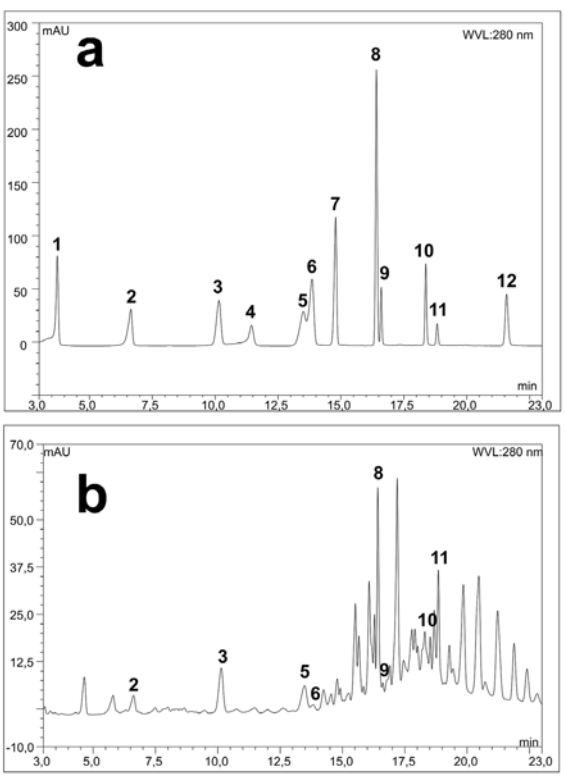

Figure 1. Chromatogram of I. glauca subsp. sivasica extract (a) standard phenolic compounds (b) Isatis (1) gallic acid (2) protocatechuic acid (3) p-OH-benzoic acid (4) chlorogenic acid (5) vanillic acid (6) caffeic acid (7) syringic acid (8) p-coumaric acid (9) rutin (10) rosmarinic acid (11) benzoic acid (12) quercetin

Table 2. Phenolic compounds of I. glauca subsp. sivasica extract

	Phenolic Compounds	*Isatis glauca subsp. sivasica*
		mg phenolic/ g extract
1	Gallic acid	n.d.
2	Protocatechuic acid	0.705
3	p-OH Benzoic acid	1.783
4	Chlorogenic acid	n.d.
5	Vanillic acid	2.879
6	Caffeic acid	0.103
7	Syringic acid	n.d.
8	p-Coumaric acid	1.158
9	Rutin	0.194
10	Rosmarinic acid	0.652
11	Benzoic acid	6.954
12	Quercetin	n.d.
	Total	14.432

n.d. = not dedected

3.2. Collagen and NO_x Levels

Topically administrated *Isatis* extract altered collagen and NO_x levels in diabetic wound tissue on both day 3 and day 7 compared to the control group as shown in Table 3. On day 3 and day 7, statistically increased collagen amount was determined in the *Isatis* group compared to the control group (P< 0.001) (Fig. 2). Similarly, NO_x levels in the *Isatis* group were also elevated significantly on day 3 and day 7 compared to the control group (P< 0.001) (Fig. 3).

Wound Sizes and WCRs

Fig. 4 shows the statistically significant decrease of wound size after *Isatis* extract administration on day 3 and day 7 compared to control group (P< 0.001). *Isatis* group

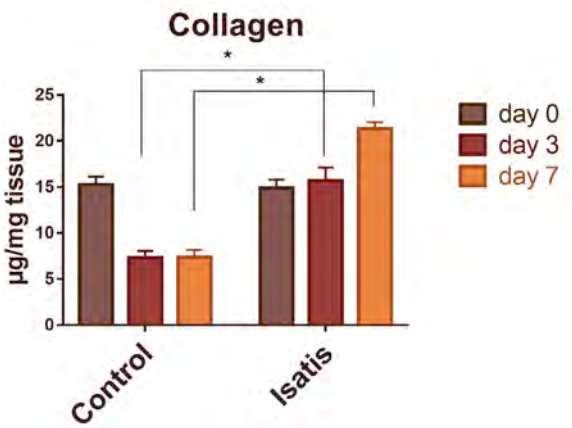

Figure 2. Comparison of *Isatis* and control groups in terms of collagen

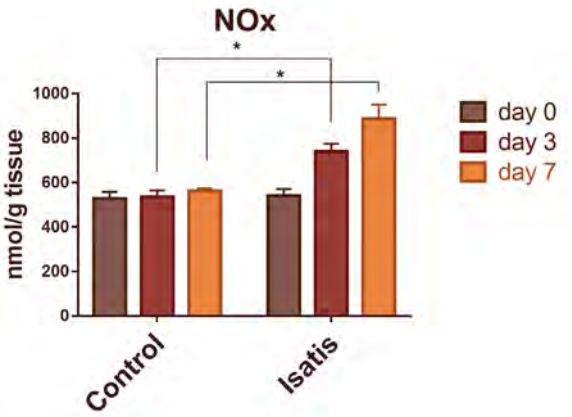

Figure 3. Comparison of *Isatis* and control groups in terms of NOx levels

displayed a higher WCR on day 3 and day 7 compared to control group (Table 4).

DISCUSSION

Since the wound healing is impaired in patients with diabetes, it is very important in terms of the life quality. New healing methods are increasingly gaining attention and are being researched in order to promote the diabetic wound healing process. Plant extracts have been used for this purpose since ancient times. This work aimed to investigate the effect of I. glauca subsp. sivasica extract on wound healing process of the STZ-induced diabetic Wistar rats. The I. glauca subsp. sivasica was chosen for this work because I. glauca and its various subspecies are traditionally used in the treatment of wounds as reported in ethnobotanical works [8,9].

The family of phenolic compounds are generally categorized into two class termed as phenolic acids and flavonoids. Besides ten phenolic acids, two flavonoids were analyzed for calibration and identification in this work. Our results showed that different ranges of concentration of pro-

Table 3. The collagen and NOx levels in diabetic wound tissue

	Collagen (µg/mg tissue)	*NOx (nmol/g tissue)*
Control group		
day 0	*15,24±0,87*	*528,26±30,41*
day 3	*7,32±0,73*	*535,43±30,38*
day 7	*7,36±0,81*	*562,10±11,27*
Isatis group		
day 0	*14,88±0,93*	*541,26±30,22*
day 3	*15,72±1,40**	*739,20±36,00**
day 7	*21,32±0,74**	*887,04±64,04**

*P<0.001 compared to control group on same day

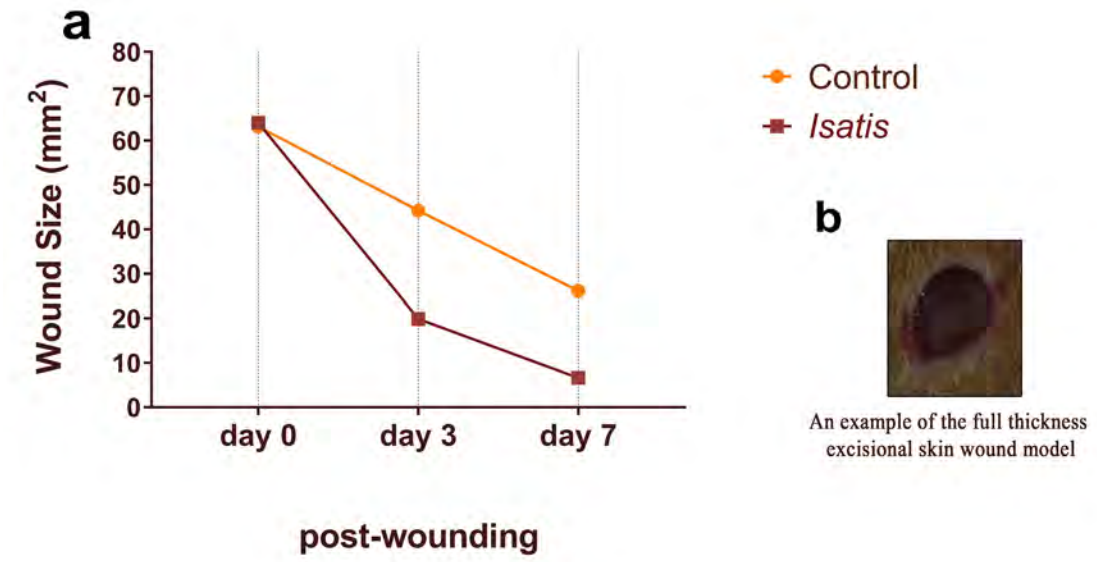

Figure 4. (a) Comparison of *Isatis* and control groups in terms of wound sizes depending on time (b) an example of the full thickness excisional skin wound model

	Wound size (mm²) and WCR (%)
Control group	
day 0	*63,15±3,48*
day 3	*44,22±2,41 (29,97 %)*
day 7	*26,11±1,72 (58,65 %)*
Isatis group	
day 0	*64,03±3,17*
day 3	*19,94±2,56* (68,86 %)*
day 7	*6,64±0,98* (89,63 %)*

*P<0.001 compared to control group on same day

Table 4. Wound sizes and WCRs during diabetic wound healing process

tocatechuic acid, rutin, vanillic acid, p-hydroxybenzoic acid, rosmarinic acid, p-coumaric acid, caffeic acid, and benzoic acid were contained in the *Isatis* extract. Phenolic compounds are commonly used in the treatment of various disorders thanks to its antioxidant and antimicrobial activity [17]. The *Isatis* extract can be considered as a source of bioactive compounds. The evaluated outputs are nearly similar to the phenolic compounds of the other members of the *Isatis* genus. Karakoca et al. [3] reported that I. floribunda contains phenolic components such as p-hydroxybenzoic acid, catechin, chlorogenic acid, caffeic acid, ferulic acid, quercetin, cinnamic acid and p-coumaric acid. In another study, Miceli et al. [20] showed that chlorogenic acid, sinapic acid, caffeic acid, ferulic acid, rutin, p-coumaric acid, apigenin-glucoside, isovitexin and vicenin-2 detected in I. tinctoria.

Collagen and NO are two important molecules that play a role in the complex wound healing process. Collagen is a major ECM component made up of amino acids (3 chains in triple helix form), and it accounts for about 75% of dry weight of the human skin. The synthesis, accumulation, deposition and degradation of collagen are important for proper wound healing process [21]. An important task of collagen is to increase the wound tensile strength by providing a structural support [13]. NO, an endogenous gasotransmitter, is synthesized from L-arginine by nitric oxide synthases (NOS), and has roles in the regulation of antimicrobial action, vascular homeostasis and inflammation during the wound healing process [16]. It has been demonstrated that both collagen and NO content decreased in the wounds of diabetes-induced animals and chronic wounds of diabetic patients [15,16]. These decreases may be one of the underlying causes of the damaged wound healing in diabetic patients. In our study, a statistically significant elevation in collagen and NO_x levels on days 3 and 7 were founded in the *Isatis* group compared with the control group.

However, there is no study showing the effects of I. glauca subsp. sivasica or another *Isatis* species on collagen and NO contents in the literature. These effects of *Isatis* may be due to its chemical composition. Kumar et al. [22] showed that the administration of vanillic acid increases NO levels in hypertensive rats. Additionally, it has reported that rutin enhances NO and collagen production in endothelial and fibroblast cells, respectively [23,24]. *Isatis* extract may also have increased the collagen and NO level due to the vanillic acid and rutin content (Table 2).

According to Kızıl et al. [25], palmitic, oleic, erucic, stearic, linoleic and linolenic acids were detected in the fatty acid composition of I. glauca. Lambertucci et al. [26] reported that palmitic acid induces NO production and of inducible nitric oxide synthases (iNOS) protein content in

muscle cells. Additionally, de Lima et al. [27] demonstrated that fatty acids (palmitic, stearic, oleic, linoleic acids) increase NO production in macrophages at low concentrations. Taken together, these results suggest that I. glauca subsp. sivasica extract can increase NO content in diabetic wound tissue through the composition of fatty acids and phenolic compounds. Furthermore, NO enhances the production and deposition of collagen during wound healing in non-diabetic or diabetic experimental models [28-31]. Hence, it can be stated that *Isatis glauca subsp. sivasica* extract contributes to diabetic healing process via increased collagen and nitric oxide levels.

Wound closure occurs due to the movement and proliferation of epithelial cells at the edge of the wound area (called as epithelialization). Diabetes mellitus causes non-closing (non-healing) wounds or impaired wound healing [11]. In our study, a statistically significant decrease in the wound sizes were measured in the *Isatis* group compared to the control group on day 3 and day 7 ($p<0,001$). In addition, WCRs detected in the *Isatis* group reached about 69% and 90%, in contrast to only 30% and 59% in the control group on day 3 and 7, respectively. The presented results suggested that this *Isatis* species accelerates the wound healing process supporting its traditional use.

CONCLUSION

This work shows that I. glauca subsp. sivasica extract can contribute to promote diabetic wound healing process by increasing collagen and NO levels and WCR on days 3 and 7. In this context, the I. glauca subsp. sivasica extract can be a potential therapeutic agent for the management of diabetic wounds.

CONFLICT OF INTEREST

Authors approve that to the best of their knowledge, there is not any conflict of interest or common interest with an institution/organization or a person that may affect the review process of the paper.

AUTHOR CONTRIBUTION

Kaan Kaltalioglu and Sule Coskun Cevher designed the study. KK performed all experiments. KK and SCC analysed the data. KK and SCC wrote the paper.

References

1. Güner A, Aslan S, Ekim T, Vural M, Babaç MT. Türkiye Bitkileri Listesi (Damarlı Bitkiler), first ed. Flora Araştırmaları Derneği ve Nezahat Gökyiğit Botanik Bahçesi Yayını, İstanbul, 2012.
2. Yıldız N, Karakaş Ö. Qualitative and Quantitative Determination of Tryptanthrin, Indirubin, Indican and Isatin Indole Alkaloids During Vegetative and Flowering Stages in the Roots and Leaves of *Isatis constricta* P. H. Davis. Tarla Bitkileri Merkez Araştırma Enstitüsü Dergisi 28 (2019) 59–66.
3. Karakoca K, Özüsağlam MA, Çakmak YS, Erkul SK. Antioxidative, antimicrobial and cytotoxic properties of isatis floribunda boiss. ex bornm. Extracts. EXCLI Journal 12 (2013) 150–167.
4. Küpeli E, Orhan İ, Yeşilada E. Evaluation of Some Plants Used in Turkish Folk Medicine for Their Anti-inflammatory and Antinociceptive Activities. Pharmaceutical Biology 45 (2007) 547–555.
5. Hamburger M. *Isatis tinctoria* - From the Rediscovery of an Ancient Medicinal Plant Towards a Novel Anti-Inflamatory Phytopharmaceutical. Phytochemistry Reviews 1 (2002) 333–344.
6. Tuzlacı E, Doğan A. Turkish folk medicinal plants, IX: Ovacık (Tunceli). Marmara Pharmaceutical Journal 14 (2010) 136–143.
7. Rezaeipoor R, Ziaei Sanei L, Kamalinejad M. Effects of *Isatis cappadocica* on humoral immune responses. Fitoterapia 71 (2000) 14-18.
8. Ozturk M, Uysal I, Gucel S, Altundag E, Dogan Y, Baslar S. Medicinal Uses of Natural Dye-Yielding Plants in Turkey. Research Journal of Textile and Apparel 17 (2013) 69–80.
9. Baytop T. Therapy with Plants in Turkey (Past & Present), second ed. Nobel Tıp, İstanbul, 1999.
10. Guo S, DiPietro LA. Factors Affecting Wound Healing. Journal of Dental Research 89 (2010) 219–229.
11. Li H, Fu X, Zhang L, Huang Q, Wu Z, Sun T. Research of PDGF-BB gel on the wound healing of diabetic rats and its pharmacodynamics. Journal of Surgical Research 145 (2008) 41–48.
12. Kaltalioglu K, Balabanli B, Coskun-Cevher S. Phenolic, Antioxidant, Antimicrobial, and In-vivo Wound Healing Properties of Potentilla erecta L. Root Extract in Diabetic Rats. Iranian Journal of Pharmaceutical Research 19 (2020) 264–274.
13. Brett D. A review of collagen and collagen-based wound dressings. Wounds 20 (2008) 347–356.
14. Schäfer M, Werner S. Oxidative stress in normal and impaired wound repair. Pharmacological Research 58 (2008) 165–171.
15. Blakytny R, Jude E. The molecular biology of chronic wounds and delayed healing in diabetes. Diabetic Medicine 23 (2006) 594–608.
16. Malone-Povolny MJ, Maloney SE, Schoenfisch MH. Nitric Oxide Therapy for Diabetic Wound Healing. Advanced Healthcare Materials 8 (2019) e1801210.
17. Bektas E, Kaltalioglu K, Sahin H, Turkmen Z, Kandemir A. Analysis of phenolic compounds, antioxidant and antimicrobial properties of some endemic medicinal plants. International Journal of Secondary Metabolite 5 (2018) 75–86.
18. Tsuda K, Nakatani T, Sugama J, Okuwa M, Sanada H. Influence of the timing of switching a protein-free to a protein-containing diet on the wound healing process in a rat all-layer skin defect. International Wound Journal 7 (2010) 135–146.
19. Miranda KM, Espey MG, Wink DA. A rapid, simple spectrophotometric method for simultaneous detection of nitrate and nitrite. Nitric Oxide 5 (2001) 62–71.
20. Miceli N, Filocamo A, Ragusa S, Cacciola F, Dugo P, Mondello L, Celano M, Maggisano V, Taviano MF. Chemical characterization and biological activities of phenolic-rich fraction from cauline leaves of *Isatis tinctoria L.* (Brassicaceae) growing in Sicily, Italy. Chemistry & Biodiversity 14 (2017) e1700073.
21. dos Santos Gramma LS, Marques FM, Vittorazzi C, de Andrade, TAM, Frade MAC, de Andrade TU, Endringer DC, Scherer R, Fronza M. Struthanthus vulgaris ointment prevents an over expression of inflammatory response and accelerates the cutaneous wound healing. Journal of Ethnopharmacology 190 (2016) 319–327.

22. Kumar S, Prahalathan P, Raja B. Antihypertensive and antioxidant potential of vanillic acid, a phenolic compound in l-NAME-induced hypertensive rats: A dose-dependence study. Redox Report 16 (2011) 208–215.
23. Ugusman A, Zakaria Z, Chua KH, Nordin NAMM, Abdullah Mahdy Z. Role of rutin on nitric oxide synthesis in human umbilical vein endothelial cells. Scientific World Journal (2014) 2014: 1–9.
24. Choi SJ, Lee SN, Kim K, Joo da H, Shin S, Lee J, Lee HK, Kim J, Kwon SB, Kim MJ, Ahn KJ, An IS, An S, Cha HJ. Biological effects of rutin on skin aging. International Journal of Molecular Medicine 38 (2016) 357–363.
25. Kızıl S, Turk M, Çakmak Ö, Özgüven M, Khawar KM. Microelement Contents and Fatty Acid Compositions of some *Isatis* Species Seeds. Notulae Botanicae Horti Agrobotanici Cluj-Napoca 37 (2009) 175–178.
26. Lambertucci RH, Leandro CG, Vinolo MA, Nachbar RT, Dos Reis Silveira L, Hirabara SM, Curi R, Pithon-Curi TC. The effects of palmitic acid on nitric oxide production by rat skeletal muscle: mechanism via superoxide and iNOS activation. Cellular Physiology and Biochemistry 30 (2012) 1169–1180.
27. de Lima TM, de Sa Lima L, Scavone C, Curi R. Fatty acid control of nitric oxide production by macrophages. FEBS Letters 580 (2006) 3287–3295.
28. Witte MB, Thornton FJ, Efron DT, Barbul A. Enhancement of fibroblast collagen synthesis by nitric oxide. Nitric Oxide 4 (2000) 572–582.
29. Witte MB, Kiyama T, Barbul A. Nitric oxide enhances experimental wound healing in diabetes. British Journal of Surgery 89 (2002) 1594–1601.
30. Achuth HN, Moochhala SM, Mahendran R, Tan WT. Nitrosoglutathione triggers collagen deposition in cutaneous wound repair. Wound Repair and Regeneration 13 (2005) 383–389.
31. Luo J, Chen AF. Nitric oxide: a newly discovered function on wound healing. Acta Pharmacologica Sinica 26 (2005) 259–264.

Hittite Journal of Science and Engineering, 2021, 8 (2) 149–160
ISSN NUMBER: 2148–4171
DOI: 10.17350/HJSE19030000225

Investigation of The Posture Positions of The Apparel Workshop Employees with The Rapid Entire Body Assessment(REBA) and Rapid Upper Limb Assessment(RULA) Method

Senol Yavuz[1] Berna Gur[1] Ahmet Dogan Cakir[1] Dursun Ali KOSE[2]
[1]Hitit University, Department of Property Protection and Security, Corum, Turkey
[2]Hitit University, Department of Chemistry, Corum, Turkey

Article History:
Received: 2021/03/03
Accepted: 2021/06/21
Online: 2021/06/30

***Correspondence to**: Senol Yavuz, Hitit University, Property Protection and Security, 19500, Corum, TURKEY*
E-Mail: senolyavuz@hitit.edu.tr

ABSTRACT

As the industry made progress, human labor force gained importance as an element of work life. The science of ergonomics came into being in order to take necessary precautions by determining the convenience of human motions with anatomy and risks and possible dangers during work. Through the methods of risk assessment, risks and possible dangers are determined to create a healthy environment for workers. Through REBA and RULA risk assessment methods, worker motions and postures are studied to determine convenience by calculating risk scores related to worker motions. The aim of REBA and RULA risk assessment methods is to study whether or not the worker is functioning in accordance with his/her skills and to prevent labor accidents and occupational diseases as a result of the data obtained. In this study, REBA and RULA risk scores are tried to be calculated by studying the motions of apparel workshop employees working in the fabric cutting, quality, packaging, ironing and stain removal sections. According to the analysis obtained, REBA score for the fabric cutting employee is 6, RULA score for the sewing machine operator is 4, REBA score for the quality control employee is 4, REBA score for the stain removal employee is 3, REBA score for the ironing employee is 6 and REBA score for the packaging employee is 5. According to the scores obtained through the use of REBA and RULA risk assessment method, the motions and postures of employees are determined to be at dangerous levels. The results obtained by examining the postures of the employees according to the REBA and RULA risk tables, and the results confirming the hazard class of the workplace show that it can be used in ergonomic risk analysis.Among the primary precautions needed to be taken to prevent the risks can be having the employee work at different tasks within certain intervals, monitoring the health, providing occupational health and safety educational programs.

Keywords:
Ergonomics, REBA, Risk assessment, RULA.

INTRODUCTION

The human labor force gained importance with the industrial revolution. At first, there was barely any study on occupational accidents and diseases. As the time went on, the term "occupational health and safety" gained importance primarily in England and later on in other European countries with "providing the workers a healthy and safe environment" in mind as occupational health issues rose and accidents began happening due to the nature of the work. In time, the Occupational Health and Safety legislation (numbered 6331) has been implemented so as to prevent occupational accidents and diseases[1].

Thanks to the technology on the rise, employees' activities in the workplace has been studied with the Occupational Health and Safety applications. Determining the dangers and risks by studying employees' activities and working environments led to the development of proactive approaches. Employees have been raising their awareness with the help of risk assessment methods, environment observations and occupational health and safety education programmes[2,3].

The Occupational Health and Safety legislation (numbered 6331) imposes the employer to conduct risk

assessment or have it done. The main aim of risk assessment is to take precautions by determining the risks and dangers at the work place providing the workers with a safe environment to work at. Proactive approach is the efforts made before the occupational accidents or disease comes to happen[3].

Prolonged working hours, faulty postures, non-ergonomic weight lifting motions and repetitive motions causing physical and mental fatigue are all known to cause occupational diseases[4,5]. It's crucial to study employees' structural and psychological properties. Human muscle and skeletal system is capable of some certain movement power and skills, detecting the environment and defending itself when needed. That's why there must be a harmony between an employee's motions and his/her basic characteristics[6].

Ergonomics studies the compatibility of the job with the worker but not the compatibility of the worker with the job. Additionally, it takes the physical properties of the worker into account. The term "ergonomics" is comprised of two counterparts : "ergo" which means "labor" and "nomos" meaning "law"[7]. It was first used in England in 1949[8,9].

Arranging the working environment ergonomically, leads to employees' being protected against occupational risks and encourages productivity thus leading the establishment to make more profit[10]. "Human-tools and equipment-working environment" harmony is known to be of a great importance. Whereas certain educational programmes have been implemented by some companies in order to promote employees' compliances with tools and equipment and working environment, some physical rearrangements in the workplace are also put into action[11]. Environmental and physical risks present in the workplace and employees' postures and repetitive movements may result in muscular and skeletal impairments[12]. According to the data supplied by the Social Security Institution, muscular and skeletal system diseases make up 7,5% of the occupational diseases[13]. According to the statistics, besides the occupational accidents, it's clear that occupational diseases are important, as well. Unless the necessary precautions are taken, the rate of muscular and skeletal diseases will eventually rise[13].

The most important way to prevent muscular and skeletal diseases by foreseeing the ergonomical dangers is to implement the risk assessment enabling to determine such dangers. As the ergonomical risk assessment is properly implemented in instituons and corporations, the dangers and as well as the ergonomical risks that the employees and the employers can possibly be facing could be foreseen effectively[14].

Rapid Entire Body Assessment (REBA) and Rapid Upper Limb Assessment (RULA) in Ergonomical Risk Analysis

Today, one of the most common occupational health diseases is muscular and skeletal diseases. 29% of loss in the quality and productivity in a workplace stems from muscular and skeletal diseases [15]. The physical labor burden analysis is done to show the faulty posture effects employees' health negatively. The muscular and skeletal diseases caused by the faulty posture is closely related to the environmental conditions, frequency of the work and the amount of the weights lifted [16]. Various methods have been developed to determine the risk of such factors turning into a cause of health issue in people. These methods are grouped as three. They are namely as;

- Personal Survey Method,
- Methods Based on Systematic Observations,
- Direct Measurement Method

Systematic Methods are also divided into two as Basic and Advanced Observations. Basic observations utilize methods like RULA(Rapid Upper Limb Assessment), REBA(Rapid Entire Body Assessment), NIOSH(Lifting Equation Calculator), ROSA((Rapid Office Strain Assessment) etc. while advanced observations utilize methods like Ergo-Man, 3DSSPP, Jack, RAMSIS Modelling etc[17].

REBA method is used to determine the amount of risk a posture or a movement poses. The torso, neck, legs, arms (lower and upper) in a certain position and twists in wrists,

Table 1. RULA and REBA score and risk groups [20].

Rula		*Reba*	
Score	*Risk*	*Score*	*Risk*
1-2	*Acceptable*	*1*	*Insignificant risk*
3-4	*Detailed inspection, may need changes*	*2-3*	*Low risk, may need changes*
5-6	*Detailed inspection, immediate change*	*4-7*	*Medium risk, detailed inspection, immediate change*
7	*Re-evaluation, application change*	*8-10*	*High risk, re-evaluation, application change*
		>11	*Very high risk, application change*

relativity of twist effects to the amount of load are expressed through numeric values varying from 1 to15[18]. As determining the numeric values (scores), the body is divided into two groups: Group A, which is made up of torso, neck and legs and Group B, which is made up of upper arms, lower arms and wrists. Scores resulted from Group A wascombined the Score A. The final Score A is derived by adding the force/load score. The posture scores in Group B were determined and combine the Score B. Scores A and B are added up to derive Score C. The risk levels of posture positions and related risk priorities are determined with help of data. RULA method is somewhat similar to REBA. In the RULA method, feet positioning and work-limb match and activities in addition to the areas studied in REBA method are all taken into account to derive a score. In REBA and RULA methods, the risk level is determined in accordance with the score intervals [19].

MATERIALS AND METHODS

In the apparel production workshops, from fabric cutting to packaging, 6 different tasks employing fabric cutters, machine operators, quality controllers, stain removers, ironers and packer-ups have been analyzed in ergonomic risk perspective by the use of REBA and RULA methods regarding 2 types of postures. REBA method have been utilized for tasks such as fabric cutting, quality control, stain removal, ironing and packaging whereas RULA method have been preferred for tasks carried out in sitting position such as machine sewing [25].

The Task of Fabric Cutting by Using Fabric Cutting Saw

In Fig. 1 body angles of the worker were estimated by using Angle Meter software and the analysis results by the REBA method are presented on Table 1.

The neck and the body of the worker aligned on a straight angle varying from 0° to 20° and because of the lack of neck turns, bending and stretching movements, risk score of the neck has been considered as 1. Torso lean of the worker was estimated approximately 46° and because the value falls within the 20° – 60° interval and due to the lack of turning and bending movements, risk score of the torso has been considered as 3.

Risk score has been considered as 1 in the evaluation of the feet, since the worker's both feet stepped on the ground. As these values were calculated on the REBA Score A table, the risk score has been detected as 2. The approximate angle of the upper arm of the worker was estimated as 97°. Since the value is greater than 90°, the risk score has been estimated as 4. The angle of the lower arm was approximately estimated as 37o and since the value is below 60° the risk score has been estimated as 2.

The wrist angle was considered as 0 for it works on a straight position. The risk score has been estimated as 1 since the angle is below 15°. As these values were calculated on the REBA Score B table, the risk score has been estimated as 5. As the REBA A and B scores were co-calculated on the REBA Score C table, the outcome has become risk score of 4.Adding 2 more scores -one of which has been added as an additional 1 score due to the body parts immobilized for more than a minute whereas the other 1 score has been added due to movements repeated for 4 times or more in a minute without walking – a total of REBA Risk Score of 6 has been calculated. That figure corresponds with a "medium risk and requires precautions" level on REBA Risk Evaluation Table.

The Task of Sewing by Using a Sewing Machine

The body angles of the worker seen in the Fig. 2 were approximately measured using Angle Meter software and RULA method was utilized since the worker worked in seated position and the analysis results are presented in Table 2. The upper arm angle measured at 60°. This angle is considered within 45° – 60° interval and the risk score has been measured as 3. Rise in shoulder's position, stretch in arms and restricted upper arm movements wasn't detected. However, judging from the fact that the arms were supported by the counter, the risk score has been reduced by 1 point and the revised risk score has been estimated as 2. The worker's lower arm's working position was estimated as 108°. As this value is greater than 100° on the calculation table, the risk score has been estimated as 2.As the wrist angle was considered lower

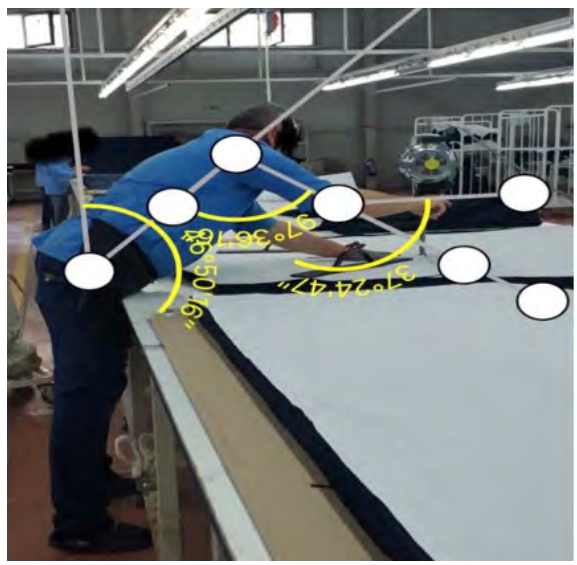

Figure 1. The task of fabric cutting.

Table 2. REBA analysis of fabric cutting task.

Table 2a. Posture A score.

Posture A Score = 2		Neck											
		1				2				3			
Legs		1	2	3	4	1	2	3	4	1	2	3	4
Torso	1	1	2	3	4	1	2	3	5	3	3	5	6
	2	2	3	4	5	3	4	5	6	4	5	6	7
	3	2	4	5	6	4	5	6	7	5	6	7	8
	4	3	5	6	7	5	6	7	8	6	7	8	9
	5	4	6	7	8	6	7	8	9	7	8	9	9

Table 2b. Posture B score.

Posture B Score= 5		Lower arm					
		1			2		
Upper arm	Wrist	1	2	3	1	2	3
	1	1	2	2	1	2	3
	2	1	2	3	2	3	4
	3	3	4	5	4	5	5
	4	4	5	5	5	6	7
	5	6	7	8	7	8	8
	6	7	8	8	8	9	9

Table 2c. Total score.

Total C Score= 4		Posture B Score											
		1	2	3	4	5	6	7	8	9	10	11	12
Posture A Score	1	1	1	1	2	3	3	4	5	6	7	7	7
	2	1	2	2	3	4	4	5	6	6	7	7	8
	3	2	3	3	3	4	5	6	7	7	8	8	8
	4	3	4	4	4	5	6	7	8	8	9	9	9
	5	4	4	4	5	6	7	8	8	9	9	9	9
	6	6	6	6	7	8	8	8	8	10	10	10	10
	7	7	7	7	8	9	9	9	10	10	11	11	11
	8	8	8	8	8	9	10	10	10	10	11	11	11
	9	9	9	9	10	10	10	11	11	11	12	12	12
	10	10	10	10	11	11	11	11	12	12	12	12	12
	11	11	11	11	11	11	12	12	12	12	12	12	12
	12	12	12	12	12	12	12	12	12	12	12	12	12
Activite Score 2													
REBA Risk Score = 6													

than 15°, the risk score has been considered as 2 according to the calculation table. The wrist twist angle was also considered lower than 15° and risk score has been considered as 1 according to the calculation table. As the values obtained were evaluated on the RULA A Score Table, the risk score has been estimated as 3.

The worker's neck angle was measured approximately as 36°. Since this value is greater than 20° according to the calculation table, the risk score has been considered as 2. Because there weren't any stretching or rotating motions on the neck, no others score has been added. Torso lean was approximately estimated as 23° and since this value falls within 20° – 40° interval, the risk score has been considered as 3. No other score has been added due to lack of rotating or leaning sideways motion on the torso.

Figure 2. The task of sewing.

Table 3. RULA analysis for fabric sewing.

Table 3a. Posture A score.

Posture A Score = 3			Wrist							
			1		2		3		4	
			Wrist Twist							
		Lower Arm	1	2	1	2	1	2	1	2
Upper Arm For Supporting Arms, it gets -1 Point. For this reason, The upper Arm Score is evaluated as 3-1 = 2 Point. ÜST KOL	1	1	1	2	2	2	2	3	3	3
		2	2	2	2	2	3	3	3	3
		3	2	3	3	3	3	3	4	4
	2	1	2	3	3	3	3	4	4	4
		2	3	3	3	3	3	4	4	4
		3	3	4	4	4	4	4	5	5
	3	1	3	3	4	4	4	4	5	5
		2	3	4	4	4	4	4	5	5
		3	4	4	4	4	4	5	5	5
	4	1	4	4	4	4	4	5	5	5
		2	4	4	4	4	4	5	5	5
		3	4	4	4	5	5	5	6	6
	5	1	5	5	5	5	5	6	6	7
		2	5	6	6	6	6	7	7	7
		3	6	6	6	7	7	7	7	8
	6	1	7	7	7	7	7	8	8	9
		2	8	8	8	8	8	9	9	9
		3	9	9	9	9	9	9	9	9

Table 3b. Posture B score.

Posture B Score = 4		Torso											
		1		2		3		4		5		6	
Legs		1	2	1	2	1	2	1	2	1	2	1	2
Neck	1	1	3	2	3	3	4	5	5	6	6	7	7
	2	2	3	2	3	4	5	5	5	6	7	7	7
	3	3	3	3	4	4	5	5	6	6	7	7	7
	4	5	5	5	6	6	7	7	7	7	7	8	8
	5	7	7	7	7	7	8	8	8	8	8	8	8
	6	8	8	8	8	8	8	8	9	9	9	9	9

Table 3c. Total score.

C Total Score = 4		RULA B Score						
		1	2	3	4	5	6	7+
RULA A score	1	1	2	3	3	4	5	5
	2	2	2	3	4	4	5	6
	3	3	3	3	4	4	5	6
	4	3	3	3	4	5	6	6
	5	4	4	4	5	6	7	7
	6	4	4	5	6	6	7	7
	7	5	5	6	6	7	7	7
	8	5	5	6	7	7	7	7

Lastly, the task was carried out in sitting position with the legs supported thus scoring 1 regarding the risk score for the legs. As the risk scores obtained was evaluated on the RULA B Score table, the risk score has been measured as 4 points. As the RULA A and B scores have been placed on the RULA C Score table, the risk score measures at 4 points. That value (Fig. 2) corresponds with "the may need changes" risk level on RULA Risk Evaluation Table.

The Task of Product Quality Control

The position we will see in Fig. 3 contains the worker doing the quality control task whose certain bodily angles were approximately measured by Angle Meter software and the analysis results by REBA method have been presented in Table 3.

Table 4. REBA analysis for the product quality control task.

Table 4a. Posture A score.

Posture A Score = 2		Neck											
		1				2				3			
Legs		1	2	3	4	1	2	3	4	1	2	3	4
Torso	1	1	2	3	4	1	2	3	5	3	3	5	6
	2	2	3	4	5	3	4	5	6	4	5	6	7
	3	2	4	5	6	4	5	6	7	5	6	7	8
	4	3	5	6	7	5	6	7	8	6	7	8	9
	5	4	6	7	8	6	7	8	9	7	8	9	9

Table 4b. Posture B score.

Posture B Score = 3		Lower arm					
		1			2		
Upper arm	Wrist	1	2	3	1	2	3
	1	1	2	2	1	2	3
	2	1	2	3	2	3	4
	3	3	4	5	4	5	5
	4	4	5	5	5	6	7
	5	6	7	8	7	8	8
	6	7	8	8	8	9	9

Table 4c. Total score.

Total C Score= 2		Posture B Score											
		1	2	3	4	5	6	7	8	9	10	11	12
Posture A Score	1	1	1	1	2	3	3	4	5	6	7	7	7
	2	1	2	2	3	4	4	5	6	6	7	7	8
	3	2	3	3	3	4	5	6	7	7	8	8	8
	4	3	4	4	4	5	6	7	8	8	9	9	9
	5	4	4	4	5	6	7	8	8	9	9	9	9
	6	6	6	6	7	8	8	8	8	10	10	10	10
	7	7	7	7	8	9	9	9	10	10	11	11	11
	8	8	8	8	8	9	10	10	10	10	11	11	11
	9	9	9	9	10	10	10	11	11	11	12	12	12
	10	10	10	10	11	11	11	11	12	12	12	12	12
	11	11	11	11	11	11	12	12	12	12	12	12	12
	12	12	12	12	12	12	12	12	12	12	12	12	12
Activite Score 2													
REBA Risk Score = 4													

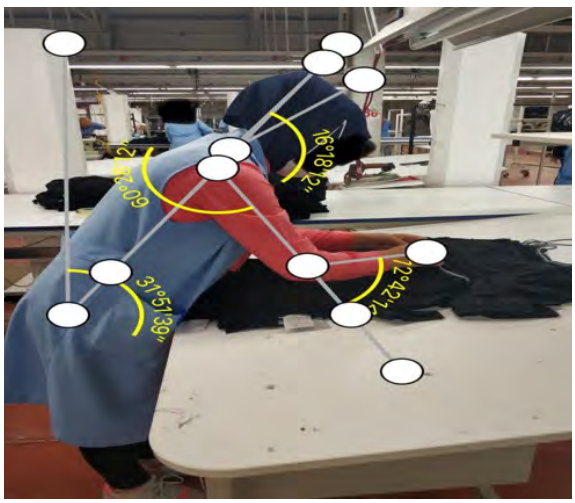

Figure 3. The task of product quality control.

The worker's neck angled at around 16° and the neck risk score has been calculated as 1. The worker's torso angle was around 31° and the risk score has been calculated as 3 according to the table of calculation. For the worker stood on both her feet, the risk score has been calculated as 1. As these values have been calculated on REBA A Score table, the risk score has been estimated as 2.

The worker's upper arm angle was approximately at 60° and since this value falls within 45° – 90° interval, the risk score has been calculated as 3. As the lower arm angle was calculated 72°, the risk score coherent with the calculation table has been estimated as 1.Because the wrist working angle was less than 15°, the risk score has been estimated as 1. As these values were evaluated on the REBA B Score table, risk score has been estimated as 2.

Table 5. REBA analysis for stain removal task.

Table 5a. Posture A score.

Posture A Score = 1		Neck											
		1				2				3			
Legs		1	2	3	4	1	2	3	4	1	2	3	4
Torso	1	1	2	3	4	1	2	3	5	3	3	5	6
	2	2	3	4	5	3	4	5	6	4	5	6	7
	3	2	4	5	6	4	5	6	7	5	6	7	8
	4	3	5	6	7	5	6	7	8	6	7	8	9
	5	4	6	7	8	6	7	8	9	7	8	9	9

Table 5b. Posture B score.

Posture B Score = 1		Lower arm					
		1			2		
Wrist		1	2	3	1	2	3
Upper arm	1	1	2	2	1	2	3
	2	1	2	3	2	3	4
	3	3	4	5	4	5	5
	4	4	5	5	5	6	7
	5	6	7	8	7	8	8
	6	7	8	8	8	9	9

Table 5c. Total score.

Total C Score= 1		Posture B Score											
		1	2	3	4	5	6	7	8	9	10	11	12
Posture A Score	1	1	1	1	2	3	3	4	5	6	7	7	7
	2	1	2	2	3	4	4	5	6	6	7	7	8
	3	2	3	3	3	4	5	6	7	7	8	8	8
	4	3	4	4	4	5	6	7	8	8	9	9	9
	5	4	4	4	5	6	7	8	8	9	9	9	9
	6	6	6	6	7	8	8	8	8	10	10	10	10
	7	7	7	7	8	9	9	9	10	10	11	11	11
	8	8	8	8	8	9	10	10	10	10	11	11	11
	9	9	9	9	10	10	10	11	11	11	12	12	12
	10	10	10	10	11	11	11	11	12	12	12	12	12
	11	11	11	11	11	11	12	12	12	12	12	12	12
	12	12	12	12	12	12	12	12	12	12	12	12	12
Activite Score 2													
REBA Risk Score = 3													

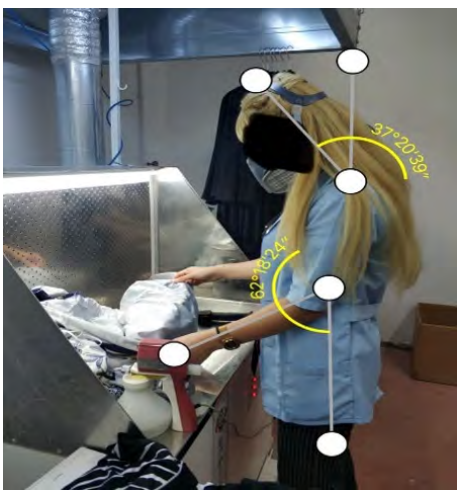

Figure 4. The task of stain removal.

Adding 2 more scores -one of which has been added as an additional 1 score due to the body parts immobilized for more than a minute or use of more than one body parts whereas the other 1 score has been added due to movements repeated for 4 times or more in a minute without walking – a total of REBA Risk Score of 4 has been calculated. That figure corresponds with a "medium risk and requires precautions" level on REBA Risk Evaluation Table.

The Task of Stain Removal

The position we will see in Fig.4 contains the worker doing the stain removal task whose certain bodily angles were approximately measured by Angle Meter software and the analysis results by REBA method have been presented in Table 4.

Table 6. REBA analysis for the task of product ironing.

Table 6a. Posture A score.

Posture A Score = 2		Neck											
		1				2				3			
Legs		1	2	3	4	1	2	3	4	1	2	3	4
Torso	1	1	2	3	4	1	2	3	5	3	3	5	6
	2	2	3	4	5	3	4	5	6	4	5	6	7
	3	2	4	5	6	4	5	6	7	5	6	7	8
	4	3	5	6	7	5	6	7	8	6	7	8	9
	5	4	6	7	8	6	7	8	9	7	8	9	9

Table 6b. Posture B score.

Posture B Score = 1		Lower arm					
		1			2		
Wrist		1	2	3	1	2	3
Upper arm	1	1	2	2	1	2	3
	2	1	2	3	2	3	4
	3	3	4	5	4	5	5
	4	4	5	5	5	6	7
	5	6	7	8	7	8	8
	6	7	8	8	8	9	9

Table 6c. Total score.

Total C Score= 4		Posture B Score											
		1	2	3	4	5	6	7	8	9	10	11	12
Posture A Score	1	1	1	1	2	3	3	4	5	6	7	7	7
	2	1	2	2	3	4	4	5	6	6	7	7	8
	3	2	3	3	3	4	5	6	7	7	8	8	8
	4	3	4	4	4	5	6	7	8	8	9	9	9
	5	4	4	4	5	6	7	8	8	9	9	9	9
	6	6	6	6	7	8	8	8	8	10	10	10	10
	7	7	7	7	8	9	9	9	10	10	11	11	11
	8	8	8	8	8	9	10	10	10	10	11	11	11
	9	9	9	9	10	10	10	11	11	11	12	12	12
	10	10	10	10	11	11	11	11	12	12	12	12	12
	11	11	11	11	11	11	12	12	12	12	12	12	12
	12	12	12	12	12	12	12	12	12	12	12	12	12
Activite Score 2													
REBA Risk Score = 6													

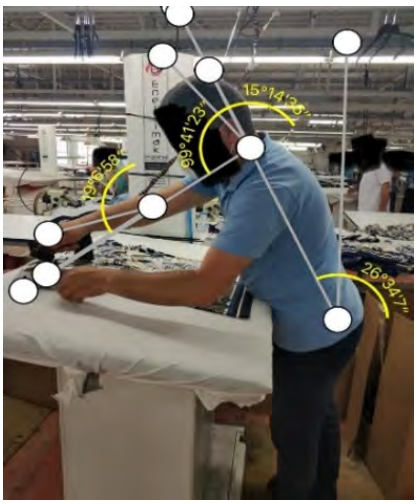

Figure 5. The task of product ironing.

The worker's neck angled at around 37° and since this value is greater than 20°, the risk score for the neck was calculated as 2°. The worker carried out the task on a straight posture and that's why the risk score was calculated as 1.For the worker stood on both her feet, the risk score was calculated as 1. As these values was calculated on REBA A Score table, the risk score was estimated as 1. Since the upper arm angle of the worker was evaluated within the 0° -20°interval, it was calculated as 1 risk score according to the calculation table.

For the worker's lower arm angle was calculated as 62°, the risk score on the table has been estimated as 1. Because the wrist working angle was less than 15°, the risk score has been calculated as 1. As these values were calculated on REBA B score table, the risk score has been estimated as 1. As REBA A and REBA B scores have been placed on

Table 7. REBA analysis for product packaging.

Table 7a. Posture A score.

Posture A Score = 2		Neck											
		1				2				3			
Legs		1	2	3	4	1	2	3	4	1	2	3	4
Torso	1	1	2	3	4	1	2	3	4	1	2	3	4
	2	1	2	3	4	1	2	3	5	3	3	5	6
	3	2	3	4	5	3	4	5	6	4	5	6	7
	4	2	4	5	6	4	5	6	7	5	6	7	8
	5	3	5	6	7	5	6	7	8	6	7	8	9

Table 7b. Posture B score.

Posture B Score = 1		Lower arm					
		1			2		
Wrist		1	2	3	1	2	3
Upper arm	1	1	2	2	1	2	3
	2	1	2	3	2	3	4
	3	3	4	5	4	5	5
	4	4	5	5	5	6	7
	5	6	7	8	7	8	8
	6	7	8	8	8	9	9

Table 7c. Total score.

Total C Score= 4		Posture B Score											
		1	2	3	4	5	6	7	8	9	10	11	12
Posture A Score	1	1	1	1	2	3	3	4	5	6	7	7	7
	2	1	2	2	3	4	4	5	6	6	7	7	8
	3	2	3	3	3	4	5	6	7	7	8	8	8
	4	3	4	4	4	5	6	7	8	8	9	9	9
	5	4	4	4	5	6	7	8	8	9	9	9	9
	6	6	6	6	7	8	8	8	8	10	10	10	10
	7	7	7	7	8	9	9	9	10	10	11	11	11
	8	8	8	8	8	9	10	10	10	10	11	11	11
	9	9	9	9	10	10	10	11	11	11	12	12	12
	10	10	10	10	11	11	11	11	12	12	12	12	12
	11	11	11	11	11	11	12	12	12	12	12	12	12
	12	12	12	12	12	12	12	12	12	12	12	12	12
Activite Score 2													
REBA Risk Score = 5													

Figure 6. The task of product ironing.

the REBA C score table, the risk score has been estimated as 1.Adding 2 more scores -one of which has been added as an additional 1 score due to the body parts immobilized for more than a minute or use of more than one body parts whereas the other 1 score has been added due to movements repeated for 4 times or more in a minute without walking – a total of REBA Risk Score of 3 has been calculated. That figure corresponds with a "low risk and may require precautions" level on REBA Risk Evaluation Table.

The Task Of Product Ironing

The position we will see in Fig.5 contains the worker doing the product ironing task whose certain bodily angles were approximately measured by Angle Meter software and the analysis results by REBA method have been presented in Table 5.The worker's neck angled at around 15°

and since this value is lower than 20°, the risk score for the neck was calculated as 1°.

The worker's torso angle was around 26° and since this value falls within 20° - 60° interval,the torso risk score has been calculated as 3 . For the worker stood on both her feet, the risk score has been calculated as 1. As these values have been calculated on REBA A Score table, the risk score has been estimated as 2. For the worker's upper arm angle was approximately calculated as 99° and because this value was greater than 90°, the risk score has been calculated as 4.

For the worker's lower arm angle was calculated as 20°, the risk score on the table has been estimated as 2. Because the wrist working angle was less than 15°, the risk score has been calculated as 1. As these values were calculated on REBA B score table, the risk score has been estimated as 5.As REBA A and REBA B scores have been placed on the REBA C score table, the risk score has been estimated as 4.

Adding 2 more scores -one of which has been added as an additional 1 score due to the body parts immobilized for more than a minute or use of more than one body parts whereas the other 1 score has been added due to movements repeated for 4 times or more in a minute without walking – a total of REBA Risk Score of 6 has been calculated. That figure corresponds with a "medium risk and requires precautions" level on REBA Risk Evaluation Table.

The Task of Product Packaging

The position we will see in Fig. 6 contains the worker folding the product for packaging task whose certain bodily angles were approximately measured by Angle Meter software and the analysis results by REBA method have been presented in Table 6.The worker's neck angled at around 0° – 20° interval and the risk score has been calculated as 1 according to the table.The worker's torso angle was calculated as around 33° and since this value falls within 20° - 60° interval, the torso risk score has been calculated as 3.For the worker stood on both her feet, the risk score has been calculated as 1.

As these values have been calculated on REBA A Score table, the risk score has been estimated as 2. For the worker's upper arm angle was approximately calculated as 77° and because this value falls within 45°-90° interval, the risk score has been calculated as 3 according to the calculation table. As the lower arm angle was calculated lower than 60°, the risk score has been considered as 2 according to the calculation table. Because the wrist working angle was less than 15o, the risk score has been estimated as 1. As these values were evaluated on the REBA B Score table, risk score has been estimated as 4. As REBA A and REBA B scores values have been placed on the REBA C score table, the risk score has been estimated as 3.

Adding 2 more scores -one of which has been added as an additional 1 score due to the body parts immobilized for more than a minute or use of more than one body parts whereas the other 1 score has been added due to movements repeated for 4 times or more in a minute without walking – a total of REBA Risk Score of 5 has been calculated. That figure corresponds with a "medium risk and requires precautions" level on REBA Risk Evaluation Table.

RESULTS AND DISCUSSION

Even though there are more than a hundred methods of risk assessment in the literature, mostly Finney Kinney or Matris methods are put into work by occupational health and safety professionals. In the chemical industries, the Hazop risk assessment method employs REBA and RULA methods to assess ergonomic posture of the workers. In the literature related to REBA and RULA ergonomic risk assessment method, studies in the fields such as construction and logistics can be found. This very study will indeed contribute to the REBA and RULA methods' applications. While other risk assessment methods calculate risks and dangers, they often tend to neglect employees' anatomical properties. Adjustment of the work to the employees-not employees' adjustment to the work- and reduction of occupational diseases are the main focus of ergonomical risk assessment.

In the study with fabric cutting saw, the REBA score was calculated as 6 and the risk level was determined as medium. The RULA risk score of the employee in the fabric sewing work was calculated as 4.The level of risk which the employee is exposed has been determined to require change. The risk to which the employee doing the quality control work is exposed was determined to be moderate, with a REBA score of 4.The risk score of the employee performing the stain removal work is 3 according to REBA. The level of risk exposure of workers is low and prevention may be required in the long term. According to the ergonomic risk analysis of the ironing employee, the REBA risk score is 6 and the risk level exposed is moderate, so it is necessary to take precautions. With a REBA score of 5, the risk level of the product packaging worker was medium.

By assessing apparel workshop employees' postures ergonomically, we can conclude the employees cutting fabric with saw, controlling the quality, doing the packaging and ironing face a medium level of danger according to the risk scores obtained and that there's the need to take precautions. It is established that the employee sewing the fabric with sewing machine faces varying levels of danger; the

stain removal employee faces a low level of danger while retaining the need to take possible precautions. According to the data obtained, having medium levels of danger doesn't necessarily mean the halt of the work. However, the muscular and skeletal diseases can be avoided in the medium or long run by taking necessary precautions.

The risks identified in the ergonomic risk analysis applied to the logistics sector by Kırcı and his colleagues indicate that there are 7 high-risk and 5 very high-risk working postures compared to those working in the textile sector, that those who do the work of pushing, pulling, lifting the load work in more dangerous jobs, and that the logistics sector is a more dangerous line of business. When the level of risks obtained as a result of the examination of the posture positions of the employees doing the cleaning work during the cleaning of outer glass and inner glass, sweeping and wiping of the floor is examined by Özay and Özcan, with the reveal of 4 medium risk 1 low risk risk levels it was determined that the risk levels of the posture positions of the employees in the textile sector with the cleaning workers are examined were close to each other [26].By examining the postures of the employees working in the ladle preparation process in the casting workshop with the Digital Human Modeling simulation in the CATIA V5 software by Erdemir and Eldem, the use of the Rapid Entire Body Assessment method which is an ergonomic risk assessment method, with the digital method, increases the accuracy of the study [5].When the studies in the literature are examined, it has been determined that the risks vary according to the basis of the work done.It has been determined that there are posture positions that include high and very high risks in the very dangerous line of business, medium and low risks in the works in the dangerous line of business, and more low risks and moderate risks in the less dangerous lines of business.

The academic study in the ergonomics will contribute to the literature by increasing the employees' performances, maintaining the safety, professional fulfillment and satisfaction by the work carried out.

ACKNOWLEDGEMENT

I would like to thank Burhan YILDIZ, the owner of Reha Tekstil A.Ş., and the friend who is an occupational health and safety expert, who helped us do this job.

CONFLICT OF INTEREST

Authors approve that to the best of their knowledge, there is not any conflict of interest or common interest with an institution/organization or a person that may affect the review process of the paper.

AUTHOR CONTRIBUTION

Senol Yavuz; planning of the study, literature review, article the writing, evaluation of the results, concept, design. Berna Gur; article writing, literature review, journal research. Ahmet Dogan CAKIR; implementation of risk analysis, data collection and processing, evaluation of results. Dursun Ali KOSE; article writing, evaluation of results, review of the article.

References

1. Bayraktaroğlu, S. İnsan Kaynakları Yönetimi, Genişletilmiş 6. Baskı, Adapazarı: Sakarya Kitabevi. 2015.
2. World Health Organization. Occupational Health a Manual for Primary Health Care Workers. World Health Organization Regional Office for the Eastern Mediterranean Cairo;. p.14-20. 2001.
3. Aktay N. İş Sağlığı ve Güvenliği Eğitimi ile İş Güvenliği Kültürü Arasındaki İlişki, İş Müfettiş Yardımcılığı Etüdü, İstanbul. 2012.
4. Akay D., Dağdeviren M., ve Kurt M., Çalışma Duruşlarının Ergonomik Analizi, Gazi Üniversitesi Mühendislik Mimarlık Fakültesi Dergisi, 18(3): 73-84. 2003.
5. Erdemir F., Eldem C., Bir döküm atölyesindeki çalışma duruşlarının dijital insan modelleme tabanlı REBA yöntemi ile ergonomik analizi, Politeknik Dergisi, 23(2): 435-443. 2020.
6. Kahraman, M. F. Ergonomik Risk Değerlendirme Yöntemlerinin Çok Ölçütlü Karar Verme Teknikleri İle Önceliklendirilmesi ve Bütünleşik Bir Model Önerisi, Gazi Üniversitesi Fen Bilimleri Enstitüsü, Yüksek Lisans Tezi. 2012.
7. Sabancı A., Sümer S., Ergonomi. Nobel Akademik Yayıncılık Yayın No:80 3. Basım ISBN:978-605-5426-79-8 Ankara. 2015.
8. Zander, J., Principles of Ergonomics, Agricultural University Wageningen. 1973.
9. Aytaç, S. ve Kaya, Ö. Ergonominin Çalışma Yaşamındaki Önemi. İş Yazıları Dergisi, Sayı: 14, S. 1-14. 2019.
10. Sağıroğlu, H., Coşkun, M. ve Erginel, N. REBA İle Bir Üretim Hattındaki İş İstasyonlarının Ergonomik Risk Analizi. Mühendislik Bilimleri ve Tasarım Dergisi, Sayı:3 (3), S. 339-345. 2015.
11. Demir, M. Konaklama İşletmelerinde Ergonominin İşgören Verimliliği Üzerine Etkileri. İş, Güç, Endüstri İlişkileri ve İnsan Kaynakları Dergisi, Sayı: 5 (2), S. 10-18. 2003.
12. Neşeli, C. Ergonomik Risk Analizi Yöntemlerinin Karşılaştırılması ve Bir Kalıp İmalat Firmasında Uygulaması. İzmir Katip Çelebi Üniversitesi. 2016.
13. Çakır, O., İnşaat İşlerinde Ergonomik Risklerin Reba, Rula ve Niosh Risk Değerlendirme Yöntemleri İle İncelenmesi, Üsküdar Üniversitesi, Sağlık Bilimleri Enstitüsü, İş Sağlığı ve Güvenliği Anabilim Dalı, Yüksek Lisans Tezi. 2019.
14. Gürler Turan, Ö. Ofis Çalışmalarında Ergonomik Risklerin İş Sağlığı Ve Güvenliği Açısından Değerlendirilmesi, İstanbul Aydın Üniversitesi Fen Bilimleri Enstitüsü İş Sağlığı ve Güvenliği Ana Bilim Dalı, Yüksek Lisans Tezi. 2016.
15. Chiasson, M. È., Imbeau, D., Aubry, K., Delisle, A. Comparing the results of eight methods used to evaluate risk factors associated with musculoskeletal disorders. International Journal of Industrial Ergonomics, 42(5), 478-488. 2012.
16. Özoğul, B., Çimen, B., Kahya, E. Bir Metal Sanayi İşletmesinde Ergonomik Risk Analizi, Journal of Engineering Sciences and Design, 6(OS: Ergonomi2017), 159 – 175. 2018.
17. Kahya, E., Gülbandılar, S., Gürleyen, E. Nöroloji Yoğun Bakım

Ünitesinde Çalışan Hemşirelerin Maruz Kaldığı Fiziksel Zorlanmaların Analizi. Ergonomi, 1(1), 39-48. 2018.
18. Çoker, İ., Selim, H.. Bir Tekstil İşletmesinde Kas İskelet Sistemi Rahatsızlıklarına Yönelik Ergonomik Risk Değerlendirme. Avrasya Sosyal ve Ekonomi Araştırmaları Dergisi, 6(5), 230-240. 2019.
19. Polat, O., Mutlu, Ö., Çakanel, H., Doğan, O., Özçetin, E., Emre, Ş. E. N. Bir Mobilya Fabrikasında Çalışan İşçilerin Çalışma Duruşlarının REBA Yöntemi İle Analizi. Mühendislik Bilimleri ve Tasarım Dergisi, 5, 263-268. 2017.
20. Şeren, T., Öz, E., Asansör Montaj İşlemlerinin Ergonomik Yönden Değerlendirilmesi, Journal of Engineering Sciences and Design, 6(ÖS: Ergonomi2017), 40-48. 2018.
21. Felekoğlu, B., Taşan, S. Ö. İş ile ilgili kas iskelet sistemi rahatsızlıklarına yönelik ergonomik risk değerlendirme: Reaktif/ proaktif bütünleşik bir sistematik yaklaşım. Journal of the Faculty of Engineering & Architecture of Gazi University, 32(3). 2017.
22. Delice, E., Ayık İ., Abidinoğlu O.N., Ciftci N. N., Sezer Y. Ergonomik Risk Değerlendirme Yontemleri ve AHP yontemi Calışma Duruşlarının Analizi: Ağır Ve Tehlikeli İşler icin Bir Uygulama, Journal of Engineering Sciences and Design, 6(OS: Ergonomi2017), 112-124. 2018.
23. Aydın, F., Çidem, Ç., Kahya, E. Kabin Üretimi Yapan Bir İşletmenin Kaynak Atölyesinde İş Sağlığı Ve Güvenliği Risk Değerlendirmesi. Ergonomi, 1(3), 137-147. 2018
24. Yavuz, Ş., Çakır, A., D., Gür, B. Hazir Giyim Atölyesinde Çalışanların Duruşlarının Ergonomik Açıdan İncelenmesi, 6.Uluslararası İş Güvenliği ve Çalışan Sağlığı Kongresi, 26-27 Kasım, İstanbul, 134-134, 2020.
25. Kirci, B.K., Özay, M. E., Uçan, R.,A Case Study in Ergonomics by Using REBA, RULA and NIOSH Methods: Logistics Warehouse Sector in Turkey, Hittite Journal of Science and Engineering, 2020, 7 (4) 257–264. DOI: 10.17350/HJSE19030000194, 2020.
26. Özay, E. M, Özcan, G., Temizlik Çalışanlarının Çalışma Duruş Pozisyonlarının REBA Yöntemi ile Ergonomik Açıdan İncelenmesi. Çanakkale Onsekiz Mart Üniversitesi Fen Bilimleri Enstitüsü Dergisi, 6 (1) , 122-132. DOI: 10.28979/comufbed.638149, 2020.

Hittite Journal of Science and Engineering, 2021, 8 (2) 161–169
ISSN NUMBER: 2148–4171
DOI: 10.17350/HJSE19030000226

Modification of ΔlogR method and Nonlinear Regression Application for Total Organic Carbon Content Estimation from Well Logs

Can Polat[1] **Tuna Eren**[2]
[1]Izmir Katip Celebi University, Department of Petroleum and Natural Gas Engineering, Izmir, Turkey
[2]Eni International Resources Limited, Ankara, Turkey

ABSTRACT

ΔlogR method is one of the most widely utilized techniques for estimation of Total Organic Carbon (TOC) content form well logs. The traditional ΔlogR method reveals the assumption of linear relationship between logarithmic resistivity and porosity log. In this study, the method is modified by means of integral calculus to acquire the actual trend between logarithmic resistivity and porosity log. Furthermore, unlike to the traditional method, the maturity is additionally represented with logarithm of organic maturation temperature. Nonlinear regression is applied to optimize the unclear organized parameters required for computation of TOC content. The final forms of the equations are observed to be appropriate for the nonlinear regression application. The TOC estimations are observed to be improved with the modified versions in case traditional methods are unsatisfactory due to the related assumption expressed above. With the introduced methodology the TOC of unconventional reservoirs and source rocks can be more accurately calculated.

Article History:
Received: 2021/03/08
Accepted: 2021/06/22
Online: 2021/06/30

***Correspondence to**: Can Polat, Izmir Katip Celebi University, Department of Petroleum and Natural Gas Engineering, Izmir, Turkey*
E-mail: can.polat@ikcu.edu.tr;
Phone: +90 505 737 6766.

Keywords: Total organic carbon, Well logs, ΔlogR method, Nonlinear regression, Unconventional resources

INTRODUCTION

Recent studies reveal that unconventional resources are gaining importance with the developments in the utilization of these resources. The unconventional reservoirs are handled in terms of their hydrocarbons in place with the calculation methodologies valid for petroleum systems [1]. These formations are mostly tiny grained, rich in total organic content and are sedimentary rocks [2]. The formations of unconventional reservoirs are usually made up of shales and alike rocks. Total Organic Carbon (TOC) is a term that is a property used to determine whether such formations can be economically viable or not [3]. For instance, the gas content in formations is found to have a linear relationship with the TOC [4]. Generally speaking, Total Organic Carbon (TOC) content value that is higher than 2.0 wt% is an important aspect in turning shale gas resources into a reservoir [5]. Ahmed and Meehan in their study stated that production performance of unconventional wells is highly dependent on the accurate placement of the horizontal wells and application of the correct fracture stages in the reservoir intervals with high rock quality properties and prolific production capability [6]. However, the significance of reservoir's fracture capability and as important as this the well placement into the highest total organic content zone is not comprehended as required. Therefore, the TOC estimation is a very important aspect to be taken into consideration for successful unconventional campaign reinstatements.

In source rocks, organic carbon is present in kerogen, bitumen and hydrocarbons [7]. Kerogen maturation brings the generation of oil and gas in the source rock. TOC determination is essential for proper evaluation of both unconventional reservoirs and source rocks. The possibility of generation of sufficient quantity of oil and gas increases with TOC content. According to Thomas, the weight percentage of the organic carbon in the source rock should be at least 0.5 wt% to regard the rock as a fair source rock from the point of potentiality in generating hydrocarbons [8]. Besides, with kerogen maturation the carbon concentration rises [1].

According to Steiner et al., TOC from a core sample can be determined mainly in two ways [7]. In the first

procedure (LECO-based measurement), the inorganic carbon is removed by acidification, and the remaining organic carbon is detected by carbon analyzer by means of combusting the organic carbon to CO2. In the second procedure (Rock-Eval method), a pulverized rock sample is subject to step-wise pyrolysis temperature rise. Perpetual monitoring of CO2 and CO during pyrolysis and oxidation make it possible to differentiate between organic and inorganic carbon oxides. The loss of some hydrocarbons in consequence of drying and washing process is the disadvantageous point of the first method. Reliance on the assumption that the weight percent of carbon in hydrocarbon is 0.83 and inability to discern the origin of CO and CO2 in case of overlapping related to pyrolysis and oxidation are the negative sides of the second procedure. It is possible to acquire accurate TOC estimations by means of these measurement techniques. However, the stated TOC estimations are time consuming and costly [9].

One of the most common methods to determine TOC is the use of logging data that belongs to the reservoir interval [10]. The advantage point in using well logs is that they provide continuance in TOC content estimation. Resistivity logs being indicators for hydrocarbons in the pore spaces can be evaluated with porosity logs that can be utilized to reveal the kerogen existence. One of the early research works in relation to that is the study conducted by Passey et al. [11]. In their study they proposed a practical method known as ΔLogR method, in which they used the well log data to identify the TOC in organic rich rocks. The method involves the process of overlapping the resistivity log displayed on a logarithmic scale with one of the porosity logs to reveal the baseline corresponding to nil carbon content. TOC is estimated based on the departures from this baseline. Besides, uranium content deducted from natural gamma spectroscopy can be indicative for TOC. Uranium content is evaluated with thorium or potassium content to develop correlations for TOC estimation [10]. It is also proved that the density log can be properly correlated with TOC [10]. Furthermore, in their study Decker et al. stated that rig site gas content measurements are proven to be more effective through density log measurements to quantify the gas content of the shale intervals [12].

The ΔLogR method is a practical and commonly utilized method to estimate TOC content. Based on the range of the training data, the traditional approach in ΔLogR method may yield considerably improper estimates of TOC for some intervals. This study involves the modification of the traditional formulation. The modified method is utilized with the intend of improving the estimation where traditional method fails due to the reason mentioned above.

Unconventional resource exploration is gaining utmost importance globally. TOC is a terminology which is the very starting point for the determination of whether such resources are economically viable or not. For this reason, one of the most significant contributions of present study is to reveal the TOC content of the unconventional resources utilizing the methodologies by means of making use of the well logs is introduced in the scope of this research work. The present research study is also important for its capability to test the source rocks' potentiality to generate hydrocarbons.

METHODS

Traditional Formulation

The resistivity and porosity curves in the log interval corresponding to the zone free of organic matter can be coincided by scaling the porosity curve. The line passing through the coincided curves located in the interval corresponding to the zone free of organic matter is known as baseline. The magnitude of departure of resistivity and porosity curves from the baseline and the determined level of organic maturity provides the total organic carbon [11] (Eq. (1) and Eq. (2)).

$$TOC = \Delta \log R \times 10^{(a+b\times LOM)} \tag{1}$$

ΔlogR can be expressed as the log of the difference between the resistivity reading from the log and the resistivity value obtained by means of the curve passing through baseline resistivity and transit time values with a slope of p (Eq. (2)). Here, difference in transit time is multiplied by a factor p to reveal the equivalent difference in terms of logarithm of resistivity. In this method, linear relationship between logarithmic resistivity and porosity log is assumed. Actually, the relationship is not strongly linear. The validity of the assumption depends on the range of the porosity log. The departures from the linearity may lead to requirement of checking the validity of this assumption.

$$\Delta \log R = \log_{10}\left(R/R_l\right) + p\times\left(\Delta t - \Delta t_l\right) \tag{2}$$

The extended form of Eq. (1) is as follows

$$TOC = \Delta \log\left(R\right) + a_1\times\left(\Delta t - a_2\right)\times 10^{(a_3+a_4\times LOM)} \tag{3}$$

where

$$a_1 = p \tag{4}$$

$$a_2 = \Delta t_l + \log_{10}\left(R_l\right)/p \tag{5}$$

R, Δt, R_l, $Δt_l$ and *LOM* denote the resistivity, and transit time readings on the corresponding logs, resistivity and transit time reading on the baseline, and level of organic maturity, respectively.

In this study, the parameters a_1, a_2, a_3 and a_4 were optimized by means of application of the Levenberg–Marquardt algorithm [13] [14].

Modified Version

A more proper relationship can be obtained with the help of Archie equation [15] (Eq. (6)) which associates the resistivity of the brine saturated rock to the porosity.

$$R_o = R_w / \phi^m \tag{6}$$

The porosity can be expressed as a function of transit time. The resultant equation is:

$$R_o = R_w \Big/ \left[\left(\Delta t - \Delta t_m \right) \Big/ \left(\Delta t_f - \Delta t_m \right) \right]^m \tag{7}$$

Δt_m, Δt_f, R_w, R_o and m represent transit time of matrix and fluid (brine) in the pores, resistivity of the brine, and the brine saturated zone and cementation exponent of the rock, respectively.

Eq. (7) can be utilized to calculate the resistivity for the sample free from organic matter at the considered transit time. Taking the logarithm of both sides in Eq. (7), and derivative with respect the transit time, gives the following equations (Eq. (8) and Eq. (9))

$$\log_{10} R_o = \log_{10} \left\{ R_w \Big/ \left[\left(\Delta t - \Delta t_m \right) \Big/ \left(\Delta t_f - \Delta t_m \right) \right]^m \right\} \tag{8}$$

$$\frac{d \log_{10} R_o}{d \Delta t} = -\frac{1}{\ln 10} \frac{m}{\Delta t - \Delta t_m} \tag{9}$$

Eq. (9) can be used to compute the slope of the curve at the considered transit time. In the study of Wang et al., p in Eq. (2) is replaced with the expression on the right hand side of Eq. (9) to avoid the dependency on the assumption of linear relationship [16]. However, this approach may cause excessive magnitudes for the slope term and negative ΔlogR values accordingly. A proper relationship between logarithmic resistivity and transit time can be obtained by taking the integral of both sides in Eq. (9). The starting points of the integral are logarithmic resistivity and transit time readings corresponding to the baseline.

$$\int_{\log_{10} R_l}^{\log_{10} R_o} d \log_{10} R_o = \int_{\Delta t_l}^{\Delta t} -\frac{1}{\ln 10} \frac{m}{\Delta t - \Delta t_m} \Delta t \tag{10}$$

which gives

$$\log_{10} R_o = \log_{10} R_l - \frac{m}{\ln 10} \ln \left(\frac{\Delta t - \Delta t_m}{\Delta t_l - \Delta t_m} \right) \tag{11}$$

Ro in Eq. (10) can be considered as the resistivity of the sample free from organic matter. The magnitude of ΔlogR can be obtained subtracting logarithm of this value from the logarithm of resistivity value obtained from the well log.

$$\Delta \log R = \log_{10} R - \log_{10} R_o \tag{12}$$

Combination of Eq. (11) and Eq. (12) leads to the following equation

$$\Delta \log R = \log_{10} \left(R / R_l \right) + \frac{m}{\ln 10} \ln \left(\frac{\Delta t - \Delta t_m}{\Delta t_l - \Delta t_m} \right) \tag{13}$$

According to traditional formulation [11], TOC can be obtained using the Eq. (1) also given below

$$TOC = \Delta \log R \times 10^{(a + b \times LOM)} \tag{1}$$

Due to the lack of measurement of thermal maturity in the form of LOM, Wag et al. proposed using T_{max} instead of LOM in Eq. (1) [16]. Then, equation for TOC has the following form

$$TOC = \Delta \log R \times 10^{(a + b \times T_{\max})} \tag{14}$$

Note that the formulation presented by Wang et al. involves gamma ray values incorporated into within the ΔlogR equation and is expressed as follows.

$$TOC = \left(a \Delta \log R + b \left(GR - GR_l \right) \right) \times 10^{(c + d \times T_{\max})} \tag{15}$$

Where GR and GR_l denote gamma ray and base line gamma ray readings, respectively. The unknown parameters *a, b, c* and *d* are to be optimized.

Utilization of Eq. (14) brought problems related to Jacobian matrix in the application nonlinear regression. The problem can be solved by using logarithm of T_{max} instead of T_{max} in Eq. (14). Utilization of Tmax instead of LOM requires somewhat strong linear relationship between T_{max} and LOM. Indeed, it was observed that the strength of the linear relationship was preserved in logical intervals of T_{max} (410-510 °C) and LOM (0-20) in case of using logarithm of T_{max} instead of T_{max}. Hence, the following equation is used to compute TOC in the absence of LOM values.

$$TOC = \Delta \log R \times 10^{(a + b \times \log_{10}(T_{\max}))} \tag{16}$$

The simplified form is as follows

$$TOC = \Delta \log R \times 10^{a} T_{\max}{}^{b} \tag{17}$$

The final form is as follows

$$TOC = \left[\Delta \log \left(R \right) + \frac{m}{\ln 10} \ln \left(\Delta t - a_1 \right) - a_2 \right] \times 10^{a_3} T_{\max}{}^{a_4} \tag{18}$$

Or

$$TOC = \left[\Delta \log \left(R \right) + \frac{m}{\ln 10} \ln \left(\Delta t - a_1 \right) - a_2 \right] \times 10^{(a_3 + a_4 \times LOM)} \tag{19}$$

Where

$$a_1 = \Delta t_m \tag{20}$$

$$a_2 = \frac{m}{\ln 10} \ln \left(\Delta t_l - \Delta t_m \right) + \log_{10} R_l \tag{21}$$

In this study, the parameters a_1, a_2, a_3 and a_4 were optimized by means of application of the Levenberg–Marquardt algorithm.

A specific interval can be considered to specify transit time and resistivity corresponding to the baseline and matrix transit time. The magnitude of these parameters can vary considerably based on the alteration in mineral composition. Hence, it is a more favorable approach to group them into one parameter for optimization rather than evaluating them explicitly. Different from those, the cementation exponent (m) is not tried to be optimized as optimization process yields unrealistic m values. Rather, this parameter is evaluated explicitly. In this context, different logical cementation exponent values were tried and corresponding results were compared.

Combination of ΔlogR with other methods might be considered for improving estimation of TOC similar to the procedure presented in the study of Wang et al. [16]. It should be checked whether the developed formulation is appropriate for nonlinear regression application. It was observed that the formulations utilized in this study were inappropriate for nonlinear regression application in case it involved additional unknown parameters. This study basically focuses on the improvement of the traditional ΔlogR method.

Density and neutron readings can be alternative to sonic readings for TOC estimation. In fact, sonic readings are more preferable since these readings are less adversely affected from improper hole conditions [11]. Therefore, sonic readings were evaluated to estimate the TOC in this study.

Levenberg–Marquardt algorithm for Nonlinear Regression

The related tool of Matlab software was utilized for nonlinear regression application. As a default, the tool utilizes Levenberg-Marquardt (LM) algorithm, a standard method for non-linear least squares problems. The algorithm takes advantage of steepest descent method or Gauss-Newton method based on the value of the damping factor. In case the algorithm tends to behave more like steepest descent method in relation to the reduced damping factor, its converge speed is slow but improvement in minimization is more guaranteed. Improvement in minimization leads to increase in the damping factor and the similarity to Gauss-Newton method and converge speed is advanced as a result [17]. Note that the initial values of the LM parameters are calculated using the related equations involving one or more of estimated baseline transit time and resistivity, matrix transit time, cementation factor, the slope, and initial values are kept constant.

In the regression process, the target is to minimize the following summation

$$\sum_{i=1}^{m}\left[y_i - f\left(x_i,\beta\right)\right]^2 \tag{22}$$

Where y_i, $f(x_i,\beta)$, β represent the targeted (measured) and calculated resultant parameters, and parameter set to be optimized, respectively.

One of the following equations is used to compute the parameter vector δ to be added to vector β to update it at each iteration [18].

$$\left(J^T J + \lambda I\right)\delta = J^T\left[y - f\left(\beta\right)\right] \tag{23}$$

$$\left(J^T J + \lambda diag\left(J^T J\right)\right)\delta = J^T\left[y - f\left(\beta\right)\right] \tag{24}$$

I in Eq. (23) is the identity matrix. In the study of Fletcher, I was replaced with the diagonal matrix comprised of the diagonal elements of J^TJ to improve the converge [19]. J is the Jacobian matrix and expressed as follows:

$$J_i = \frac{\partial f\left(x_i,\beta\right)}{\partial \beta} \tag{25}$$

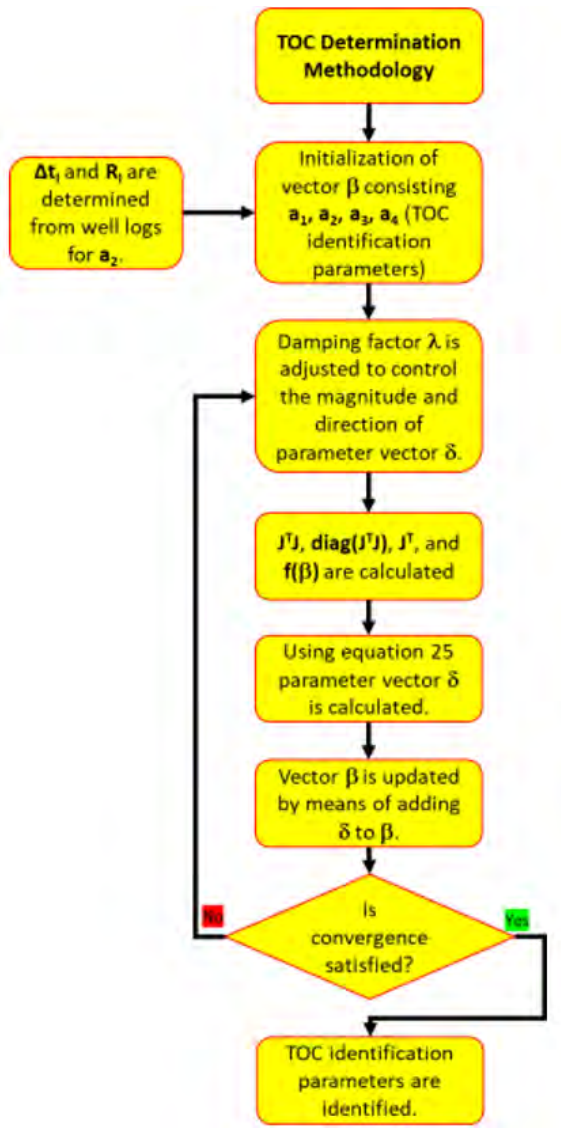

Figure 1. Methodology for Levenberg–Marquardt algorithm.

Iterative calculation is required to optimize the parameters. At each iteration, Eq. (24) is computed for δ. J^TJ, the diagonal elements of J^TJ and $f(\beta)$ are computed using the latest vector β. The vector β is updated at each iteration with the addition of new δ. The damping factor λ is adjusted at each iteration to control the direction and magnitude of δ (Fig. 1).

The algorithm detects a local minimum which might not be the global minimum. The initial value of the parameters to be optimized should be determined in a way to guarantee the global minimum. In accordance with this purpose, transit time and resistivity readings corresponding to the estimated baseline can be taken as initial values. Matrix transit times are available for different rock types. Mineral composition of the rocks can be determined to figure out the distribution of the matrix transit times. Based on these observations, a proper initial value for matrix transit time can be specified. Passey et al. in their study proposes values for a_1 and a_3, and a_4 in Eq. (3) [11]. These values might be taken as initial values. Apart from these, specification of proper initial values is achieved by means of trial-and-error method.

RESULTS AND DISCUSSION

Fig. 2-3 show the measured TOC values, and the TOC values as a result of application of traditional formulation and modified version with respect to depth for different wells. The measured values shown in Fig. 2 and Fig. 3 were obtained from the study of Passey et al. and Wang et al., respectively [11] [16]. Here, Passey's formulation denotes the traditional approach involving the utilization of Eq. (1) or Eq. (14) depending on the representation for maturity. The parameters were optimized using the measured TOC values corresponding to Well-A1 and Well-A2 for the first formation while all the available measured TOC values are utilized for parameter optimization for the second formation due to considerable departure from the measured TOC values in some intervals (Well-C2 and Well-D2). The modified and traditional formulations involve utilization of LOM (Eq. (18)) and T_{max} (Eq. (17)) values for the first and second formations, respectively.

In Fig. 2, the well that is highly categorized to possess reservoir potential is "Well-A1". For other wells the reservoir potentiality is varying among each other throughout the depth intervals, for example, for well "Well-C1", the lower interval is observed to have a high reservoir potentiality.

As it is observed in Fig. 3, for "Well-A2", the interval in between 1135-1155 m is considered to possess strong reservoir properties from the TOC potential standing point of view. The rest of the wells are noted to have varying TOC potential in reference to each other, and can be categorized to be marginally possessing reservoir potentiality.

Table 1 and Table 2 show the tried cementation exponents (m) and the corresponding optimized parameter values and root mean square errors (RMSE), normalized root mean square errors (NRMSE) and Pearson correlation coefficient (r). Implementation of the nonlinear regression yields the a_2 values in the 5th column while a_2 values in the 6th column are obtained solving the Eq. (21) with $t_m(a_1)$, t_l and Rl values in the 2th, 3th and 4th columns, respectively. The a_2 values in the 5th and 6th columns are compared in order to check the accuracy of the t_l and R_l combination estimated based on the corresponding readings from well logs. Table 3 and Table 4 show the mean and standard deviation of resistivity and transit time values for each well.

Table 1. The tried cementation exponents (m) and the corresponding optimized parameter values, root mean square errors (RMSE), normalized root mean square errors (NRMSE) and Pearson correlation coefficient (r) for the first formation.

m	$t_m(a_1)$	t_l	R_l	a_2	a_2	a_3	a_4	RMSE	NRMSE	r
1.40	68.353	99	0.7	1.905	1.926	2.633	-0.234	1.419	0.266	0.897
1.80	60.172	99	0.7	2.693	2.706	2.478	-0.212	1.283	0.241	0.912
2.00	55.869	99	0.7	3.104	3.115	2.423	-0.204	1.258	0.236	0.915
2.40	46.988	99	0.7	3.955	3.964	2.340	-0.193	1.244	0.233	0.916
3.00	33.236	99	0.7	5.291	5.299	2.258	-0.181	1.254	0.235	0.916
4.00	9.701	99	0.7	7.641	7.648	2.179	-0.170	1.285	0.241	0.914
					Passey's:	2.237	-0.179	1.326	0.249	0.913

Table 2. The tried cementation exponents (m) and the corresponding optimized parameter values, root mean square errors (RMSE), normalized root mean square errors (NRMSE) and Pearson correlation coefficient (r) for the second formation.

m	$t_m(a_2)$	t_l	R_l	a_2	a_2	a_3	a_4	RMSE	NRMSE	r
1.40	49.553	61	10	2.482	2.482	43.348	-16.217	1.658	0.435	0.796
1.80	47.265	61	10	3.055	3.048	41.582	-15.557	1.616	0.424	0.808
2.00	46.036	61	10	3.355	3.350	40.902	-15.305	1.604	0.421	0.812
2.40	43.471	61	10	3.982	3.985	39.841	-14.911	1.587	0.416	0.816
3.00	39.456	61	10	4.981	5.000	38.746	-14.506	1.575	0.413	0.819
4.00	32.497	61	10	6.773	6.820	37.637	-14.098	1.566	0.411	0.821
					Passey's:	34.670	-13.012	1.569	0.411	0.820

Table 3. The mean and standard deviation of resistivity and transit time values for the first formation.

	Well-A1	Well-B1	Well-C1	Well-D1	Well-E1
Mean(Δt)	127.083	104.900	88.286	103.550	98.133
Standard Deviation (Δt)	10.210	9.586	11.164	16.311	9.824
Mean (R)	0.793	3.044	16.366	3.378	3.348
Standard Deviation (R)	0.172	0.891	16.549	1.368	1.965

Table 4. The mean and standard deviation of resistivity and transit time values for the second formation.

	Well-A2	Well-B2	Well-C2	Well-D2	Well-E2
Mean(Δt)	78.553	89.530	64.937	67.276	74.730
Standard Deviation (Δt)	13.563	1.975	6.170	4.022	2.805
Mean(R)	19.269	6.308	99.385	13.690	87.037
Standard Deviation (R)	10.794	1.281	22.114	5.139	58.241

As can be seen from the Table 1 and Table 2, altering the m value does cause very little changes in the RMSE and NRMSE values. Actually, the main affected parameter

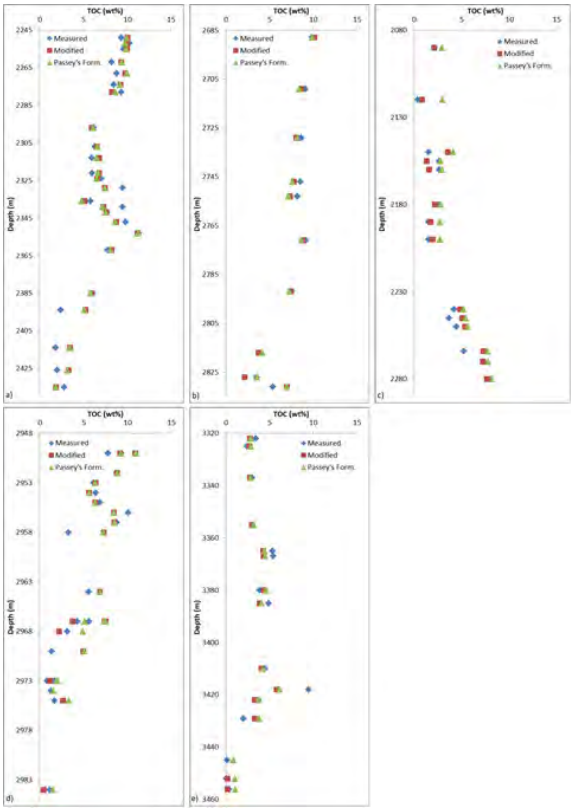

Figure 2. Comparison of the measured TOC values with the TOC values computed using modified version and traditional formulation for a) Well-A1, b) Well-B1, c) Well-C1, d) Well-D1, e) Well-E1.

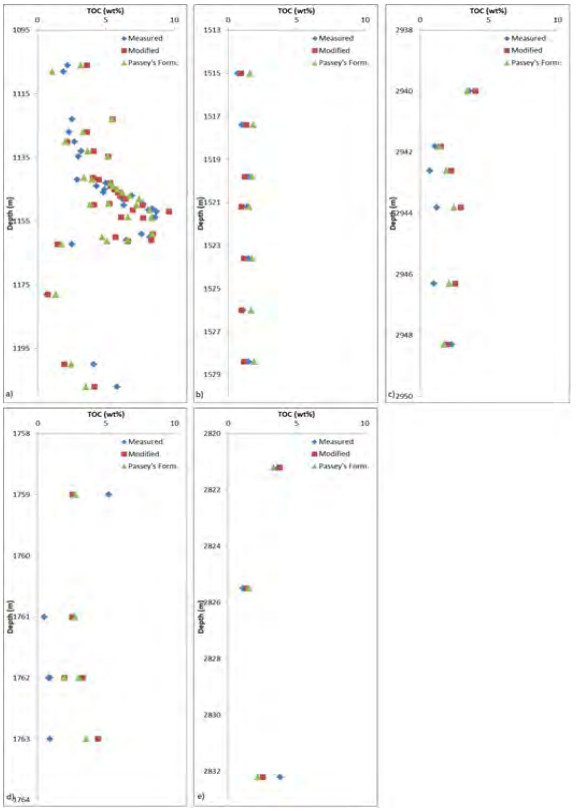

Figure 3. Comparison of the measured TOC values with the TOC values computed using modified version and traditional formulation for a) Well-A2, b) Well-B2, c) Well-C2, d) Well-D2, e) Well-E2.

is matrix transit time. Hence, an appropriate cementation exponent and matrix transit time combination is to be selected based on RMSE or NMRSE values and the previous observations. Cementation exponent of 2.4 and 2 and the corresponding optimized values were selected to calculate TOC in the first and second formations, respectively. The transit time values are close to the calculated transit time based on the mineral composition of shale in the study of Wang et al. [16], and the values of the determined cementation exponents are close to the generally observed cementation exponent values (around 2). On this respect, it can be asserted that the determined combinations satisfy the expectations. Note that the selected cementation exponent and transit time combination for the first formation yields the lowest RMSE and NRMSE values among the tried combinations.

Comparison of the a_2 values in the 5th and 6th columns reveals that the optimized a_2 values shown the 5th column of the Table 1 and Table 2 can be attained with the single baseline transit time and resistivity combination which is also consistent to the combination to be obtained with the help of well logs.

In the study of Passey et al. [11], the logarithm of resistivity is plotted against sonic transit time using the sonic porosity relationship proposed by Magara [20] and the boundaries are marked on the plot. It is observed the best line (drawn to fit the curve to form a linearship between the logarithm of resistivity and transit time as a requirement of Passey's method) deviates from the plot basically in the range of 70-90 μsec/ft. In this study, the same types of plots are constructed for the two formations considered. In Fig. 4, the straight line corresponding to traditional formulation is coincided with the actual curve corresponding to modified version close baseline transit time and logarithmic resistivity. Note that actual curve is formed by means of Archie equation (Eq. (7)) and rectangular markers indicate the transit time values (training values) used in the optimization process. As it can be seen from Fig. 4, the best line deviates from the actual curve basically below 90 μsec/ft for the first formation. This range basically is compatible with the range for Well-C1 (Table 3). It is seen that, for well-C1, the modified version generally yields better match with the measured TOC values (Fig. 2) and results in smaller RMSE value in comparison to traditional formulation. RMSE is calculated as 1.034 (r = 0.910) and 1.436 (r = 0.914) by means of the application of the modified version and traditional formulation, respectively. For the second formation, the difference between the slopes of the curves is highly low between 60-70 μsec/ft (Fig. 5). To increase the difference, only the values corresponding to the transit time values higher

than 70 μsec/ft were utilized for optimization. The resultant plot is shown in Fig. 6. Note that the straight line deviates considerably from the actual curve between 60-70 μsec/ft different from the previous case. This range is basically compatible with the range for Well-C2 and Well-D2 (Table 4). The deviation actually reflects on the calculated TOC values for Well-C2 and Well-D2 in favor of the modified version as expected. In this case, RMSE is calculated as 1.790 (r = 0.218) and 2.306 (r = -0.0186) by means of the modified version and traditional formulation, respectively. Note that previous values are 1.879 (r = 0.133) and 1.616 (r = 0.260) for the modified version and traditional formulation, respectively. Furthermore, it should be noted that the estimation of TOC contents for the intervals corresponding to the transit times above 70 μsec/ft were not considered for improvement although the straight line considerably deviates from the actual curve above 70 μsec/ft. This is related to the result of the optimization method, which reveals that relationship between logarithmic resistivity and transit time is not significant in that interval. These comparisons illustrate the significance of utilization of the modified version to achieve better results for the intervals where the validity of the assumption about linearity is not satisfactory.

Passey et al. in their study emphasize the effect of clay minerals on the resistivity of the formations apart from the effect of porosity [11]. They apply Waxman-Smith equation to realize the effect of clay minerals on the relationship between logarithm of resistivity and sonic transit time. It is proved that the clay minerals lowers the resistivity of the rocks however the curves plotted for different clay concentrations are shown to be almost parallel to each other, that is to say these curves have almost same slopes. Beside this, the effect of igneous rocks and salty zones on the resistivity log should be considered [11]. Invariance of the curve slopes in consideration of change in mineral composition being valid, the modified version requires basically the accurate determination of the resistivity and transit time values corresponding to the baseline. Considerable deviations from the measured TOC values are especially observed for Well-C2 and Well-D2 for the second formation. Whether these deviations stem from the measurement errors is indefinite.

The comparison with the measured TOC and the calculated RMSE values prove the accuracy of the modified versions. It is advisable to utilize the traditional formulation with the modified version to detect the deviations of the linear curve from the actual curve, which stem from the assumption of linear relationship between logarithm of resistivity and transit time in the traditional approach. The results indicate that better estimation of TOC can be made utilizing the modified version for these sections lack of training. The magnitude of resistivity and transit time corresponding to the baseline vary depending on the mineral composition

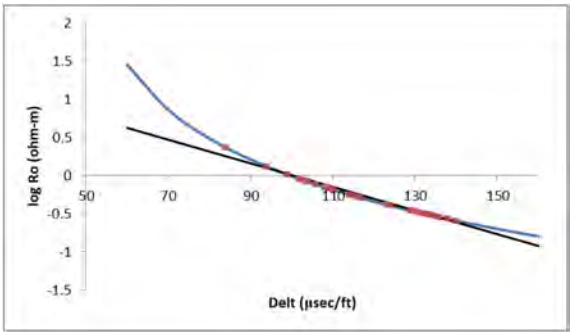

Figure 4. The comparison of the actual curve based on the Archie equation and the straight line corresponding to traditional formulation for the first formation.

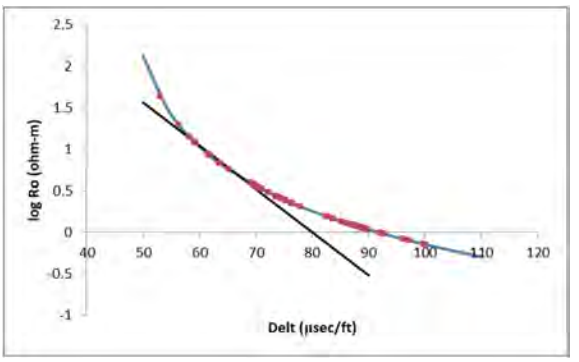

Figure 5. The comparison of the actual curve based on the Archie equation and the straight line corresponding to traditional formulation for the second formation as a result of first trial.

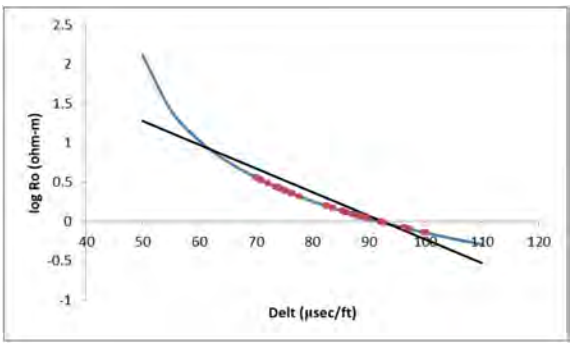

Figure 6. The comparison of the actual curve based on the Archie equation and the straight line corresponding to traditional formulation for the second formation as a result of second trial.

of the matrix. To enhance the solution in this case, the intervals should be partitioned and matched based on the baseline resistivity and transit time values and regression should be applied for each partitioned interval group. By this way, each interval group will correspond to specific optimized parameters. Sufficient data should be provided to perform this methodology properly.

The change in porosity is another factor to be accounted for. The effect of increase in porosity is similar to the effect of increase in TOC in mature source rock [11]. Hence, it may be hard to distinguish these two effects. Utilizing

the measured porosity values can be helpful in this case. On the contrary, the effect of decrease in porosity can be easily distinguishable with increase in resistivity and reduction in transit time.

CONCLUSION

This study involves the modification of the traditional approach to enhance TOC estimation. The modified formulations are observed to be appropriate for the non-linear regression application. The comparison with the measured TOC and the calculated RMSE values prove the accuracy of the modified versions. The comparisons illustrate the significance of utilization of the modified version to achieve better results for the intervals where the validity of the assumption of linear relationship between logarithmic resistivity and sonic transit time is not satisfactory. It is advisable to utilize the traditional formulation with the modified version to detect the deviations which stem from this assumption. With the methodology presented in this research work the TOC of unconventional reservoirs and source rocks can be more accurately calculated.

ACKNOWLEDGEMENTS

In this study, the related tool of Matlab software was utilized for nonlinear regression application. Authors are thankful to the corresponding author's faculty for providing the academic version of the Matlab software.

NOMENCLATURE

Δ_t = sonic transit time on the logs, μsec/ft
Δ_{tf} = sonic transit time of fluid, μsec/ft
Δ_{tl}= sonic transit time on the baseline, μsec/ft
Δ_{tm} = sonic transit time of matrix, μsec/ft
a = parameter to be optimized
a_1 = parameter to be optimized
a_2 = parameter to be optimized
a_3 = parameter to be optimized
a_4 = parameter to be optimized
b = parameter to be optimized
c = parameter to be optimized
d = parameter to be optimized
GR_l = base line gamma ray log, API Unit
GR = gamma ram log, API Unit
J = jacobian matrix
J^T = transpose of jacobian matric
LOM = level of organic maturity
m = cementation exponent of the rock
p = slope
r= Pearson correlation coefficient
R = resistivity log, ohm-m
R_l = resistivity reading on the baseline, ohm-m
R_o = resistivity of the brine saturated zone, ohm-m
R_w = resistivity of the brine, ohm-m
T_{max} = maximum pyrolysis temperature, °C
TOC = total organic carbon content, wt%
x = input function data
y = measured parameter

Greek:

λ = damping factor
ϕ = porosity, fraction
δ = vector to update β
β = parameter to be optimized

CONFLICT OF INTEREST

Authors approve that to the best of their knowledge, there is not any conflict of interest or common interest with an institution/organization or a person that may affect the review process of the paper.

AUTHOR CONTRIBUTION

Can Polat and Tuna Eren: Conceptualization, Methodology, Software. Can Polat: Data Curation, Writing- Original Draft Preparation. Can Polat and Tuna Eren: Visualization, Investigation. Can Polat: Supervision. Can Polat and Tuna Eren: Writing- Reviewing and Editing.

References

1. Ma YZ, Holditch SA. Unconventional Oil and Gas Resources Handbook: Evaluation and Development. Gulf Professional Publishing, USA, 2015.
2. Tuft AL. Unconventional Oil and Shale Gas: Growth, Extraction, and Water Management Issues (Energy Science, Engineering and Technology). Nova Science Pub Inc, UK, 2015.
3. Mahmood MF, Ahmad Z, Ehsan M. Total Organic Carbon Content and Total Porosity Estimation in Unconventional Resource Play Using Integrated Approach Through Seismic Inversion and Well Logs Analysis within the Talhar Shale, Pakistan. Journal of Natural Gas Science and Engineering 52 (2018) 13–24.
4. Edward D, Holstein E. Petroleum Engineering Handbook – Volume V: Reservoir Engineering and Petrophysics. Society of Petroleum Engineers, Richardson, Texas, 2007.
5. Zou C. Unconventional Petroleum Geology, second ed. Elsevier Inc, USA, 2017.
6. Ahmed U, Meehan DN. Unconventional Oil and Gas Resources: Exploitation and Development Gulf Professional Publishing, USA, 2016.
7. Steiner S, Ahsan SA, Raina I, Dasgupta S, Lis GP. Interpreting Total Organic Carbon TOC in Source Rock Oil Plays. Paper presented at the Abu Dhabi International Petroleum

Exhibition & Conference, Abu Dhabi, UAE, 7–10 November, SPE, pp. 1–18, 2016.
8. Thomas BM. Geochemical Analysis of Hydrocarbon Occurrences in Northern Perth Basin, Australia. American Association of Petroleum Geologists Bulletin 63 (1979) 1092–1107.
9. Mahmoud A, Elkatatny S, Mahmoud M, Abouelresh M, Abdulraheem A, Ali A. Determination of the Total Organic Carbon (TOC) Based on Conventional Well Logs Using Artificial Neural Network. International Journal Coal Geology 179 (2017) 72–80.
10. Huang R, Wang Y, Cheng S, Liu S, Cheng L. Selection of Logging–Based TOC Calculation Methods for Shale Reservoirs: A Case Study of the Jiaoshiba Shale Gas Field in the Sichuan Basin. Natural Gas Industry B 2 (2015) 155–161.
11. Passey QR, Creaney S, Kulla JB, Moretti FJ, Stroud JD. A Practical Model for Organic Richness from Porosity and Resistivity Logs. American Association of Petroleum Geologists Bulletin 74 (1990) 1777–1794.
12. Decker AD, Hill DG, Wicks DE. Log–based Gas Content and Resource Estimates for the Antrim Shale, Michigan Basin. Paper presented at the Low Permeability Reservoirs Symposium, Denver, Colorado, 26–28 April, SPE, pp. 659–669, 1993.
13. Levenberg K. A Method for the Solution of Certain Problems in Least Squares. Quarterly of Applied Mathematics 2 (1944) 164–168.
14. Marquardt D. An Algorithm for Least–Squares Estimation of Nonlinear Parameters. SIAM Journal on Applied Mathematics 11 (1963) 431–441.
15. Archie GE. The Electrical Resistivity Log as an Aid in Determining Some Reservoir Characteristics. Transactions of the AIME, 146 (1942) 54–62.
16. Wang P, Chen Z, Pang X, Hu K, Sun M, Chen X. Revised Models for Determining TOC in Shale Play: Example from Devonian Duvernay Shale, Western Canada Sedimentary Basin. Marine and Petroleum Geology 70 (2016) 304–319.
17. Lourakis MIA. A Brief Description of the Levenberg–Marquardt Algorithm Implemented by levmar. https://www.researchgate.net/publication/239328019_A_Brief_Description_of_the_Levenberg–Marquardt_Algorithm_Implemened_by_levmar. Accessed June 3, 2021.
18. Wikipedia contributors. Levenberg–Marquardt Algorithm. Wikipedia, The Free Encyclopedia. https://en.wikipedia.org/wiki/Levenberg%E2%80%93Marquardt_algorithm. Accessed February 12, 2021.
19. Fletcher R. A modified Marquardt Subroutine for Nonlinear Least Squares. Atomic Energy Research Establishment, Rpt. AERE–R 6799, Harwell, 1971.
20. Magara K. Compaction and Fluid Migration: Practical Petroleum Geology Developments in Petroleum Science, Vol. 9, Elsevier Science&Technology, Amsterdam, 1978.

Hittite Journal of Science and Engineering, 2021, 8 (2) 171–177
ISSN NUMBER: 2148–4171
DOI: 10.17350/HJSE19030000227

Development of a Nanofibrous Scaffold Based on Bovine Tissue-derived ECM and Poly(ε-caprolactone) for Tissue Engineering Applications

Mahmut Parmaksiz
Ankara University, Department of Tissue Engineering, Biomaterials and Nanobiotechnology Laboratory, Ankara, Turkey

ABSTRACT

In this study, nanofibrous biohybrid scaffolds were developed by electrospinning using poly(ε-caprolactone) (PCL) and decellularized bovine tissue derived extracellular matrix (ECM). At the first part of the study, bovine ECM was decellularized by treatment with detergent for 24h and then combined with PCL. Following the evaluation of the decellularization efficiency via spectrophotometric DNA content analysis, the composite scaffolds were characterized by using SEM and FT-IR spectroscopy. Moreover, to assess the biocompatibility of the scaffolds an in-vitro cell culture based cytotoxicity test was performed. The results indicated that, DNA content of the bovine tissue was reduced by ~80% compared to the native tissue after decellularization. While FT-IR results indicated the presence of ECM in the composite scaffolds, SEM findings showed that the porous nanofibrous structure of the scaffold changed depending on the incorporated ECM amount. Cell culture based studies also revealed that, the scaffolds containing different amounts of ECM did not have any toxic effect on cell viability during 48 hours of culture period.

Keywords:
Biomaterial; Tissue engineering; Decellularization; Electrospinning.

Article History:
Received: 2021/03/11
Accepted: 2021/06/10
Online: 2021/06/30

***Correspondence to**: Mahmut Parmaksiz, Ankara University Stem Cell Institute and Ankara University Faculty of Science, Tissue Engineering, Biomaterials and Nanobiotechnology Laboratory, Ankara/Turkey*
E-Mail: parmaksiz@ankara.edu.tr
Phone: +90 (312) 583 67 00 (6662)

INTRODUCTION

The main focus of tissue engineering approach is the development of biomaterial scaffolds exhibiting similarity to the three-dimensional (3D) architecture, and its natural bioactive microenvironment of the target tissue or organ. Up till now, this goal has not been fully achieved, owing to the difficulty in completely mimicking the versatile bio-functional composition and structure of the natural extracellular matrix (ECM) [1]. A number of scaffold manufacturing techniques such as, solvent casting and electrospinning have been utilized in order to obtain 3D porous or nanofibrous scaffolds somewhat architecturally resembling the natural ECM by using natural or synthetic biocompatible polymers [2]. In particular, FDA-approved synthetic resorbable polymers such as poly(ε-caprolactone) (PCL), poly(lactic-co-glycolic acid) (PLGA), and other α-hydroxy acid polymers etc. in such forms have been widely utilized in a variety of tissue engineering applications, some of which have reached clinical applications [3]. However, in addition to being biocompatible and structurally-resembling the tissue, tissue engineering scaffolds are expected to support cell attachment and proliferation, as well as promote angiogenesis, and regeneration when transplanted. Nevertheless, the biofunctional active content of the natural ECM, required for these biological processes cannot be realistically simulated on developed scaffolds using the aforementioned polymers by common manufacturing techniques, such as electrospinning.

To overcome the limitations due to lack of bioactivity, alternative modification methods based on incorporating one or more ECM proteins such as fibronectin or laminin into such biomaterials have been evaluated. However, the natural ECM has a unique bioactive composition and structure, mainly composed of structural and functional biomolecules such as collagen, fibronectin, elastin, laminin, glycosaminoglycans and other glycosylated proteins [4]. Therefore, considering the complex bioactive compositions of the natural ECM, it does not seem possible to fully mimic the ECM with the conventional scaffold production methods. On the other hand, although the functions of the ECM are quite similar in terms of tissue types, bioactive contents show differences, which is also a limitation that cannot be overcome.

In recent years, ECM-based biomaterial fabrication technology called "decellularization" has come to the fore in order to create more realistic tissue scaffolds. This technology is based on developing biocompatible ECM-based scaffolds by removing the cells and nuclear material from natural tissues and organs by chemical, physical and/or enzymatic methods [5]. The success of the applied decellularization method depends on the preservation of the existing natural bioactive content of the ECM in the target tissue/organs during the process. Until this time, bioactive ECM-based materials have been developed via decellularization technology from a variety of tissues or organs including the bone, cartilage, small intestine submucosa, liver, heart etc. [6]. Although the decellularization approach seems to be advantageous, this technology also has obvious disadvantages. In fact, some issues such as the selection of decellularization protocol, shaping the biomaterial into the appropriate architecture, the mechanical properties of the formed scaffold and the large-scale production issues are still controversial. On the other hand, although synthetic polymers have limitations in terms of providing bioactivity, they have remarkable features in that they have adjustable mechanical properties and allow mass production. Therefore, the joint rational use of these two technologies could enable the production of bioactive superior tissue engineering scaffolds suitable for diverse regenerative applications [7].

This study aimed to bring together the natural ECM and a synthetic resorbable biopolymer forming a hybrid scaffold for prospective use in tissue engineering applications. At first, bovine liver tissue was decellularized to obtain the bioactive ECM. Decellularization efficiency and the features of the liver ECM were evaluated. Then, the PCL polymer incorporating the liver ECM was electrospun to form a nanofibrous bioactive scaffold. The chemical, morphological and in-vitro cytotoxicity evaluations of the hybrid scaffolds were carried out.

MATERIALS AND METHODS

Materials

Polycaprolactone (PCL), tetrahydrofuran (THF), dimethylformamide (DMF), sodium dodecyl sulfate (SDS) and the enzymes were purchased from Sigma-Aldrich (St. Louis, MO, USA). PBS, culture mediums and supplements was supplied from Biological Industries (Beit Ha-Emek, Israel). Bovine liver tissues were kindly supplied from the Ankara Meat and Milk Board veterinary-controlled slaughterhouse (Ankara, Turkey).

Isolation and characterization of bovine-derived liver tissue ECM

Within the scope of the study, bovine liver tissues were transferred to the laboratory in cold phosphate-buffered saline (PBS, pH: 7.4) buffer within 2-4 hours after slaughtering. Tissue samples were repeatedly washed with 0.9% saline solution and then were cut into approximately 1 mm^3 pieces before decellularization. The tissue pieces were washed with PBS for 2 hours to remove blood and waste tissues. In order to remove cells and DNA from tissues, samples were treated with 0.1% SDS solution prepared in distilled water for 20-24 hours at room temperature. At the end of the period, samples were collected and serially washed with saline solution for 2 hours. Finally, the decellularized samples were frozen at -80 °C for 24 hours and then lyophilized at -76 °C under 0.29 mbar pressure.

In order to evaluate the decellularization efficiency, samples were weighed and treated with a buffer containing 20 mg/mL proteinase K at 55°C for 48 hours [7]. Subsequently, DNA was extracted using phenol/chloroform/isoamyl alcohol method. Then, the amount of DNA reduction compared to the control was determined by taking measurements with NanoDrop ™ One Microvolume UV-Vis Spectrophotometer (Thermo Fisher Scientific, MA).

Beside the DNA content, quantification the sulfated glycosaminoglycan (sGAG) of decellularized ECM were performed after proteinase K digestion by using the Blyscan sGAG Assay Kit (Biocolor, Newtownabbey, U.K.) [4,5]. Briefly, following digestion, tissue lysates were collected and mixed with dimethylmethylene blue dye. sGAG content of the native and decellularized tissues were determined by measurements at 656 nm (SpectraMax M5, Molecular Devices, San Jose, CA).

Preparation of bioactive ECM powder

For the purpose of bioactive composite material development, decellularized ECM in lyophilized form was digested in 1 mg/mL pepsin solution prepared in 0.01N HCl for 48 hours and then neutralized. After digestion, ECM in gel form was molded and lyophilized. The lyophilized sponges were immersed in liquid nitrogen and homogenized (Retsch MM400) for 10 minutes to obtain ECM powder with a size of approximately 50-60 μm (Fig. 1A).

Production of ECM/PCL composite material

Fibrous bioactive composite nanofibers were developed by use of the electrospinning technique with different ratios of ECM powder and PCL (Fig. 1B). For this purpose, different concentrations of decellularized ECM powder (1%, 0.1%) were added into tetrahydrofurane (THF): dimethylformamide (DMF) (1:1) solution and sonicated for 15 minutes. Then, 14% PCL (80,000) (w / v) was added to

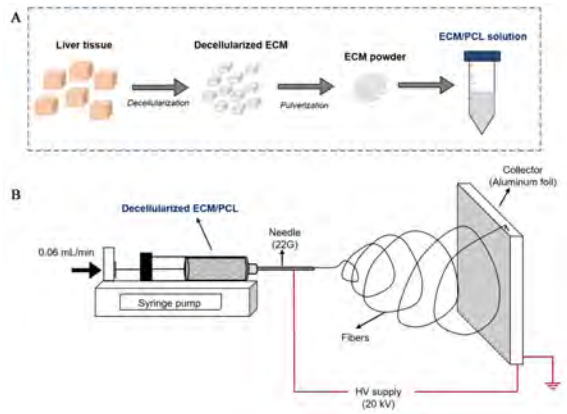

Figure 1. Schematic illustration of the experimental design. (A) Isolation of liver ECM and preparation of ECM/PCL composite solution, (B) the electrospinning process.

the solvent and vortexed for 2 hours with short breaks.

The prepared ECM/PCL solutions were loaded into injectors with a needle tip of 22G diameter and placed into the syringe pump. Then, the electrospinning was conducted at a speed of 0.06 mL/min flow rate under 20 kV and against aluminum sheets at a distance of 15 cm. In addition, in order to develop the biofilm, the prepared decellularized ECM/PCL solutions were placed in Teflon molds (100 µL/cm^2) and then incubated at 37 °C for 48 hours.

Morphological characterization of the materials

Scanning electron microscopy (SEM) analyses were carried out to evaluate the surface morphology of decellularized ECM/PCL composite scaffolds. For this purpose, the samples were coated with a thin gold layer and then analyzed with a ZEISS EVO 40 model SEM device.

FT-IR analysis

FT-IR analysis of decellularized ECM/PCL composite scaffolds prepared in different forms was carried out in order to evaluate the chemical properties of the structures. For this purpose, samples were homogenized and loaded into a Shimadzu IRAffinity model FT-IR device. Analysis was performed in the wavelength range of 600-4000 cm^{-1}.

In-vitro cytotoxicity test

Indirect in-vitro cytotoxicity tests were performed according to the International Organization for Standardization; ISO 10993-5 guidelines to evaluate the potential toxic effects of the scaffolds on human adipose-derived stem cells (hASCs) through MTT based viability assay. Briefly, commercial hASCs (TCC® PCS-500-011™) were maintained in DMEM F-12 medium containing 10% FBS, 10 U/mL penicillin and 10 µg/mL streptomycin and cultured in 24 well culture plates at a density of 4–5 x 10^4 cells/cm^2. hASCs were proliferated under standard culture conditions (5% CO_2, 37 °C and > 95% humidity) until they reached 80% confluence. In parallel with the culture study, the UV-sterilized scaffolds were incubated in culture medium for 48 hours to obtain the extraction medium (EM). Then, the cells were treated with the EM for 48h. During the study standard culture medium served as a negative control and medium containing 400 µL phenol as a positive control group. At the end of the culture period, waste medium was removed and the cell culture was washed with sterile PBS. Then, the MTT reactive was added into each well (diluted in DMEM F-12, 1:10) and incubated for 4 hours. The formed formazan crystals were monitored and solubilized by dissociation reagent. Cell viability was determined by measurements at 570 nm.

Statistical analysis

Statistical analyses were carried out in the GraphPad Prism 8 program using a one-way ANOVA test, and significant differences were identified through Tukey's post hoc analyses.

RESULTS AND DISCUSSION

In this study, different forms of composite scaffolds were developed by using decellularized bovine liver ECM and a biocompatible polymer (PCL) for use in prospective liver tissue engineering applications. The decellularization efficiency was determined by spectrophotometric analyses. The decellularized ECM powder was incorporated into electrospun nanofibrous membranes and films. Besides, the morphological and chemical features of the scaffolds, and their potential in-vitro cytotoxicity on cells was also investigated.

Chemicals to be used for decellularization vary according to the target tissue or organ type and its structural form. While acid-alkaline solutions are frequently used in decellularizing tissues in the form of thin membranes, it is seen that detergent-enzymatic approaches come to the fore in total organ decellularization [8]. In liver-specific decellularization studies, in addition to perfusion approaches, studies with sliced tissues draw attention [9, 10].

In the first stage of the study, in order to incorporate the active ECM components into the hybrid biomaterial to be developed in further steps, bovine liver tissue was decellularized and efficiency of the process was investigated. It was observed that the structural integrity of lyophilized natural liver tissue was disrupted and turned into a white fragile form with the effect of the decellularization protocol (Fig. 2A-C). As a matter of fact, SDS, which is an ionic and amp-

hipathic detergent, has a significant effect on ECM integrity while removing cells from tissues and organs. Thanks to these properties, SDS is frequently used in solid organ and complex tissue decellularization studies, such as for kidney, liver and cornea [11,12]. Indeed, in this study, it was determined that after decellularization of liver tissue pieces by treating in 0.1% SDS solution for 48 hours, the amount of DNA can be removed by 80% compared to the natural liver (Fig. 2D). Beside DNA, sGAG, which is one of the basic components of the ECM, plays a critical role in the regulation of cell behavior such as migration and differentiation. With these features, it is frequently included in decellularized ECM based studies [13]. The results demonstrated that the sGAG levels were significantly maintained in decellularized ECM following decellularization.

Scaffolds to be used in tissue engineering are expected to mimic the target tissue ECM structure and functions. Thus, a three-dimensional porous and nanofibrous scaffold mimicking the natural ECM architecture can be formed by electrospinning using natural or synthetic polymers. Poly (ε-caprolactone) (PCL) draws attention in 3D tissue scaffold production, with its suitable biodegradation and biocompatibility properties [14]. PCL in various concentrations can be solubilized in solvents, such as in chloroform, methanol, DMF, THF, or formic acid, and this polymer can be used for the production of nanofibers in the size range from micron to sub-nanometers [15]. In addition to the electrospun nanofibrous form, the sheet form of PCL can also be used in a number of tissue engineering applications [16, 17]. On the other hand, although scaffolds with appropriate architecture can be formed by using PCL or other synthetic polymers, the biofunctional active content of natural ECM cannot be mimicked [18]. Alternatively, coating or grafting of ECM proteins or attaching short peptide sequences to the biomaterial surface are other efforts in order to find an alternative solution to this limitation [19,20,21]. Considering the complex structure of ECM, it does not seem possible to combine all natural bioactive factors in bioscaffold with these traditional methods.

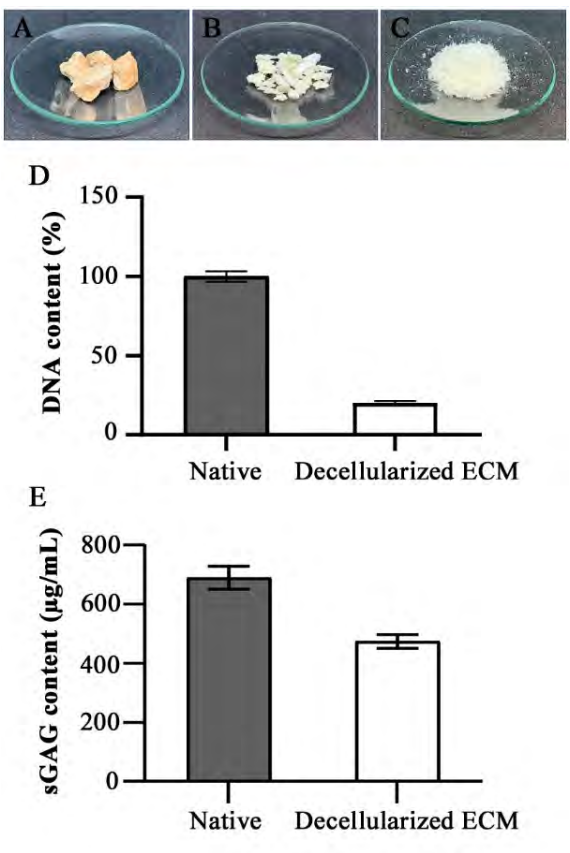

Figure 2. Schematic illustration of the experimental design. (A) Isolation of liver ECM and preparation of ECM/PCL composite solution, (B) the electrospinning process.

In our current study, liver ECM was decellularized and prepared in powder form (Fig. 2C). Then, it was used as the bioactive component for the preparation of the biocomposite PCL scaffold. SEM analysis of the electropsun constructs showed that they had a fibrous structure with varying fiber sizes. While 14% PCL-based constructs showed a homogeneous nanofiber distribution, it was observed that the homogeneous fiber formation was disrupted by the incorporated ECM in the composite group (Fig. 3A-C). Results also showed that the fiber diameters of PCL membranes without ECM were 250-750 nm (Fig. 3A). On the other hand, fibers with a size of about 3-5 µm and various bead-like structures were observed in different regions following the incorporation of ECM particles into the scaffolds. In addition, homogeneous bead-like structures were visible in the membranes containing 0.1% ECM (PCL/0.1% ECM). By the increase in ECM ratio (PCL/1% ECM), the fiber integrity deteriorated, and significant amount of particles could be observed (Fig. 3B and 3C). Similarly, PCL (PCL-F) prepared in the film form had a homogeneous surface morphology. However, it was observed that the films containing decellularized ECM had a rougher surface topography compared to that of the pure PCL films (Fig. 3D-F).

The chemical properties of the morphologically characterized biocomposite nanofiber and film constructs were evaluated by FTIR analysis. Although there are a limited number of studies on FTIR analysis of decellularized native tissues, it basically gives some clear clues regarding the basic composition of ECM. PCL basically has characteristic peaks in wavelength ranges of 1150-1250 cm^{-1} (COC, -COC-), 1250-1300 cm^{-1} (CC) 1700-1750 cm^{-1} (CH_2) and 2800-3000 cm^{-1} (CH_2) [22,23].

In addition, although the liver tissue ECM has characteristic peaks related to the protein, polysaccharide and lipid components within the structure, some of these peaks are

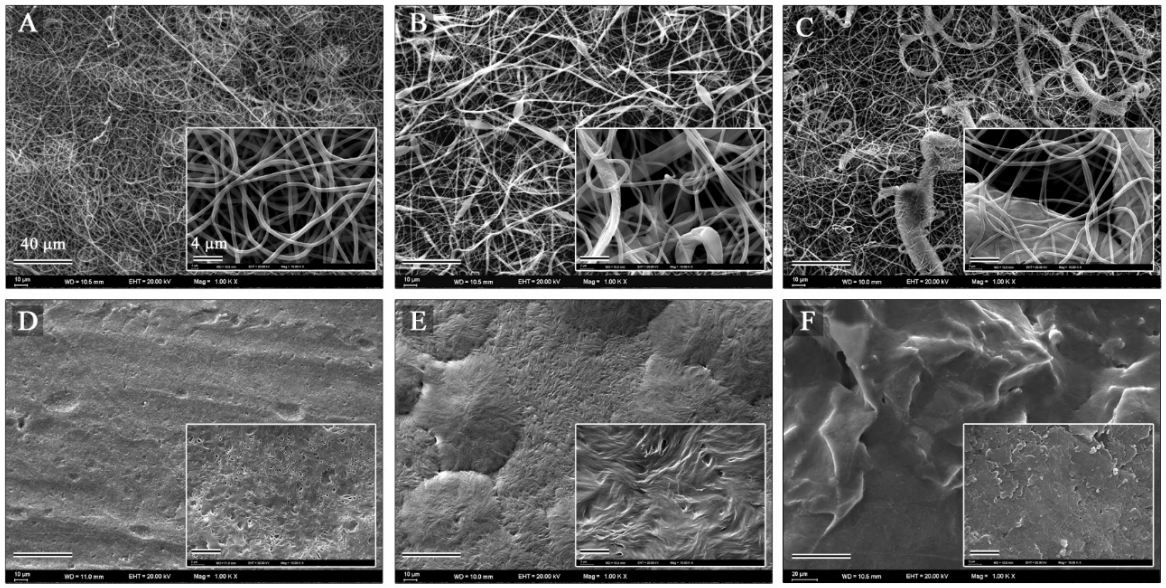

Figure 3. SEM micrographs of the composite nanofibers and films. (A) PCL-N, (B) PCL-N/0.1% ECM/PCL, (C) PCL-N/1% ECM, (D) PCL-F, (E) PCL-F/0.1% ECM/PCL, (F) PCL-F/1% ECM.

overlapping with PCL. Similar to PCL, –CH (2800-3000 cm^{-1}) tensions and bends (1300-1500 cm^{-1}) caused by the polysaccharides are also seen in the liver ECM group. It has flat peaks in the range of 3100-3600 cm^{-1} depending on the protein and water composition. On the other hand, unlike PCL, characteristic peaks of Amide I, II and III bonds are expected to be observed in the wavelength range of 1400-1700 cm^{-1} [24,25].

The findings revealed that PCL-based specimens both in the form of nanofiber and film have characteristic peaks, whereas lower intensity peaks were observed in the film membranes due to its permeability compared to fibrous membranes (Fig. 4A). In the composite scaffolds containing decellularized ECM, peaks of Amide I, II, III bonds in the range of 1500-1700 cm^{-1} were observed similar to the results of the control liver ECM (Fig. 4B-4C). These characteristic peaks, which are particularly stronger in the nanofiber formation, are the indication of the presence of ECM in the developed composite bioscaffolds.

It is critical to evaluate the biocompatibility of biomaterials to be developed for tissue engineering applications. In this framework, different biocompatibility testing approaches, such as extract dilution, direct contact, or indirect contact testings are recommended within the scope of the ISO 10993-5 guide [26,27]. The indirect in-vitro cytotoxicity test findings of the biocomposite scaffolds are presented in Fig. 5. The results showed that both the composite scaffolds, in film or nanofibrous membrane form containing different concentrations of ECM, do not have a toxic effect on the viability of cells following 48 hours of culture. The formation of MTT formazan crystals, demonstrating the metabolic activity of viable cells, was determined bothe by invert microscopy and by quantitative spectrophotometric measurements (Fig 5A-B). On the other hand, 90% of cell viability was lost in the positive control group (medium containing phenol). These findings support the potential for the use of developed biomaterials in future in-vitro and in-vivo applications.

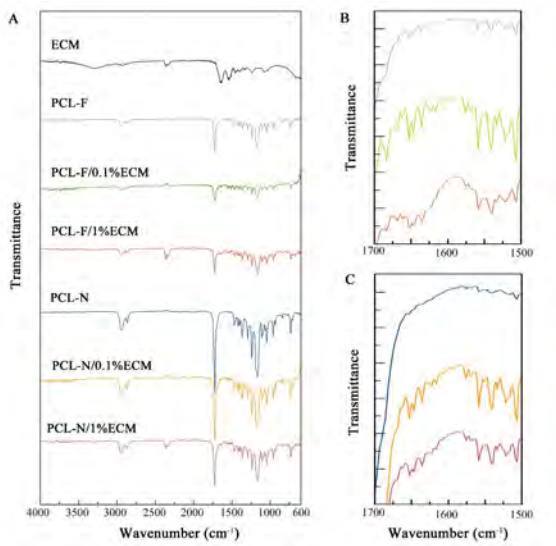

Figure 4. FTIR results of ECM/PCL composite nanofibers. (A) All groupus, (B) PCL-F, PCL-F/0.1%ECM, PCL-F/1%ECM, (C) PCL-N, PCL-N/0.1%ECM, PCL-N1%ECM.

CONCLUSION

In this study, composite scaffolds in both nanofibrous membrane and film forms could be developed using decellularized bovine ECM and synthetic PCL polymer. The presence of ECM in the biocomposite scaffolds was determined by chemical and morphological analy-

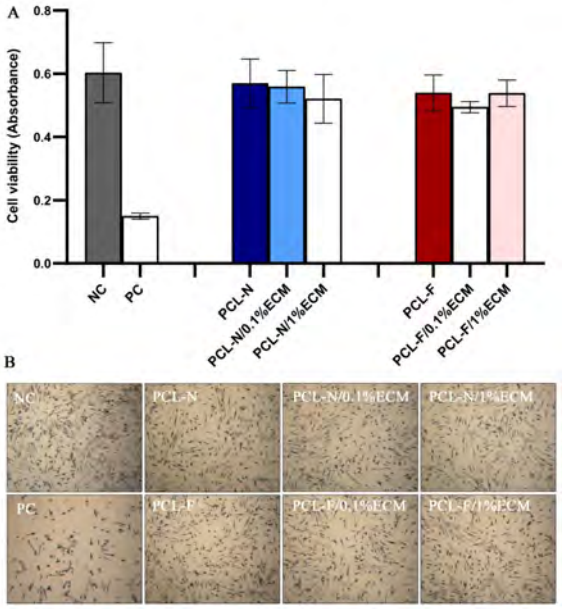

Figure 5. Indirect in-vitro cytotoxicity findings. (A) Spectrophotometric MTT findings. (B) Phase-contrast micrographs demonstrating the formation of formazan crystals on cell cultures.

ses. Subsequently, the potential cytotoxic effects of these scaffolds on human adipose mesenchymal stem cells were examined by in-vitro studies and it was found that biocompatible scaffolds could be developed. It is thought that the scaffolds in different forms containing liver ECM have the potential to be used in advanced liver tissue engineering studies.

ACKNOWLEDGMENT

I would like to thank Professors Y.M. Elçin and A.E. Elçin for their support, and Dr. M.T. Vurat and E. Emir for his help in the FT-IR analysis.

CONFLICT OF INTEREST

Authors approve that to the best of their knowledge, there is not any conflict of interest or common interest with an institution/organization or a person that may affect the review process of the paper.

References

1. Hoshiba T, Lu H, Kawazoe N, Chen G. Decellularized matrices for tissue engineering. Expert Opinion on Biological Therapy 10(12) (2010) 1717-1728.
2. Lalegül-Ülker Ö, Vurat MT, Elçin AE, Elçin YM. Magnetic silk fibroin composite nanofibers for biomedical applications: Fabrication and evaluation of the chemical, thermal, mechanical, and in vitro biological properties. Journal of Applied Polymer Science 136(41) (2019) 48040.
3. Vurat MT, Elçin AE, Elçin YM. Osteogenic composite nanocoating based on nanohydroxyapatite, strontium ranelate and polycaprolactone for titanium implants. Transactions of Nonferrous Metals Society of China 28(9) (2018) 1763-1773.
4. Parmaksiz M, Elçin AE, Elçin YM. Decellularized Cell Culture ECMs Act as Cell Differentiation Inducers. Stem Cell Reviews and Reports 16(3) (2020) 569-584.
5. Parmaksiz M, Elçin AE, Elçin YM. Decellularization of bovine small intestinal submucosa and its use for the healing of a critical-sized full-thickness skin defect, alone and in combination with stem cells, in a small rodent model. Journal of Tissue Engineering and Regenerative Medicine 11(6) (2017) 1754-1765.
6. Parmaksiz M, Dogan A, Odabas S, Elçin AE, Elçin YM. Clinical applications of decellularized extracellular matrices for tissue engineering and regenerative medicine. Biomedical Materials 11(2) (2016) 022003.
7. Parmaksiz M, Elçin AE, Elçin YM. Decellularized bovine small intestinal submucosa-PCL/hydroxyapatite-based multilayer composite scaffold for hard tissue repair. Materials Science and Engineering C 94 (2019) 788-797
8. Parmaksiz M, Elçin AE, Elçin YM. Decellularization of Bovine Small Intestinal Submucosa. In: Turksen K. (eds) Decellularized Scaffolds and Organogenesis. Methods in Molecular Biology, Humana Press, New York, pp. 129-138, 2018.
9. Baptista PM, Siddiqui MM, Lozier G, Rodriguez SR, Atala A, Soker S. The use of whole organ decellularization for the generation of a vascularized liver organoid. Hepatology 53(2) (2011) 604-617.
10. Skardal A., Smith L, Bharadwaj S, Atala A, Soker S, Zhang Y. Tissue specific synthetic ECM hydrogels for 3-D in vitro maintenance of hepatocyte function. Biomaterials 33(18) (2012). 4565–4575.
11. Ren H, Shi X, Tao L, Xiao J, Han B, Zhang Y, Yuan X, Ding Y. Evaluation of two decellularization methods in the development of a whole-organ decellularized rat liver scaffold. Liver International 33(3) (2013) 448-458.
12. Lewis PL, Yan M, Su J Shah RN. Directing the growth and alignment of biliary epithelium within extracellular matrix hydrogels. Acta Biomaterialia 85 (2019) 84-93.
13. Parmaksiz M, Lalegül-Ülker Ö, Vurat MT, Elçin AE, Elçin YM. Magneto-sensitive decellularized bone matrix with or without low frequency-pulsed electromagnetic field exposure for the healing of a critical-size bone defect. Materials Science and Engineering: C. 124 (2021) 112065.
14. Mochane MJ, Motsoeneng TS, Sadiku ER, Mokhena TC, Sefadi JS. Morphology and Properties of Electrospun PCL and Its Composites for Medical Applications: A Mini Review. Applied Sciences 9(11) (2019) 2205.
15. Schueren LVD, Schoenmaker BD, Kalaoglu OI, Clerk KD. An alternative solvent system for the steady state electrospinning of polycarbonate. European Polymer Journal 47 (2011) 1256–1263.
16. Luk JZ, Cooper-White J, Rintoul L, Taran E, Grøndahl L. Functionalised polycaprolactone films and 3D scaffolds via gamma irradiation-induced grafting. Journal of Materials Chemistry B 1(33) (2013) 4171-4181.
17. Janarthanan G, Kim IG, Chung EJ, Noh I. Comparative studies on thin polycaprolactone-tricalcium phosphate composite scaffolds and its interaction with mesenchymal stem cells. Biomaterials Research 23(1) (2019) 1-12.
18. Wang X, Ding B, Li B. Biomimetic electrospun nanofibrous structures for tissue engineering. Materials Today 16(6) (2013) 229-241.
19. Moursi AM, Damsky,CH, Lull J, Zimmerman D, Doty SB, Aota S, Globus RK. Fibronectin regulates calvarial osteoblast differentiation. Journal of Cell Science 109 (1996) 1369-1380.
20. Rosso F, Giordano A, Barbarisi M, Barbarisi A. From cell–ECM

interactions to tissue engineering. Journal of Cellular Physiology 199(2) (2004) 174-180.

21. Celiz AD, Smith JG, Patel AK, Langer R, Anderson DG, Barrett DA, Young LE, Davies MC, Denning C, Alexander MR. Chemically diverse polymer microarrays and high throughput surface characterisation: a method for discovery of materials for stem cell culture. Biomaterials Science 2(11) (2014) 1604-1611.
22. Sadeghianmaryan A, Karimi Y, Naghieh S, Sardroud HA, Gorji M, Chen X. Electrospinning of scaffolds from the polycaprolactone/polyurethane composite with graphene oxide for skin tissue engineering. Applied Biochemistry and Biotechnology 191 (2020) 567-578.
23. Hejna A, Zedler Ł, Przybysz-Romatowska M, Cañavate J, Colom X, Formela K. Reclaimed rubber/poly (ε-caprolactone) blends: Structure, mechanical, and thermal properties. Polymers 12(5) (2020) 1204.
24. Ansari T, Southgate A, Obiri-Yeboa I, Jones LG, Greco K, Olayanju A, Mbundi L, Somasundaram M, Davidson B, Sibbons PD. Development and Characterization of a Porcine Liver Scaffold. Stem Cells and Development 29(5) (2020) 314-326.
25. Saheli M, Sepantafar M, Pournasr B, Farzaneh Z, Vosough M, Piryaei A, Baharvand H. Three-dimensional liver-derived extracellular matrix hydrogel promotes liver organoids function. Journal of Cellular Biochemistry 119(6) (2018) 4320-4333.
26. Srivastava GK, Alonso-Alonso ML, Fernandez-Bueno I, Garcia-Gutierrez MT, Rull F, Medina J, Coco RM, Pastor JC. Comparison between direct contact and extract exposure methods for PFO cytotoxicity evaluation. Scientific Reports 8(1) (2018) 1-9.
27. Öztürk S, Ayanoğlu FB, Parmaksız M, Elçin AE, Elçin YM. Clinical and surgical aspects of medical materials' biocompatibility. In: Mozafari M. (eds) Handbook of Biomaterials Biocompatibility. Woodhead Publishing, United Kingdom, pp. 219-250 2020.

Hittite Journal of Science and Engineering, 2021, 8 (2) 179–187
ISSN NUMBER: 2148–4171
DOI: 10.17350/HJSE19030000228

Poly(rutin) Micro/nanogels for Biomedical Applications

Mehtap Sahiner[1] **Selin Sagbas Suner**[2]
[1]Canakkale Onsekiz Mart University, Department of Fashion Design, Canakkale, Turkey
[2]Canakkale Onsekiz Mart University, Department of Chemistry, Canakkale, Turkey

Article History:
Received: 2021/03/14
Accepted: 2021/06/02
Online: 2021/06/30

***Correspondence to**: Mehtap Sahiner, Canakkale Onsekiz Mart University, Faculty of Applied Science, Department of Fashion Design, 17100, Canakkale, TURKEY*
E-Mail: sahinerm78@comu.edu.tr
Phone: +90 (286) 218 00 18

ABSTRACT

Flavonoids are natural phenolic compounds, which are active molecules commonly found in woody and herbaceous plants used in the natural defense mechanisms of plants against harmful microorganisms. In this research, the rutin (RUT) molecule, which is a natural flavonoid, was bonded with epoxy groups of poly(ethylene glycol) diglycidyl ether crosslinker with the micro emulsion crosslinking technique to synthesize poly(rutin) (p(RUT)) micro/nanogels. These p(RUT) micro/nanogels had spherical morphologic structure with 0.3 nm-2 µm dry size range based on scanning electron microscope images. Furthermore, p(RUT) micro/nanogels were found to have injectable size range with 548±8.9 nm average size distribution in aqueous solution according to dynamic light scattering (DLS) measurements. In addition, the zeta potential measurements performed in different pH conditions and potentiometric titration of the prepared p(RUT) micro/nanogels were also determined and the isoelectronic point and pKa values of these micro/nanogels were estimated as pH 2.85 and 2.16, respectively. The effects of RUT and p(RUT) micro/nanogels on α-glucosidase (AG) (EC 3.2.1.20) enzyme activity were investigated and RUT and p(RUT) micro/nanogels stimulate this enzyme. Moreover, fibrinogen interaction results showed that p(RUT) micro/nanogels were more compatible with the vascular system than RUT, with less interaction ability between fibrinogen and p(RUT) micro/nanogels. In addition, p(RUT) micro/nanogels had the highest antioxidant scavenging ability with 251.3±20.2 gallic acid equivalency total flavonoid content (TFC) at 250 µg/mL and even 5 µg p(RUT) microgel/nanogels reduced 1.75±0.27 µmol Fe (III). Furthermore, no Fe (II) chelating activity was obtained for RUT monomer, but p(RUT) micro/nanogels had significant Fe (II) chelating activity of 43.11±17.4%.

Keywords:
Rutin; Microgel; Nanogel; Alpha-Glucosidase Enzyme; Antioxidant.

INTRODUCTION

Interest in flavonoids, which are phenolic compounds, has grown with the French paradox. Interest in bioflavonoids has increased based on Mediterranean culture, which includes a diet rich in phenol directly proportional to high fat with an inverse relationship with the risk of heart attack. Flavonoids are widely used in the food industry due to antioxidant and antimicrobial properties. Flavonoids are known to affect many biofunctions such as lowering blood pressure and having anti-inflammatory, hypocholesterolemic, anticancer platelet stabilizer, antiallergic, antidepressant and blood clotting properties [1,2]. Rutin is a known flavonoid and has two sugar molecules in its structure. Rutin's chemical name is quercetin-3-remnosyl glucoside [3]. It is present in many fruits and vegetables such as onion, tea, apple, parsley, citrus, sage, and grape [4]. It is used in the food, cosmetics, and even pharmacology industries [5,6], especially due to its antioxidant and antimicrobial properties [7]. In addition, it has many benefits for the human body, which makes rutin pharmacologically important. While it displays antioxidant properties by destroying free radicals, it has positive effects on the nervous system as well as cardiovascular health [8–10]. There are studies about its use as an anti-inflammatory and antidepressant and for patients with Alzheimer's and stroke [11]. In addition, flavonoids are known to have an inhibitory effect on cancer cells [12,13].

Alpha-glucosidase is a well-known enzyme that hydrolyzes 1,6 glycoside bonds of disaccharides, such as sucrose and maltose. Disaccharides cannot pass through the cell membrane from the digestive tract in diabetes, but due to enzymes that break down sugar with alpha-glucosidase, different disaccharide molecules are

broken down into monosaccharide units and glucose is directly transferred into the cells. However, glycogen storage diseases obstruct the body's ability to convert glycogen into glucose [14,15]. One of these diseases, Pompe disease, is a genetic deficiency of acid alpha-glycosides in patients. These enzymes trigger biochemical reactions in the body. In a healthy person with normal enzyme activity, the function of this enzyme is to destroy complex sugar molecules stored in lysosomes in cells. However, the destruction of complex sugar molecules cannot occur due to this innately deficient or insufficient enzyme, and storage begins. Enzyme replacement therapy is one of the treatment methods applied [16,17]. Cross-linked particle forms of RUT were synthesized in our previous study [9]. In this study, enzyme interaction, fibrinogen interaction and various antioxidant tests were investigated for RUT and p(RUT) microgel/nanogels to show the biomedical potential of p(RUT) microgel/nanogels.

MATERIAL AND METHODS

Materials

Rutin dihydrate (RUT, >95%, Sigma), L-alpha lecithin (granular, 98%, Acros Organic), poly (ethylene glycol) diglycidyl ether (PEGGE, Mn: 500, Aldrich), triethylamine (TEA, 99.5%, Sigma Aldrich), sodium hydroxide (Sigma-Aldrich), gasoline (95 octane, Total), cyclohexane (99.5%, Sigma-Aldrich), and ethyl alcohol (99%, Birkim) were used as received. Ultra-pure distilled water was obtained from GFL, 2108 and Millipore Direct-Q3 UV (18,2 MΩ.cm). Sodium nitrite (Merck, extra pure) and aluminum chloride (Merck, anhydrous powder sublimed from synthesis) were used for total flavonoid content (TFC) assay. Sodium acetate anhydrous (Fisher, 99%) and hydrochloric acid (Sigma, 37%) were used as received. Fe (III) chloride hexahydrate (Acros, 99%) and Fe (II) chloride tetrahydrate (Sigma Aldrich, 99%) were used for ferric reducing antioxidant power (FRAP) assay. Fe (II) sulfate heptahydrate (Merck, 99.5 %) and 5,6-Diphenyl-3-(2-pyridyl)-1,2,4-triazine-4,4-disulfonic acid disodium salt hydrate (Alfa Aesor) were used for Fe (II) chelating test. Bovine fibrinogen (Alfa Aesar) was used for fibrinogen interaction. alpha-glucosidase (obtained from Saccharomyces cerevisiae, 10 unit/mg protein) as enzyme and p-nitrophenyl-α-D-glucopyronidase as substrate were obtained from Sigma Aldrich.

Synthesis of p(RUT) Micro/nanogels

To synthesize p(RUT) micro/nanogels, RUT was crosslinked with PEGGE via water-in-oil microemulsion system in lecithin-gasoline reverse micelle medium in accordance with the previously published process [9,18]. Briefly, 2 mL of 60 mg/mL concentration RUT in 0.5 M NaOH solution was suspended in 150 mL of 0.1 M lecithin-gasoline emulsion medium with 750 rpm mixing rate at 50 °C reaction temperature. Ten minutes later, PEGGE crosslinker at 300% mole ratio of RUT and 20 µL TEA accelerator were added into the reaction medium and the same reaction conditions were maintained for 12 h. Cross-linked p(RUT) micro/nanogels were separated from the reaction medium by precipitation of the micro/nanogels using a centrifuge at 10,000 rpm for 10 min. Then, the precipitated micro/nanogels were washed with gasoline one time, cyclohexane two times, ethanol: water (80:20, v:v) mixture three times, and ethanol two times by centrifugation at 10,000 rpm for 10 min. The p(RUT) micro/nanogels were dried in an oven at 50 °C and stored in a closed container.

Characterization of p(RUT) Micro/nanogels

A scanning electron microscope (SEM, Jeol JSM-5600 LV) was used to visualize the morphological structure and for size analysis of p(RUT) micro/nanogels. SEM images were taken at 20 kV operating voltage after coating with gold/palladium for 30 seconds. Dynamic light scattering (DLS) and zeta potential (ZP) measurements of p(RUT) micro/nanogels were determined by using 90Plus/BI-MAS and ZetaPlus analyzer (Brookhaven Ins. Corp.) instruments, respectively. These measurements were repeated 10 times and the results are given with standard deviations. For the zeta analysis, 10 mg of p(RUT) micro/nanogels was suspended in 50 mL of 10-3 KCl solution and ZP values of p(RUT) micro/nanogels were measured at different pH conditions between pH 2 and pH 12. The pH value was adjusted with 0.1 M HCl and 0.1 M NaOH solutions. The isoelectric point of p(RUT) micro/nanogels was evaluated as the pH value with zero mV zeta potential. Furthermore, 50 mg of p(RUT) micro/nanogels was suspended in 10-3 KCl solution to measure the equivalent point and pKa values by potentiometric titration. In the titration, the pH value of micro/nanogel suspension was decreased to pH 2 using 0.01 M HCl solution and titrated up to pH 12 by 0.01 M NaOH solution. The chemical structures of RUT and p(RUT) micro/nanogels were characterized by FTIR spectra (PerkinElmer Spectrum 100) using attenuated total reflectance (ATR) in the range of 2000-650 cm^{-1} with a resolution of 4 cm^{-1}. Thermal stability of PEGGE-crosslinked p(RUT) micro/nanogels was investigated with thermogravimetric analysis (TGA, SII TG/DTA 6300, Japan) from 50 to 1000 °C with 10 °C/mL heating rate under nitrogen atmosphere with 100 mL/min flow rate.

Alpha-glucosidase Enzyme Activity Assay

P(RUT) micro/nanogels in 3000 µg/mL suspended solution were prepared in 67 mM PBS at pH 6.9. P(RUT)

suspended solution was diluted to 2250, 1500, 750, 375 and 187 μg/mL concentrations with pH 6.9 PBS. The RUT molecule has a suppressed enzyme peak due to high absorbance in theUV Vis spectrophotometer, so the RUT molecule (750-30 μg/mL) was studied at low concentrations. The effect of RUT or p(RUT) micro/nanogel on α-glucosidase (EC 3.2.1.20) was examined using the colorimetric substrate p-nitrophenyl-α-D-glucoside according to the literature [19]. Briefly, 70 μL containing different concentrations of RUT or p(RUT) micro/nanogel was put into the well plate with PBS as control. Enzyme solution of 0.03 unit/mL 70 μL was placed into the RUT and p(RUT) micro/nanogel solution. The mixed solution was read at 405 nm with Thermo Scientific Multiscan Go microplate reader and incubated for 10 minutes. Finally, 10 Mm substrate solution was placed into the mixed solution. After 20 minutes, the absorbance of the well plate was measured. The sample was compared to a control which had 70 μL of buffer solution. The effect of RUT or p(RUT) microgel/nanogel on α-glucosidase activity was calculated as the fraction of activity compared to the sample without added RUT or p(RUT) microgel/nanogel eluate, using Equation (1).

$$Fraction\ of\ activity = \frac{\varnothing A_{405}^{sample}}{\varnothing A_{405}^{control}} \quad (1)$$

Fibrinogen Interaction of RUT and p(RUT) Microgel/nanogel

The effects of RUT and p(RUT) microgel/nanogel on the fluorescence properties of fibrinogen were demonstrated with fluorescence spectroscopy (Thermo Scientific Lumina Spectrophotometer) according to the literature [20]. Different concentrations of RUT or p(RUT) micro/nanogel, 16-250 μg/mL in PBS, were mixed with fibrinogen solution in 1:1 ratio by volume. The width of excitation and emission slit was set as 5 nm and the excitation wavelength of 280 nm was used. The scanning range was set between 280-420 nm. The interaction of RUT and p(RUT) micro/nanogel with fibrinogen was determined in terms of the reduction in the fluorescence intensity.

Antioxidant Properties of p(RUT) Micro/nanogel

Total flavonoid content (TFC), ferric reducing antioxidant powder (FRAP) and iron chelating assays were carried out to determine the antioxidant properties of p(RUT) micro/nanogels.

The total flavonoid content (TFC) test for RUT and p(RUT) micro/nanogels was done using a UV-Vis spectrophotometer at 405 nm in accordance with the literature with some modifications [21]. RUT solution or p(RUT) micro/nanogel suspension at 500, 250, 125, and 62.5 μg/mL concentration was prepared in DI water and 0.5 mL volume RUT or p(RUT) suspension was placed in 10 mL tubes. Distilled water, 2 ml, was added into the tubes. Then, 5 minutes later 0.15 mL of 5% NaNO2 was added. After 5 minutes, 0.15 mL of 10% AlCl3.6H20 was added to this medium. After 5 minutes, 1 M 1 mL of NaOH was added to this mixture. Keeping this solution still for 15 minutes, the UV-Vis spectra of this solution was read at 405 nm wavelength. NaNO2 and AlCl3.6H20 mixture solution in DI water was used as blank. Gallic acid was used as standard.

The ferric reducing antioxidant potential (FRAP) of RUT and p(RUT) micro/nanogels was examined with a UV-Vis spectrophotometer at 595 nm according to the literature [22,23]. Briefly, 0.3 M acetate buffer was prepared at pH 3.6. Tripyridyl triazine (TPTZ) solution at 10 mM concentration was prepared using 2.5 mL 40 mM HCl. Acetate buffer at 25 mL volume was mixed with 2.5 mL TPTZ solution, and 2.5 mL 20 mM FeCl3.H2O (in acetate buffer) was mixed to achieve Fe(III)- TPTZ complex. The FRAP test was done using 3 mL of the prepared Fe-TPTZ complex solution. First, the UV-Visible spectra of Fe-TPTZ complex were measured at 595 nm. RUT solution and suspended p(RUT) micro/nanogels at 500 μg/mL concentration were prepared in acetate buffer and 5-80 μL volumes of RUT and/or p(RUT) micro/nanogel suspension was placed into the Fe-TPTZ complex solution and stirred for 4 minutes with plastic pipette tips. Then, the UV-Vis spectra were recorded and the difference between the absorbance values was calculated as μmol Fe (II) reduced. FeSO4.7H20 was used as Fe (II) source to complex with TPTZ as standard to generate a calibration curve for the determination of Fe (II) reduced by RUT and/or p(RUT) micro/nanogels. Gallic acid (GA) was taken as reference material.

Fe (II) chelating activity was studied according to the literature [24]. RUT and p(RUT) micro/nanogel were prepared at 500 μg/mL concentration in DI water and diluted to 250, 125, 62.5, and 31.125 μg/mL concentrations. Different concentrations of RUT and p(RUT) micro/nanogel, at 140 μL, were added into a 96 well plate and 20 μL of 1 mM of Fe (II) aqueous solution was added to each well. The plate was measured at 562 nm by using a microplate reader (Thermo Multiskan Go). After the measurement, 40 μL of 2.5 mM ferrozine solution in DI water was put to each well. After 5 minutes, the plate was measured at 562 nm once again.

Pure DI water without RUT or p(RUT) microgel/nanogel was used as a blank. Each concentration was tested in triplicate. The results were calculated according to Equation 2 and given as μmol Fe (II) chelating activity %.

$$\text{Fe(II) chelating activity\%} = \left(\left[1 - \frac{\Delta A_{562}^{sample}}{\Delta A_{562}^{control}} \right] \right) x100 \quad (2)$$

RESULTS AND DISCUSSION

RUT flavonoid, which also known as vitamin P, has a wide range of pharmaceutical activities in various types of diseases related to its sedative, antidepressant, anticonvulsant, anti-Alzheimer, antiarthritic, antidiabetic, anti-hypercholesterolemic, antiulcer, anti-asthmatic, anti-osteoporotic, anticancer, and antimicrobial effects [5]. RUT monomer can be crosslinked with glycerol diglycidyl ether or poly (ethylene glycol) diglycidyl ether (PEGGE) crosslinkers to synthesize p(RUT) micro/nanogels in reverse micelle microemulsion medium as reported earlier [9,18]. According to these studies, p(RUT) micro/nanogels provide sustainable and long-term RUT release as an active agent through the degradable crosslinker structure. Furthermore, antimicrobial and antioxidant effects, blood compatibility, and cytotoxicity against healthy and cancer cells were studied in the research. In this study, the effects of PEGGE-crosslinked p(RUT) micro/nanogels on enzyme activity, chelating therapy, and blood clotting mechanism by fibrinogen interaction were investigated to show the bioactivity of degradable p(RUT) micro/nanogels for different biological functions. The schematic representation of the reaction between RUT monomer and PEGGE crosslinker to prepare p(RUT) micro/nanogels is illustrated in Fig. 1a. Hydroxyl groups of RUT reacted with opened epoxy groups of the PEGGE crosslinker in basic conditions in the presence of TEA accelerator at 50 °C reaction temperature. Thus, RUT monomer crosslinked with PEGGE to synthesize p(RUT) micro/nanogels in a water-in-oil reverse micelle microemulsion medium. Also, SEM images and hydrolytic size distribution of the prepared p(RUT) micro/nanogels are illustrated in Fig. 1b and 1c.

As can be seen in the SEM image, p(RUT) micro/nanogels had spherical shapes in the range of 0.3 nm to 2 μm. The hydrolytic size distribution of these micro/nanogels was 548±8.9 nm average particle size according to DLS measurement. In addition, p(RUT) micro/nanogels have polydispersed size range with 0.452±0.041 polydispersity index value. Several studies indicated that polymeric particles in the range of hundred nanometer to few micrometer sizes can be used in a wide range of biomedical applications. Zhang et al. reported that the 1 to 10 μm size range of chitosan/peptide

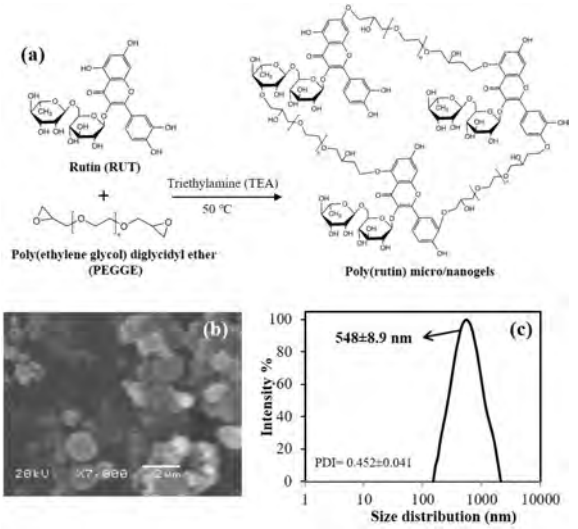

Figure 1. (a) Reaction schema for p(RUT) micro/nanogels. (b) SEM image of p(RUT) micro/nanogels and (c) hydrolytic size distribution graph measured by dynamic light scattering (DLS).

microspheres made it a promising biomaterial for wound healing applications [25]. In another study, Anderson et al. also observed that polymeric microparticles with nearly 3 nm particle size could be used as a DNA delivery system [26]. Furthermore, Decuzzi et al. proposed that the spherical shape of particles with sizes ranging between 0.7 and 3 μm is within the injectable range with good biodistribution [27]. These results indicate that p(RUT) micro/nanogels have injectable size range and can be used for in vivo applications.

The chemical structures of RUT and p(RUT) micro/nanogels were analyzed by FT-IR spectroscopy, as seen in Fig. 2a. Characteristic peaks of RUT monomer in the region between 1600 and 1562 cm^{-1} are assigned to the stretching bands of C-C aromatic groups of the flavonoid. In addition, the peaks at 1183, 1078 and 1016 cm^{-1} correspond to the stretching vibrations for the substituted benzene ring of RUT. Among these peaks, p(RUT) micro/nanogels have a ridge between 1096-1060 cm^{-1} attributed to ether linkages due to possible binding of RUT monomer with opened epoxy groups on the PEGGE crosslinker. These results support that p(RUT) micro/nanogels were successfully prepared via a crosslinking reaction of RUT with the degradable crosslinker of PEGGE. Moreover, thermal degradation of p(RUT) micro/nanogels from 50 to 1000 °C was measured by thermogravimetric analysis (TGA), as seen in Fig. 2b.

Fig. 2. (a) FT-IR spectra of RUT and p(RUT) micro/nanogels. (b) Thermal degradation profiles of p(RUT) micro/nanogels.

It is clearly seen that p(RUT) micro/nanogels had one main degradation at about 103-380 °C with 39.0% weight loss and one slight degradation step at about 400-600 °C with 47.2% weight loss. Finally, 50% of the total remaining

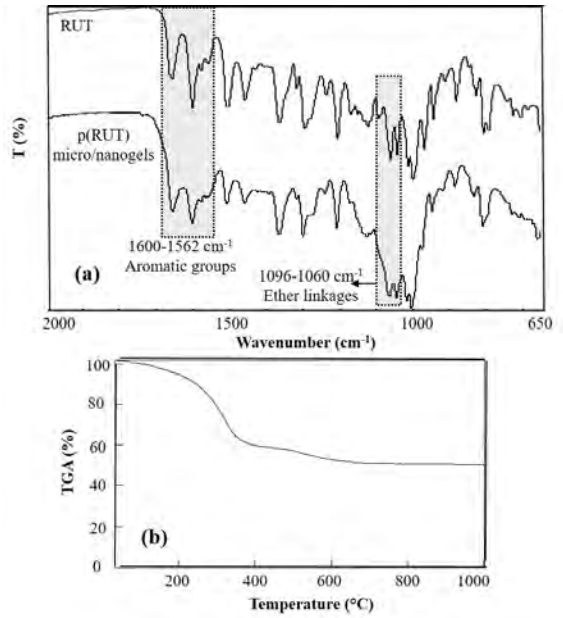

Figure 2. FT-IR spectra of RUT and p(RUT) micro/nanogels. (b) Thermal degradation profiles of p(RUT) micro/nanogels.

material was obtained at 1000 °C because of the high ratio of crosslinker in the polymeric structure. Sahiner reported that thermal degradation of RUT monomer, which has more degradable behavior than p(RUT) micro/nanogels, had a similar degradation pattern [18]. These results indicate that the crosslinker PEGGE in the micro/nanogel network increased the thermal stability of RUT.

The isoelectric point and surface charge of biomaterials should be known to understand the interaction of the materials with biomacromolecules. Therefore, zeta potential values and potentiometric titration of p(RUT) micro/nanogels in a wide range of pH conditions between pH 2 and pH 12 are demonstrated in Fig. 3a and 3b.

Zeta potential of p(RUT) micro/nanogels was +9.69±2.61 mV at pH 2, whereas negative zeta potential values were determined at conditions of pH 3 and above pH between -3.1 and -32.35 mV. The isoelectric point is the pH value at which p(RUT) micro/nanogels contain the same amount of positive and negative charges on the material surface. The isoelectric point with neutral charge on p(RUT) micro/nanogels was calculated at about pH 2.85 according to zeta potential analysis. Furthermore, potentiometric titration of p(RUT) micro/nanogels was monitored via pH analysis by titration with NaOH solution. These results indicated that pKa values of p(RUT) micro/nanogels have pH 7.06 equivalent point and 2.16 pKa value. No significant differences in isoelectric point and the pKa value of p(RUT) micro/nanogels were found depending on the unbound phenolic hydroxyl groups in RUT. Furthermore, negatively-charged p(RUT) micro/nanogels had a tendency to interact with positively-charged molecules in physiological conditions at

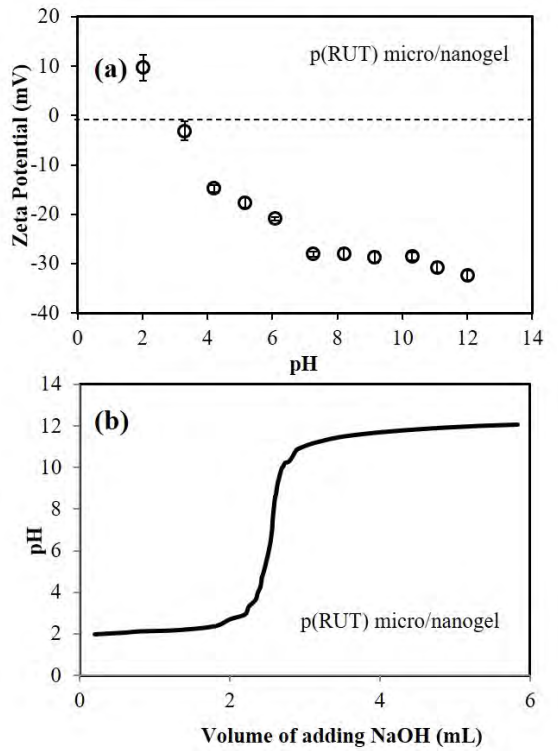

Figure 3. (a) Zeta potential values and (b) potentiometric titration of p(RUT) micro/nanogels in the range of pH 2 and pH 12. pH values of p(RUT) micro/nanogels suspension in 10-3 KCl solution was adjusted with 0.1 M NaOH and 0.1 M HCl solutions.

pH 7.4. Therefore, these p(RUT) micro/nanogels could be effective for transportation or activation/inactivation mechanisms of various positively-charged amino acids, proteins, enzymes, and vitamins as well as metal ions during biological reactions.

Enzyme activity of RUT and p(RUT) micro/nanogels was investigated on α-glucosidase enzyme, which regulates starch hydrolysis and some disaccharide to the monosaccharide units in the body. It was concluded that RUT and p(RUT) micro/nanogels stimulated the enzyme α-glucosidase. Hence, alpha-glucosidase fraction activities of RUT and p(RUT) micro/nanogels are shown in Fig. 4a and 4b.

As shown in Fig. 4a, RUT monomer has no significant activity against the enzyme with slight stimulation of alpha-glucosidase with 1.15±0.1 fraction value at 50 μg/mL concentration, a decline in activity up to 125 μg/mL and then no effect until 250 μg/mL. The alpha-glucosidase enzyme activity in the presence of p(RUT) micro/nanogels on the other hand gradually increased between 50 and 750 μg/mL with fractional activity changing from 1.2±0.3 to 1.5±0.7 as seen in Fig. 4b.

In the literature, many studies reported that inhibition or stimulation activity of alpha-glucosidase enzyme in the

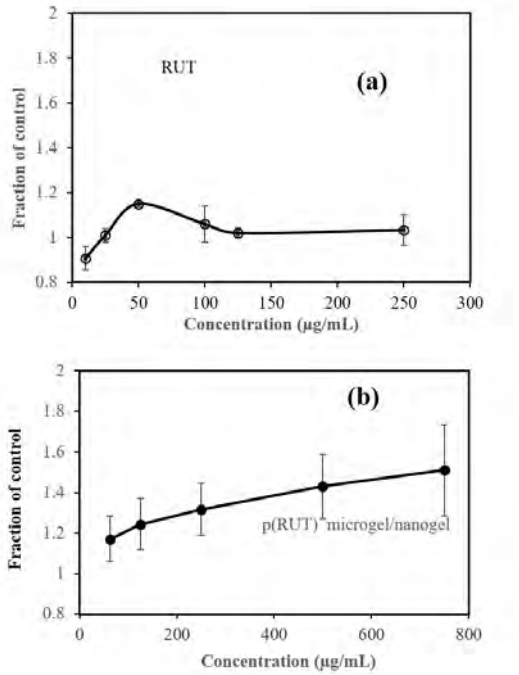

Figure 4. Fraction activity of alpha-glucosidase enzyme with (a) RUT and (b) p(RUT) micro/nanogels.

presence of phenolic materials depends on the molecular structure of flavonoids [28,29]. Alam et al. reported that the well-known flavonoid quercetin can inhibit the alpha-glucosidase enzyme prepared in butanol, ethyl acetate, hexane, and methanol solutions [29]. Another study stated that naringin molecule, a phenolic compound with two sugar units, could not inhibit the alpha-glucosidase enzyme with slight stimulating effects [19]. Very similar results were obtained for enzyme activity of RUT with naringin phenol due to the sugar unit in the chemical structure of RUT. Moreover, Dubey et al. mentioned that RUT monomer dissolved in DMSO could inhibit the alpha-amylase and alpha-glucosidase enzymes to some extent [30]. DMSO was not chosen for in vivo applications as an organic solvent because of toxicity and RUT monomer shows slight solubility in aqueous medium as buffer solutions. In addition to enzyme stimulation effects of sugar units of phenolics, lower solubility of RUT should affect the enzyme activity oppositely. Alam et al. reported that RUT is more stable against oxidation when compared with quercetin with sugar-free structure [29]. Another probability is that this stability may have been effective on its interaction with the enzyme. Our results support that p(RUT) micro/nanogels can stimulate alpha-glucosidase enzyme and this material could be used to trigger the digestion of a wide range of carbohydrates including starch, amylose, amylopectin, dextrins, maltooligosaccharides, etc. which contain alpha(1-4) or alpha(1-6) glycosidic bonds [31].

Fibrinogen is a well-known protein in the blood which plays a significant role in coagulation of blood. Phenolic compounds can interact with some proteins like fibrinogen and may affect their biological functions [20]. Therefore, the fibrinogen interaction effects of RUT and p(RUT) microgel/nanogel were investigated to find the blood compatibility of materials. As shown in Fig. 5a and 5b, RUT and p(RUT) micro/nanogels were interacted with fibrinogen at 0-250 µg/mL concentrations.

Fibrinogen has highest emission intensity at 340 nm wavelength at 0.1 mg/mL concentration in DI water with almost 64700 intensity. As can be seen in Fig. 5a, the intensity of the fibrinogen peak started to decrease after interaction with increasing concentrations of RUT. The intensity of the fibrinogen peak was nearly six-fold decreased at 250 µg/mL RUT concentration. In addition, p(RUT) micro/nanogels could slightly reduce the intensity of fibrinogen peaks up to 250 µg/mL of p(RUT) micro/nanogel concentration, as seen in Fig 5b.

It is apparent from Fig. 5c that p(RUT) micro/nanogels were not as effective as RUT molecules in interacting with fibrinogen molecules which play an important role in the coagulation of blood. These results support that p(RUT) micro/nanogels showed more blood compatibility than RUT molecule even at high concentrations with no significant effects on the biological functions of fibrinogen due to molecular interactions.

The antioxidant capacity of RUT and p(RUT) micro/nanogels was investigated by total flavonoid content (TFC) and ferric reducing antioxidant power (FRAP). TFC values of RUT and p(RUT) micro/nanogels at different concentrations are given as gallic acid equivalent (GA eq) in Fig. 6a.

The TFC value of RUT at 250 µg/mL concentration was 445.0±22.5 GA eq, but p(RUT) microgel/nanogel had a value of 251.3±20.2 GA eq TFC at the same concentration. RUT is a flavonoid used as a reference substance in TFC antioxidant tests. These results with high flavonoid content values were also obtained with the polymeric form of RUT. Furthermore, FRAP assay, known as the Fe (III) reduction test, is another antioxidant test which was performed for RUT and p(RUT) microgel/nanogel. Gallic acid (GA) was taken as reference antioxidant material for the FRAP test. As shown in Fig. 6b, 5 µg RUT and p(RUT) microgel/nanogels reduced to 19.04±3.37 and 1.75±0.27 µmol Fe (II) levels, respectively. These antioxidant tests confirm that p(RUT) microgel/nanogels have promising antioxidant ability with high TFC values and significant Fe(III) reducing ability for Fe(II) even at low concentrations. Kurisawa et al. prepared poly(rutin) by the oxidative polymerization reaction of RUT with laccase enzyme [32]. This study indicated that water soluble rutin polymer has significant superoxide scavenging capacity and high preventive ability for oxidative stress on endothelial cells related to the high antioxidant activity

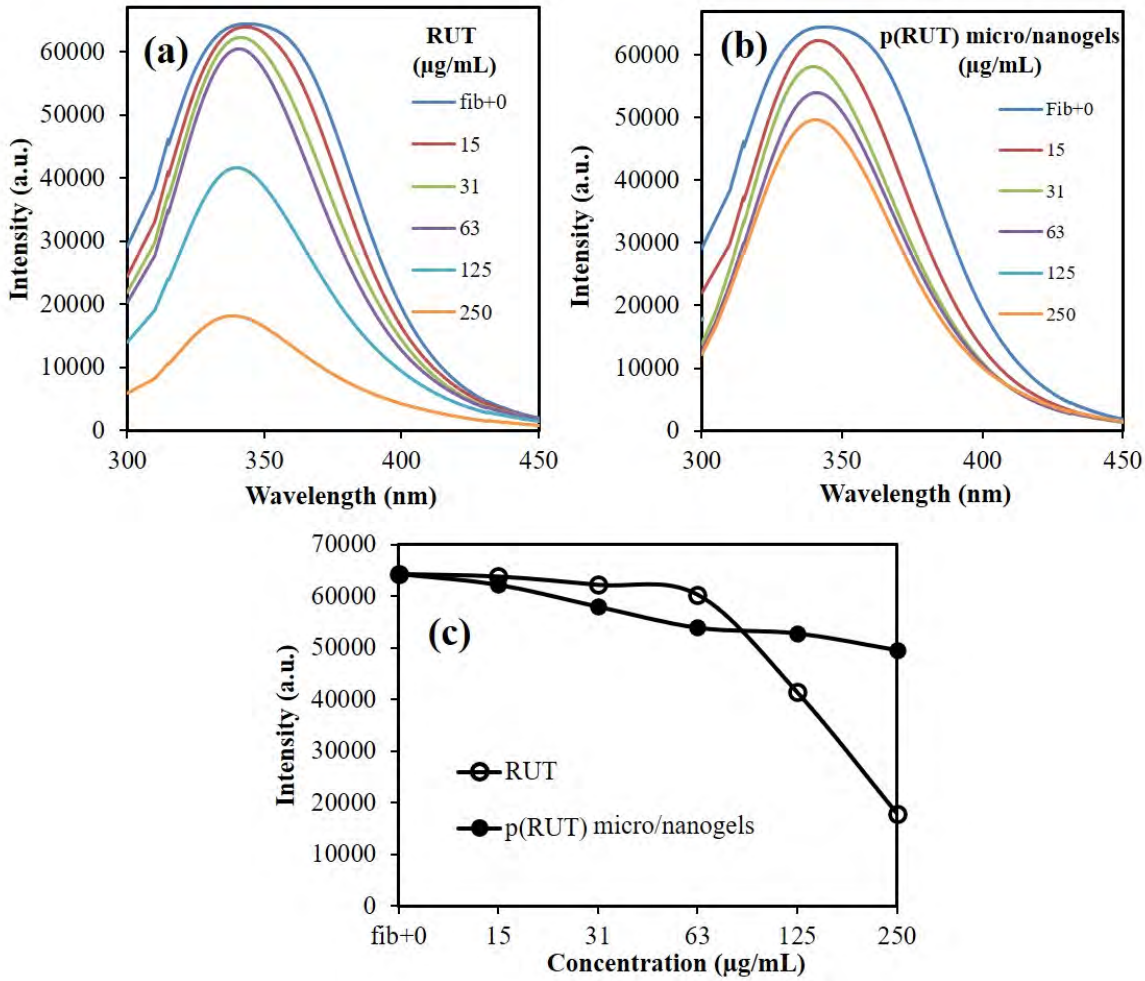

Figure 5. Fibrinogen interaction of (a) RUT and (b) p(RUT) micro/nanogels at different concentrations. (c) Emission intensity of RUT and p(RUT) micro/nanogel interactions at 340 nm wavelength.

[32]. Similarly, our results supported that p(RUT) microgel/nanogels have promising antioxidant capacity according to different antioxidant analyses.

Phenolic-based materials can used as metal chelator to regulate metal ion absorption at the required level and forms in the blood. Metal chelators are used to provide systemic iron homeostasis in the treatment of some neurodegenerative diseases such as Alzheimer and Parkinson [33]. The Fe (II) chelating capacity of RUT and p(RUT) microgel/nanogels in DI water was studied and the results are given in Fig 7.

While the RUT molecule did not chelate Fe (II), p(RUT) microgel/nanogels chelated Fe (II) at an increasing rate depending on the concentration. The Fe (II) chelating ability of p(RUT) micro/nanogels at 500 µg/mL concentration was 43.1±17.4 %. Pivec et al. prepared poly(rutin) by enzymatic polymerization of RUT and investigated the Fe (II) chelating ability of these materials. They found that high concentration of poly(rutin) at 5000 µg/mL concentration had nearly 70% Fe (II) chelation activity [34]. These results indicate that crosslinked p(RUT) microgel/nanogels had more Fe (II) chelating ability that poly(rutin) which was prepared by oxidative polymerization. Therefore, p(RUT) microgel/nanogels can be used as a metal chelator in the treatment of some neurological diseases.

CONCLUSION

Degradable p(RUT) micro/nanogels were synthesized as a therapeutic material to investigate their biological activity on different biological functions including enzyme activity, fibrinogen interaction, antioxidant capacity and Fe chelating ability. According to the low isoelectric point and pKa value at pH 2.85 and 2.16, respective, p(RUT) micro/nanogels have a negatively-charged surface at physiological conditions. It is stated in the literature that flavonoids inhibit α-glucosidase enzyme. However, the dissolved RUT and suspended p(RUT) micro/nanogels in the phosphate buffer did not inhibit the enzyme's activity. The effects of flavonoids containing sugar groups

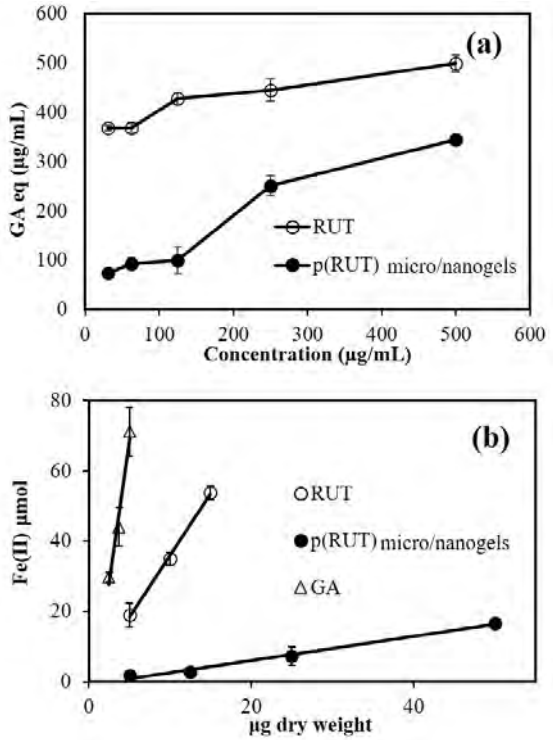

Figure 6. (a) Total flavonoid content values of RUT and p(RUT) micro/nanogels at different concentrations. (b) Ferric reducing antioxidant power (FRAP) values of RUT and p(RUT) micro/nanogels at different concentrations. (Gallic acid was used as standard antioxidant)

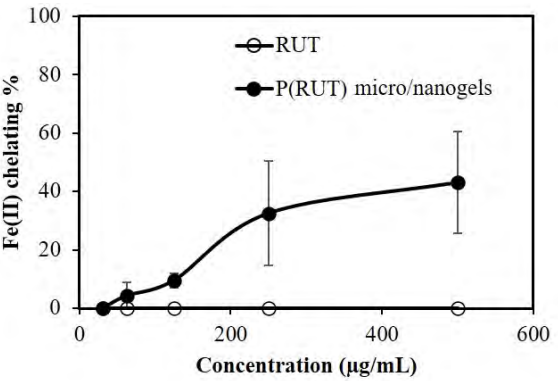

Figure 7. Fe (II) chelating activity of RUT and p(RUT) microgel/nanogels at different concentrations.

in their structure on enzymes should be investigated in more detail and even supported by in vivo studies. RUT and p(RUT) microgel/nanogel may have potential for use in the treatment of glycogen storage diseases. For such research, extensive applications should be performed. Moreover, RUT interacts extensively with fibrinogen, but p(RUT) micro/nanogels were observed to have less interaction ability with fibrinogen. By examining the interaction of fibrinogen, a blood protein, p(RUT) microgel/nanogels are more suitable for intravenous applications. Furthermore, p(RUT) microgel/nanogels had promising antioxidant ability with high total flavonoid content. In addition, p(RUT) microgel/nanogels could provide systemic iron homeostasis with their ability to reduce Fe(III) to Fe(II) and significant Fe(II) chelating activity.

ACKNOWLEDGEMENT

The authors wish to thank BAP of Canakkale Onsekiz Mart University (COMU). This work was supported by COMU-BAP through research grant no. FDH 2018-2734. Also, the authors are grateful to Prof. Dr. Nurettin Sahiner for providing support in carrying out most of the experiments.

CONFLICT OF INTEREST

Authors approve that to the best of their knowledge, there is not any conflict of interest or common interest with an institution/organization or a person that may affect the review process of the paper.

AUTHOR CONTRIBUTION

Authors Mehtap Sahiner and Selin Sagbas Suner designed the study together. The experiments were performed by Mehtap Sahiner and Selin Sagbas Suner together. The results are pointed out with equal contribution. The authors have contributed to this research equally.

References

1. Zhang Z, Yang L, Hou J, Tian S, Liu Y. Molecular mechanisms underlying the anticancer activities of licorice flavonoids. Journal of Ethnopharmacology 267(2021) 113635. doi: 10.1016/j.jep.2020.113635
2. Pratheeshkumar P, Budhraja A, Son Y-O, Wang X, Zhang Z, Ding S, et al. Quercetin inhibits angiogenesis mediated human prostate tumor growth by targeting VEGFR- 2 regulated AKT/mTOR/P70S6K signaling pathways. PLoS ONE. 7(10) (2012) e47516. doi: 10.1371/journal.pone.0047516
3. Machado DG, Bettio LEB, Cunha MP, Santos ARS, Pizzolatti MG, Brighente IMC, et al. Antidepressant-like effect of rutin isolated from the ethanolic extract from Schinus molle L. in mice: Evidence for the involvement of the serotonergic and noradrenergic systems. European Journal of Pharmacology 587(1–3) (2008) 163–168. doi: 10.1016/j.ejphar.2008.03.021
4. Gao L, Schäfer C, O'Reardon K, Gorgus E, Schulte-Hubbert R, Schrenk D. The mutagenic potency of onion juice vs. its contents of quercetin and rutin. Food and Chemical Toxicology 148(2021) 111923. doi: 10.1016/j.fct.2020.111923
5. Ganeshpurkar A, Saluja AK. The Pharmacological Potential of Rutin. Saudi Pharmaceutical Journal 25(2) (2017) 149–164. doi: 10.1016/j.jsps.2016.04.025
6. Montes A, Wehner L, Pereyra C, Martínez de la Ossa EJ.

Precipitation of submicron particles of rutin using supercritical antisolvent process. The Journal of Supercritical Fluids 118(2016) 1–10. doi; 10.1016/j.supflu.2016.07.020

7. Ekaette I, Saldaña MDA. Ultrasound processing of rutin in food-grade solvents: Derivative compounds, antioxidant activities and optical rotation. Food Chemistry 344(2021) 128629. doi: 10.1016/j.foodchem.2020.128629
8. Baldissera MD, Souza CF, Zanella R, Prestes OD, Meinhart AD, Da Silva AS, et al. Behavioral impairment and neurotoxic responses of silver catfish Rhamdia quelen exposed to organophosphate pesticide trichlorfon: Protective effects of diet containing rutin. Comparative Biochemistry and Physiology Part C: Toxicology & Pharmacology 239(2021) 108871. doi: 10.1016/j.cbpc.2020.108871
9. Sahiner N, Sagbas S, Sahiner M, Aktas N. Degradable natural phenolic based particles with micro- and nano-size range. Recent Patents on Materials Science 11(1) (2018) 33–40. doi: 10.2174/1874464811666180724124614
10. Oboh G, Adebayo AA, Ademosun AO, Olowokere OG. Rutin restores neurobehavioral deficits via alterations in cadmium bioavailability in the brain of rats exposed to cadmium. NeuroToxicology 77(2020) 12–19.
11. Habtemariam S. Rutin as a natural therapy for alzheimer's disease: insights into its mechanisms of action. Current Medicinal Chemistry 23(9) (2016) 860–873. doi: 10.2174/0929867323666160217124333
12. Kirschweng B, Tilinger DM, Hégely B, Samu G, Tátraaljai D, Földes E, et al. Melt stabilization of PE with natural antioxidants: Comparison of rutin and quercetin. European Polymer Journal 103(2018) 228–237. doi: 10.1016/j.eurpolymj.2018.04.016
13. Kook D, Wolf AH, Yu AL, Neubauer AS, Priglinger SG, Kampik A, et al. The protective effect of quercetin against oxidative stress in the human RPE in vitro. Investigative Opthalmology & Visual Science 49(4) (2008) 1712. doi: 10.1167/iovs.07-0477
14. Anderson CQ, Wechter E, Siegmund LA. Glycogen storage disease type I: don't miss the signs. The Journal for Nurse Practitioners 16(6) (2020) 442–446. doi: 10.1016/j.nurpra.2020.02.025
15. Marusic T, Zerjav Tansek M, Sirca Campa A, Mezek A, Berden P, Battelino T, et al. Normalization of obstructive cardiomyopathy and improvement of hepatopathy on ketogenic diet in patient with glycogen storage disease (GSD) type IIIa. Molecular Genetics and Metabolism Reports 24(2020) 100628. doi:10.1016/j.ymgmr.2020.100628
16. Tager JM, Oude Elferink RPJ, Reuser A, Kroos M, Ginsel LA, Fransen JAM, et al. α-Glucosidase Deficiency (Pompe's Disease). Enzyme. 38(1–4) (1987) 280–285.doi: 10.1159/000469217
17. Van Kooten HA, Roelen CHA, Brusse E, Van der Beek NAME, Michels M, Van der Ploeg AT, et al. Cardiovascular disease in non-classic Pompe disease: A systematic review. Neuromuscular Disorders 31(2) (2021) 79–90. doi: 10.1016/j.nmd.2020.10.009
18. Sahiner N. One step poly(rutin) particle preparation as biocolloid and its characterization. Materials Science and Engineering: C 44(2014) 9–16. doi: 10.1016/j.msec.2014.08.009
19. Sahiner M, Sahiner N, Sagbas S, Fullerton ML, Blake DA. Fabrication of Biodegradable Poly(naringin) Particles with Antioxidant Activity and Low Toxicity. ACS Omega 3(12) (2018) 17359–17367. doi: 10.1021/acsomega.8b02292
20. Deng L, Qi Y, Liu Z, Xi Y, Xue W. Effect of tannic acid on blood components and functions. Colloids and Surfaces B: Biointerfaces 184(2019) 110505. doi: 10.1016/j.colsurfb.2019.110505
21. Li Y, Ma D, Sun D, Wang C, Zhang J, Xie Y, et al. Total phenolic, flavonoid content, and antioxidant activity of flour, noodles, and steamed bread made from different colored wheat grains by three illing methods. The Crop Journal 3(4) (2015) 328–334. doi: 10.1016/j.cj.2015.04.004
22. Firuzi O, Lacanna A, Petrucci R, Marrosu G, Saso L. Evaluation of the antioxidant activity of flavonoids by "ferric reducing antioxidant power" assay and cyclic voltammetry. Biochimica et Biophysica Acta (BBA) - General Subjects 1721(1–3) (2005) 174–184. doi:10.1016/j.bbagen.2004.11.001
23. Tadapaneni RK, Banaszewski K, Patazca E, Edirisinghe I, Cappozzo J, Jackson L, et al. Effect of high-pressure processing and milk on the anthocyanin composition and antioxidant capacity of strawberry-based beverages. Journal of Agricultural and Food Chemistry 60(23) (2012) 5795–5802. doi: 10.1021/jf2035059
24. Suner SS, Sahiner M, Ayyala RS, Bhethanabotla VR, Sahiner N. Nitrogen-Doped Arginine Carbon Dots and Its Metal Nanoparticle Composites as Antibacterial Agent. C—Journal of Carbon Research 6(3) (2020) 58. doi: 10.3390/c6030058
25. Zhang D, Ouyang Q, Hu Z, Lu S, Quan W, Li P, et al. Catechol functionalized chitosan/active peptide microsphere hydrogel for skin wound healing. International Journal of Biological Macromolecules 173(2021) 591–606. doi: 10.1016/j.ijbiomac.2021.01.157
26. Anderson AJ, Grey E, Bongiardina NJ, Bowman CN, Bryant SJ. Synthesis and Characterization of Click Nucleic Acid Conjugated Polymeric Microparticles for DNA Delivery Applications. Biomacromolecules 22 (2021) 1127-1136. doi: 10.1021/acs.biomac.0c01563
27. Decuzzi P, Godin B, Tanaka T, Lee SY, Chiappini C, Liu X, et al. Size and shape effects in the biodistribution of intravascularly injected particles. Journal of Controlled Release 141(3) (2010) 320–327. doi: 10.1016/j.jconrel.2009.10.014
28. Sahiner N, Sagbas S, Sahiner M, Blake DA, Reed WF. Polydopamine particles as nontoxic, blood compatible, antioxidant and drug delivery materials. Colloids and Surfaces B: Biointerfaces. 172(2018) 618–626. doi: 10.1016/j.colsurfb.2018.09.019
29. Alam MA, Zaidul ISM, Ghafoor K, Sahena F, Hakim MA, Rafii MY, et al. In vitro antioxidant and, α-glucosidase inhibitory activities and comprehensive metabolite profiling of methanol extract and its fractions from Clinacanthus nutans. BMC Complementary and Alternative Medicine 17(1) (2017) 181. doi: 10.1186/s12906-017-1684-5
30. Dubey S, Ganeshpurkar A, Ganeshpurkar A, Bansal D, Dubey N. Glycolytic enzyme inhibitory and antiglycation potential of rutin. Future Journal of Pharmaceutical Sciences 3(2) (2017) 158–162. doi: 10.1016/j.fjps.2017.05.005
31. Tomasik P, Horton D. Enzymatic conversions of starch. In: Advances in Carbohydrate Chemistry and Biochemistry. 1st ed. Elsevier Inc.; 2012. p. 59–436. doi: 10.1016/B978-0-12-396523-3.00001-4
32. Kurisawa M, Chung JE, Uyama H, Kobayashi S. Enzymatic synthesis and antioxidant properties of poly(rutin). Biomacromolecules 4(5) (2003) 1394–1399. doi: 10.1021/bm034136b
33. Zhou T, Ma Y, Kong X, Hider RC. Design of iron chelators with therapeutic application. Dalton Transactions 41(21) (2012) 6371–6389. doi: 10.1039/c2dt12159j
34. Pivec T, Kargl R, Maver U, Bračič M, Elschner T, Žagar E, et al. Chemical structure-antioxidant activity relationship of water-based enzymatic polymerized rutin and itswound healing potential. Polymers 11(10) (2019) 1566. doi: 10.3390/polym11101566.

Hittite Journal of Science and Engineering, 2021, 8 (2) 189–195
ISSN NUMBER: 2148–4171
DOI: 10.17350/HJSE19030000229

The Prevalence of Neoplasm Diseases and Investigation of Some Biochemical Serum Parameters

Hasan Karagecili[1] Emrah Yerlikaya[2] Mustafa Oguzhan Kaya[3]
[1]Siirt University, Department of Nursing, Siirt, Turkey
[2]Siirt University, Department of Nutrition and Dietetics, Siirt, Turkey
[3]Kocaeli University, Department of Chemistry, Kocaeli, Turkey

Article History:
Received: 2021/04/20
Accepted: 2021/06/02
Online: 2021/06/30

***Correspondence to**: Hasan Karagecili, Siirt University, Faculty of Health, Department of Nursing, 56100 Siirt, Turkey*
E-Mail: hasankaragecili@siirt.edu.tr
Phone: +90 (484) 223 12 24
Fax:+90 (484) 223 51 56

ABSTRACT

Aim: We aimed in this work to investigate the skin, lung, and bone marrow-related cancer prevalence and biochemical serum parameters of all these cancer patients.
Materials and Methods: The skin, lung, and bone marrow cancer patient's biochemical serum data examined retrospectively using a hospital information system.
Results: Basal cell carcinoma patients number recorded as 155 with 63%, squamous cell carcinoma patients number were enrolled in73 with 30% and, malign melanoma patients number noted as 10 with 4%. Skin cancers were the most seen cancer type in 246 patients with 22% between 2013-2017 years. All cancer patient numbers were 1134 between these years. The common incidences of basal cell carcinoma and squamous cell carcinoma cancers observed on the upper part of the body, respectively on the face-cheek, nose, ear, eyelid, and lip. In this study, there was a significant difference among skin cancer patient's serum glucose, aspartate aminotransferase, alanine aminotransferase, sodium, bilirubin direct, bilirubin total, creatinine, urea level, and control group serum parameters level, $p<0.05$. The lung cancer patient numbers were 119 with 10.4%, bone marrow patients numbers were 113 with 10%. Two cancer groups were statistically different in terms of 5-years survival. Log Rank $X^2 = 8.68$, $p<0.05$.
Conclusions: We recorded that skin cancer types and regions on the upper parts of the body were more because of exposure to the sun. The lung cancer survival rate was lower than bone marrow cancer. Moreover, we strongly emphasized that measuring the biochemical serum parameters was statistically significant with the diagnosis of cancer patients.

Keywords:
Carcinoma; Malignant; Skin cancer; Lung; Incidence; Bone marrow.

INTRODUCTION

Cancer is a very complex illness happening via genetic variation or anomaly that allows the conversion of healthy cells into disordered cells, which results in interaction among the genetic factors and environmental factors [1]. Skin is the prevalent malignant neoplasms site. Skin cancers have a higher incidence than others in summation [2]. Skin cancer constitutes a prevalent group of malignant neoplasms among white people. The frequency of melanoma and non-melanoma skin cancer (NMSC) increased throughout the world [3]. Skin cancers include basal cell carcinoma (BCC) and squamous cell carcinoma (SCC), generally called NMSC, and melanoma skin cancers are the most recurrent cancer both in America and in other developed countries with mostly fair-skinned people [4]. Melanoma is the utmost mortal type of skin cancer and has turned into one of the widespread cancers among people in their teens in Canada, especially for women. Among all NMSC examples, almost 77% are BCC, and 23% are SCC. Even though seldom mortal, the high ratio of NMSC indicates a notable load of illness in the way of morbidity, the standard of living, social effect, and healthcare expenditures [5]. The incidences of skin cancers were found high in Australia. It has four times more prevalence than other whole cancers [6]. Melanoma and NMSC's risk factors include exposure to ultraviolet (UV) radiation and the susceptibility of a person's skin to UV radiation [7]. Also to X-rays, Human papilloma virüs, arsenic compounds, and other chemical products [8]. The commonly seen region of NMSC is on the head and neck area, and surgery remains the mainstay of treatment [9]. Lung cancer is the most common cancer in the world. It is one of the deadliest and most aggressive types of cancer, with a 5-years survival rate of barely 15%. Every year 1.7

million people die of lung cancer in the world. 80-90% of lung cancer cases are due to smoking, making lung cancer one of the most preventable cancer types [10]. The two main types of lung cancer are non-small cell lung cancer (NSCLC) and small cell lung cancer (SCLC). There are three types of NSCLC; 40% of the cases are adenocarcinoma, 30% of squamous cell carcinoma (SCC), and 15% of large cell carcinomas. The Small cell lung cancer rate is 15%. These tumors are classified by histology, and as the size of biopsy specimens becomes smaller, the assessment of immunohistochemistry plays an important role [11]. Bone marrow is the primary hematopoietic organ involved in many malignant diseases, include acute and chronic leukemia, multiple myeloma, myelodysplastic syndrome, and bone metastasis from solid tumors [12]. We aimed to identify the incidence of skin cancers, lung cancers, and bone marrow cancers, according to type in the Siirt province. And to compare the incidence of them with other regions, with this analysis at first, to provide up-to-date prevalence approximate by sex, age, body site, survival; and second, to research the levels of some serum parameters in cancers patients and healthy person comparatively.

MATERIALS AND METHODS

Before starting to work, both the Public Health Directorate and the Siirt State hospital preauthorization documents were about the feasibility of the work. In this study, the files of patients who applied to Siirt State Hospital and Siirt Public Health units and were diagnosed with a neoplasm or malign were between 2013-2017. Patients were diagnosed with neoplasm constituted the experimental group, and healthy subjects were the control group. The study is a retrospective study. The files of the patients were diagnosed with neoplasm were applied to the polyclinics evaluated. Our work was on women and men. The study was composed of experimental and control groups. The experimental group consisted of patients with various neoplasms (skin cancers, lung cancer, bone marrow cancer), and the control group consisted of healthy subjects who received routine control. Fasting blood glucose, amylase, alanine aminotransferase (ALT), aspartate aminotransferase (AST), lactate dehydrogenase (LDH), electrolytes values , and biochemical findings retrospectively took from patient files. Biochemical parameters studied in the biochemistry laboratory of Siirt State Hospital using Advia autoanalyzer 1800. Cancer statistics collected with an active cancer registry system in many countries of the world. While the active cancer registry was in only two provinces of our country in 2002, it was put into practice in 81 Provinces as of 2013. Statistical analyzes performed using the SPSS 21. 0 statistical program for Windows to evaluate the data obtained from patient files and the hospital information system. Independent student t-test was used for parametric tests when data distributed normally. P values were less than 0.05 were assigned statistically.

RESULTS

Skin cancers: In 2013, the number of skin cancer patients was 66 in 235 cancer cases, and the skin cancer rate was 28%. In 2014, the number of cancer patients was 321, and the number of skin cancer patients number was 57, and the rate was 17.7%. In 2015, the number of cancer patients was 314, and the number of skin cancer cases was 52 and 16.5%. In 2016, the number of cancer patients was 124, and in 36 skin cancer cases detected, and the rate was 29%. In 2017, the number of cancer patients recorded 140, and the ratio of skin cancer's in all cancers was 25%. In 2013, the number of patients with BCC 37; 21 males and 16 females, 23 patients with SCC; 14 males and nine females. Three male malignant melanoma patients. The number of BCC patients in 2014 was 31; 17 males and 14 females, Number of SCC patients 20; 14 males and six females. It was two males and one female malignant melanoma patient. The number of BCC patients in 2015 was 34; 19 males and 15 females, the number of SCC patients was 19; 14 males and five females. one male and one female malignant melanoma patient recorded. The number of patients with BCC in 2016 was 25; 12 male and 13 female, the number of SCC patients were six; four males and two females. One male malignant melanoma, one male Kaposi's sarcoma, and one female Kaposi's sarcoma were. In 2017, the number of patients with basal cell cancer was 28; 13 males and 15 females, number of SCC patients were five; three males and two females. One female malignant melanoma was. Among the related years, 143 male skin cancer patients and 103 female skin cancer patients were. The overall skin cancer rate in men was 58%, while the skin cancer rate in women was 42%. Blood serum data of patients with malignant melanoma, BCC, and SCC cancer evaluated retrospectively using a hospital information system. The incidence of patients determined. The number of BCC patients was 155 with 63%, and the number of SCC patients was 73 with 30%, and the number of patients with malignant melanoma was 10 with 4%. The most common type of cancers are skin cancers, and the rate of it among five years in all cancers types recorded as 22% with a total of 246 patients. Non-melanoma, the most common skin cancers; the most common incidences of BCC and SCC cancers was observed on the upper part of the body, respectively on the face-cheek, nose, ear, eyelid, and lip at table 1.

The number of skin cancers was observed in approximately 49 patients each year. The incidence of skin cancers

Table 1. The incidence of skin cancer in the body region of patients.

Location	BCC n	%	SCC n	%	Total n	% Total
Nose	23	17.5	5	3.8	28	21.3
Face-Cheek	29	22.1	6	4.5	35	26.7
Ear	13	9.9	10	7.6	23	17.5
Lip	6	4.5	9	6.8	15	11.4
Neck	6	4.5	2	1.5	8	6.1
Eye Lid	19	14.5	3	2.2	22	16.7
Total	96	73	35	27	131	100

was detected in almost 16 patients in the 100000 population in Siirt. All cancer incidence found as 76 patients in 100000 population. Between the given years the number of all cancer patients was calculated as 1134 years. Serum parameters levels of skin cancer patients compared with the control group serum parameters. In this study, skin cancer patient's serum glucose, AST, ALT, sodium, bilirubin direct, bilirubin total, creatinine, urea level were statistically significantly different compared with the control group's serum parameters levels, p <0.05. It can be seen below from the group's statistics, table 2.

Lung and bone marrow cancers, In 2013, 23 out of 235 cancer cases, 9.8% were Lung cancer. The number of bone marrow cancer patients was 19 and 8%. In 2014, the number of cancer patients was 321, and the number of lung cancer cases was 38, with a rate of 11.8%. Bone marrow cancer cases were 35 and 11%. In 2015, the number of cancer patients was 312, and the number of lung cancer cases was 37 and 16.5%. Bone marrow cancer cases were 31 and 9.6%. In 2016, the number of cancer patients was 124, and Lung cancer detected in 12 cases, the rate was 9.7%. Bone marrow cancer cases are 12 and 9.7%. In 2017, the number of cancer patients recorded 140, the number of lung cancers among all cancers was nine, and their rate was 6.4%. Bone marrow cancer cases were 16 and 11.4%. 2013 Number of lung cancer patients was 23; 17 Male and 6 Female, Number of bone marrow cancer patients were 19; 14 Men and 5 Women. 2014 Number of lung cancer patients was 38; 30 Male and 8 Female, Number of bone marrow cancer patients were 35; 22 males and 13 females. 2015 Number of lung cancer patients was 37; 31 Male and six females, Number of bone marrow cancer patients were 31; 23 Men and 8 Women. 2016 Number of lung cancer patients was 12; six males and six females, number of bone marrow cancer patients were 12; eight males and four females. 2017 Number of lung cancer patients was 9; nine Mae. The number of bone marrow cancer patients was 16; eight male and eight females. Between 2013 and 2017, 93 male lung cancer patients and 26 female lung cancer patients registered. The proportion of the total number of lung cancer patients seen in men was 78%, and the proportion of

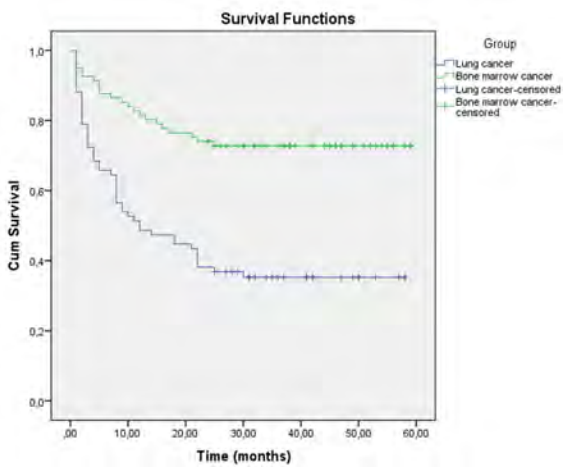

Figure 1. Kaplan-Meier, survival of lung cancer and bone marrow cancer patiens between 2013-2017 years.

women was 22%. Between 2013-2017, 75 male bone marrow cancer patients and 38 female bone cancer patients registered. The proportion of bone marrow cancer patients in the total number of patients with bone marrow cancer was 66.4%, and the rate of women was 33.6%. The number of lung cancer patients was recorded as 119 to 10.4%, while the number of bone marrow patients was 113 to 10%. The incidence of lung cancer was approximately 24 each year, and the number of bone marrow cancer patients was 23 each year. The number of all cancer patients calculated as 1134 between these years. The number of patients with lung cancer was 76, and the number of patients with bone marrow cancer was 81.49 (64.5%) of lung cancer patients, and 22 (27.2%) of bone marrow cancer patients died between these years. Kaplan-Mier test shows the comparison of two disease group's statistical differences within using long rank, Breslow, and Tarone-Ware tests. p<0,05. Fig. 1.

In 2013, for 5-year survival analysis, the number of patients with lung cancer was 23, and the number of patients with bone marrow cancer was 19. 16 (69.6%) of the lung cancer patients and 4 (21.1%) of the bone marrow cancer patients died. Two cancer groups were statistically different in terms of 5-years survival according to three tests. Graph 1. Kaplan-Miear survival analysis. Log Rank X^2 = 8.68, p = 0.001, p<0.05. Breslow X^2 = 7,249, p = 0.007, p<0.05. Tarone-Ware X^2 = 8.009, p = 0.005, p<0.05. Fig. 2.

In this study, there was a statistically significant difference between lung cancer and bone marrow cancer patient's serum glucose, AST, GGT, LDH, urea level compared with the control group's serum parameters levels, p<0.05. Cancer patient's biochemical serum markers Pearson Correlation analyses did. As shown in table 3.

There was a positive correlation between serum levels of AST and LDH. A positive relationship was between se-

Table 2. The skin cancer patient and control group statistics.

	Patient Group				Control Group			
	N	*Mean*	*Std. Deviation*	*Std. Error Mean*	*N*	*Mean*	*Std. Deviation*	*Std. Error Mean*
Age	36	59,0556	22,46896	3,74483	40	39,5500	13,97424	2,20952
Glucose mg/dl	36	106,5000	28,47906	4,74651	40	95,8500	11,21023	1,77249
Creatinine mg/dl	36	0,9214	0,24316	0,04053	40	0,7558	0,16659	0,02634
AST U/L	36	22,5278	6,70388	1,11731	40	18,1000	5,75482	0,90992
ALT U/L	36	18,4167	6,55689	1,09282	40	32,6500	9,84899	1,55726
GGT U/L	27	29,5185	25,11262	4,83293	36	20,5278	10,86406	1,81068
Amylase U/L	25	72,2800	36,92167	7,38433	34	65,0294	24,24807	4,15851
LDH U/L	30	258,2000	124,52375	22,73482	35	176,1714	43,11031	7,28697
Biluribin D. mg/dl	23	0,2426	0,25234	0,05262	39	0,1328	0,05652	0,00905
Sodium mmol/L	35	139,7143	4,42966	0,74875	35	137,6857	1,81126	0,30616
Potassium mmol/L	34	4,2676	0,44635	0,07655	35	4,2086	0,46233	0,07815
Albumin g/dl	25	4,1920	0,46361	0,09272	32	3,9438	0,67151	0,11871
Bilirubin T. mg/dl	24	0,6992	0,33521	0,06842	40	0,5290	0,23366	0,03695
Phosphor mg/dl	18	3,0389	0,71549	0,16864	28	3,5643	0,53070	0,10029
Calcium mg/dl	30	9,0757	0,55776	0,10183	37	9,1262	0,44774	0,07361
Magnesium mg/dl	19	2,1474	0,57083	0,13096	31	1,9484	0,16707	0,03001
Uric Acid mg/dl	17	4,1412	1,38251	0,33531	28	4,0143	1,10913	0,20960
Urea mg/dl	36	34,2444	12,36436	2,06073	40	23,5063	6,38312	1,00926
Chlore mmol/L	22	101,6364	3,86123	0,82322	34	103,3529	1,73873	0,29819

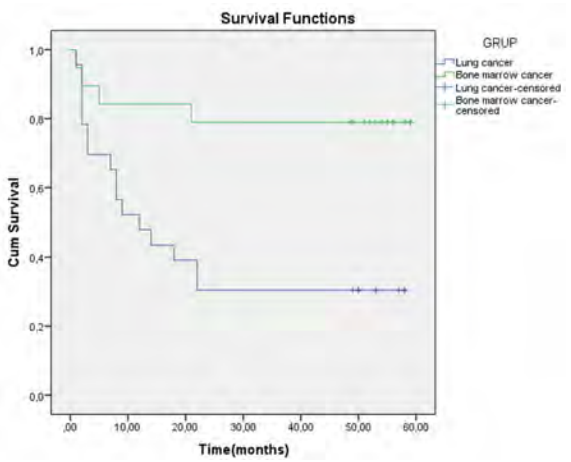

Figure 2. Kaplan-Meier, 5-years survival of lung cancer and bone marrow cancer patients.

rum AST and LDH levels. Their levels increased in a correlatively (r= 0,490**, p=0,001). Fig. 3.

In this study, there was a positive correlation (r= 0,534**, p=0,001) between serum levels of ALT and Uric acid. Fig. 4.

AST and Urea levels were found correlated positively. (r= 0,602**, p=0,001). Fig. 5.

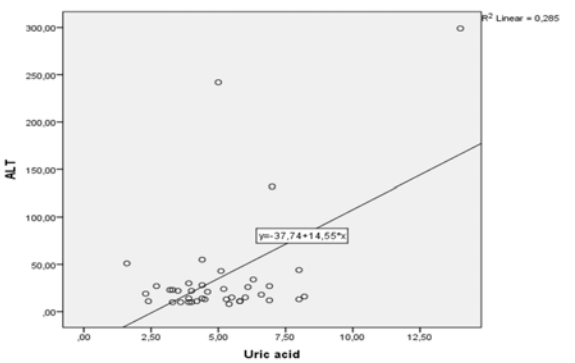

Figure 3. Serum AST and LDH levels correlation.

DISCUSSION

Risk factors of skin cancers include; having light skin color, excessive sunlight, exposure to X-rays, exposure to chemicals such as coal tar or arsenic, a family history of skin cancer, diseases of genetic repair disorders [13]. When the cases evaluated in terms of incidence, the most common type of cancer was skin cancer (27. 7%) in Hatay in 2008 [14]. We also detected that the most observed cancer type in Siirt was skin cancer too. The rate of five years in all cancers recorded as 22% in Siirt. When the

Table 3. Skin, lung, and bone marrow cancer patients biochemical serum markers Pearson Correlation analysis.

		Creatinin mg/dl	AST U/L	ALT U/L	LDH U/L	Potassium mmol/L	Albumin g/dl	Bilirubin total mg/dl	Uric acid mg/dl	Urea mg/dl
Creatinin mg/dl	Pearson Correlation	1	,169	,119	,053	,333**	-,184	,023	,444**	,563**
	Sig. (2-tailed)		,135	,295	,661	,003	,143	,852	,005	,000
AST U/L	Pearson Correlation	,169	1	,796**	,490**	,299**	-,282*	,234	,699**	,602**
	Sig. (2-tailed)	,135		,000	,000	,008	,023	,058	,000	,000
ALT U/L	Pearson Correlation	,119	,796**	1	,331**	,213	-,144	,257*	,534**	,498**
	Sig. (2-tailed)	,295	,000		,005	,061	,254	,037	,000	,000
LDH U/L	Pearson Correlation	,053	,490**	,331**	1	-,129	-,404**	,341**	,517**	,430**
	Sig. (2-tailed)	,661	,000	,005		,287	,001	,006	,001	,000
Potassium mmol/L	Pearson Correlation	,333**	,299**	,213	-,129	1	,081	-,220	,401*	,267*
	Sig. (2-tailed)	,003	,008	,061	,287		,521	,076	,013	,020
Albumin g/dl	Pearson Correlation	-,184	-,282*	-,144	-,404**	,081	1	-,351**	-,477**	-,402**
	Sig. (2-tailed)	,143	,023	,254	,001	,521		,006	,004	,001
Bilirubin total mg/dl	Pearson Correlation	,023	,234	,257*	,341**	-,220	-,351**	1	,252	,263*
	Sig. (2-tailed)	,852	,058	,037	,006	,076	,006		,165	,036
Uric asit mg/dl	Pearson Correlation	,444**	,699**	,534**	,517**	,401*	-,477**	,252	1	,751**
	Sig. (2-tailed)	,005	,000	,000	,001	,013	,004	,165		,000
Urea mg/dl	Pearson Correlation	,563**	,602**	,498**	,430**	,267*	-,402**	,263*	,751**	1
	Sig. (2-tailed)	,000	,000	,000	,000	,020	,001	,036	,000	

**. Correlation is significant at the 0.01 level (2-tailed).
*. Correlation is significant at the 0.05 level (2-tailed).

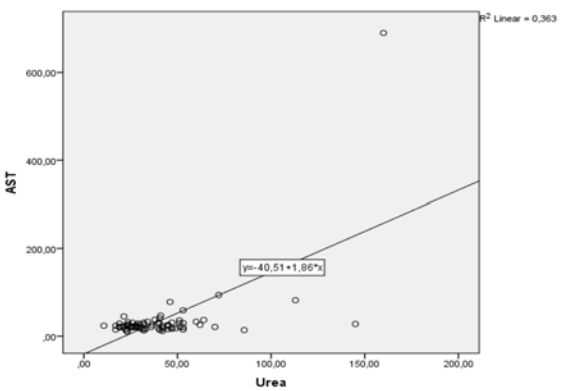

Figure 4. Serum ALT and Uric acid levels correlation.

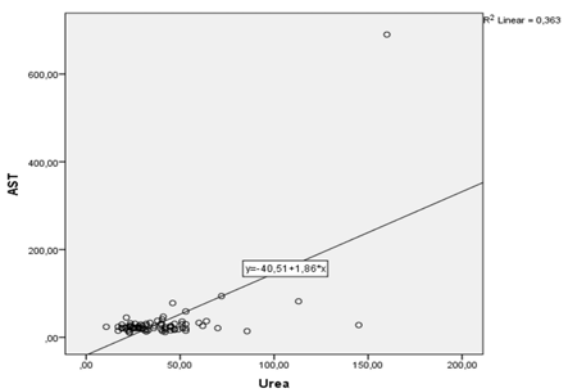

Figure 5. Serum AST and Urea levels correlation.

literature reviewed, skin cancer is more likely to occur in males than in females [14]. In a study in both women and men, the median diagnosis age was 71 years. NMSC is observed most often on the face and body [15]. The prevailing sites opened to strong sunlight, such as hands, the face, neck, and forearms [16]. Our study complies with this study, NMSC has occurred on face site, but the average age of skin cancer in our study was 60 years and low. According to another study, a significant increase in skin cancer in the province of Hatay requires serious attention to environmental factors and genetics. The risk factors for enlargement of skin cancers are going ultraviolet rays, ionizing radiation, human papillomavirus infections, infrared radiation, inorganic arsenic, trauma, immunosuppression, and genetic diseases. It reported that alcohol and smoking, nutrition, and obesity participated enlargement of various cancers such as skin cancers [14]. For all skin cancers, 60% of the cases and more were on the regions of skin most opened to the sun, corresponding to the face, scalp, and neck [17]. A rising tendency in inpatient NMSC and melanoma skin cancer of the head and neck region, correlating to an increase in reconstructive procedures applied in the inpatient setting and high expense load [18]. In our study, BCC lesions were commonly observed in the face-cheek region 30 % (29/96), nose 24 % (23/96), and lesions with SCC were most frequently in-ear region 28. 6% (10/35). Precaution actions such as using a broad-spectrum sunscreen, wearing protective dressing,

looking for shade, and limiting the time open-air during mid-day hours are very beneficial when started in early life [19]. Increasing the level of education and consciousness of people in less developed countries is crucial for early diagnosis of the patient and timely treatment to decrease the mortality of the illness [20]. From our literature reviews, people should attend to some scientific outcomes to live healthily and especially not get caught skin cancer. We do not recommend anyone go out in the open air between 10 am and 4 pm when the sun's rays are potent. Outdoor activities must perform in the morning or evening. People must use sunscreen even if they have a darker skin tone. Lips, ears, hands, and necks should not forget. Protective clothes must be wear. Tanning beds must be skipped. Medications must be checked. Protective moisturizers and makeup should be used throughout the year. If skin cancers are detected early, they can be treated successfully. People can go to the dermatologist once a year to do a skin cancer scan. It has described that the cancer tissue displayed a high ratio of aerobic glycolysis than other tissues, and it recommends the analysis of biochemical markers in neoplasm. Blood serum; alkaline phosphatase, lactate dehydrogenase, calcium, magnesium, and amylase studied in various cancers as potential diagnostic and prognostic biochemical markers. It was observed that AST and ALT as tumor markers used in the control of malignant of the head and neck and cervix uteri [21]. The serum LDH levels of the skin, lung, and bone marrow patients whose data we examined were statistically significant compared with the control group. A high increase in serum activities of ALT, AST, and GGT was noted in both liver and colon cancer patients relative to the control group and among cancer types. These enzymes can be used as tumor markers in the prognosis, diagnosis, and treatment of cancer, especially in colon and liver cancers [22]. In our study, a significant difference was in these enzyme levels after patients with skin and lung cancer diseases compared with the control group.

In the study based on the province of Siirt, the rate of males was higher than females in terms of lung and bone marrow cancers. Cancer increases with aging. The incidence of these cancers was lower than in western regions. The survival rate of lung cancers was lower than bone marrow cancers. While lung cancer is one of the deadliest cancers with five-year survival rates of at most 15%, the population (80% of the sample) believe that survival rates exceed 20% [10]. In 2013, For 5-year survival analysis, the number of patients with lung cancer was 23, and the number of patients with bone marrow cancer was 19. 16 (69.6%) of the lung cancer patients and 4 (21.1%) of the bone marrow cancer patients died. Two cancer groups were statistically different in terms of 5-years survival. Log Rank X2 = 8.68, $p = 0.003$, $p<0.05$. In this study, there was a statistically significant difference between lung cancer and bone marrow cancer patient's serum glucose, AST, GGT, LDH, urea levels compared with the control group serum parameters level, $p<0.05$. The Kaplan-Meier test was used for the survival comparison of patients in the two disease groups. There was a significant difference at $p <0.001$ level between the two groups. Because serum or plasma provides the physiological and pathological state, it offers the most useful studied biological substances for cancer biomarkers [23]. Breast cancer patients with high LDH levels have a 1.42-fold increased risk of death [24]. From our results, LDH and AST can be used as biochemical markers in skin cancers, lung cancers, and bone marrow cancer cases. LDH can be considered a good biomarker for the diagnosis of liver, muscular, and cancer diseases [25]. In this study, a positive correlation found between serum levels of AST and LDH, ALT and Uric acid, and AST and urea. Their levels increased correlatively. In this study, skin cancer patient's serum glucose, AST, ALT, sodium, bilirubin direct, bilirubin total, creatinine, urea level were statistically significantly different compared with the control group's serum parameters levels, $p <0.05$. Also, a statistically significant difference was between lung cancer and bone marrow cancer's serum glucose, AST, GGT, LDH, Urea levels, and the serum parameters of the control group, $p <0.05$. For this reason, it is important to study the biochemical parameters found to be statistically significant in all situations that show the symptoms of these diseases and to make their measurements more sensitive.

CONCLUSION

In conclusion, with our outcomes and the literature, the BCC and SCC observed ratio and the locations of them on the body were significant to comply with the literature and lower even though Siirt were in the Southeast region and takes too much sun in a day. Biochemical serum parameters measured in this article were convenient to investigate and detect skin, lung, and bone marrow, cancer patients. Besides, this study was retrospective, only the recorded in one state hospital data analyzed. Therefore, multicenter studies with large patient populations are also needed.

ACKNOWLEDGEMENT

This study was supported by Siirt University Scientific Research Projects Coordination (2017-SİÜSYO-66).

CONFLICT OF INTEREST

Authors approve that to the best of their knowledge, there is not any conflict of interest or common interest with an institution/organization or a person that may affect the review process of the paper.

AUTHOR CONTRIBUTION

Hasan Karagecili; Concept, Design, Supervision, Data collection and processing, Analysis, Writing the article, References and fundings

Emrah Yerlikaya; Supervision, Data collection and processing, Analysis, Critical review, References and fundings

Mustafa Oğuzhan Kaya; Supervision, Data collection and processing, Analysis, Literature review, Critical review

References

1. Nair M, Sandhu SS, Sharma AK. Cancer molecular markers: A guide to cancer detection and management. Semin Cancer Biol 52 (2018) 39–55.
2. Duartea AF, Pinto BS, Freitas A et al. Skin cancer healthcare impact: A nation-wide assessment of an administrative database. Cancer Epidemiol 56 (2018) 154–160.
3. Apalla Z, Lallas A, Sotiriou E et al. Epidemiological trends in skin cancer. Dermatol Pract Concept 7(2) (2017) 1-6.
4. Brunssen A, Waldmann A, Eisemann N et al. Impact of skin cancer screening and secondary prevention campaigns on skin cancer incidence and mortality: A systematic review. J Am Acad Dermatol 76 (2017) 129-39.
5. O'Sullivan DE, Brenner DR, Demers PA et al. Indoor tanning and skin cancer in Canada: A meta-analysis and attributable burden estimation. Cancer Epidemiol 59 (2019) 1–7.
6. Cho EA, Moloney FJ, Cai H et al. Safety and tolerability of an intratumorally injected DNAzyme, Dz13, in patients with nodular basal-cell carcinoma: a phase 1 first-in-human trial (DISCOVER). Lancet 381 (2013) 1835–43.
7. Chang NB, Feng R, Gao Z et al. Skin cancer incidence is highly associated with ultraviolet-B radiation history. Int J Hyg Envir Heal 213 (2010) 359–368.
8. Didona D, Paolino G, Bottoni U et al. Non Melanoma Skin Cancer Pathogenesis Overview. Biomedicines (2018); 6(1): 6. DOI: 10.3390/biomedicines6010006.
9. Kansara S, Bell D, Weber R. Surgical management of non melanoma skin cancer of the head and neck. Oral Oncology 100 (2020) 1044853.
10. Ziebarth N.R. Lung cancer risk perception biases. Preventive Medicine 110 (2018) 16–23.
11. Götte M, Kovalszky I. Extracellular matrix functions in lung cancer, Matrix Biol (2017), https://doi.org/10.1016/j.matbio.2018.02.018.
12. Mu C.F, Shen J, Liang J, Zheng H.S, Xiong Y, Wei Y.H, Fanzhu Li. Targeted drug delivery for tumor therapy inside the bone marrow. Biomaterials 155 (2018) 191-202.
13. Kayabaşoğlu G. An Alternative Flap Approach For Auricle Reconstruction. Sakaryamj 3(1) (2013) 32-35.
14. Arıca S, Nazlıcan E, Özer C et al. The frequency and distribution of cancer cases in Hatay District in 2008. J Clin Exp Invest 2(2) (2011) 192-195.
15. Eisemann N, Waldmann A, Geller AC et al. Non-Melanoma Skin Cancer Incidence and Impact of Skin Cancer Screening on Incidence. J Invest Dermatol 134 (2014) 43-50.
16. Armstrong BK, Cust AE. Sun exposure and skin cancer, and the puzzle of cutaneous melanoma A perspective on Fears et al. Mathematical models of age and ultraviolet effects on the incidence of skin cancer among whites in the United States. American Journal of Epidemiology 1977; 105: 420–427. Cancer Epidemiol 48 (2017) 147–156.
17. Rubió-Casadevall J, Hernandez-Pujol AM, Ferreira-Santos MC et al. Trends in incidence and survival analysis in non-melanoma skin cancer from 1994 to 2012 in Girona, Spain: A population-based study. Cancer Epidemiol 45 (2016) 6–10.
18. Egeler SA, Huang A, Johnson AR et al. Regional incidence of and reconstructive management patterns in melanoma and nonmelanoma skin cancer of the head and neck: A 3-year analysis in the inpatient setting. Journal of Plastic, Reconstructive and Aesthetic Surgery 73 (2020) 507-515.
19. Chougule A, Hussain S, Agarwal DP. Prognostic and diagnostic value of serum pseudocholinesterase serum aspartate transaminase, and serum alanine transaminase in malignancies treated by radiotherapy. J Cancer Res Ther 4(1) (2008) 21-25.
20. Khazaei Z, Ghorat F, Jarrahi AM et al. Global incidence and mortality of skin cancer by histological subtype and ıts relationship with the human development ındex (HDI); An Ecology Study in 2018. World Cancer Research Journal 2019; 6: e1265.
21. AL-Janabi, AAHS, Ali ZQ, Noree ZM. Lactate dehydrogenase as an indicator of liver, muscular and cancer diseases. J Coast Life Med 3(7) (2015) 543-546.
22. Ojo O.C, Asaolu M.F, Akinlua I, Oyeyemi A.O, Atiba A.S. Serum Marker Enzymes Activities in Cancer Patients. Journal of Chemistry and Biochemistry December 4(2) (2016) 15-21.
23. Li X. et al. The effect of preoperative serum triglycerides and high-density lipoprotein-cholesterol levels on the prognosis of breast cancer. The Breast 32 (2017) 1-6.
24. Liu X. et al. Prognostic significance of pretreatment serum levels of albumin, LDH and total bilirubin in patients with nonmetastatic breast cancer Carcinogenesis, 36(2) (2015) 243–248.
25. McRee AL, Mays D, Kornides ML et al. Counseling About Skin Cancer Prevention Among Adolescents: What Do Parents Receive From Health Care Providers? J Adolescent Health 61 (2017) 533-536.